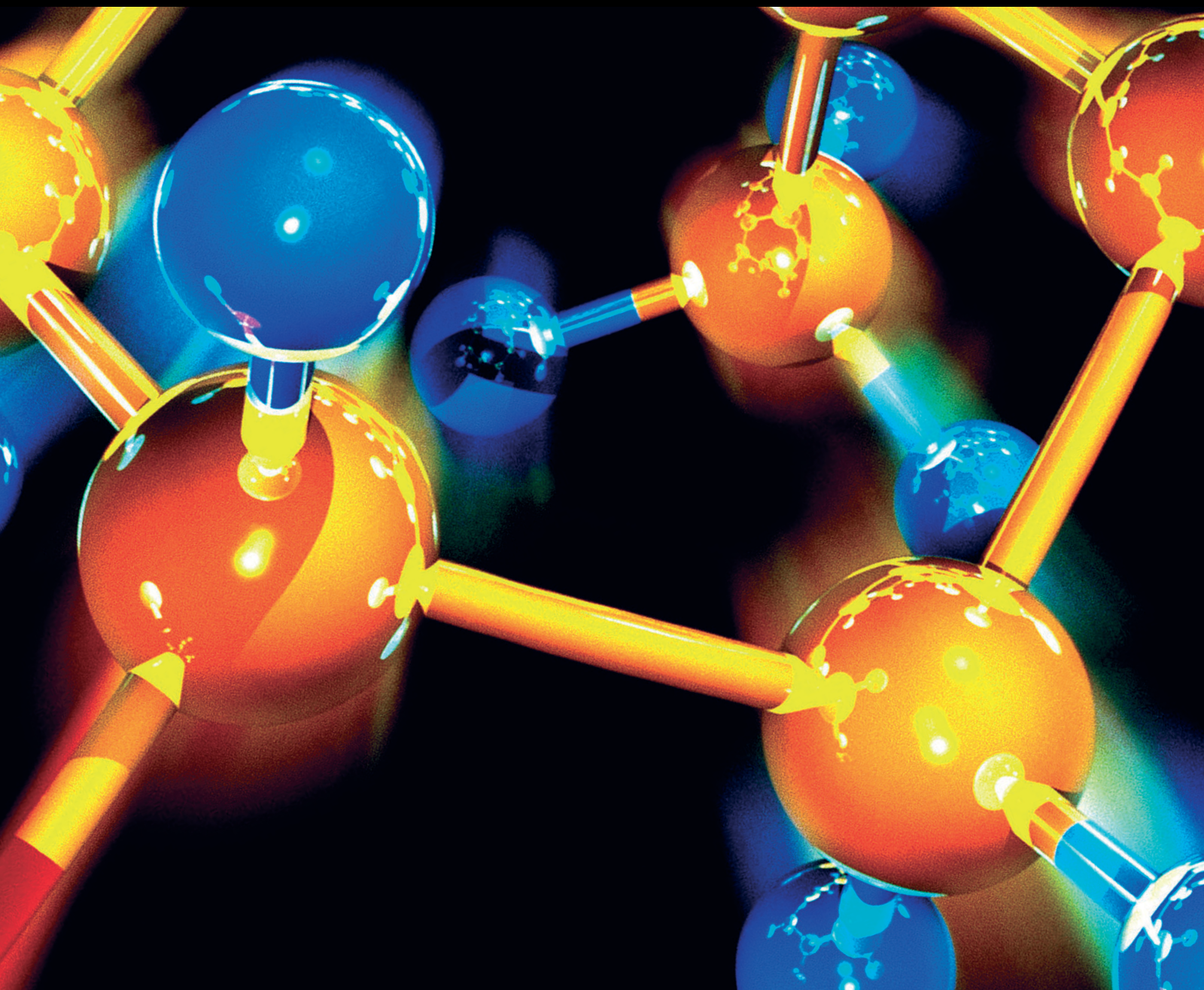


Composite/Hybrid Materials for Wastewater Treatments

Lead Guest Editor: Ibrahim H. Alsohaimi

Guest Editors: Mohamed R. Berber, Hassan M. A. Hassan, and Mohammad Saad Algamdi



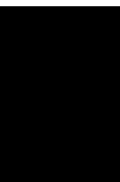


Composite/Hybrid Materials for Wastewater Treatments

**Composite/Hybrid Materials for
Wastewater Treatments**

Lead Guest Editor: Ibrahim H. Alsohaimi

Guest Editors: Mohamed R. Berber, Hassan M. A.
Hassan, and Mohammad Saad Algamdi



Copyright © 2020 Hindawi Limited. All rights reserved.

This is a special issue published in "Journal of Chemistry." All articles are open access articles distributed under the Creative Commons Attribution License, which permits unrestricted use, distribution, and reproduction in any medium, provided the original work is properly cited.

Chief Editor

Kaustubha Mohanty, India

Associate Editors

Mohammad Al-Ghouti, Qatar


Tingyue Gu , USA

Teodorico C. Ramalho , Brazil

Artur M. S. Silva , Portugal

Contents

Separating and Characterizing Functional Nitrogen Degraders via Magnetic Nanoparticle-Mediated Isolation

Yujiao Sun , Meng Yin, Danyang Zheng, Lei Wang, Xiaohui Zhao, and Jie Li
Research Article (12 pages), Article ID 1841364, Volume 2020 (2020)



Current Advances of Polymer Composites for Water Treatment and Desalination

Mohamed R. Berber 
Review Article (19 pages), Article ID 7608423, Volume 2020 (2020)


Assessment of Sewage Water Treatment Using Grinded Bauxite Rock as a Robust and Low-Cost Adsorption

Mutairah Shaker Alshammari 
Research Article (5 pages), Article ID 7201038, Volume 2020 (2020)


Ultrasonic-Assisted Synthesis and Characterization of Chitosan-Graft-Substituted Polyanilines: Promise Bio-Based Nanoparticles for Dye Removal and Bacterial Disinfection

Mutairah Shaker Alshammari , Amr A. Essawy , A. M. El-Nggar, and S. M. Sayyah
Research Article (9 pages), Article ID 3297184, Volume 2020 (2020)

Continuous Adsorption Modeling and Fixed Bed Column Studies: Adsorption of Tannery Wastewater Pollutants Using Beach Sand

Ghita El Mouhri , Mohammed Merzouki, Hajar Belhassan, Youssef Miyah, Halima Amakdouf, Rabea Elmoutassir, and Anissa Lahrichi
Research Article (9 pages), Article ID 7613484, Volume 2020 (2020)



Synthesis, Characterization, and Evaluation of Evaporated Casting MWCNT/Chitosan Composite Membranes for Water Desalination

Mohammed Alsuhybani, Ahmed Alshahrani , and Ahmed S. Haidyrah
Research Article (9 pages), Article ID 5207680, Volume 2020 (2020)

Environmentally Friendly and Recyclable Natural-Mediator-Modified Magnetic Nanoparticles for Laccase-Catalyzed Decolorization

Kun Zhang, Yeying Wu, Juan Huang , and Youxun Liu 
Research Article (12 pages), Article ID 4140565, Volume 2019 (2019)

Adsorption of COD in Coking Wastewater on Nitric Acid-Modified Blue Coke Activated Carbon

Xu Jiang , Xinzhe Lan, Yonghui Song, and Xiangdong Xing 
Research Article (11 pages), Article ID 8593742, Volume 2019 (2019)

Synthesis of a Superhydrophobic Polyvinyl Alcohol Sponge Using Water as the Only Solvent for Continuous Oil-Water Separation

Junyong Chen, Junhui Xiang , Xian Yue, Huaxin Li, and Xianbo Yu
Research Article (8 pages), Article ID 7153109, Volume 2019 (2019)

Research Article

Separating and Characterizing Functional Nitrogen Degraders via Magnetic Nanoparticle-Mediated Isolation

Yujiao Sun , Meng Yin, Danyang Zheng, Lei Wang, Xiaohui Zhao, and Jie Li

College of Water Science, Beijing Normal University, Beijing 100875, China

Correspondence should be addressed to Yujiao Sun; sun201405@163.com

Received 25 December 2019; Revised 7 March 2020; Accepted 9 March 2020; Published 14 April 2020

Guest Editor: Ibrahim H. Alsohaimi

Copyright © 2020 Yujiao Sun et al. This is an open access article distributed under the Creative Commons Attribution License, which permits unrestricted use, distribution, and reproduction in any medium, provided the original work is properly cited.

Magnetic nanoparticle-mediated isolation (MMI) is a new method for isolating active functional microbes from complex microorganisms without substrate labeling. In this study, the composition and properties of magnetic nanoparticles (MNPs) were characterized by a number of techniques, indicating that MNPs have characteristics such as microinterfaces and can be efficiently fixed on the surface of microbial cells. It also introduced the MMI technology in activated sludge after stable long-term treatment. With further addition of promotor carbon sources, the enrichment of the functional nitrogen degraders in MMI was significantly higher than in samples without MNPs, showing the advantages of MMI in identifying the active degraders. Redundancy analysis (RDA) also showed that the functional nitrogen degraders such as *Comamonadaceae_unclassified* and *Thiobacillus* absolutely dominated in situ ammonia degradation, and the change in dominant genera had the same trend as the degradation rate of ammonia nitrogen. In the magnetically functionalized system, the separated functional nitrogen degraders significantly improved ammonia nitrogen degradation efficiency, making it basically stable at more than 80%, up to 91.6%. These results prove that the complex flora created after the addition of MNPs is more adaptable to newly introduced pollutants, and MMI is a powerful tool for studying pollutant-degrading microorganisms under in situ conditions.

1. Introduction

With China's rapid industrial development, petrochemical, gas, pharmaceutical, and metallurgical industries have produced and will continue to produce vast amounts of wastewater that contain high concentrations of ammonia nitrogen. In 2015, the discharge of ammonia nitrogen pollutants was as high as 2.299 million tons [1]. The direct discharge of excessive ammonia nitrogen into water bodies causes eutrophication. Moreover, nitrate and nitrite, the oxidation products of ammonia, will affect aquatic ecosystems and human health [2]. Since 1998, China has revised a series of environmental quality standards to control the discharge of ammonia nitrogen and nitrate into water bodies. However, given the outdated industrial equipment and ineffective pollution control in China, large amounts of wastewater with excessive levels of ammonia continue to be discharged into water systems. Therefore, research on the removal of ammonia from water is crucial.

Biological denitrification is the most widely used nitrogen removal method because of its simple operation and excellent ammonia nitrogen removal rate. Moreover, biological denitrification does not produce secondary pollution. Some new methods with high efficiencies and low consumption have been applied to wastewater treatment in recent years [3]. These methods include simultaneous nitrification and denitrification, short-range nitrification and denitrification, and anaerobic oxidation.

Microorganisms that are involved in biological denitrification include ammonia-oxidizing Archaea (AOA), ammonia-oxidizing bacteria (AOB), and nitrite-oxidizing bacteria (NOB) [4]. AOB are Gram-negative autotrophs are widely found in soil, water, and sewage treatment systems [5]. There are two categories of AOB: β -proteobacteria, which includes *Nitrosomonas* and *Nitrosospira*, and γ -proteobacteria, which includes *Nitrosococcus* [6, 7]. Archaea has three main phyla: Euryarchaeota, Crenarchaeota, and Thaumarchaeota. AOA is another microorganism that can

oxidize ammonia nitrogen and is more dominant than AOB in nutrient-poor environments [8, 9]. AOA contains two main clusters: Thaumarchaeota groups I.1a and I.1b [10]. Pure strains of *Nitrosopumilus maritimus* SCM1 [11] and *Nitrosocaldus yellowstonii* [12] have been isolated. Pure cultures of *Candidatus Nitrosopumilus sediminis* AR2 [13], *Candidatus Nitrosoarchaeum limnia* SFB1 [14], *Candidatus Nitrosotalea devanaterri* [15], and *Candidatus Nitrosoarchaeum limnia* BG20 [16] have been obtained from hot springs, soils, and sediments and through enrichment. NOB are Gram-negative bacteria that complete the oxidation of nitrite to nitrate. The NOB *Nitrobacter* and *Nitrospira* are currently used in wastewater biological treatment [17–21].

The majority of microbes (>99%) with crucial environmental functions cannot be cultivated under standard laboratory conditions [22]. Ammonia nitrogen-degrading bacteria are particularly difficult to culture. Moreover, given the complexity of the microbial community structure, microorganisms cannot be effectively separated and cultured individually. Thus, studying the in situ ecological function of microorganisms using traditional culture methods is difficult. Magnetic nanoparticle-mediated isolation (MMI) is a cultivation-independent method which has been recently developed for the in situ separation of active functional microorganisms from complex microbial systems. As a universal tool for remote operation and control, the magnetic nanoparticles (MNPs) can be used to functionalize living cells, and the MNP functionalization of living cells can selectively control cells in vivo [23–25]. Therefore, this technology can provide a powerful tool to identify functional living cells. After all the microorganisms in the system are functionalized, a specific contaminant substance is added as the sole carbon source. Degrading bacteria will then use this material to multiply quickly, and during the process of microbial proliferation, the density of MNPs on its surface gradually decreases, thus eventually losing its magnetic properties and cannot be captured by an external magnetic field. After magnetic separation, functional bacteria are obtained to achieve in situ enrichment and separation of target microorganisms [26]. Microbial cells that have been isolated by this technique remain active and can be used in the study of microbial community structure and ecological functions.

Some scholars have used MNPs for the separation and screening of pollutant-degrading bacteria. For example, Wang et al. [27] used Fe_3O_4 MNP separation technology to study alkane-degrading bacteria in soil and experimentally confirmed that Oxalobacteraceae and Moraxellaceae are functional microorganisms in the degradation process. In this study, the composition and properties of the MNPs were characterized by some methods, and MMI was used for the first time in long-term domesticated activated sludge systems, adding urea as a carbon source to enhance the activity of ammonia nitrogen-degrading bacteria. MMI was used to realize the in situ separation of functional ammonia nitrogen-degrading bacteria, and its effect on ammonia nitrogen degradation in an activated sludge system after long-term domestication was studied. By high-throughput DNA sequencing, the microbial community structure was

analyzed to reveal the dominant microorganisms in the ammonia nitrogen degradation process. Our findings aim to provide a novel approach for improving the quality of activated sludge after long-term domestication.

2. Materials and Methods

2.1. Contaminated Sites and Sample Collection. Activated sludge was collected from a wastewater treatment plant (WWTP) in Shanxi Province, China ($38^{\circ}42'N$, $110^{\circ}10'E$). This plant uses sequencing batch reactor activated sludge process to treat domestic wastewater. The activated sludge was taken from a sequencing batch reactor in the field. The operating conditions of the reactor were stable at the time of sampling, and the removal rates of chemical oxygen demand (COD) and $\text{NH}_3\text{-N}$ were above 95%. The samples were filtered, centrifuged, and stored at 4°C for further study.

2.2. Synthesis and Characterization of MNPs. MNPs were synthesized according to a previously reported method [28]: 1 mL of FeCl_2 (1.0 M) was mixed with 2 mL of FeCl_3 (2.0 M). Then, 25 mL of NaOH (2.0 M) was added dropwise to the mixture. After 30 min of continuous shock, the black Fe_3O_4 composite MNPs were retrieved using a magnet and then washed with 30 mL of deionized water several times until the pH was neutral (7.0). The concentration of synthetic MNPs was 9.1 g/L.

The morphology of MNPs was investigated by scanning electron microscopy (SEM, S4800, Hitachi, Tokyo, Japan) and transmission electron microscopy (TEM, JEM-2100F, Jeol, Tokyo, Japan). The elemental composition and distribution were determined using TEM coupled with energy-dispersive X-ray spectroscopy (TEM-EDS, X-MAXN, HORIBA, Fukuoka, Japan). Nitrogen adsorption-desorption isotherms were obtained using a QUADRASORB SI Autosorb-SI analyzer (Quantachrome, Boynton, FL, USA); the analysis conditions were set to a degassing temperature of 100°C and a degassing time of 6 hours, and specific surface area and pore size distribution were evaluated by the Brunauer–Emmett–Teller (BET) method and the Barrett–Joyner–Halenda (BJH) method. X-ray diffraction (XRD) patterns of MNPs were recorded on a PANalytical B.V instrument (X'pert pro MPD, Almelo, Holland) using a Co source. XRD analysis was carried out to study the crystallinity of the MNPs on a diffractometer (X'pert pro MPD, Almelo, Holland) with nickel-filtered $\text{Cu K}\alpha$ X-ray photoelectron spectroscopy (XPS, ESCALAB 250XI, Thermo, MA, USA). The measurements were used to determine the compositions and chemical states of the MNPs. The magnetic properties were measured with a vibrating sample magnetometer (VSM-Versalab, Quantum Design, San Diego, USA).

2.3. Functionalization of Sludge Samples. The activated sludge was functionalized with MNPs according to a previously reported method [27]. Sludge and nanoparticle concentrations were determined as follows: 1.0 mL of synthetic MNPs was mixed with 0.01 to 1.099 mg of sludge

samples. After 5 min of slight shaking, and a magnet was used to attract the magnetized functional sludge. Microbial concentrations (copies/mL) in the supernatant and magnetic-functionalized sludge were determined by real-time fluorescence quantitative PCR (qPCR).

2.4. Biodegradation of Ammonia Nitrogen. There were four experimental groups: raw sludge with/without urea (CKU/CKN) and MNP-functionalized sludge with/without urea (MNPU/MNPN). Urea was added as the sole carbon source to the control reaction systems, and 20 mL of 20 g/L urea solution was added to the reaction system every 3 days. Ammonia nitrogen was maintained in a supersaturated state during the experiment. The experiment was conducted at 25°C for 40 days. Samples were collected on days 0, 5, 10, 20, 30, and 40 of the experiment. All the samples from CKU and CKN were directly stored for chemical and biological analysis. For water samples from MMI microcosms, the functional ammonia nitrogen-degrading bacteria were separated from the inert microbes by a magnet and remained in the aqueous phase (magnetic-free cells, MFCs), followed by chemical and biological analysis. MFCs from MNPN and MNPU samples were designated as MFCN and MFCU, respectively.

2.5. DNA Extraction, Amplification, and Sequencing. Sludge DNA was extracted using the phenol-chloroform extraction method. DNA samples were purified using a DNA product purification kit (TIANquick Midi Purification Kit, Tiangen, China). To determine fragment lengths, purified DNA was resolved via electrophoresis on 1% agarose gel. The concentration and purity (concentration > 50 ng/ μ L, OD 260/280 between 1.8 and 1.2) of DNA samples were quantified with an ND-2000 UV-Vis spectrophotometer (NanoDrop Technologies, USA).

Due to the moderate molecular size of 16S rRNA, its genetic sequence changes slowly during the evolution of organisms, which can be used to mark the evolutionary distance and kinship of organisms, becoming the most commonly used biomarker in current research [29]. To determine the microbial community structure, the fragments of hypervariable V3V4 variable region of 16S rRNA genes were amplified with a primer pair of 338F (5'-ACTCCTACGGGAGGCAGCAG-3') and 806R (5'-GGACTACHVGGGTWTCTAAT-3'). PCR reactions, containing 25 μ L 2x Premix Taq (Takara Biotechnology, Dalian Co. Ltd., China) and 1 μ L of each primer (10 mM) and 3 μ L DNA (20 ng/ μ L) template in a volume of 50 μ L were amplified by thermocycling: 5 min at 94°C; 30 cycles of 30 s at 94°C; 30 s at 52°C; and 30 s at 72°C; followed by 10 min at 72°C. The length and concentration of the PCR products were detected via 1% agarose gel electrophoresis, purified by EZNA Gel Extraction Kit (Omega, USA). Sequencing libraries were generated using NEBNext[®] Ultra[™] DNA Library Prep Kit for Illumina[®] (New England Biolabs, MA, USA) following manufacturer's recommendations, and index codes were added. Finally, the library was sequenced on an IlluminaHiSeq2500 platform and 250 bp paired-end reads

were generated. Sequence analysis was performed by Usearch software. Sequences with $\geq 97\%$ similarity were assigned to the same OTU. An OTU is thought to possibly represent a species.

2.6. Chemistry and Data Analysis. International standard methods [30] were used to measure NH_4^+ -N, NO_2^- -N, and NO_3^- -N. The data analysis was performed on Excel 2016. RDA was processed and plotted using CANOCO 4.5 to analyze the relationship between ammonia nitrogen degradation efficiency and the functional ammonia nitrogen-degrading bacteria.

3. Results and Discussion

3.1. MNP Characterization. The TEM images show the morphology and nanoparticle distribution of MNPs (Figure 1(a)). The synthesized MNPs were roughly globular and aggregated together because of magnetization (Figure 1(a)). The diameters of the MNP aggregates were in the range of 50–100 nm. As shown in Figure 1(b), the MNPs have a diameter of approximately 5–10 nm, which are much smaller than the diameter of the cell. Due to the small size effect and high surface energy, MNPs could be efficiently fixed on the surface of microbial cells. The MNPs had evident lattice fringes, and the crystalline composition was further elucidated by HRTEM. The interplanar distances of MNPs were 0.253 nm and 0.148 nm, corresponding to the (311) and (440) lattice planes of Fe_3O_4 , respectively. EDS mapping showed the distribution of elements (Figure 1(c)). Figure 1(d) clearly shows that C was mainly distributed in the space between particles, while O and Fe were uniformly distributed in the particles.

The representative XRD pattern of the obtained material is shown in Figure 2(a). The pattern had diffraction peaks at 2θ of 30.2°, 35.5°, 43.3°, 53.6°, 57.1°, 62.7°, and 74.2° which could be assigned to the (311), (222), (400), (422), (511), (440), and (533) planes of Fe_3O_4 (JCPDS 88-0315). The elemental composition and chemical states of the Fe_3O_4 @C/CNFs were further investigated by XPS analysis. According to the survey scan (Figure 2(b)), there were mainly three elements, which were C, O, and Fe. The O 1s spectrum (Figure 2(c)) had two peaks at 530.3 eV and 531.8 eV, corresponding to lattice oxygen (M-O) of Fe_3O_4 and hydroxyl groups (-O-H), respectively. The C 1s spectrum (Figure 2(d)) consisted of three peaks at 285.0 eV, 286.3 eV, and 288.9 eV, which correspond to carbon bonds (C-C), carbon oxygen bonds (C-O), and carbon hydrogen bonds (C-CO₃), respectively. Two peaks with binding energies at 711.5 eV and 724.9 eV were obtained in the Fe 2p spectrum (Figure 2(e)) and could verify the presence of Fe_3O_4 . Fe_3O_4 is a typical magnetic material, and the magnetic hysteresis loop of the obtained material at maximum field strength of 30 kOe is shown in Figure 2(f). The saturation magnetization (M_s) of the material was 22.01 emu/g, the coercivity (H_c) was 105.22 Oe, and the remnant magnetization (M_r) was 1.03 emu/g.

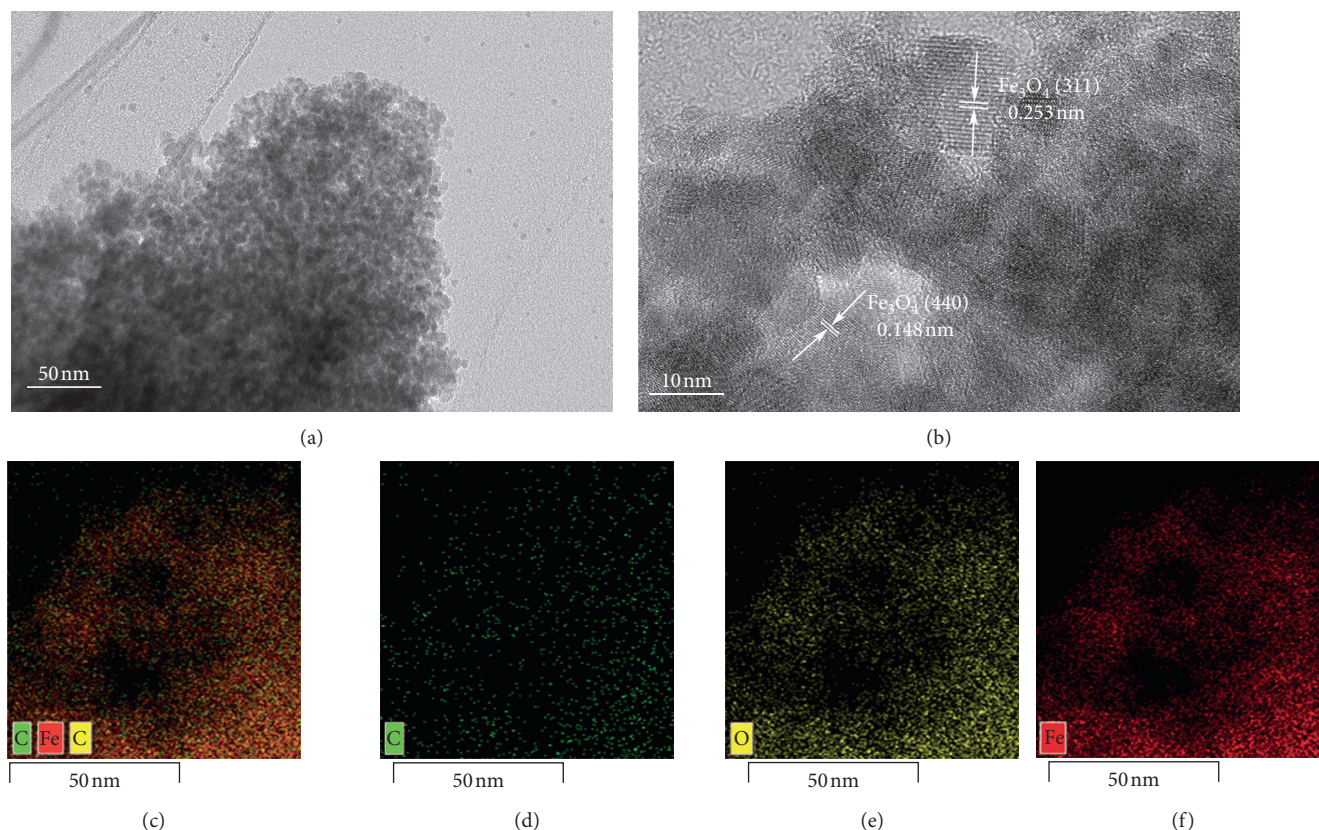


FIGURE 1: The TEM image (a), HRTEM image (b), EDS mapping layered image (c), element C layered image (d), element O layered image (e), and element Fe layered image (f) of the MNPs.

The N_2 adsorption-desorption isotherms of MNPs are shown in Figure 3. MNPs show type II adsorption isotherms, so the surface area was calculated as $213.180 \text{ m}^2/\text{g}$ by the BET method (inset). According to the BJH method, MNPs had typical micropores with pore widths of 0.57, 1.18, and 2.5–4.3 nm. The pore volume was $0.092 \text{ cm}^3/\text{g}$. In recent years, some researchers have developed a series of nanomaterials with nano- Fe_3O_4 as the core. For example, Kazemifard et al. [31] synthesized a series of magnetic KOH/ Fe_3O_4 at Al_2O_3 core-shell nanomaterials via the incipient wetness impregnation method, with a maximum surface area of $20.46 \text{ m}^2/\text{g}$. Bangari et al. [32] developed Fe_3O_4 -functionalized boron nitride nanosheets with a surface area of $119 \text{ m}^2/\text{g}$. It can be seen that the surface area of these materials is much smaller than the MNPs prepared by the coprecipitation method in this paper, while the comparatively large surface area and pore volume provide more exposure opportunities and adsorption spaces. This also provides a large contact area between the magnetic nanoparticles and the cells.

3.2. Optimal Conditions for the MNP Functionalization of Sludge Microcosm. Microbes in activated sludge are attracted to synthetic MNPs via strong electrostatic interactions [33]. Magnetic hysteresis loop data (Figure 2(f)) show that MNPs have an extremely strong magnetic force, and magnetic separation can be achieved with conventional

permanent magnets. Sludge magnetic functionalization results also showed that cells functionalized with MNPs were highly magnetic and could be readily collected. To achieve the highest magnetic functionalization efficiency using the lowest amount of MNPs, the optimal weight ratio of sludge to MNPs (from 0.01 to 1,099, w/w) was quantitatively analyzed using qPCR. The functional efficiency of the sludge was expressed as the ratio of the number of microorganisms in the sludge to the total (supernatant and sludge) microbiological quantity. In this study, 100% magnetic functionalization efficiency of the sludge indicated that all the microorganisms in the sludge were magnetically functionalized, whereas 0% indicated that no sludge bacteria were magnetically functionalized. The magnetic functionalization efficiency of the sludge is shown in Figure 4. The results showed that when the ratio of sludge to MNPs was less than 549 (w/w), magnetic functionalization efficiency exceeded 90%. When the ratio of sludge to MNPs exceeded 604 (w/w), the magnetic functionalization efficiency decreased rapidly. When the ratio increased to 1099 (w/w), magnetic functionalization efficiency was only 27.9%. The low magnetic functionalization efficiency likely resulted from the large sizes of the sludge particles or microbial cells. Also, microbial cells are functionalized by MNPs via the interaction of MNPs with functional groups, such as carboxyl groups ($-\text{COOH}$), thiol ($-\text{SH}$), and amino groups ($-\text{NH}_2$), on microbial cell membranes [27, 34]. Given that all microbial cells have functional groups, magnetic functionalization is

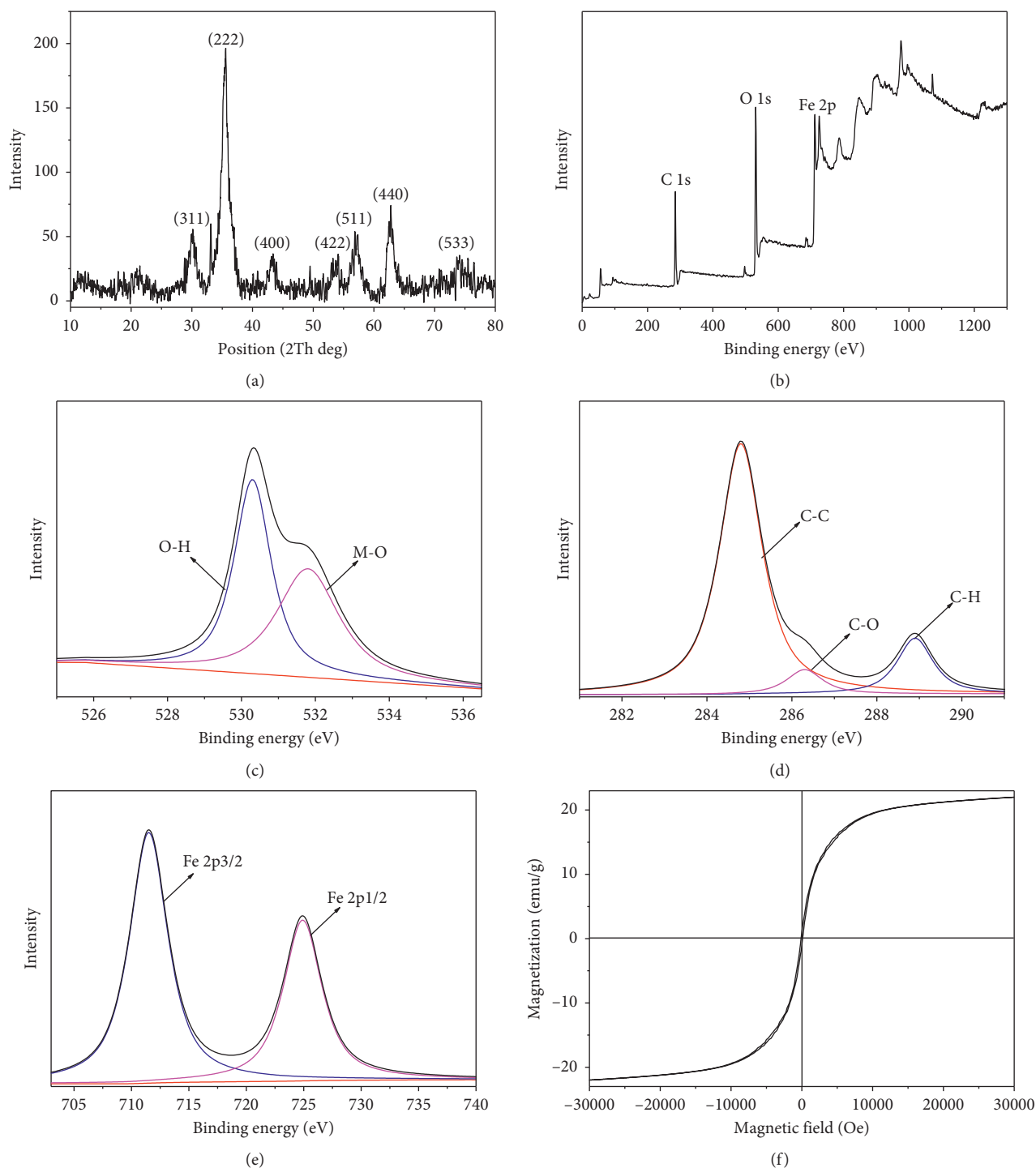


FIGURE 2: XRD patterns (a); survey scan (b); O 1s (c), C 1s (d), and Fe 2p (e) XPS spectra; and magnetic hysteresis loop (f) of MNPs.

not selective, and all microbial cells can be magnetized. Based on the results of the optimization experiment, 5 g of sludge was mixed with 9.1 mg of MNPs for ammonia nitrogen biodegradation experiments.

3.3. Ammonia Nitrogen Degradation Experiment. The degradation of ammonia and the change in the concentrations of nitrite and nitrous nitrogen are shown in Figures 5 and 6.

The concentration of ammonia nitrogen showed a significant decrease with time in all groups added with urea (CKU and MNPU), while nitrate nitrogen and nitrite nitrogen accumulate continuously, indicating that there are a large number of active ammonia-oxidizing bacteria in the system [21]. Ammonia-oxidizing bacteria convert ammonia nitrogen into nitrite via ammonification, and nitrifying bacteria convert nitrite to nitrate via nitrification. It can also be seen from Figure 5 that the ammonia nitrogen degradation

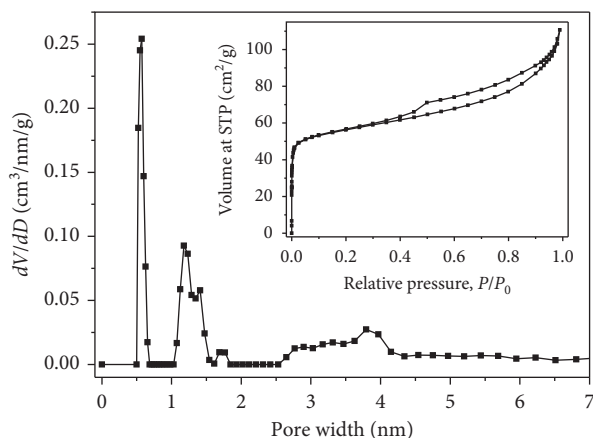


FIGURE 3: The pore size distribution and N_2 adsorption-desorption isotherms of the MNPs.

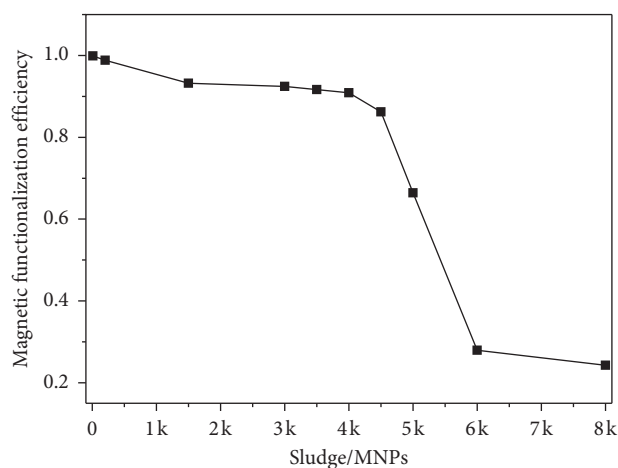


FIGURE 4: Sludge magnetic functionalization efficiency against the ratio of sludge to MNPs (0.1~10,000, w/w).

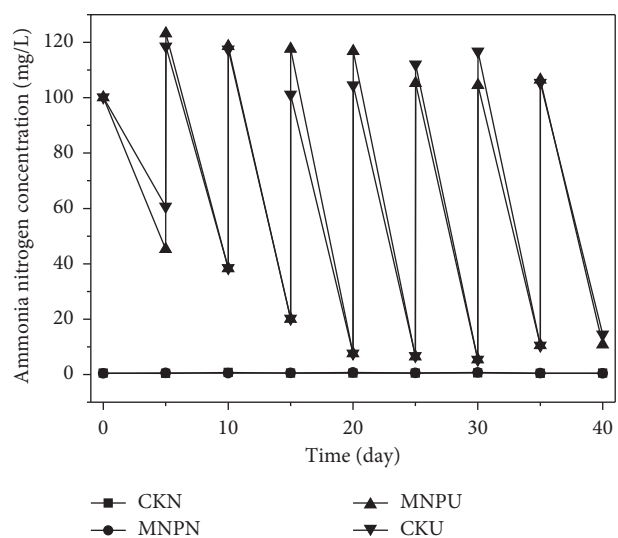


FIGURE 5: The degradation process of ammonia nitrogen, where arrows indicate the addition of ammonia to the reaction system.

efficiency of the two groups with or without MNPs increased gradually as the reaction progressed. After 20 days, the degradation efficiency exceeded 90%, indicating that MNPs had no effect on the bacterial activities or the ammonia nitrogen degradation performance [26]. And this is similar to the results of separation of functional alkane degradation agents using magnetic nanoparticles by Wang et al. [27]. The long-term acclimated sludge already contains a large number of target pollutant-degrading microorganisms. From Figure 6, it can be seen that after introducing a new pollutant, urea, in the long-term domesticated sludge, the concentrations of nitrate nitrogen and nitrite nitrogen were slightly higher than the samples without MNPs, indicating that functional microorganisms in the process of pollutant degradation can be enriched more thoroughly by adding MNPs in this system, and then the conversion of ammonia nitrogen into nitrous nitrogen and nitrate nitrogen may be promoted more completely. Therefore, the addition of MNPs can improve the quality of long-term acclimated sludge and make it more suitable for newly introduced pollutants.

3.4. Microbial Community and Diversity Analysis

3.4.1. Microbial Diversity in the Samples. High-throughput sequencing analysis was performed with DNA from CKN, CKU, MNPN, and MNPU samples. The microbial diversity index (Shannon) is obtained, and the results are shown in Figure 7. Shannon is the index commonly used to estimate microbial diversity and reflect alpha diversity in a sample. The larger the Shannon value, the higher the community diversity.

The Shannon indexes of microbial diversity in CKN and CKU were not significantly different. The former ranged from 8.38 to 8.75, and the latter ranged from 8.42 to 8.65. On day 0, the Shannon indexes of MFCN and MFCU were similar at 3.32 and 3.64, respectively. The Shannon index of MNPN did not significantly change (3.19–3.32) during the experiment; this finding indicates that the number of microbial communities remained stable in this system. The Shannon index of MNPU gradually increased (3.64–5.12) as the experiment progressed, indicating that more microorganisms with ammonia nitrogen degradation function appeared in this process. Compared with the system without MNPs, it shows that only a part of the microorganisms can degrade ammonia nitrogen in this microbial community. On the contrary, it also shows that MMI can effectively isolate active functional microorganisms to improve the sludge quality after long-term domestication and make it more adaptable to external environmental changes.

3.4.2. Community Composition Analysis at the Phylum Level. Microbial classification based on phylum is shown in Figure 8. There was no significant difference between CKN and MNPN treatments, indicating no microbial community change in the groups with or without MNP functionalization. Thus, MNP functionalization did not change the microbial activities or community structure.

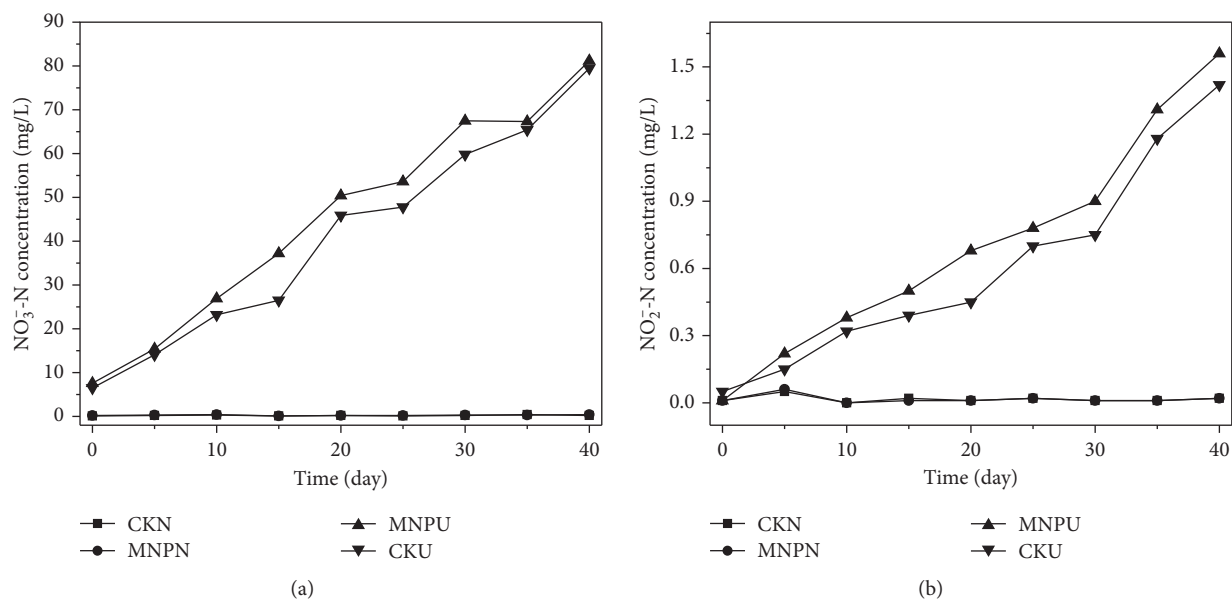


FIGURE 6: The nitrate (a) and nitrous nitrogen (b) concentration changes, respectively.

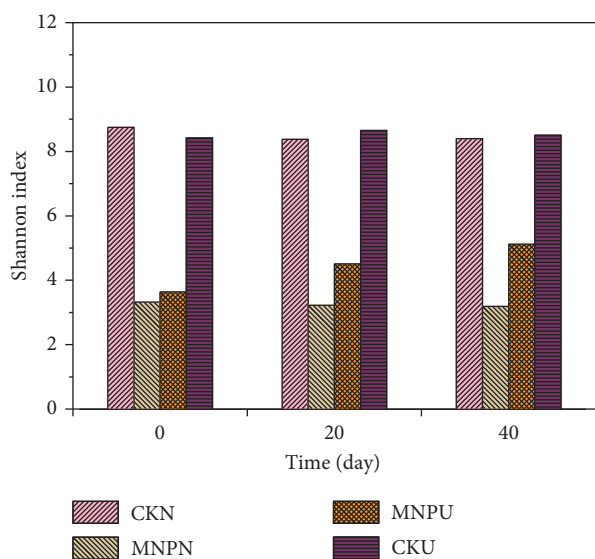


FIGURE 7: Microbial diversity index (Shannon).

Sequence comparison in the constructed libraries revealed that the dominant bacterial phyla include Proteobacteria, Chloroflexi, Bacteroidetes, Spirochaetae, Firmicutes, and Gemmatimonadetes. Proteobacteria (44.3%–65.1%) was the absolute dominant population in all samples [35]. Proteobacteria species are facultative or obligate anaerobes and are Gram-negative bacteria [36]. As reported by Wang et al. [37], in samples of activated sludge collected from a domestic sewage treatment plant after traditional long-term domestication, Proteobacteria finally accounted for 67.3% of total effective bacterial sequences, which was consistent with the result observed in this study. Proteobacteria include ammonia-oxidizing, nitrite-oxidizing, and denitrifying bacteria, which play an important role in the biological removal of nitrogen [38]. In CKU and MNPU, the

number of Proteobacteria gradually increased from 49.9% (MNPU-0) and 48.9% (CKU-0) to 65.0% (MNPU-30) and 63.2% (CKU-30). On the one hand, the increasing degradation rate of ammonia nitrogen indicates that ammonia- and nitrite-oxidizing Proteobacteria can use urea as a carbon source. On the other hand, it also shows that the addition of MNPs has a certain enrichment effect on functional microorganisms. During days 30–40 of the reaction, the number of Proteobacteria decreased to 61.1% (MNPU-40) and 60.8% (CKU-40); this decrease likely resulted from the decreased nutrient availability in the system at the late stages of the experiment. The decrease mentioned above may facilitate the increase of autotrophic bacteria, such as Firmicutes and Bacteroidetes; these phyla occupy some of the ecological niches of Proteobacteria [39]. In CKN and MNPN, the number of Proteobacteria gradually decreased. This result could also be attributed to dwindling carbon and nutrient concentrations in the system, and heterotrophic microorganisms are also less likely to survive as the carbon nutrient source decreases, thus changing microbial diversity.

Chloroflexi accounted for 6.0%–14.3% of the bacterial phyla in the system. Chloroflexi comprise Gram-negative and facultative or obligate anaerobic bacteria, with important roles in the degradation of organic matter (such as COD_{Cr}) [40]. In the four experimental groups, the number of Chloroflexi decreased during the later stages of the experiment. This decrease may be related to the gradual depletion of organic matter.

Bacteroidetes (8.3%–11.2%) are the third most dominant bacterial phylum in the reaction system. Bacteroidetes include Gram-negative, organic-nutritive bacteria, and some nitrogen-resistant bacteria (such as Sphingobacteria) that are implicated in denitrification. Certain Bacteroidetes species can also hydrolyze complex solid organic matter, such as proteins and lipids [41]. Hence, in CKU and MNPU, the number of Bacteroidetes gradually increased as the

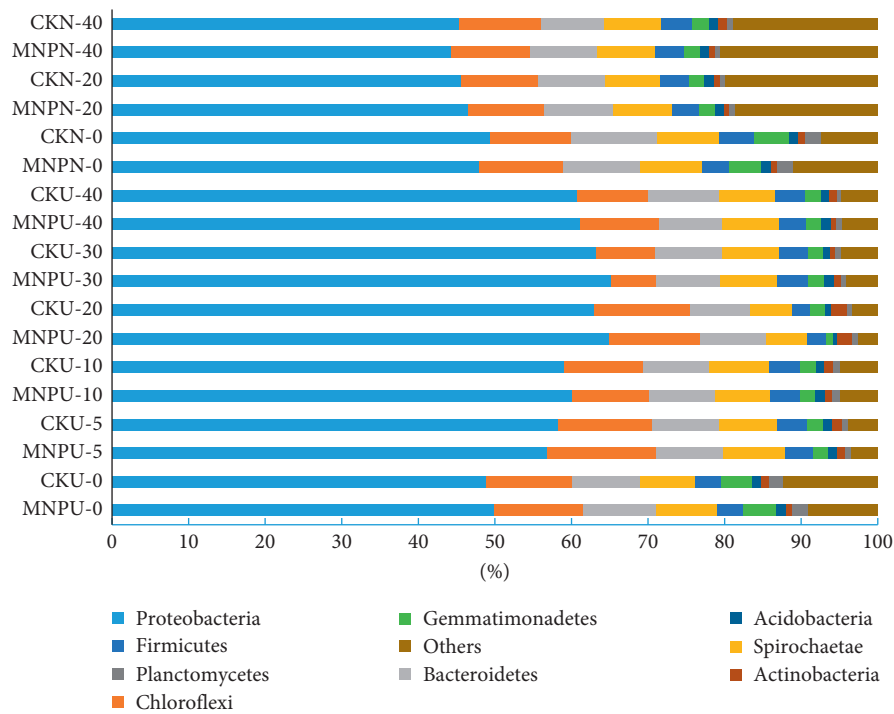


FIGURE 8: Classification of microbes according to phylum.

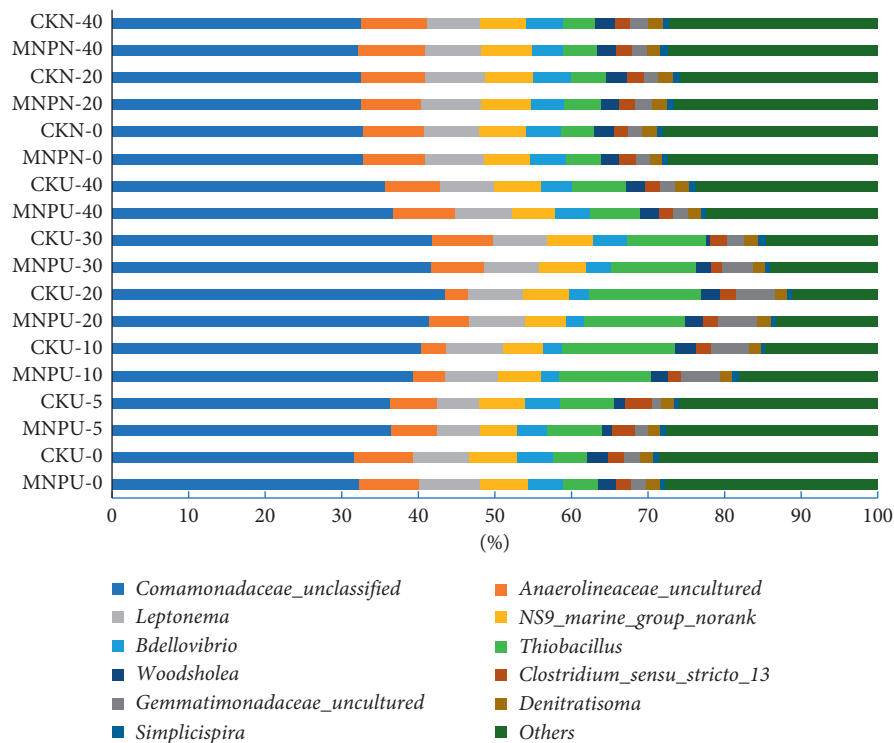


FIGURE 9: Classification of microbes according to family and genus.

experiment progressed. The increase in the number of Bacteroidetes is related to its two functions mentioned above. However, in CKN and MNPN, the number of Bacteroidetes decreased significantly. This decrease is likely related to the decrease in organic matter concentration.

3.4.3. Community Composition Analysis at the Family and Genus Levels. In order to understand the effect of MNPs on the community structure during ammonia nitrogen degradation, the bacterial community composition was also analyzed at the taxonomic level of the family and genus (Figure 9).

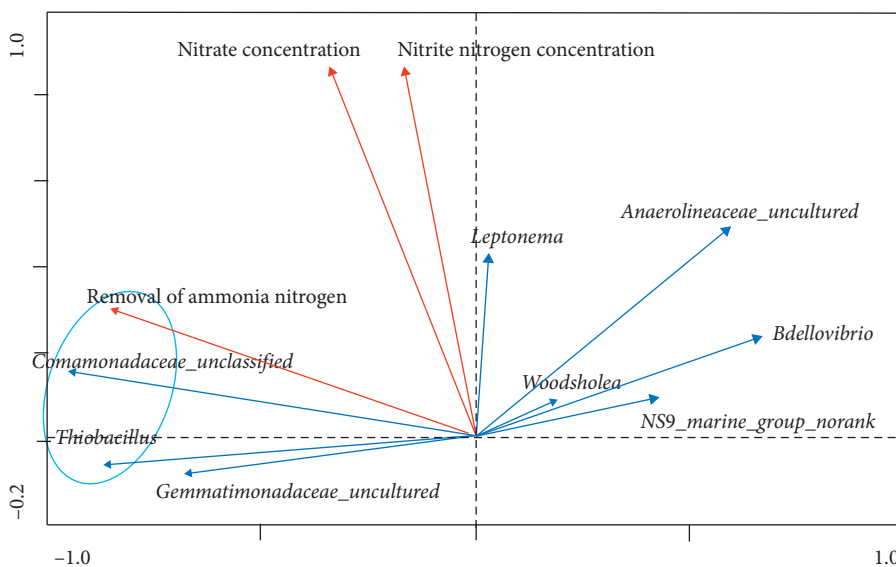


FIGURE 10: RDA analysis of advantage bacterium and major environmental factor.

The dominant genera included *Comamonadaceae_unclassified* (32.2%–43.5%), *Thiobacillus* (4.4%–15.0%), *Anaerolineaceae_uncultured* (3.1%–8.6%), *Leptonema* (5.5%–8.1%), *NS9_marine_group_norank* (5.2%–6.6%), *Bdellovibrio* (2.3%–4.9%), *Gemmatimonadaceae_uncultured* (1.2%–5.2%), and *Woodsholea* (0.7%–2.8%).

In MNPU and CKU, the population of *Comamonadaceae_unclassified*, *Thiobacillus*, *Leptonema*, and *Gemmatimonadaceae_uncultured* and the degradation rate for ammonia nitrogen gradually increased from the start of the reaction to approximately 30 days of the experiment. After 30 days, the bacterial population and degradation rate both decreased.

Among them, the changes in the numbers of β -Proteobacteria *Comamonadaceae_unclassified* and *Thiobacillus* were the most obvious. In addition, Park et al. [42] observed that in the process of processing high-intensity nitrogen wastewater through a hollow fiber-membrane biofilm reactor system, the *Comamonadaceae* and *Thiobacillus* were also the dominant bacteria. *Comamonadaceae_unclassified*, which has excellent ammonia-degrading ability, is present in nitrification-denitrification activated sludge [43]. *Thiobacillus* is mainly present in sediments and moist soils. *Thiobacillus denitrificans* in genus *Thiobacillus* is a sulfur autotrophic and denitrifying bacterium [2]. *T. denitrificans* is a common bacterium in sewage treatment. *T. denitrificans* utilizes nitrates as electron acceptors to produce nitrogen under limited carbon conditions. This microbe also oxidizes sulfur-containing compounds to form sulfates [44, 45]. Figure 9 shows that the population of *Thiobacillus* significantly increased at all stages (MNPU: 7.3% to 15.0%; CKU: 7.2% to 12.2%). This increase is related to the strong nitrate-reducing capacity of *Thiobacillus*. Therefore, *Comamonadaceae_unclassified* and *Thiobacillus* should dominate the degradation of ammonia nitrogen. In the experimental group with MNPs, the active nitrogen degraders gradually lost their magnetic properties due to splitting, and remained

in the MFCU component. Therefore, the populations of these two bacteria were higher in MNPU than CKU, which further confirms that the MNPs had a good aggregation effect on the functionalized degradation bacteria.

The population of *Leptonema* and *Gemmatimonadaceae_uncultured* increased with the degradation rate of ammonia nitrogen. This change, however, was not very obvious. *Leptonema* belongs to Leptospirosis. *Gemmatimonadaceae_uncultured* is a class of Gram-negative bacteria. Zhang et al. [46] successfully isolated *Gemmatimonas aurantiaca*, which belongs to Gemmatimonadaceae, and found that it has a high capacity for phosphorus degradation. At present, studies on these two bacteria are limited.

In addition, *Anaerolineaceae_uncultured*, which belongs to Chloroflexi, was present in the reaction system. This microbe, which can degrade carbohydrates, amino acids, and other cell materials, is usually present in the soil. Studies have also shown that this microbe can decrease the concentration of sulfide and ammonia in the soil [47]. Guo et al. [48] found that *Anaerolineaceae_uncultured* and *NS9_marine_group_norank* were relatively rich in a sequencing batch reactor (PNSFD-SBR), and both *Anaerolineaceae_uncultured* and *NS9_marine_group_norank* dominated the sludge fermentation and denitrification process. Moreover, the population of these two bacterial species initially decreased and then increased. This pattern likely occurred because the bacteria gradually adapted to the new environment in the process, thus improving nitrogen removal.

Bdellovibrio is a class of parasites that can infect and attack microorganisms and cause microbial cleavage. *Bdellovibrio* has a strong ability to lyse protein and can use the amino acids of host cells to grow and reproduce [49]. These bacteria are ubiquitous in nature and can be detected in sewage, sediments, and contaminated rivers at various stages of treatment.

From Figures 8 and 9, the increase and decrease of dominant bacteria in CKN were consistent with MNPN, indicating that the MNPs do not adversely affect ammonia nitrogen degradation. In the meantime, the external carbon source promoted the succession of the sludge community structure via long-term domestication, and the addition of MNPs improved the community structure to a certain extent and made it more adaptive to changes in the external environment.

3.4.4. RDA Analysis of Dominant Bacterium. Figure 10 shows the RDA of the dominant bacterium and major environmental factors. It provided further evidence that *Comamonadaceae_unclassified* and *Thiobacillus* were highly correlated with the ammonia nitrogen removal rate. It has been proved again that MNPs have a good aggregation effect on functional degrading bacteria. This method provides opportunities for deeper insights into the actual roles and ecological traits of the activated sludge and helps in effective management for WWTPs.

4. Conclusions

In the present study, the functional nitrogen degraders were identified from the active sludge after long-term treatment. We found that the degradation efficiency of ammonia nitrogen gradually increased with the progress of the reaction in the two experimental groups with an added carbon source. Ten days after the start of the reaction, the degradation rate of ammonia nitrogen exceeded 80% and with a maximum value of 91.6%. The degradation rates in MNPU were higher than those in other samples, which indicated that MNPs enriched the numbers of ammonia nitrogen-degrading bacteria and increased the degradation rate of ammonia nitrogen.

High-throughput sequencing revealed that the Shannon indexes of CKU, CKN, and MNPN were stable over the whole experimental period. However, the Shannon index of MNPU increased continuously during the reaction, indicating that functional nitrogen degraders gradually dominated the reaction system and that the MNPs successfully separated ammonia nitrogen-degrading bacteria from the system.

Analysis of the microbial community structure revealed that at the phylum level, Proteobacteria, Chloroflexi, and Bacteroidetes dominated the microbial community. At the family and genus levels, *Comamonadaceae_unclassified*, *Thiobacillus*, and *Anaerolineaceae_uncultured* dominated. RDA showed that *Comamonadaceae_unclassified* and *Thiobacillus* were identified as the functional nitrogen degraders in the system. The differences in the community structure of the nitrogen degraders between groups with or without MNPs suggested that MMI is an efficient method for identifying functional yet uncultivable degraders for contaminant in situ. Our work also proves that the addition of MNPs can improve the long-term acclimated sludge and make it more adaptable to the newly introduced pollutants.

Data Availability

All data analyzed or generated during the study are included within the article.

Conflicts of Interest

The authors declare that they have no conflicts of interest.

Acknowledgments

This research was supported by the National Natural Science Foundation of China (Grant no. 51378064) and “Double First-class” Project Fund of Beijing Normal University.

References

- [1] Ministry of Environmental Protection of the People's Republic of China, *China State of the Environment Bulletin*, Ministry of Environmental Protection, Beijing, China, 2015.
- [2] M. Chen, X.-F. Zhou, Y.-Q. Yu et al., “Light-driven nitrous oxide production via autotrophic denitrification by self-photosensitized *Thiobacillus* denitrificans,” *Environment International*, vol. 127, pp. 353–360, 2019.
- [3] F. Zhang, Y. Peng, Z. Wang, and H. Jiang, “High-efficient nitrogen removal from mature landfill leachate and waste activated sludge (WAS) reduction via partial nitrification and integrated fermentation-denitrification process (PNIFD),” *Water Research*, vol. 160, pp. 394–404, 2019.
- [4] Z. Wang, X. Zhang, X. Lu et al., “Abundance and diversity of bacterial nitrifiers and denitrifiers and their functional genes in tannery wastewater treatment plants revealed by high-throughput sequencing,” *PLoS One*, vol. 9, no. 11, Article ID e113603, 2014.
- [5] T. Zhang, L. Ye, A. H. Y. Tong, M.-F. Shao, and S. Lok, “Ammonia-oxidizing archaea and ammonia-oxidizing bacteria in six full-scale wastewater treatment bioreactors,” *Applied Microbiology and Biotechnology*, vol. 91, no. 4, pp. 1215–1225, 2011.
- [6] I. M. Head, W. D. Hiorns, T. M. Embley, A. J. McCarthy, and J. R. Saunders, “The phylogeny of autotrophic ammonia-oxidizing bacteria as determined by analysis of 16S ribosomal RNA gene sequences,” *Journal of General Microbiology*, vol. 139, no. 6, pp. 1147–1153, 1993.
- [7] A. Teske, E. Alm, J. M. Regan, S. Toze, B. E. Rittmann, and D. A. Stahl, “Evolutionary relationships among ammonia- and nitrite-oxidizing bacteria,” *Journal of Bacteriology*, vol. 176, no. 21, pp. 6623–6630, 1994.
- [8] I. Kasuga, H. Nakagaki, F. Kurisu, and H. Furumai, “Pre-dominance of ammonia-oxidizing archaea on granular activated carbon used in a full-scale advanced drinking water treatment plant,” *Water Research*, vol. 44, no. 17, pp. 5039–5049, 2010.
- [9] S. Leininger, T. Urich, M. Schloter et al., “Archaea predominate among ammonia-oxidizing prokaryotes in soils,” *Nature*, vol. 442, no. 7104, pp. 806–809, 2006.
- [10] G. W. Nicol and C. Schleper, “Ammonia-oxidising Crenarchaeota: important players in the nitrogen cycle?” *Trends in Microbiology*, vol. 14, no. 5, pp. 207–212, 2006.
- [11] M. Könneke, A. E. Bernhard, J. R. de la Torre, C. B. Walker, J. B. Waterbury, and D. A. Stahl, “Isolation of an autotrophic ammonia-oxidizing marine archaeon,” *Nature*, vol. 437, no. 7058, pp. 543–546, 2005.

- [12] J. R. de la Torre, C. B. Walker, A. E. Ingalls, M. Könneke, and D. A. Stahl, "Cultivation of a tmophilic ammonia oxidizing archaeon synthesizing crenarchaeol," *Environmental Microbiology*, vol. 10, no. 3, pp. 810–818, 2008.
- [13] S.-J. Park, G. Rohit, M.-C. Ana-Belen et al., "Genomes of two new ammonia-oxidizing archaea enriched from deep marine sediments," *PLoS One*, vol. 9, no. 5, Article ID e96449, 2014.
- [14] P. C. Blainey, A. C. Potanina, C. A. Francis, and S. R. Quake, "Genome of a low-salinity ammonia-oxidizing archaeon determined by single-cell and metagenomic analysis," *PLoS One*, vol. 6, no. 2, Article ID e16626, 2011.
- [15] L. E. Lehtovirta-Morley, K. Stoecker, A. Vilcinskas, J. I. Prosser, and G. W. Nicol, "Cultivation of an obligate acidophilic ammonia oxidizer from a nitrifying acid soil," *Proceedings of the National Academy of Sciences*, vol. 108, no. 38, pp. 15892–15897, 2011.
- [16] A. C. Mosier, E. E. Allen, M. Kim, S. Ferreira, and C. A. Francis, "Genome sequence of "Candidatus Nitrosoarchaeum limnia" BG20, a low-salinity ammonia-oxidizing archaeon from the san francisco bay estuary," *Journal of Bacteriology*, vol. 194, no. 8, pp. 2119–2120, 2012.
- [17] Z. Huang, P. B. Gedalanga, P. Asvapathanagul, and B. H. Olson, "Influence of physicochemical and operational parameters on *Nitrobacter* and *Nitrospira* communities in an aerobic activated sludge bioreactor," *Water Research*, vol. 44, no. 15, pp. 4351–4358, 2010.
- [18] D.-J. Kim and S.-H. Kim, "Effect of nitrite concentration on the distribution and competition of nitrite-oxidizing bacteria in nitrification reactor systems and their kinetic characteristics," *Water Research*, vol. 40, no. 5, pp. 887–894, 2006.
- [19] H.-P. Kooops and A. Pommerening-Röser, "Distribution and ecophysiology of the nitrifying bacteria emphasizing cultured species," *Fems Microbiology Ecology*, vol. 37, no. 1, pp. 1–9, 2001.
- [20] R. Nogueira and L. F. Melo, "Competition between *Nitrospira* spp. and *Nitrobacter* spp. in nitrite-oxidizing bioreactors," *Biotechnology and Bioengineering*, vol. 95, no. 1, pp. 169–175, 2006.
- [21] S. Siriping and B. E. Rittmann, "Diversity study of nitrifying bacteria in full-scale municipal wastewater treatment plants," *Water Research*, vol. 41, no. 5, pp. 1100–1120, 2007.
- [22] T. Kaerberlein, K. Lewis, and S. S. Epstein, "Isolating "uncultivable" microorganisms in pure culture in a simulated natural environment," *Science*, vol. 296, no. 5570, pp. 1127–1129, 2002.
- [23] R. F. Fakhruddin and V. N. Paunov, "Fabrication of living cellosomes of rod-like and rhombohedral morphologies based on magnetically responsive templates," *Chemical Communications*, vol. 18, no. 18, pp. 2511–2513, 2009.
- [24] A. K. F. Dyab, M. Ozmen, M. Ersoz, and V. N. Paunov, "Fabrication of novel anisotropic magnetic microparticles," *Journal of Materials Chemistry*, vol. 19, no. 21, pp. 3475–3481, 2009.
- [25] X. Zhao, H. Li, A. Ding, G. Zhou, Y. Sun, and D. Zhang, "Preparing and characterizing Fe_3O_4 @cellulose nanocomposites for effective isolation of cellulose-decomposing microorganisms," *Materials Letters*, vol. 163, pp. 154–157, 2015.
- [26] D. Zhang, J. P. Berry, D. Zhu et al., "Magnetic nanoparticle-mediated isolation of functional bacteria in a complex microbial community," *The ISME Journal*, vol. 9, no. 3, pp. 603–614, 2015.
- [27] X. Wang, X. Zhao, H. Li et al., "Separating and characterizing functional alkane degraders from crude- oil-contaminated sites via magnetic nanoparticle-mediated isolation," *Research in Microbiology*, vol. 167, no. 9–10, pp. 731–744, 2016.
- [28] D. Y. Zhang, R. F. Fakhruddin, M. Özmen et al., "Functionalization of whole-cell bacterial reporters with magnetic nanoparticles," *Microbial Biotechnology*, vol. 4, no. 1, pp. 89–97, 2014.
- [29] T. Coenye and P. Vandamme, "Intragenomic heterogeneity between multiple 16S ribosomal RNA operons in sequenced bacterial genomes," *FEMS Microbiology Letters*, vol. 228, no. 1, pp. 45–49, 2003.
- [30] American Public Health Association, *APHA Standard Methods for the Examination of Water and Wastewater*, American Public Health Association, Washington, DC, USA, 1998.
- [31] S. Kazemifard, H. Nayebzadeh, N. Saghatoleslami, and E. Safakish, "Assessment the activity of magnetic $\text{KOH}/\text{Fe}_3\text{O}_4/\text{Al}_2\text{O}_3$ core-shell nanocatalyst in transesterification reaction: effect of Fe/Al ratio on structural and performance," *Environmental Science and Pollution Research*, vol. 25, no. 32, pp. 32811–32821, 2018.
- [32] R. S. Bangari, A. K. Singh, S. Namsani, J. K. Singh, and N. Sinha, "Magnetite-coated boron nitride nanosheets for the removal of arsenic(V) from water," *ACS Applied Materials & Interfaces*, vol. 11, no. 21, pp. 19017–19028, 2019.
- [33] X. Y. Cui, J. Yin, Y. Lin, N. Li, M. Wang, and D. S. Shen, "Towards a definition of harmless nanoparticles from an environmental and safety perspective," *Journal of Chemistry*, vol. 2016, Article ID 8608567, 12 pages, 2016.
- [34] Z. Lin, Y. Xu, Z. Zhen et al., "Application and reactivation of magnetic nanoparticles in *Microcystis aeruginosa* harvesting," *Bioresource Technology*, vol. 190, pp. 82–88, 2015.
- [35] Z. Wang, Y. Yang, Y. Dai, and S. Xie, "Anaerobic biodegradation of nonylphenol in river sediment under nitrate-or sulfate-reducing conditions and associated bacterial community," *Journal of Hazardous Materials*, vol. 286, pp. 304–314, 2015.
- [36] Y. Yang, Y. Dai, Z. Wu, S. Xie, and Y. Liu, "Temporal and spatial dynamics of archaeal communities in two freshwater lakes at different trophic status," *Frontiers in Microbiology*, vol. 7, 2016.
- [37] B. Wang, M. Zhao, Y. Guo, Y. Peng, and Y. Yuan, "Long-Term partial nitrification and microbial characteristics in treating low C/N ratio domestic wastewater," *Environmental Science: Water Research & Technology*, vol. 4, no. 6, pp. 820–827, 2018.
- [38] M. Kumar and J.-G. Lin, "Co-existence of anammox and denitrification for simultaneous nitrogen and carbon removal-Strategies and issues," *Journal of Hazardous Materials*, vol. 178, no. 1–3, pp. 1–9, 2010.
- [39] H. Lu, Z. Xue, P. Saikaly, S. P. Nunes, T. R. Bluver, and W.-T. Liu, "Membrane biofouling in a wastewater nitrification reactor: microbial succession from autotrophic colonization to heterotrophic domination," *Water Research*, vol. 88, pp. 337–345, 2016.
- [40] L. M. C. Daniel, E. Pozzi, E. Foresti, and F. A. Chinalia, "Removal of ammonium via simultaneous nitrification-denitrification nitrite-shortcut in a single packed-bed batch reactor," *Bioresource Technology*, vol. 100, no. 3, pp. 1100–1107, 2009.
- [41] V. R. Hill, A. M. Kahler, N. Jothikumar, T. B. Johnson, D. Hahn, and T. L. Cromeans, "Multistate evaluation of an ultrafiltration-based procedure for simultaneous recovery of enteric microbes in 100-liter tap water samples," *Applied and Environmental Microbiology*, vol. 73, no. 13, pp. 4218–4225, 2007.

- [42] J.-H. Park, O. Choi, T.-H. Lee, H. Kim, and B.-I. Sang, "Pyrosequencing analysis of microbial communities in hollow fiber-membrane biofilm reactors system for treating high-strength nitrogen wastewater," *Chemosphere*, vol. 163, pp. 192–201, 2016.
- [43] A.-J. Li, S.-F. Yang, X.-Y. Li, and J.-D. Gu, "Microbial population dynamics during aerobic sludge granulation at different organic loading rates," *Water Research*, vol. 42, no. 13, pp. 3552–3560, 2008.
- [44] W. Tao, J. Wen, Y. Han, and M. P. Huchzermeier, "Nitrogen removal in constructed wetlands using nitrification/anammox and nitrification/denitrification: effects of influent nitrogen concentration," *Water Environment Research*, vol. 84, no. 84, pp. 2099–2105, 2012.
- [45] M. G. Prokopenko, M. B. Hirst, L. De Brabandere et al., "Nitrogen losses in anoxic marine sediments driven by Thioploca-anammox bacterial consortia," *Nature*, vol. 500, no. 7461, pp. 194–198, 2013.
- [46] H. Zhang, Y. J. Sekiguchi, S. Hanada et al., "Gemmatimonas aurantiaca gen. nov., sp. nov., a Gram-negative, aerobic, polyphosphate-accumulating micro-organism, the first cultured representative of the new bacterial phylum Gemmatimonadetes phyl. nov.," *International Journal of Systematic and Evolutionary Microbiology*, vol. 53, no. 4, pp. 1155–1163, 2003.
- [47] T. Yamada, Y. Sekiguchi, H. Imachi, Y. Kamagata, A. Ohashi, and H. Harada, "Diversity, localization, and physiological properties of filamentous microbes belonging to Chloroflexi subphylum I in mesophilic and thermophilic methanogenic sludge granules," *Applied and Environmental Microbiology*, vol. 71, no. 11, pp. 7493–7503, 2005.
- [48] Y. Guo, Y. Peng, B. Wang, B. Li, and M. Zhao, "Achieving simultaneous nitrogen removal of low C/N wastewater and external sludge reutilization in a sequencing batch reactor," *Chemical Engineering Journal*, vol. 306, no. 15, pp. 925–932, 2016.
- [49] S. Feng, C. H. Tan, F. Constancias et al., "Predation by Bdellovibrio bacteriovorus significantly reduces viability and alters the microbial community composition of activated sludge flocs and granules," *FEMS Microbiology Ecology*, vol. 93, no. 4, Article ID fix020, 2017.

Review Article

Current Advances of Polymer Composites for Water Treatment and Desalination

Mohamed R. Berber ^{1,2}

¹Department of Chemistry, College of Science, Jouf University, Sakaka, Saudi Arabia

²Department of Chemistry, Faculty of Science, Tanta University, Tanta 31527, Egypt

Correspondence should be addressed to Mohamed R. Berber; mrberber@science.tanta.edu.eg

Received 17 December 2019; Revised 12 February 2020; Accepted 17 February 2020; Published 13 April 2020

Academic Editor: James Barker

Copyright © 2020 Mohamed R. Berber. This is an open access article distributed under the Creative Commons Attribution License, which permits unrestricted use, distribution, and reproduction in any medium, provided the original work is properly cited.

Over the past five years, a lot of research activities in polymer composites were done in order to improve environmental sustainability and to present advantages for commercial applications of water treatment and desalination. Polymers offered tunable properties, improved processability, remarkable stability, high surface area for fast decontamination, selectivity to eliminate different pollutants, and cost-cutting of water treatment. Hence, the development of polymeric materials is one of the future directions to meet the environmental water standards and to supply the water requirements of the growing populations. This review highlighted the very recent achievements in fabrication, characterization, and applications of polymeric composites used for water treatment and desalination. The polymeric modifications, the addition of functional groups, and the assemblies of nanomaterials were also discussed in detail. In particular, great attention was paid to the recent advances in polymer/polymer composites, polymer/carbon composites, and polymer/clay composites, presenting their usage in the removal of various types of contaminants, e.g., metal ions, dyes, and other toxic pollutants. The review also summarized the main advantages and disadvantages of the different adsorbent materials. Specific attention was paid to the mechanism of adsorption, including chemisorption and physisorption mechanisms. In addition, the challenges and the future perspectives were identified to reach the optimal performance of the different adsorbents.

1. Introduction

Polymer composites are defined as a combination of polymers with other organic or inorganic materials to provide new material with target properties, like low density, toughness, stiffness, thermal behavior, chemical and mechanical stability, and other specific properties depending on the target of use. A lot of polymer composites were introduced with significant use in water treatment and desalination, including graphene-based composites, carbon-based composites, and clay-based composites [1–3].

The polymer composite research was offered due the need for materials with better adsorption and removal characteristics of metal ions, dyes, and other toxic pollutants. The polymers used for these composites have been mainly classified on the basis of source (natural and synthetic polymers) and also on the basis of structure (linear,

branched, and crosslinked polymers). This review describes the source and the structure of these polymers and their composites, properties, and applications in water treatment and desalination as follows [4–8].

2. Polymer-Polymer Composites

Polymers are organic materials with a number of excellent characteristics, namely, high mechanical strength, remarkable flexibility, chemical stability, and high surface area. These properties made polymers work as a host for different organic and inorganic materials. Thus, we became able to synthesize different composites with target properties. Hence, polymer composites have attracted much attention for water treatment and desalination. Polymer-polymer composites offered the possibility of tuning the adsorptive properties through blending, crosslinking, and surface

functionalizing. The main advantages of this category of composites are the simplicity of preparation and applications, the high chemical stability at the harsh operation conditions, the use for the removal of a wide range of pollutants, and the good recyclability with high adsorption capacities. However, on the other hand, the main drawback is still the high cost of production.

2.1. Polymer-Based Adsorbents for Dye Removal. A lot of polymer-polymer composites were synthesized and offered for the purpose of dyes removal from wastewater. For example, Elkady et al. synthesized a copolymer of styrene and acrylonitrile through a solution polymerization process. The obtained copolymer was fabricated to a nanofiber through an electrospinning technique. Then, the surface of this nanofiber was functionalized by the chemical addition of carboxylic acid groups to improve the dyes absorptivity [9]. The scanning electron microscopy (SEM) confirmed the changes of the nanofiber after the functionalization process, indicating a uniform shape for the carboxylated nanofibers compared to the nonfunctionalized nanofibers. These morphological changes affected the adsorption process of dyes from wastewater. Specifically, the adsorption capacity of the basic violet dye reached 67.11 mg/g in less than 30 min after the surface modification of the nanofiber.

With no doubt, the low specific surface area and the lack of surface porosity of these two polymers could not be the key factors to achieve such adsorption. Hence, it can be said that the charged groups created on the surface of the copolymer as well as the morphological changes of the nanofiber structure have played important roles to reach such high adsorption value. In this regard, a low-cost, multifunctional, and straw based adsorbent was synthesized by immobilizing ternary carboxylic acid and acrylamide units on straw powders. As reported in this study, the abundant carboxyl and amino groups added to the composite structure have provided a high adsorption capacity of dyes removal. In particular, the adsorption capacities for MB and MO reached 120.84 and 3053.48 mg/g, respectively, which were 3 and 54 times higher than those of unmodified straw [10].

Cyclodextrin-based composites have also drawn a wide attention as a new generation of adsorbents for dye removal from wastewater due to their extraordinary physicochemical properties and cavities [11–13]. These advanced structural properties of cyclodextrin composites promoted the practical industrial application compared to native cyclodextrin itself [14]. The recent advances of these novel composite materials were reviewed by Zhou et al. [15]. For example, cyclodextrin polymer was crosslinked with polydopamine to prepare an eco-friendly composite for the removal of different dyes. The high adsorption efficiency of these dyes was correlated to the new structural characteristics and the functional groups of the polymer composite [16]. β -Cyclodextrin immobilized with starch showed similar behavior for dye removal from wastewater [17]. The obtained irregular surface and the functional groups of the β -cyclodextrin-starch composite (i.e., COOH, NH₂, and OH) played significant roles in the dye capture and removal compared to each of β -cyclodextrin and starch separately. It is worth

noting that the pores as well as the functional groups of the composite have improved the interparticle diffusion and the electrostatic interaction of the dyes. Thus, a high adsorption value was attained. In a similar study, an efficient composite for dyes removal was successfully synthesized by grafting cyclodextrin and amino hyperbranched polymer onto cotton fibers. This composite also showed remarkable adsorption properties for dye removal thanks to the created functional groups [18].

In the same direction, cellulose extracted from agro-wastes was grafted with the monomers of 2-acrylamido-2-methylpropane sulfonic acid and acrylic acid in the presence of a crosslinker to obtain highly efficient polymer composites for dye removal. The SEM image of the obtained polymer composite (Figure 1) showed smooth and long fiber-like threads for untreated cellulose; however, in the case of the crosslinked graft copolymers, flaky and highly thick threads were obtained, indicating surface functionalization of cellulose. The adsorption behavior of this cellulose composite was investigated towards the elimination of cationic (malachite green and crystal violet) and anionic (Congo red; CR) dye from aqueous medium, studying the effect of different adsorption parameters. As discussed, the cationic dyes were removed at pH 7.0 in 90 min, while the anionic dye was adsorbed at pH of 2.2 in 8 h. The adsorption data fitted well the Langmuir isotherm and the pseudo-second-order model. This study showed that cellulose based copolymers can work as potential adsorbents for uptake of both anionic and cationic dyes from industrial wastewater [19]. Cellulose as a natural polymer was also functionalized with a hyperbranched polyethylenimine for selective removal and separation of different dyes. Specifically, polyethylenimine was covalently linked to the backbone of cellulose molecules through a Schiff-base formation. The NH₂ groups of polyethylenimine and the CHO groups on oxidized-cellulose were linked together, forming a polymer composite. The adsorption behavior of the formed composite was investigated for the elimination of CR and basic yellow dyes in aqueous media. The maximum adsorption capacity of Congo red dye reached 2100 mg/g and 1860 mg/g for basic yellow dye. The composite also showed selective adsorption of different dyes, including reactive red and brilliant blue; however, the absorptivity was very low for eosin and bright yellow dyes [20]. It is worthy of note that the hyperbranched structure of the polymer composite worked as a brush, improving the interparticle diffusion of some dye molecules into the composite (depending on the dye size). Thus, a higher adsorption capacity and selectivity is obtained.

In this regard, diethylenetriamine was incorporated with polyacrylonitrile using the electrospinning technique to prepare a composite with a high adsorption efficiency of dyes. The morphology of the prepared composite was investigated by SEM. After the composite formation, the surface of the nanofiber became rougher compared to the untreated fiber (see Figure 2). This roughness was a result of the incorporation of diethylenetriamine units. This chemical modification of the composite structure affected the removal efficiency of the direct dyes. Also, it is important to note that the amount of dye adsorbed had been affected by the ratio of

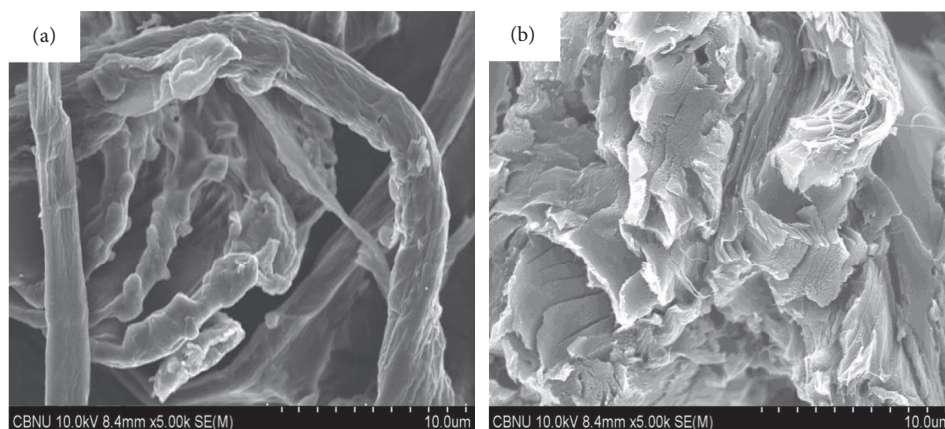


FIGURE 1: SEM images of cellulose (a) before and (b) after copolymerization with 2-acrylamido-2-methylpropane sulfonic acid and acrylic acid (reproduced with a permission from [19]).

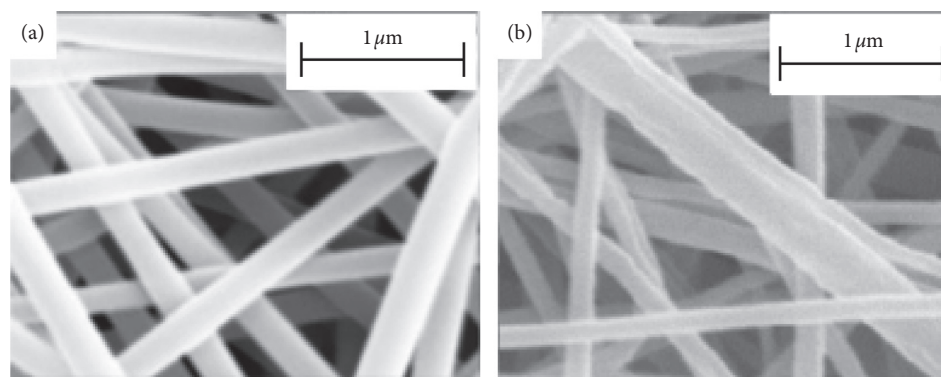


FIGURE 2: SEM images of diethylenetriamine incorporated with polyacrylonitrile (a) before and (b) after surface modification (reproduced with a permission from [21]).

the diethylenetriamine added to the composite, indicating how important the composition ratio is in the composite [21].

2.2. Polymer-Based Membranes for Desalination and Oil Removal. Desalination process is a technique for the removal of mineral components from saline water. For that target, many polymer composites were introduced with high potential. For example, a composite membrane of polyvinyl alcohol, cellulose acetate, and polyethylene glycol was prepared and introduced for desalination of groundwater and extremely saline seawater. The values of both water flux and salt rejection were evaluated as a measure of membrane efficiency. The antimicrobial activity was also evaluated for different types of bacteria. The composite membrane showed excellent performance for the desalination of groundwater and the saline water. The flux reduction was reduced significantly when polyethylene glycol was added to the composite structure. The composite structure showed a remarkable performance for antimicrobial activity [22].

In a recent study, a composite membrane was prepared by the addition of p-nitrophenol (PNP) as a plasticizer to cellulose triacetate. The properties of this membrane were tuned to improve its use for desalination as follows. The

pristine cellulose triacetate membrane was firstly soaked in a PNP solution and then rinsed with water to obtain the target membrane. This modified membrane showed a reduced salt flux without disclosing the water flux. Accordingly, it showed improved water-salt selectivity [23]. The structural characteristics of cellulose triacetate and modified cellulose triacetate films were evaluated through photo images and polarized optical microscopy images (see Figures 3(a) and 3(b)). Typically, the pristine cellulose triacetate film showed whiteness and opaqueness (Figure 3(a) upper panel), indicating the presence of a crystalline region as confirmed by the birefringence of Figure 3(b) (upper panel). This crystalline structure disappeared in the swelled cellulose triacetate film due to the presence of PNP moieties (Figure 3(a), middle panel). The water rinsing led to the retrieval of the whiteness and the impermeable properties of the cellulose triacetate film and also the birefringence (Figures 3(a) and 3(b), lower panels), indicating the recrystallization of the cellulose triacetate polymer chains.

The role of PNP treatment in tuning transport properties during the desalination process was illustrated in Figure 4. As seen from image a, untreated cellulose triacetate membrane contained a large crystallite region embedded into an amorphous region. Then when soaked into PNP (Figure 4(b)), both the crystalline and the amorphous

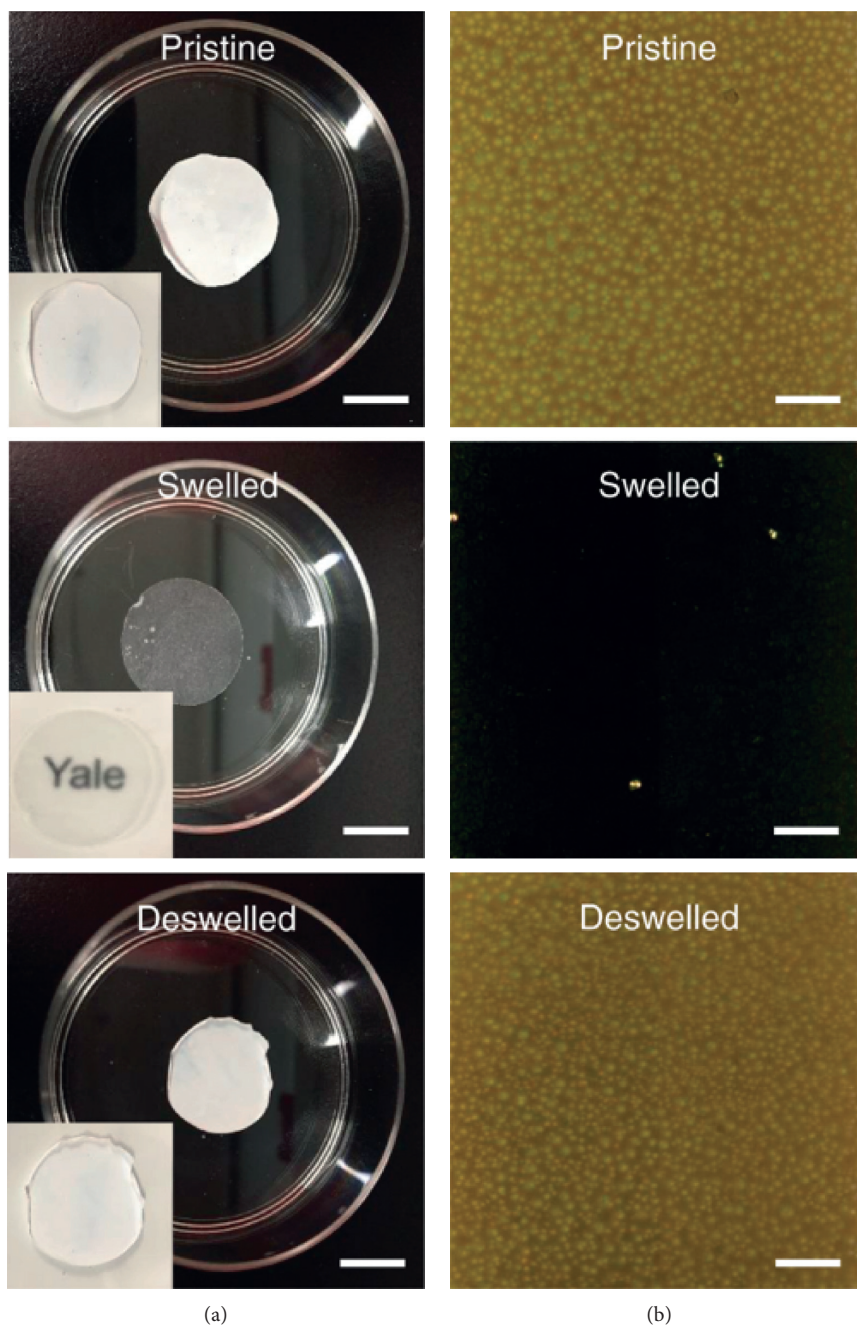


FIGURE 3: (a) Digital photos and (b) polarized optical microscopy images of cellulose triacetate and modified cellulose triacetate films (reproduced with a permission from [23]).

regions swelled where PNP worked as a plasticizer to enhance the chains flexibility. When the polymer matrix was rinsed with water, a rearrangement of the cellulose triacetate chains was obtained, leading to a recrystallization process of the polymer chains (Figure 4(c)). This process formed smaller crystallites; thus, an increase in the amorphous and crystalline regions is obtained. Hence a reduction in the number of nonselective pathways is obtained.

Quaternary ammonium modified polystyrene resins were prepared to improve the oil removal capability of polystyrene. Specifically, the quaternary ammonium

surfactants were firstly ion-exchanged with the sulfonic acid groups of polystyrene resin. The formed composite was then grafted with hexadecyl pyridinium, hexadecyltrimethyl ammonium, and tetrabutyl ammonium bromides to change the surface electrostatic and hydrophobic characteristics of the resin. This process made the resin more reactive for the removal the oil droplets by the coalescence filtration process, because a strong hydrophobic and less negative charged resin is obtained [24]. In this regard, Xuanyi Tang et al. prepared a composite of fibric peat modified by hexadecyltrimethylammonium bromide to improve the

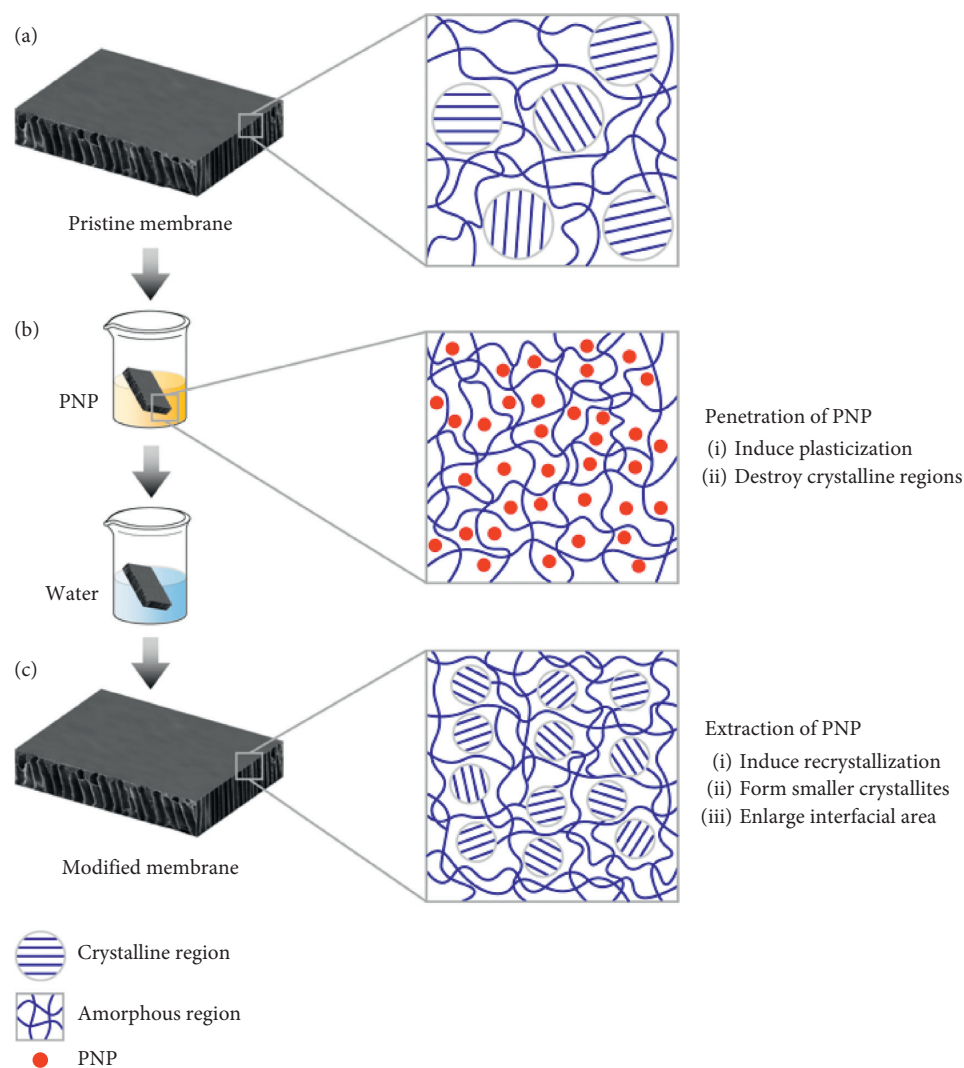


FIGURE 4: A schematic illustration of desalination using PNP treated cellulose triacetate (reproduced with a permission from [23]).

sorption performance of polycyclic aromatic hydrocarbons. It is worth noting that this technique enhanced the hydrophobicity of the fibric peat, leading to enhancement in the sorption rate and capacity of polycyclic aromatic hydrocarbons from wastewater [25].

2.3. Polymer-Based Adsorbents for Heavy Metals Removal.

The development of the industrial technology has led to the problem of heavy metals which are discharged to the environment through the wastes of painting and electroplating. The adsorption process of heavy metals using low-cost materials is one of the most potential techniques for the removal of heavy metals from wastewater. At present, polymer-polymer composites are receiving a great deal of attention, since they have potential absorptivity, improved stability, and high mechanical feasibility. Copolymerization of polymers is a technique in which two polymers or more are combined together to produce a new material with a target application. For water treatment purposes, the copolymerization process has provided an improvement for

the adsorption capacity of single polymers, also improving the polymers aggregation in alkaline medium and polymer disintegration in aqueous solution. The removal mechanism using copolymers is illustrated in Figure 5. The size exclusion mechanism of metals removal since the polymer composite membrane worked as a physical barrier. One of the key factors that control the size exclusion mechanism is the pore size of the membrane and the particle size of the target contaminants [26].

Very recently, Checkol et al. [27] showed a polymer-polymer matrix of polystyrene sulfonate/3,4-ethylenedioxythiophene and lignin for the elimination of heavy metals. The polystyrene moieties in the composite made the copolymer work as a cation exchanger, and the sulfonate groups and the lignin moieties enhanced the adsorption capacity of the toxic metals due to the various binding sites on the composite. This study showed that lead ions were adsorbed/desorbed on/from the polymer composite in neutral media when a negative/positive potential was sequentially applied. The adsorption capacity reached

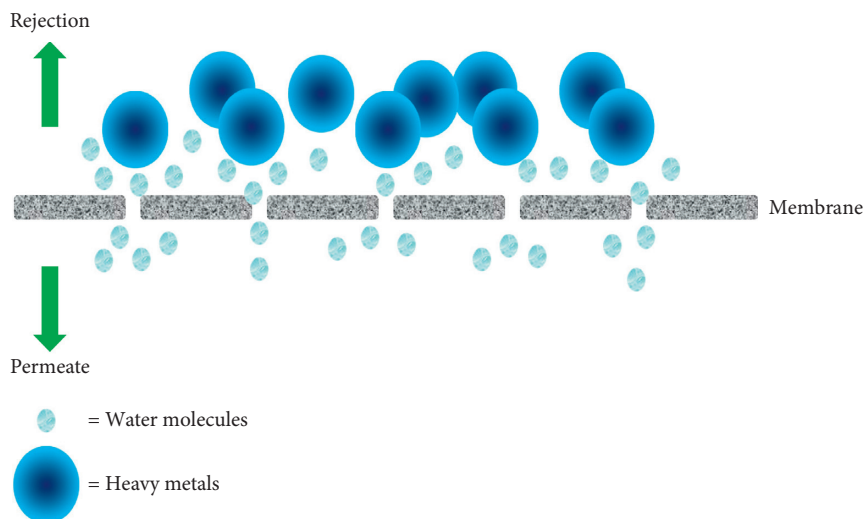


FIGURE 5: Size exclusion/steric hindrance mechanism by low pressure membrane.

245.5 mg/g by the polymer-polymer composite and almost doubled (452.8 mg/g) when lignin moieties were added to the polymer mixture. In this regard, poly(styrene-maleic anhydride) copolymer was modified with cyclopropane and tetramethylenediamine to fabricate a highly adsorbent polymer composite for the elimination of heavy metals. The adsorption selectivity of the metal ions was investigated by the formulated composite at various conditions. The composite showed a high tendency for the removal of some selected metal ions. The affinity order of the composite was copper (II) > zinc (II) > lead (II). The kinetic studies indicated that the adsorption onto the composite followed the pseudo-second-order kinetics and the Langmuir adsorption isotherm [28]. Also, in a recent study, glycidyl methacrylate was grafted with starch. The resultant composite was further coated with polyamine through a cycloaddition between the NH_2 of diethylenetriamine and the epoxy groups of glycidyl methacrylate. This polymer composite showed improved adsorption properties towards the heavy metal ions, in particular Cu and Pb ions. The adsorption behaviors were explained by a chelation interaction [29].

Porous organic polymers show promising applications in the area of wastewater treatment. Yu et al. introduced a general synthetic route for the porous organic polymer composites which have been used as efficient adsorbents of heavy metals. Specifically, they covalently linked cyclodextrin and EDTA-modified chitosan by pentafluoropyridine to obtain a porous organic polymeric composite using pentafluoropyridine as an environmentally benign solvent. The new polymer composite showed a fast kinetic process for the adsorption of many heavy metals. More importantly, the composite showed five cycles of use with a 91% adsorption capacity at the fifth cycle. The host-guest inclusion and the chelating effects were the reasons for the high removal efficiency of these polymers [30].

Conducting polymer-based composites are receiving a great deal of attention owing to their potential applications for the elimination of different metal ions. Polypyrrole is a conducting polymer with remarkable properties for the

elimination of heavy metals because of its simple preparation process and its biocompatibility properties [31]. Different metal ions were efficiently removed using polypyrrole based composites, in particular, polypyrrole-polyaniline composites, which contained both imine and amine groups that chelated metal ions species through an electrostatic interaction and hydrogen bonding [31].

Understanding how the functional groups of the polymer composite affect the interaction with the heavy metals is of great interest as it will support the future studies to reach the optimum removal efficiency of the target pollutants. For that purpose, Zhang et al. prepared a biosorbent using pine sawdust and citric acid to simultaneously remove the copper ions from wastewater. The study indicated that the functional groups of the composite (hydroxyl and carboxyl) were the reason behind the high adsorption capacity of the copper ions. Specifically, at $\text{pH} > 3$, COOH groups transformed to COO^- groups. Hence, there was an electrostatic interaction between the positive copper ions and the negative charges of the composite. Moreover, the hydroxyl groups contributed to the adsorption of copper ions through a hydrogen bonding network [32].

3. Polymer-Carbon Composites

Carbon is an atom with a unique electronic structure, able to form covalent bonds with many other metals and nonmetals. Carbon can exist in different molecular forms. Therefore, a lot of different carbon nanomaterials were synthesized and were used for different applications. Carbon at the nanoscale has many unique properties compared to the other adsorbent materials, namely, high mechanical properties, high electrical conductivity, and high thermal stability. Carbon nanomaterials are classified into different types based on the carbon shape and the geometrical structure. To date, activated carbon, carbon mesosphere, carbon nanotubes, graphite, and graphene are well known carbon nanomaterials and have been used for different applications. The polymer composites of carbon nanomaterials are receiving a

great deal of attention in different applications, particularly in water treatment and desalination, where the polymer composites of carbon materials possessed excellent properties like high aqueous solubility, large surface area, and enhanced thermal and mechanical stability. These remarkable properties were favorable for the elimination of organic and inorganic pollutants from wastewater. In the following sections, the synthesis, characterization, and water treatment applications of different types of polymer-carbon composites are discussed.

3.1. Polymer-Based Carbon Nanotubes Composites. Carbon nanotube (CNT) is a form of the nanocarbon materials with a one-dimension cylindrical nanostructure. CNT possesses an extraordinary graphic nature with a high surface area making it a promising candidate for water treatment and desalination. Despite all these excellent properties, CNTs lack surface functional groups and also possess poor dispersibility in aqueous media. These limitations resulted in a low adsorption performance when CNTs are used as adsorbents. Accordingly, the surface functionalization of CNTs is an important research target in order to improve the water dispersibility and the adsorption performance of CNTs.

3.1.1. For Oil Removal. In a recent study single-walled CNTs were added to a copolymer membrane of poly(*N*-isopropylacrylamide)-co-(acrylamide) for the separation of water-oil mixture (see Figure 6). CNT is used for that purpose because it has an oleophilic property. The fabricated single-walled CNTs-based copolymer membrane showed a 99.99% removal of oil. The photothermal-response property of the single-walled CNTs-based membrane was noticed to increase the flux of water by light illumination. [33] These research results promoted the applications of CNTs-based polymer for oil removal and stimulated the research groups to find new polymer composites based on CNTs.

In a recent study, multiwalled CNTs were incorporated into a block copolymer of polysulfone/polyether to form a CNTs-polymer membrane which is used to separate oil from water-oil mixture. The study showed the effect of multiwalled-CNTs ratio on the removal efficiency of oil. As noticed, the increase of multiwalled CNTs up to 2.0 wt% has improved the oil rejection of membrane from 91.4% to 99.79%. The permeation flux has increased three times when multiwalled-CNTs loading ratio reached 0.5 wt%. The further increase of multiwalled-CNTs loading ratio above 2 wt% has led to a 30% decrease in the permeate flux [34]. These studies showed how CNTs are promising candidates for enhancing the removal efficiency of oil from water-oil mixture where CNTs offer self-cleaning and antifouling functions to the polymeric membranes.

3.1.2. For Heavy Metal Removal. Polymer functionalization (physical or chemical) of CNTs is considered as one of the most effective routes to enhance not only the CNTs adsorption properties, but also their hydrophilicity and water

solubility. This kind of functionalization showed remarkable electric conductivity and mechanical properties. CNTs were grafted with different polymers to synthesize efficient nanoadsorbents of heavy metals. For example, poly-hydroxybutyrate-grafted-CNT composite was synthesized and applied as a nanoadsorbent for the elimination of As, Cr, Pb, Cd, Cu, Ni, Zn, and Fe metal ions from industrial wastewater through a batch adsorption process. As proved in this study, the polymer functionalization lowered the degree of agglomeration of CNTs, leading to a significant enhancement in the adsorption characteristic of CNTs. The mechanisms of adsorption by this CNT-polymer composite were ion exchange and electrostatic forces [35].

CNTs coated with polyamidoamine were also synthesized as a nanoadsorbent and applied for the adsorption of Co, Zn, and As. Notably, the adsorption capacities of the studied metal ions were 432, 494, and 470 mg/g for As, Co, and Zn ions, respectively [36]. In another study, CNTs were incorporated into a polymer hydrogel comprising polyacrylamide and sodium alginate. In this hydrogel, polyacrylamide worked first as flexible network, and then the addition of sodium alginate constructed the rigid network. The addition of CNTs was done to reinforce the mechanical strength and elasticity of the polymer composite structure as well as enhancing the adsorption properties of the polymer composite. This composite exhibited a macroporous structure with a very low density and a high water content, thanks to the addition of CNTs. The adsorption capacity of the fabricated polymer-CNT composite was 1.28 times higher than that of polymer composite only. Figure 7 simply summarizes the synthetic route of this polymer-CNT composite, its morphological structure, and its adsorptive characteristics [37]. Also in another study, polyaniline grafted multiwalled-CNT composite was prepared by an oxidation polymerization process. This composite was then doped with para-toluene-sulfonic acid hydrophilic groups. The addition of such para-toluene-sulfonic acid groups provided the polymer-CNT composite with additional functional groups that were able to enhance the water dispersion of the composite as well as increasing the adsorption characteristics towards chromium ions which are bound to the adsorbent via its amine, imine, and hydroxyl functional groups [38].

3.1.3. For Dye Removal. The composite research of CNTs has attracted much attention to improve CNT-surface characteristics and accordingly enhance its absorptivity of organic pollutants, in particular organic dyes. Surface functionalization of CNTs with polymers is a facile approach to fabricate nanoadsorbent-based CNTs with enhanced adsorption capability of dyes. In a recent study, multiwalled CNTs were grafted with poly(sodium-*p*-styrene sulfonate). Specifically, CNTs were first coated with dopamine and then self-polymerized to produce polydopamine-CNT composite. The obtained functional polydopamine-CNT composite showed remarkable water dispersibility with enhanced removal of methylene blue dye at various adsorption conditions. The adsorption capacity reached 174 mg/g after 25 min

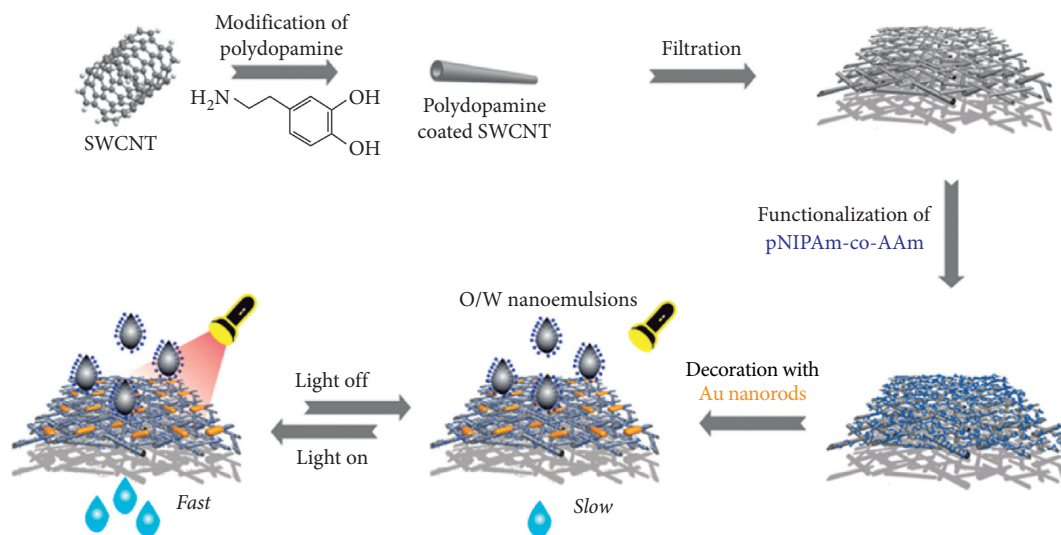
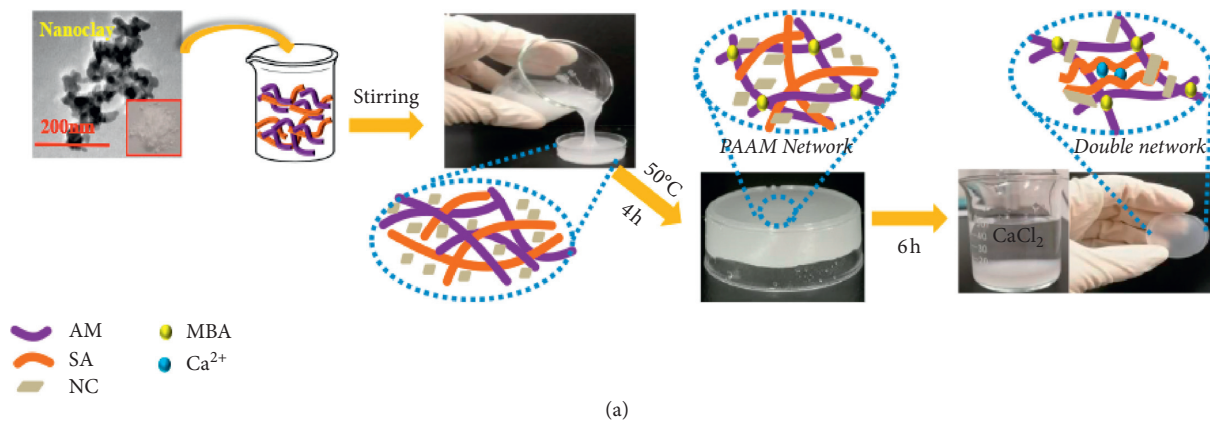
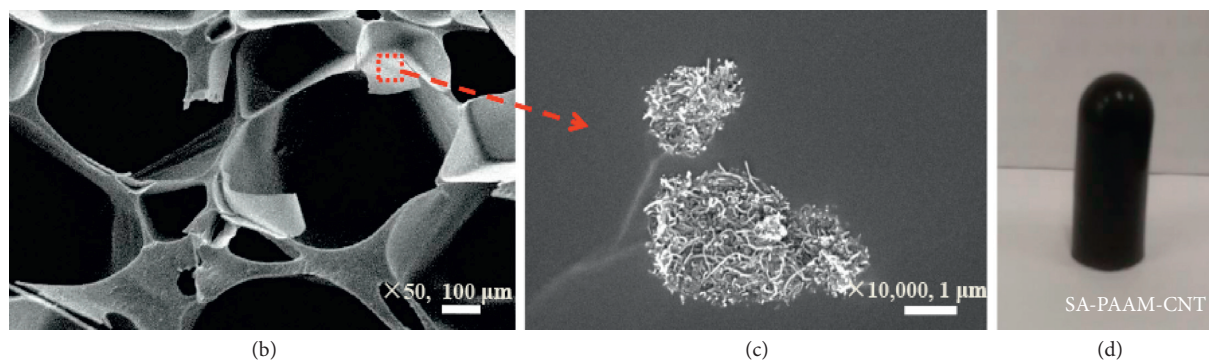


FIGURE 6: Schematic illustration of synthesis of singled-walled CNTs incorporated copolymer membrane of poly(*N*-isopropylacrylamide)-co-(acrylamide) and their use in oil removal from water-oil mixture (reproduced with a permission from [33]).



(a)



(b)

(c)

(d)

FIGURE 7: (a) Schematic illustration of composite formation, (b) SEM image of the freeze-dried polymer network hydrogel, (c) a magnified area of CNT distributed in the polymer matrix, and (d) polyacrylamide-sodium alginate-CNT composite (reproduced with a permission from [37]).

[39]. Another composite based on grafting polyaniline on the surface multiwalled CNTs was recently offered with enhanced adsorptive properties of alizarin yellow dye. The composite was prepared through in situ polymerization of surface oxidized multiwalled CNTs [40]. The maximum adsorption capacity for alizarin yellow dye by this polymer-CNT composite was 884.80 mg/g. The data of the adsorption

behavior fitted well the pseudo-second-order and the Langmuir isotherm models, respectively. Additionally, the energy changes of the composite showed that the adsorption of alizarin yellow dye was exothermic and spontaneous in nature. Accordingly, this polymer-CNT composite could work as a potential adsorbent for the removal of other organic dyes.

3.2. Polymer-Graphene Composites. Graphene is a 2D carbon-based material with a single layer of carbon atoms. Graphene has very interesting physicochemical properties which make it an attractive material for many applications. [41] Graphene-based composite materials are gaining a lot of research interest as nanoadsorbents because such composites possess a three-dimensional structure which provides a higher porosity and a larger specific surface area and aspect ratio, as well as excellent electrical conductivity, mechanical properties, and thermal stability. Hence, a higher absorptivity of organic and inorganic pollutants can be easily obtained. Graphene composites can also be fabricated into membranes for ultrafiltration systems. Therefore, graphene-based composites are excellent candidates for water treatment and desalination.

Polymer-graphene composites are receiving significant importance in water treatment and desalination processes because this kind of composite materials combined the advantages of polymers and graphene, providing a promising adsorbent that can improve the fouling resistance, the selectivity/permeability, the chlorine resistance, and the mechanical stress of the corresponding membranes. Polymer-graphene composites can be synthesized by different techniques depending on the required properties in the target membrane. In the following paragraphs, the preparation techniques as well as the recent water treatment applications of polymer-graphene composites are highlighted.

3.2.1. Preparation Techniques of Polymer-Graphene Composites

(1) *Spraying Technique.* Spraying method is a technique in which a spray-gun is used to spray the polymer-graphene solution onto a preheated substrate. This spraying technique produces a large-area membrane with controllable density. The disadvantage of this technique is the difficulty to obtain a uniform and homogenous membrane.

(2) *Vacuum Filtration Technique.* The vacuum filtration technique is a two-step process in which graphene is dispersed first and then deposited on a matrix of polymer membrane by vacuum filtration process. This process is very simple and can be used to prepare a uniform polymer-graphene membrane.

(3) *Spin-Coating Technique.* This is a very common and simple technique to prepare a membrane of polymer-graphene composite. Typically, a graphene dispersion is dropped on a rotating-spin coater to fabricate the membrane. By using this technique, a uniform and sizable membrane can be obtained with a controlled thickness.

(4) *Layer-by-Layer Self-Assembly Technique.* The layer-by-layer self-assembly is one of the most commonly used techniques to fabricate a polymer-graphene composites into membrane. It is an environment-friendly technique and can be used in aqueous media. Please see the details of Figure 8.

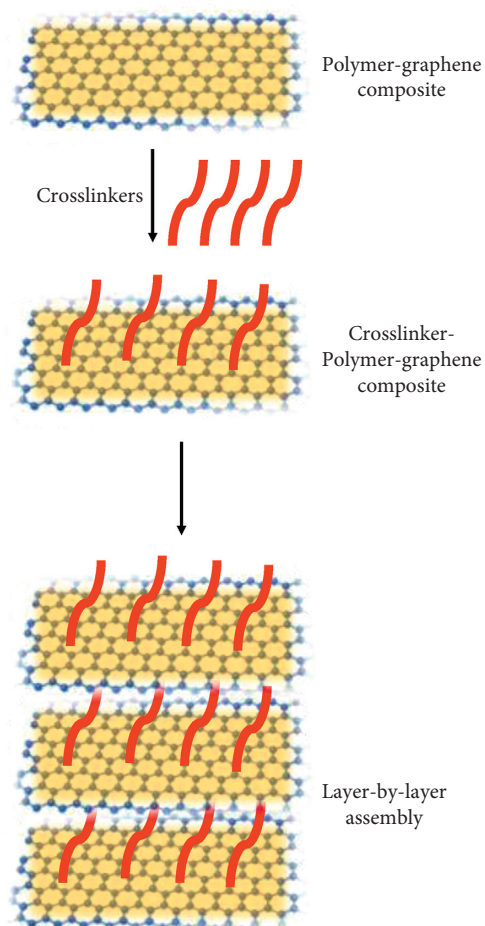


FIGURE 8: A diagrammatic illustration of layer-by-layer self-assembly technique of preparing polymer-graphene composites into membrane.

3.2.2. Applications of Polymer-Graphene Composites for Water Treatment and Desalination. In a recent study, graphene was combined with sodium alginate to prepare a nanocomposite adsorbent. The composite exhibited an enlarged free volume with excellent separation performance and high permeate flux [42]. As illustrated in Figure 9, the hybrid possessed a well-aligned mortar and brick architecture where water channels existed. The structural defects and the free volume cavities of the hybrid have worked for selectivity and permeability of water channels.

In a similar study, poly(N,N-2-ethyl amino ethyl methacrylate) as a temperature-responsive polymer was grafted with graphene oxide in order to prepare a nanomembrane for ultrafiltration. In this composite, poly(N,N-2-ethyl amino ethyl methacrylate) induced stimuli to carbon dioxide and argon, producing a controlled pore size into the membrane. The amine group of poly(N,N-2-ethyl amino ethyl methacrylate) polymer reacted with carbon dioxide in water, protonated, and then deprotonated when argon is fed to the medium. Such change in the morphological shape of the polymer led to a change in separation properties of the cast membrane (see the details of Figure 10). This nano-filtration membrane was tested for the rejection of

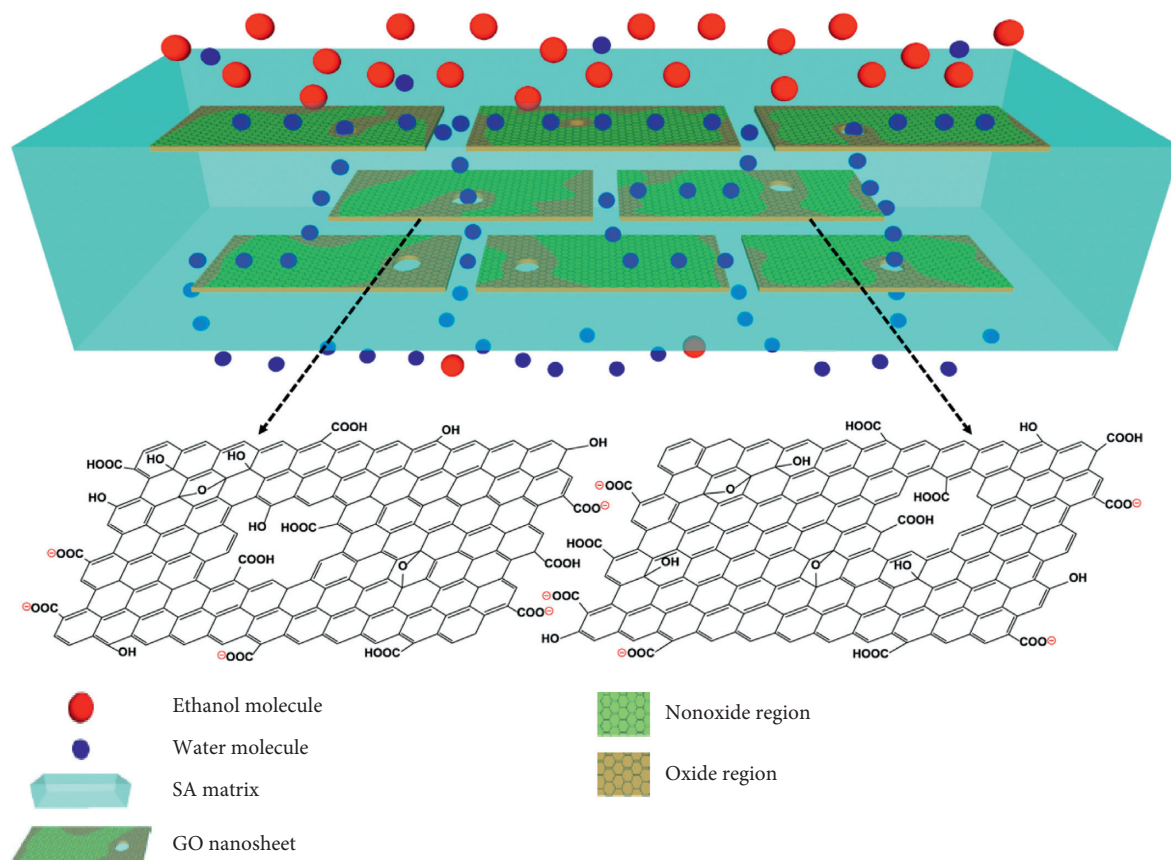


FIGURE 9: A diagrammatic illustration of the mechanism of selective water permeation using graphene-sodium alginate blend (reproduced with a permission from [42]).

rhodamine-B and the methylene orange dyes. The average rejection rates for these two dyes were 98.9 and 96.5%, respectively. In addition, the membrane had remarkable repellency to many salts such as magnesium, calcium, and sodium chlorides [43]. For the same target, a crosslinked (N-isopropylacrylamide and N,N-methylenediacrylamide) polymer was grafted with graphene (see Figure 11). The obtained membrane showed excellent mechanical characteristics with remarkable separation performance and water flux. The water flux of the obtained membrane was 25.8 L/m²h. This value represented three orders of magnitude of the value of the commercial cellulose triacetate membrane [44].

Adsorption capacity, oil-water selectivity, mechanical stability, and reusability at harsh operation conditions are essential parameters for oil-water separation technology. The current state of the art membranes usually sacrifices the mechanical properties and/or recyclability versus membrane performance, i.e., adsorption capacity and selectivity. Thus, it is important to consider all the above-mentioned properties together, in order to offer an efficient membrane for oil-water separation. In a recent study, reduced graphene oxide was grafted polydopamine polymer to fabricate a carbon-based polymer membrane with a light weight and a high separation efficiency of oil from water. This membrane showed an improved chemical stability at harsh operation conditions of acidity and salt concentration. In addition, the separation efficiency of oil reached 99.6%. This remarkable

performance was due to the degree of oleophobicity of reduced graphene oxide as well as the superhydrophilicity of polydopamine polymer. The only disadvantage of this membrane was the instability at the alkaline conditions, where the polydopamine polymer dissolved in the alkaline media. [45] In a similar work, a robust and reusable sponge membrane was synthesized by combining poly(-dimethylsiloxane) polymer and graphene oxide nanomaterials through a chemical amidation process (see Figure 12). In this polymer-carbon composite, graphene oxide worked as a mechanical fortifier, contributing to the durability of the formed sponge. This composite was tested for the separation of various oils and organic pollutants. The adsorption capacity of the sponge was 724 times its original weight. This study opened the door to develop porous polymer composite membranes with high separation characteristics of oil-water emulsion [46].

To reduce the production cost and to demolish the negative impacts on the environment, cellulose as a natural polymer was applied in the polymer-graphene composites to improve the oil-water separation process. Cellulose showed the advantages of being a low-cost biodegradable material and having high mechanical characteristics. In another study, cellulose-graphene composite membrane was fabricated with ultralight weight and superhydrophobic properties. The obtained aerogel composite showed an excellent adsorption capacity, approximately 80 to 197 times

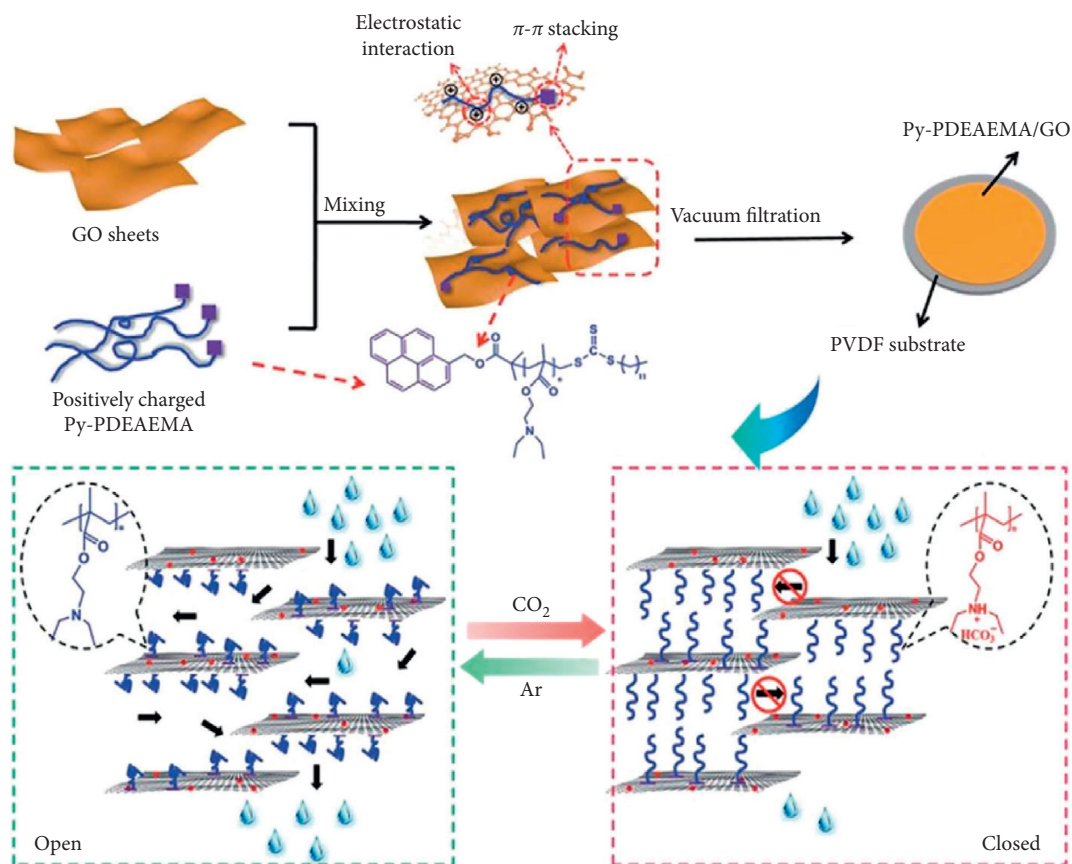


FIGURE 10: Synthetic protocol of poly(N,N-2-ethyl amino ethyl methacrylate)-graphene oxide composite for dyes and salts rejection (reproduced with a permission from [43]).

(oil/organic solvents) its original weight. This performance was obtained due to the multilayered sheet structure of the composite and the large porosity on the composite (see Figure 13). In addition, the composite revealed high mechanical stability even after 100 times of cycling-compression testing [47].

3.3. Polymer-Based Activated Carbon Composites for Water Treatment and Desalination. Activated carbon is an amorphous solid carbonaceous material consisting of graphitic lattice. It has many forms including granules, powder, fibers, and cloths. Activated carbon is one of the carbon-based materials used for water treatment and desalination, because it is inexpensive, can be produced from agro-wastes, has a high surface area and porosity. Despite these advantages, some of the activated carbon forms, especially powdered ones, are difficult to remove from the treated aqueous media, because they have very fine powdered forms. Also, they aggregate, leading to a decrease in their adsorptive characteristics. Accordingly, there was a need for new techniques of using activated carbons as potential adsorbents.

The composite formation of activated carbon with polymers has proved to be a promising technique for water treatment and desalination. In a recent study, a composite of cellulose triacetate and activated carbon was prepared by an

evaporation/precipitation technique for potential elimination of heavy metals from wastewater.

In this study, the use of a low solvent diffusion process at a low casting temperature demolished the aggregation of activated carbon in the matrix structure. Accordingly, a homogenous membrane was obtained. The addition of activated carbon to cellulose triacetate also supported the production of a less fragile membrane. This cellulose triacetate-activated carbon composite membrane was very efficient for the elimination of arsenic acid from aqueous media, achieving a very high removal value [48]. Polypyrrole as a synthetic polymer was also used to form a composite with activated carbon for the elimination of lead ions from aqueous media. In that work, polypyrrole-activated carbon composite was obtained by a carbonization process of polypyrrole-activated carbon in the presence of a chemical activator. The structural and morphological characterizations supported the composite applicability as an adsorbent. The adsorption capacity of this composite improved with the progress of time and the increase of initial concentration, while it demolished with the increase of adsorbent dose. The adsorption equilibrium of lead ions was described by both Langmuir and Freundlich models. The maximum adsorption reached 50.0 mg/g after 4 h at pH 5.5. The kinetic studies of the composite suggested that the adsorption is a chemisorption process rather than a diffusion process [49].

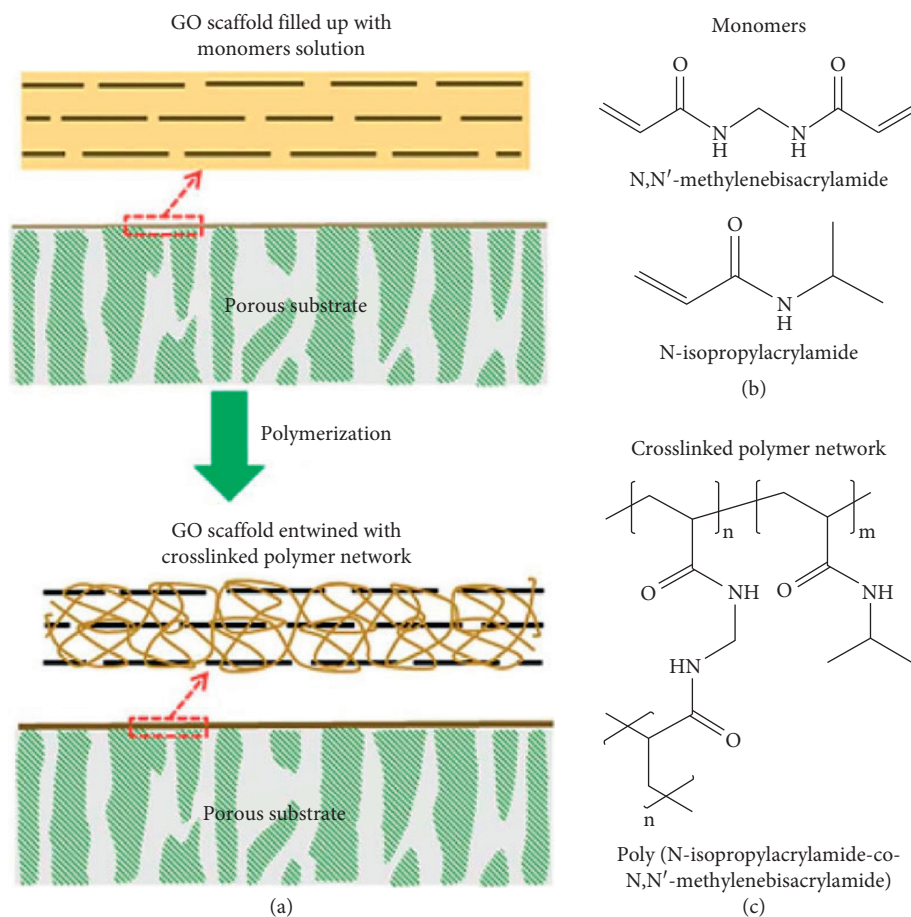


FIGURE 11: Synthetic protocol of crosslinked (N-isopropylacrylamide and N,N-methylenediacylamide)-graphene composite (reproduced with a permission from [44]).

4. Polymer-Clay Composites

Several treatment technologies were explored for the treatment of wastewater sources with the adsorption technique which is a favored process because of its effectiveness, ease of operation, and efficiency. Polymers were used in a composite structure with clays because they can be easily manipulated and produced in a flexible structure. In this section, polymer-clay composites are explored as potential adsorptive materials compared to their individual adsorbents.

Clays are low-cost natural materials, used as adsorbents of many micropollutants. They have a positive or negative layered structure with interlayered anions or cations, respectively. Their use as adsorbents depends on many parameters including porosity, surface area, and particle size. The drawbacks of clays as adsorbents are mainly their pH-dependence and poor wettability. Thus, clay composite structures were offered to overcome these drawbacks and also to improve their performance in removal selectivity of inorganic and organic contaminants from aqueous media. Clays worked as host matrixes to hold polymers or used as fillers to improve the polymer mechanical properties. Polymer-clay composites attracted attention in water treatment because they exhibited a wide range of pore

structures, good surface areas, an ultralight weight gathered with high stiffness, improved processability and stability, good selectivity towards different pollutants, cost effectiveness, and almost no loss on regeneration for reuse. They also offered an easy process for recovering from treated water. Polymer-clay composites can be obtained in different forms by intercalation, coating/wrapping, flocculation, or exfoliation (see Figure 14). In the following paragraphs, the recent polymer-clay composites for water treatment are highlighted.

4.1. Polymer-Cationic Clay Composites for Water Treatment and Desalination. A polymer grafted clay composite compiling polyvinylpyridine as a stimuli-responsive polymer and montmorillonite as a cationic clay was synthesized as a novel adsorbent of pollutants with response to pH. The composite structure showed remarkable characteristics, i.e., a high polymer loading without polymer-leaching, a lower pH/charge dependency, and a high zeta potential. These enhanced properties explained the significant performance towards the elimination of inorganic and organic pollutants, in comparison with the commercial adsorbents. Specifically, at low to moderate pH, the stimuli-responsive polymer accepted protons, leading to an enhancement in the

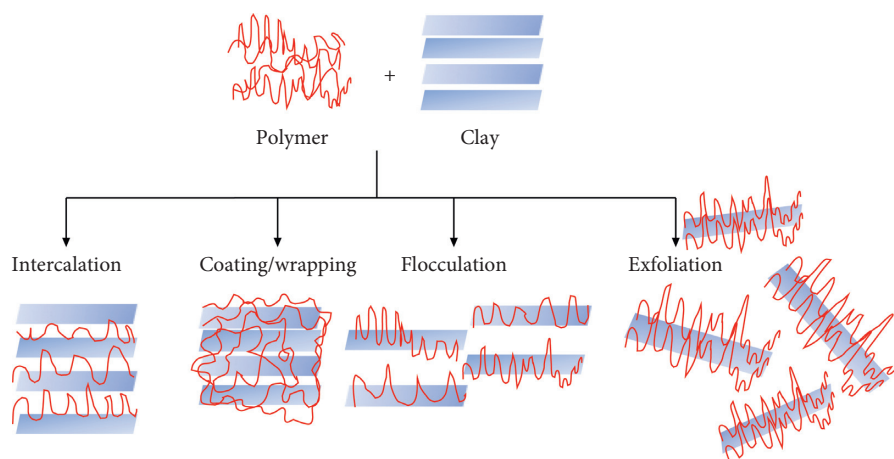


FIGURE 14: A schematic illustration of polymer-clay interaction.

adsorption of the pollutants. However, at elevated pH, the stimuli-responsive polymer lost the protons, leading to desorption of the pollutants. Also, the elimination of micropollutants, e.g., sulfentrazone, arsenate, and atrazine, from wastewater was explored by this composite [50]. In a similar work, exfoliated and intercalated montmorillonites were grafted with different stimuli-responsive polymers, i.e., sodium 2-acrylamido-2-methylpropane sulfonate and *N*-isopropylacrylamide, using a surfactant-free technique. The prepared composite showed excellent removal capacities towards cobalt, nickel, and methylene blue dye. The results of this composite showed a reduction of surface tension which resulted in improving the absorptivity of the clay, and accordingly an efficient removal of the metal ions and the dye molecules was obtained. This composite also showed reuse of four times with no loss in removal efficiency [51]. In another study, a novel biocomposite was synthesized by incorporating a modified-montmorillonite cationic clay into a polyethylenimine-modified carboxymethyl-chitosan matrix. The composite was prepared to remove the Hg ions from water. The composite showed a superior removal performance towards Hg ions from aqueous media. The adsorption capacity reached 1875 mg/g, representing the highest record so far among the literature polymer/clay adsorbents of Hg ions. This remarkable performance was mainly due to the enhanced porosity of the composite and the increased chelation sites onto the composite structure [52]. For the same target, montmorillonite was complexed with polyvinyl alcohol and poly(4-styrenesulfonic acid-co-maleic acid) to offer efficient and cost-effective adsorbents [53].

For dyes removal, a novel hydrogel composite of responsive polymers with montmorillonite was prepared using bis[2-(methacryloyloxy)ethyl] phosphate as a crosslinker. The composite was used for the elimination of methyl red (MR), methylene blue (MB), and crystal violet (CV) from wastewater. Many parameters were applied to obtain a maximum adsorption capacity of the target dyes. Using this composite, the dye removal reached 51% for MR, 89% for MB, and 80% for CV at pH 7 and about 23% for MR, 93% for MB, and 86% for CV at pH 12. The maximum adsorption

capacity of this hydrogel composite showed 113, 155, and 176 mg/g for MR, MB, and CV, respectively. The desorption of the dyes from the composite was simply performed in ethanol solution [54]. For the same target, a hydrogel of acrylamide, *N*-isopropyl acrylamide, and montmorillonite was synthesized for the elimination of methylene blue (see Figure 15). The prepared composite showed a good swelling-deswelling property. The adsorption process was highly dependent on the pH and the temperature of the medium. The kinetic studies showed that the adsorption behavior follows the pseudo-second order. The composite also showed a good regeneration capacity with 5 cycles of adsorption-desorption processes. In general, the composite showed a potential use as an environment-friendly adsorbent with efficient absorptivity of dyes from wastewater [55].

4.2. Polymer-Anionic Clay Composites for Water Treatment and Desalination. Anionic-clays were also applied as potential adsorbents for water treatment. In a recent study, a novel composite of magnesium-aluminum based layered double hydroxides (LDH) with polydopamine was prepared for the elimination of copper ions from aqueous media (see Figure 16). The results of this study showed a remarkable improvement in the adsorption efficiency of copper ions. The composite showed a two-time higher absorptivity of copper ions compared to pristine layered double hydroxides. The maximum adsorption capacity of copper ions reached 193.78 mg/g using this composite. The composite was used 4 times with no loss of adsorption capacity. The mechanism of adsorption was due to electrostatic interaction with copper ions [56].

A hydrogel of Co/Al layered double hydroxide-polyacrylamide composite was synthesized via in situ polymerization of acrylamide at room temperature in the presence of LDH. The mechanism of hydrogel composite formation was described by coordination and hydrogen bonding interactions between the amide groups of acrylamide and hydroxyl groups of LDH sheets. The composite was utilized for the elimination of methyl orange from wastewater, showing a high adsorption efficiency [57].

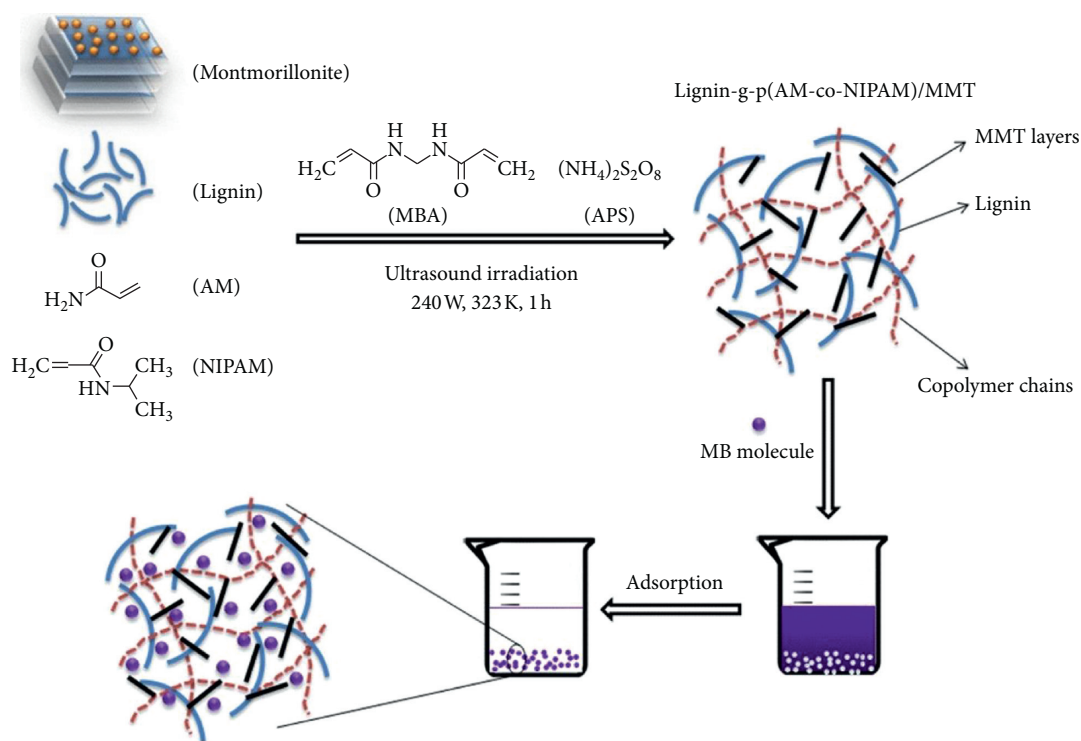


FIGURE 15: A schematic illustration of synthesis of acrylamide and N-isopropyl acrylamide-montmorillonite composite, and its use for methylene blue elimination from aqueous media (reproduced with a permission from [55]).

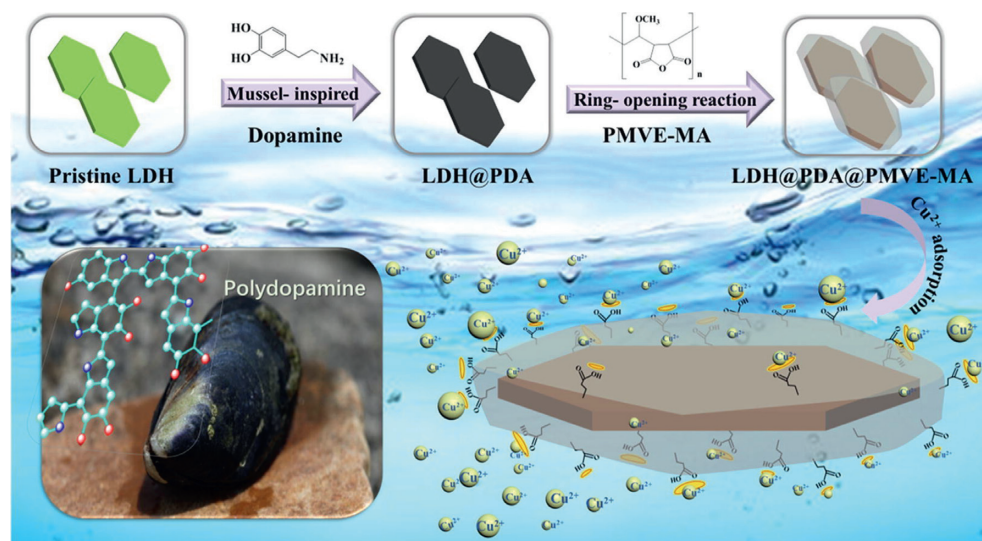


FIGURE 16: A schematic illustration of using polydopamine-LDH composite for elimination of copper ions from wastewater (reproduced with a permission from [56]).

5. The Mechanisms of Adsorption

Understanding the mechanism of adsorption is of great importance, since it helps to control and to improve the removal of the different pollutants, as well as increasing the adsorption efficiency. In order to get in-depth insights into the adsorption mechanism, kinetic, isothermal, and thermodynamic studies were performed and applied to the adsorption behavior of the different pollutants. As reported, various adsorption mechanisms have been proposed based

on the adsorbent and adsorbate types, sources, structures, and forces of attraction. In this section, the different adsorption mechanisms are highlighted.

5.1. Chemisorption Mechanisms. Chemisorption mechanisms involve the electrostatic interaction mechanism, the ionic exchange mechanism, the reduction/oxidation mechanism, and the complex formation mechanism (chelation) (see Figure 17). These mechanisms can work

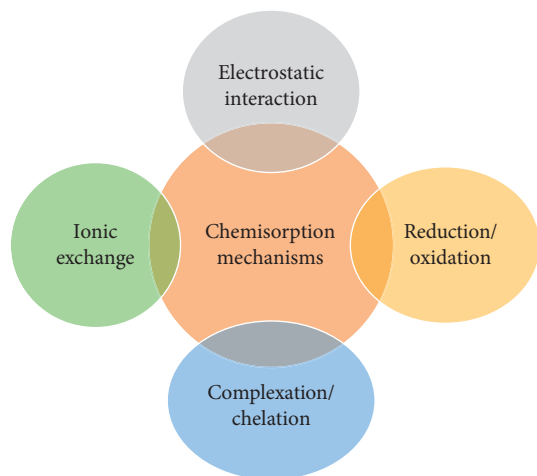


FIGURE 17: Diagrammatic illustration of the different mechanisms involved in chemisorption process.

separately or altogether to remove the pollutants. Specifically, the type of the functional groups present into/onto the adsorbent determines how the adsorption process works (see Figure 18) [49, 58, 59]. For example, if the carboxylic acid groups, the amino groups, or even the hydroxyl groups are present in a protonated form, they undergo a complexation/chelation process to remove the pollutants, but if they are present in a deprotonated form, they undergo an electrostatic interaction process with the pollutants. From the thermodynamic point of view, chemisorption mechanism is usually accompanied by an exothermic process, meaning that energy is liberated during the pollutant adsorption. The enthalpy involved in this process has usually a negative value. This is because of the decrease of the movement of the pollutants when get adsorbed on the surface of the adsorbent. Such process also involves a decrease in the medium entropy because the adsorption is a spontaneous process [60]. The isothermal adsorption studies of the chemisorption mechanism usually show a monolayer formation of the pollutants on the surface of the adsorbent [61]. Furthermore, the chemisorption mechanism may not be detected at low pressure and/or temperature and it became predominant only when the adsorption conditions are changed. From the kinetic point of view, chemisorption mechanism usually follows a pseudo-second-order process which means that the adsorption process usually depends on both the adsorbent and the adsorbate concentrations [62, 63].

5.2. Physisorption Mechanisms. Physisorption mechanism occurs between the adsorbates and the adsorbents via Van der Waals forces. Figure 18 shows a schematic illustration of physical adsorption mechanism (lower panel). As indicated, the surface of the adsorbents lacks functional groups compared to the surface of chemisorption mechanism which contained a lot of functional groups (upper panel). Therefore, the adsorbates tend to physically attach to the adsorbent surface through the weak Van der Waals forces. Physisorption usually occurs at solid surfaces with weak

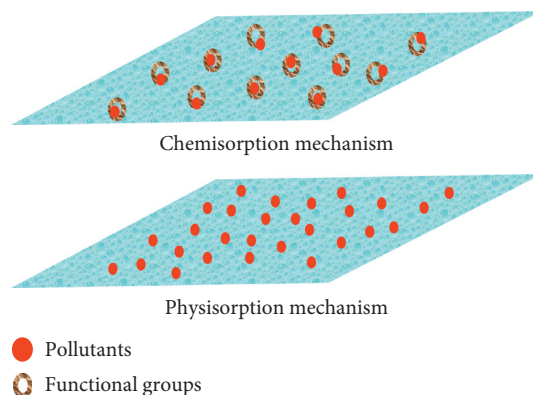


FIGURE 18: Diagrammatic illustration of chemisorption and physisorption mechanism.

binding forces. This mechanism is reversible in nature at a certain extent and is mainly dependent on the pressure and the temperature of the adsorption medium. Thus, the rates of adsorption and desorption are very fast. In the context of kinetics, physisorption mechanism usually follows the pseudo-second order, which means that the adsorption process is mainly dependent on the concentration and the structure of the adsorbents. Hence, porous materials with high surface area are better adsorbents for the physisorption mechanisms. In the context of thermodynamics, physisorption mechanism does not require high activation energy for the adsorption to proceed.

6. Conclusions and Perspectives

As shown in this review, both natural and synthetic polymers displayed remarkable adsorptive properties when combined with different adsorbent materials, i.e., carbon-based materials, clays, and other polymers. The polymer composite research opened new research route for a pollution-free environment. Polymers in a composite structure showed a simple and easy fabrication process, a good mechanical performance, and additional binding sites for adsorption of organic pollutants. A lot of research was done to modify the polymer structures to reach high adsorption performance, durability, recyclability, and selectivity of many organic and inorganic pollutants. Despite all the reviewed research articles, polymer composites for water treatment and desalination did not reached their optimal performance especially for the large scale production of such adsorptions. The future perspectives to reach optimal performance of the adsorbents are as follows:

- Integrating nanoadsorbent materials with bio-adsorbent carriers in a low cost
- Adding/increasing the number of functional groups that are able to enhance the adsorption efficiency, which can be done by exploring new functional materials and/or designing hybrid technologies
- Searching for more agro-wastes as adsorbents to decrease the production costs and to sustain the adsorbent-based market

- (d) Studying in detail the mechanism of adsorption to understand the science behind the adsorption behavior and accordingly improve the impacts of the different adsorbents at different conditions
- (e) Improving the selectivity of the adsorbents through the selection of the functional groups created on the adsorbents
- (f) Improving the pretreatment strategies and processability of the biomass feedstock before being used as adsorbents
- (g) Decreasing the operational costs to reach the large scale applications of the adsorbents, which can be done by offering new techniques of pollutants removal

Conflicts of Interest

The author declares no conflicts of interest.

References

- [1] H. Pang, Y. Wu, X. Wang, B. Hu, and X. Wang, "Recent advances in composites of graphene and layered double hydroxides for water remediation: a review," *Chemistry—An Asian Journal*, vol. 14, no. 15, pp. 2542–2552, 2019.
- [2] X. Liu, R. Ma, X. Wang et al., "Graphene oxide-based materials for efficient removal of heavy metal ions from aqueous solution: a review," *Environmental Pollution*, vol. 252, pp. 62–73, 2019.
- [3] X. Wang, L. Chen, L. Wang et al., "Synthesis of novel nanomaterials and their application in efficient removal of radionuclides," *Science China Chemistry*, vol. 62, no. 8, pp. 933–967, 2019.
- [4] D. Chen, L. Wang, Y. Ma, and W. Yang, "Super-adsorbent material based on functional polymer particles with a multilevel porous structure," *NPG Asia Materials*, vol. 8, no. 8, p. e301, 2016.
- [5] B. Samiey, C.-H. Cheng, and J. Wu, "Organic-inorganic hybrid polymers as adsorbents for removal of heavy metal ions from solutions: a review," *Materials*, vol. 7, no. 2, pp. 673–726, 2014.
- [6] A. H. Karoyo, J. Yang, and L. D. Wilson, "Cyclodextrin-based polymer-supported bacterium for the adsorption and in-situ biodegradation of phenolic compounds," *Frontiers in Chemistry*, vol. 6, no. 403, 2018.
- [7] H. Guan, D. Zou, H. Yu et al., "Adsorption behavior of iodine by novel covalent organic polymers constructed through heterostructural mixed linkers," *Frontiers in Materials*, vol. 6, no. 12, 2019.
- [8] N. Pandey, S. K. Shukla, and N. B. Singh, "Water purification by polymer nanocomposites: an overview," *Nanocomposites*, vol. 3, no. 2, pp. 47–66, 2017.
- [9] M. Elkady, M. El-Aassar, and H. Hassan, "Adsorption profile of basic dye onto novel fabricated carboxylated functionalized Co-polymer nanofibers," *Polymers*, vol. 8, no. 5, p. 177, 2016.
- [10] Q. Liu, Y. Li, H. Chen et al., "Superior adsorption capacity of functionalised straw adsorbent for dyes and heavy-metal ions," *Journal of Hazardous Materials*, vol. 382, Article ID 121040, 2020.
- [11] Y. Zhou, Y. Hu, W. Huang, G. Cheng, C. Cui, and J. Lu, "A novel amphoteric β -cyclodextrin-based adsorbent for simultaneous removal of cationic/anionic dyes and bisphenol a," *Chemical Engineering Journal*, vol. 341, pp. 47–57, 2018.
- [12] W. Huang, Y. Hu, Y. Li et al., "Citric acid-crosslinked β -cyclodextrin for simultaneous removal of bisphenol a, methylene blue and copper: the roles of cavity and surface functional groups," *Journal of the Taiwan Institute of Chemical Engineers*, vol. 82, pp. 189–197, 2018.
- [13] Y. Li, Y. Zhou, Y. Zhou, J. Lei, and S. Pu, "Cyclodextrin modified filter paper for removal of cationic dyes/Cu ions from aqueous solutions," *Water Science and Technology*, vol. 78, no. 12, pp. 2553–2563, 2019.
- [14] Q. Liu, Y. Zhou, J. Lu, and Y. Zhou, "Novel cyclodextrin-based adsorbents for removing pollutants from wastewater: a critical review," *Chemosphere*, vol. 241, Article ID 125043, 2020.
- [15] Y. Zhou, J. Lu, Y. Zhou, and Y. Liu, "Recent advances for dyes removal using novel adsorbents: a review," *Environmental Pollution*, vol. 252, pp. 352–365, 2019.
- [16] H. Chen, Y. Zhou, J. Wang, J. Lu, and Y. Zhou, "Polydopamine modified cyclodextrin polymer as efficient adsorbent for removing cationic dyes and Cu²⁺," *Journal of Hazardous Materials*, vol. 389, Article ID 121897, 2020.
- [17] H. Zhang, Y. X. Li, P. L. Wang et al., "Synthesis of β -cyclodextrin immobilized starch and its application for the removal of dyestuff from waste-water," *Journal of Polymers and the Environment*, vol. 27, no. 5, pp. 929–941, 2019.
- [18] X. Yue, F. Jiang, D. Zhang, H. Lin, and Y. Chen, "Preparation of adsorbent based on cotton fiber for removal of dyes," *Fibers and Polymers*, vol. 18, no. 11, pp. 2102–2110, 2017.
- [19] R. Kumar, R. K. Sharma, and A. P. Singh, "Removal of organic dyes and metal ions by cross-linked graft copolymers of cellulose obtained from the agricultural residue," *Journal of Environmental Chemical Engineering*, vol. 6, no. 5, pp. 6037–6048, 2018.
- [20] W. Zhu, L. Liu, Q. Liao et al., "Functionalization of cellulose with hyperbranched polyethylenimine for selective dye adsorption and separation," *Cellulose*, vol. 23, no. 6, pp. 3785–3797, 2016.
- [21] A. Almasian, M. E. Olya, and N. M. Mahmoodi, "Preparation and adsorption behavior of diethylenetriamine/polyacrylonitrile composite nanofibers for a direct dye removal," *Fibers and Polymers*, vol. 16, no. 9, pp. 1925–1934, 2015.
- [22] M. A. Ashraf, M. J. Maah, A. K. Qureshi, M. Gharibreza, and I. Yusoff, "Synthetic polymer composite membrane for the desalination of saline water," *Desalination and Water Treatment*, vol. 51, no. 16–18, pp. 3650–3661, 2013.
- [23] X. Lu, X. Feng, Y. Yang et al., "Tuning the permselectivity of polymeric desalination membranes via control of polymer crystallite size," *Nature Communications*, vol. 10, no. 1, p. 2347, 2019.
- [24] Y. Zhou, X. Tang, Y. Xu, and J. Lu, "Effect of quaternary ammonium surfactant modification on oil removal capability of polystyrene resin," *Separation and Purification Technology*, vol. 75, no. 3, pp. 266–272, 2010.
- [25] X. Tang, Y. Zhou, Y. Xu, Q. Zhao, X. Zhou, and J. Lu, "Sorption of polycyclic aromatic hydrocarbons from aqueous solution by hexadecyltrimethylammonium bromide modified fibric peat," *Journal of Chemical Technology & Biotechnology*, vol. 85, no. 8, pp. 1084–1091, 2010.
- [26] N. Abdullah, N. Yusof, W. J. Lau, J. Jaafar, and A. F. Ismail, "Recent trends of heavy metal removal from water/wastewater by membrane technologies," *Journal of Industrial and Engineering Chemistry*, vol. 76, pp. 17–38, 2019.

- [27] F. Checkol, A. Elfving, G. Greczynski, S. Mehretie, O. Inganäs, and S. Admassie, "Highly stable and efficient lignin-PEDOT/PSS composites for removal of toxic metals," *Advanced Sustainable Systems*, vol. 2, no. 1, Article ID 1700114, 2018.
- [28] M. Hosseinzadeh, "Removal of heavy metal ions from aqueous solutions using modified poly(styrene-alt-maleic anhydride) copolymer as a chelating resin," *Russian Journal of Applied Chemistry*, vol. 91, no. 12, pp. 1984–1993, 2018.
- [29] Y. Chen, W. Zhao, H. Wang, X. Meng, and L. Zhang, "A novel polyamine-type starch/glycidyl methacrylate copolymer for adsorption of Pb (II), Cu (II), Cd (II) and Cr (III) ions from aqueous solutions," *Royal Society Open Science*, vol. 5, no. 6, Article ID 180281, 2018.
- [30] T. Yu, Z. Xue, X. Zhao, W. Chen, and T. Mu, "Green synthesis of porous β -cyclodextrin polymers for rapid and efficient removal of organic pollutants and heavy metal ions from water," *New Journal of Chemistry*, vol. 42, no. 19, pp. 16154–16161, 2018.
- [31] H. N. Muhammad Ekramul Mahmud, A. K. O. Huq, and R. B. Yahya, "The removal of heavy metal ions from wastewater/aqueous solution using polypyrrole-based adsorbents: a review," *RSC Advances*, vol. 6, no. 18, pp. 14778–14791, 2016.
- [32] R. Zhang, Y. Zhou, X. Gu, and J. Lu, "Competitive adsorption of methylene blue and Cu₂₊ onto citric acid modified pine sawdust," *CLEAN—Soil, Air, Water*, vol. 43, no. 1, pp. 96–103, 2015.
- [33] L. Hu, S. Gao, X. Ding et al., "Photothermal-responsive single-walled carbon nanotube-based ultrathin membranes for on/off switchable separation of oil-in-water nanoemulsions," *ACS Nano*, vol. 9, no. 5, pp. 4835–4842, 2015.
- [34] J. Saadati and M. Pakizeh, "Separation of oil/water emulsion using a new Psf/pebax/F-MWCNT nanocomposite membrane," *Journal of the Taiwan Institute of Chemical Engineers*, vol. 71, pp. 265–276, 2017.
- [35] M. T. Bankole, A. S. Abdulkareem, I. A. Mohammed et al., "Selected heavy metals removal from electroplating wastewater by purified and polyhydroxybutyrate functionalized carbon nanotubes adsorbents," *Scientific Reports*, vol. 9, no. 1, p. 4475, 2019.
- [36] B. Hayati, A. Maleki, F. Najafi et al., "Heavy metal adsorption using PAMAM/CNT nanocomposite from aqueous solution in batch and continuous fixed bed systems," *Chemical Engineering Journal*, vol. 346, pp. 258–270, 2018.
- [37] Y. Yue, X. Wang, Q. Wu, J. Han, and J. Jiang, "Assembly of polyacrylamide-sodium alginate-based organic-inorganic hydrogel with mechanical and adsorption properties," *Polymers*, vol. 11, no. 8, p. 1239, 2019.
- [38] R. Kumar, M. O. Ansari, A. Alshahrie et al., "Adsorption modeling and mechanistic insight of hazardous chromium on para toluene sulfonic acid immobilized-polyaniline@CNTs nanocomposites," *Journal of Saudi Chemical Society*, vol. 23, no. 2, pp. 188–197, 2019.
- [39] Y. Xie, C. He, L. Liu et al., "Carbon nanotube based polymer nanocomposites: biomimic preparation and organic dye adsorption applications," *RSC Advances*, vol. 5, no. 100, pp. 82503–82512, 2015.
- [40] K. Wu, J. Yu, and X. Jiang, "Multi-walled carbon nanotubes modified by polyaniline for the removal of alizarin yellow r from aqueous solutions," *Adsorption Science & Technology*, vol. 36, no. 1-2, pp. 198–214, 2018.
- [41] P. Jayakaran, G. S. Nirmala, and L. Govindarajan, "Qualitative and quantitative analysis of graphene-based adsorbents in wastewater treatment," *International Journal of Chemical Engineering*, vol. 2019, Article ID 9872502, 17 pages, 2019.
- [42] K. Cao, Z. Jiang, J. Zhao et al., "Enhanced water permeation through sodium alginate membranes by incorporating graphene oxides," *Journal of Membrane Science*, vol. 469, pp. 272–283, 2014.
- [43] L. Dong, W. Fan, X. Tong, H. Zhang, M. Chen, and Y. Zhao, "A CO₂-responsive graphene oxide/polymer composite nanofiltration membrane for water purification," *Journal of Materials Chemistry A*, vol. 6, no. 16, pp. 6785–6791, 2018.
- [44] S. Kim, X. Lin, R. Ou et al., "Highly crosslinked, chlorine tolerant polymer network entwined graphene oxide membrane for water desalination," *Journal of Materials Chemistry A*, vol. 5, no. 4, pp. 1533–1540, 2017.
- [45] N. Liu, M. Zhang, W. Zhang et al., "Ultralight free-standing reduced graphene oxide membranes for oil-in-water emulsion separation," *Journal of Materials Chemistry A*, vol. 3, no. 40, pp. 20113–20117, 2015.
- [46] J. Zhao, H. Chen, H. Ye, B. Zhang, and L. Xu, "Poly (dimethylsiloxane)/graphene oxide composite sponge: a robust and reusable adsorbent for efficient oil/water separation," *Soft Matter*, vol. 15, no. 45, pp. 9224–9232, 2019.
- [47] H.-Y. Mi, X. Jing, A. L. Politowicz, E. Chen, H.-X. Huang, and L.-S. Turng, "Highly compressible ultra-light anisotropic cellulose/graphene aerogel fabricated by bidirectional freeze drying for selective oil absorption," *Carbon*, vol. 132, pp. 199–209, 2018.
- [48] L. P. Terrazas-Bandala, G. G. Sanchez, R. G. Valls et al., "Influence of humidity, temperature, and the addition of activated carbon on the preparation of cellulose acetate membranes and their ability to remove arsenic from water," *Journal of Applied Polymer Science*, vol. 131, no. 8, 2014.
- [49] A. A. Alghamdi, A.-B. Al-Odayni, W. S. Saeed, A. Al-Kahtani, F. A. Alharthi, and T. Aouak, "Efficient adsorption of lead (II) from aqueous phase solutions using polypyrrole-based activated carbon," *Materials*, vol. 12, no. 12, p. 2020, 2019.
- [50] I. Gardi and Y. G. Mishael, "Designing a regenerable stimuli-responsive grafted polymer-clay sorbent for filtration of water pollutants," *Science and Technology of Advanced Materials*, vol. 19, no. 1, pp. 588–598, 2018.
- [51] A. M. Atta, H. A. Al-Lohedan, Z. A. AlOthman, A. A. Abdel-Khalek, and A. M. Tawfeek, "Characterization of reactive amphiphilic montmorillonite nanogels and its application for removal of toxic cationic dye and heavy metals water pollutants," *Journal of Industrial and Engineering Chemistry*, vol. 31, pp. 374–384, 2015.
- [52] H. Zeng, L. Wang, D. Zhang, F. Wang, V. K. Sharma, and C. Wang, "Amido-functionalized carboxymethyl chitosan/montmorillonite composite for highly efficient and cost-effective mercury removal from aqueous solution," *Journal of Colloid and Interface Science*, vol. 554, pp. 479–487, 2019.
- [53] F. Medhat Bojnour and M. Pakizeh, "Preparation and characterization of a nanoclay/PVA/Psf nanocomposite membrane for removal of pharmaceuticals from water," *Applied Clay Science*, vol. 162, pp. 326–338, 2018.
- [54] M. T. Nakhjiri, G. Bagheri Marandi, and M. Kurdtabar, "Effect of bis [2-(methacryloyloxy)ethyl] phosphate as a crosslinker on poly (AAm-co-AMPS)/Na-MMT hydrogel nanocomposite as potential adsorbent for dyes: kinetic, isotherm and thermodynamic study," *Journal of Polymer Research*, vol. 25, no. 11, p. 244, 2018.
- [55] Y. Wang, Y. Xiong, J. Wang, and X. Zhang, "Ultrasonic-assisted fabrication of montmorillonite-lignin hybrid hydrogel: highly efficient swelling behaviors and super-

- sorbent for dye removal from wastewater,” *Colloids and Surfaces A: Physicochemical and Engineering Aspects*, vol. 520, pp. 903–913, 2017.
- [56] J. Dou, Q. Huang, H. Huang et al., “Mussel-inspired preparation of layered double hydroxides based polymer composites for removal of copper ions,” *Journal of Colloid and Interface Science*, vol. 533, pp. 416–427, 2019.
- [57] X.-J. Yang, P. Zhang, P. Li et al., “Layered double hydroxide/polyacrylamide nanocomposite hydrogels: green preparation, rheology and application in methyl orange removal from aqueous solution,” *Journal of Molecular Liquids*, vol. 280, pp. 128–134, 2019.
- [58] B. Nayak, A. Samant, R. Patel, and P. K. Misra, “Comprehensive understanding of the kinetics and mechanism of fluoride removal over a potent nanocrystalline hydroxyapatite surface,” *ACS Omega*, vol. 2, no. 11, pp. 8118–8128, 2017.
- [59] F. Zhao, E. Repo, D. Yin, Y. Meng, S. Jafari, and M. Sillanpää, “EDTA-Cross-Linked β -cyclodextrin: an environmentally friendly bifunctional adsorbent for simultaneous adsorption of metals and cationic dyes,” *Environmental Science & Technology*, vol. 49, no. 17, pp. 10570–10580, 2015.
- [60] M. N. Sahmoune, “Thermodynamic properties of heavy metals ions adsorption by green adsorbents,” in *Green Adsorbents for Pollutant Removal: Fundamentals and Design*, G. Crini and E. Lichtfouse, Eds., Springer, Cham, Switzerland, pp. 193–213, 2018.
- [61] H. N. Tran and H.-P. Chao, “Adsorption and desorption of potentially toxic metals on modified biosorbents through new green grafting process,” *Environmental Science and Pollution Research*, vol. 25, no. 13, pp. 12808–12820, 2018.
- [62] K. L. Tan and B. H. Hameed, “Insight into the adsorption kinetics models for the removal of contaminants from aqueous solutions,” *Journal of the Taiwan Institute of Chemical Engineers*, vol. 74, pp. 25–48, 2017.
- [63] Y. Liu, X. Liu, W. Dong, L. Zhang, Q. Kong, and W. Wang, “Efficient adsorption of sulfamethazine onto modified activated carbon: a plausible adsorption mechanism,” *Scientific Reports*, vol. 7, no. 1, Article ID 12437, 2017.

Research Article

Assessment of Sewage Water Treatment Using Grinded Bauxite Rock as a Robust and Low-Cost Adsorption

Mutairah Shaker Alshammari 

Chemistry Department, College of Science, Jouf University, P.O. Box: 2014, Sakaka, Saudi Arabia

Correspondence should be addressed to Mutairah Shaker Alshammari; msshammari@ju.edu.sa

Received 19 December 2019; Revised 12 January 2020; Accepted 22 January 2020; Published 27 February 2020

Guest Editor: Mohammad Saad Algamdi

Copyright © 2020 Mutairah Shaker Alshammari. This is an open access article distributed under the Creative Commons Attribution License, which permits unrestricted use, distribution, and reproduction in any medium, provided the original work is properly cited.

The shortage of water resources in Saudi Arabia is becoming an increasingly serious problem. Management of sewage water is an attractive option to reduce the contamination of water resources such as ground water. This work aims to use bauxite rock as a low-cost adsorbent/coagulant for sewage water treatment in a simple and rapid technique. Different doses (1, 2, 3, 4 and 5 g/l) of the grinded bauxite was used as an adsorbent/coagulant. The results revealed that, at rock doses of 1, 2, 3, 4, and 5 g/l, the COD concentration was decreased from 326 to 134, 98, 83, 70, and 65 mg/l, respectively, while the BOD concentration was lowered from 243 to 196, 104, 71, 60, 51, and 47 for the same rock doses. This was reflected on the turbidity of the treated effluent from each treatment step. Also, the FC counts were reduced to 2 log units. Furthermore, the dose of 3 g/l of the grinded bauxite rock was found to be the least economic dose for the treatment of sewage water. Bauxite mineral has been used explicitly in a high-performance, very affordable method for wastewater treatment.

1. Introduction

As the population of the world grows and water resource problems keep making headlines, it has never been more essential to preserve water supplies to our maximum extent capacity and to make sure that the water at our disposal is clean and free from pollutants. Organic loads, nutrients, and pathogens contribute major threats in water resources. The removal of such contaminants in wastewater is one of the fundamental aims in waste management. A range of techniques were used for the treatment of various types of wastes to suitable standards [1, 2]. However, conventional waste treatment technologies are expensive. Consequently, several research efforts are running to develop low-cost treatment technologies appropriate in developing countries [2]. Furthermore, during the last few decades, stringent regulation of waste discharge into the environment is receiving wider attentions. To comply with these standards and preserve safe environment, it has become necessary to find some cost-effective treatment techniques. In order to achieve

cost-effective technologies, natural materials such as rocks and sands are widely applied in wastewater treatment for removing pollutants [3]. Several methods were established to remove hazardous substances from wastewater such as precipitation, reverse osmosis, ion exchange, and adsorption [4, 5].

Among all past strategies, adsorption using clay and other composite materials is regarded to be a particularly effective technique, mainly by using minimal-cost and economical methods to eliminate contaminants from industrialized wastewater and aqueous solutions [6–8].

Natural clay minerals and activated carbon with large removal capability are the most popular sorption approaches [9, 10]. Several studies centered on the use of low-cost, extremely efficient pollutant sorbents and also examined the sorption activities of several recycled materials and chemicals [11]. Most of these are clay composites [12], agricultural products, certain aquatic plants, and micro-organisms [11]. Many of these studies have already shown that natural materials are capable of acting as good adsorbents for hazardous contaminants like heavy metals [13, 14], while the kinds and quality of clay materials are also essential as they

are included in selecting which contaminants to address. Ali et al. [15] conducted the adsorption of harmful pollutants from wastewater applying natural zeolite. The results suggest that clinoptilolite removal for ammonium varied from 70 to 92 percent, whilst at different circumstances, it varied from 70 to 99 percent for heavy metals. Bhattacharya et al. [16] examined the adsorption performance of zinc from an aquatic environment with different adsorbents; the results obtained revealed that the percentage of zinc removal rised by raising the adsorbent dosage to achieve full adsorption at 98 percent and pH around 5 and 7 [17]. The adsorption of Cd^{+2} on the surface of nanomaterial based on wollastonite prepared with/without CuO was examined. The results showed that at optimum operating conditions (at pH 9), cadmium ions removal reached 98.88%.

Combined with the growing need for superior quality of water, a growing research for the use of low-cost materials as an adsorbent for water treatment will be an initiative that would be a serious environmental success. Therefore, the main aim of this study is intended to examine and evaluate the ability of certain metal ions to removal using bauxite rocks as natural and low-cost material for the treatment of water and sewage water in Saudi Arabia. The removal experiments were conducted and optimized in the laboratory using the original concentration of metal ions, solution pH, and contact time as variables.

2. Materials and Methods

2.1. Rock Samples. In the northeastern part of the city of Hail, 200 kilometers from the province of Baqa'a lies the village of Zubayra rich in bauxite ore, which is the basic raw material for the production of aluminum, where it is available in large quantities. Bauxite was collected from Zubayra city [18]. The rock was initially grinded to 0.5–1 mm particle diameter and dried. Scanning Electron Microscope (SEM) Model Quanta 250 FEG (Field Emission Gun) attached with EDX Unit (Energy Dispersive X-ray Analyses), with accelerating voltage 30 K-V., magnification 14x up to 1000000 and resolution for Gun.1n) has been performed.

2.2. Sewage Water Samples. Sewage water samples were brought from Sakaka wastewater treatment plant. Within 2 hours after collection, sewage water samples were analyzed [19].

2.3. Method of Jar Test. Jar testing is a process of observing a full-scale method of water purification, offering a sensible idea of how a chemical treatment will operate and perform with a specific type of raw water. Because it imitates full-scale service, process technicians could use jar analysis to identify which chemical treatment looks best with the raw water of their system. Sewage water samples were subjected to a jar test for application of grinded rock adsorption. Different doses of rock (1, 2, 3, 4, and 5 g/l) were tested for the treatment of sewage water. The flash mixing speed was 250 rpm for 1 minute followed by flocculation at 100 rpm for 30 minutes. The flocculation speed was chosen as 100 rpm

due to the precipitation of the grinded rocks and to be in contact with the sewage samples. The test was carried out in 1 liter beakers. The same procedures were carried out in a blank (sample without addition of grinded rock) [19].

2.4. Analysis. During the time of study, the efficiency of the treatment procedure was studied. For samples (raw and treated sewage water), physicochemical and biological analyzes were performed. PH, total suspended solids (TSS), chemical oxygen demand (COD), biological oxygen demand (BOD), and fecal coliform were included in the physicochemical analyzes. The analyses were performed in accordance with the American Public Health Association, Standard Water, and Wastewater Analysis Methods [19].

3. Results and Discussion

3.1. Material Characterization. The main composition of the ore is presented in Table 1. Based on multipoint EDX assessment, there are obviously noticeable round hematite particles with other elements in these regions that is supposed to be given a high bauxite content of Fe_2O_3 . The findings of these analyses that are provided are another evidence of the complicated structure of bauxite and support the data found in the literature suggesting that bauxite minerals are interconnected rather than separately occurring.

3.2. Sewage Water Characteristics. From the results depicted in Table 2 and Figure 1, it is clear that the sewage water used in this study is classified as a low-strength wastewater [20]. The average values for COD, BOD, and TSS were 326, 242.3, and 123.5 mg/l, respectively. The BOD/COD ratio shows the biodegradability of the used wastewater.

3.3. Efficiency of the Treatment Process. In an attempt to enhance the sedimentation of sewage water, the grinded bauxite rock was used. Figure 2 shows the variation of EC, TDS, and turbidity along with the different doses of rock. The levels of TDS and EC were inversely proportional with the turbidity of the raw sewage as well as the samples.

Figure 3 shows the depletion of the concentration of COD with various doses of the rock. It is clear that the concentration of COD reduced by increasing the dose of the rock. The concentration of COD was reduced from 326 to 134, 98, 83, 70, and 65 mg/l at rock doses of 1, 2, 3, 4, and 5 g/l, respectively. The same pattern was noted for both BOD and TSS reduction.

Figure 4 shows the performance of the treatment of sewage water with bauxite rocks. By applying bauxite as an adsorbent, the FC amount was decreased by two logs. The FC count was reduced from 5.5×10^7 to 4.2×10^5 , 3.4×10^5 , 2.8×10^5 , 2.4×10^5 , and 2×10^5 MPN/100 ml for raw sewage, 1, 2, 3, 4 and 5 g/l rock, respectively. Table 3 summarizes the performance of bauxite rock for the treatment of sewage water.

TABLE 1: The bauxite rock's main chemical composition.

Element	Weight (%)	Atomic (%)
O	30.52	49.61
Al	34.51	33.27
Si	1.69	1.56
Ca	0.27	0.17
Fe	33.02	15.38

TABLE 2: Physicochemical features of the wastewater*.

Parameter	Unit	Minimum	Maximum	Average
pH	—	7.3	8.0	
EC	mS	485.1	676.0	576.4
Turbidity	NTU	95	121	111.0
TDS	mg/l	325	406	66.4
COD	mg/l	274.0	370.0	326.0
BOD	mg/l	205	275	243.3
BOD/COD		0.74	0.75	0.745
TSS	mg/l	110	135	123.5
FC	MPN/100 ml	3.3×10^7	7.0×10^7	5.5×10^7

*number of samples = 13.

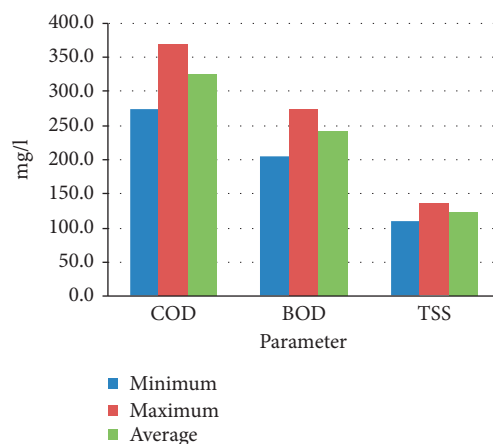


FIGURE 1: Characteristic of raw sewage water COD, BOD, and TSS.

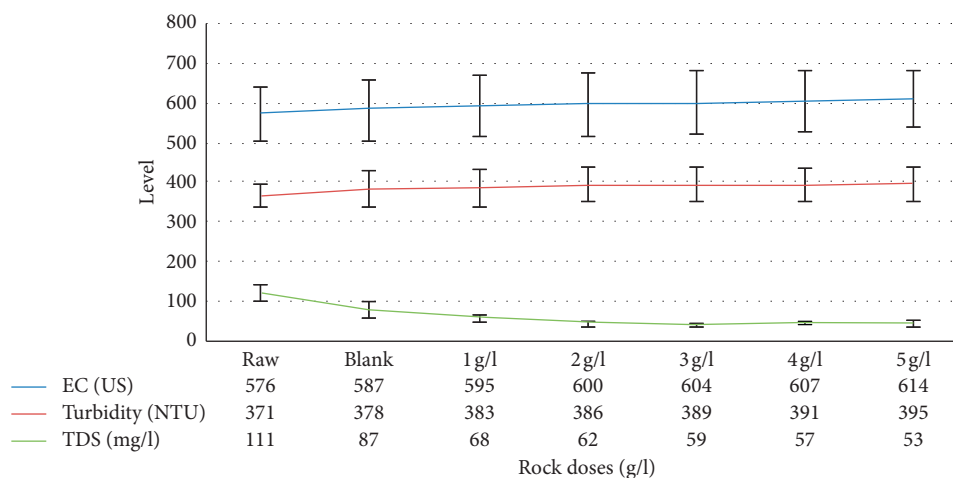


FIGURE 2: Variation of the levels of EC, Turbidity, and TDS along the treatment steps.

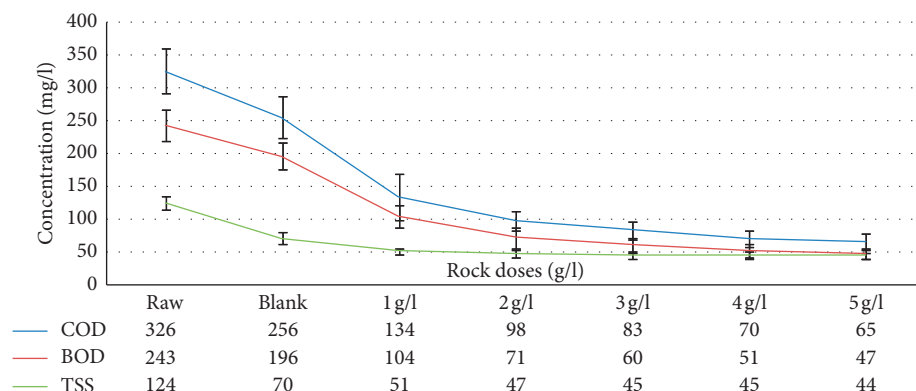


FIGURE 3: Depletion of the COD concentration with the rock dose.

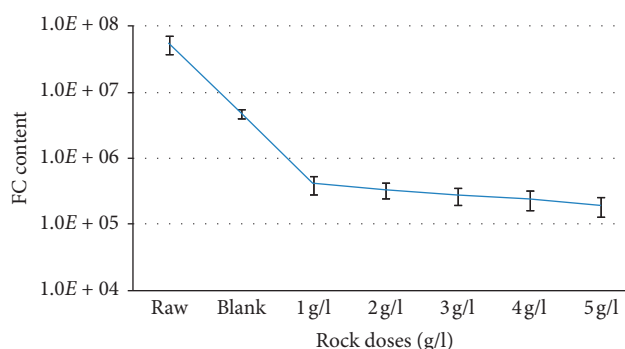


FIGURE 4: Variation of the FC count along with the treatment steps.

TABLE 3: Complete analysis of the raw waste water and different treated effluents.

Parameter	Raw	Blank	% R	1 g/l	%R 1 g/l	2 g/l	%R 2 g/l	3 g/l	%R 3 g/l	4 g/l	%R 4 g/l	5 g/l	%R 5 g/l
pH	7.5	7.9		8.0		8.0		7.8		7.7		7.5	
EC (μ S)	576	587		595		600		604		607		614	
TDS (mg/l)	371	378		383		386		389		391		395	
Turbidity (NTU)	111	87	22	68	21	62	28	59	32	57	34	53	39
COD	326	256	22	134	48	98	61	83	67	70	72	65	75
BOD	243	196	20	104	47	71	63	60	69	51	74	47	76
BOD/COD	0.75	0.74		0.72	0.73			0.72		0.72		0.72	
TSS	124	70	43	51	28	47	33	45	36	45	36	44	38
FC	5.5×10^7	4.9×10^6	90.26	4.2×10^5	91.30	3.4×10^5	93.00	2.8×10^5	94.33	2.4×10^5	94.99	2.0×10^5	95.99

3.4. Removal Mechanisms. There were two main mechanisms for removal of the organic loads from sewage water. The first was adsorption on the surface of the rock particles. The second was the coagulation that occurred due to the presence of Al and Fe in the rock composition. By increasing the rock dose, the surface area increased as well as the dissolution of some component of the rock. This was the reason for increasing the removal efficiency of the organic loads reflected by COD, BOD and TSS and in the consequence, increased the TDS of the treated samples. Raising the dose of rock has also enhanced the turbidity of the treated samples. It was observed that the adsorption capacity

was not significantly raised by raising the rock dose from 3 to 5 g/l. The FC count also decreased by using the grinded rock as the coagulant. The main mechanism for removal of FC bacteria was the adsorption on the surface of the rock. Since it has a positively charged surface (due the presence of Fe and Al), the FC bacteria had negatively charged functional groups. Grehs et al., [21] examined the removal of microorganisms by using aluminium sulphate. They noticed that, as well as the bacterial numbers, turbidity and color were decreased by 1-2 logs. The removal of solid materials from water coagulation and flocculation methods are of major importance. Such methods could minimize color strength

and decrease turbidity levels, organic compounds [22]. Aboubaraka et al. [23] examined graphene oxide for the elimination of turbidity from water, and his results were found to be higher than those obtained in this study.

4. Conclusions

The Bauxite can be crushed to a certain particle size to create a material with high performance in decreasing the water pollution as indicated by COD and BOD values. The findings showed that the COD concentration reduced from 326 to 134, 98, 83, 70, and 65 mg/l while the BOD concentration decreased from 243 to 196, 104, 71, 60, 51, and 47 at rock doses of 1, 2, 3, 4, and 5 g/l for both parameters. In addition, the use of such approach is known to be a rapid strategy of treating sewage water in different areas to reduce the potential for drinking water supplies (such as groundwater).

Data Availability

The data (including the results and all the values of the physicochemical analysis of water before and after treatment) used to support the findings of this study are included within the article. The data are represented in Figures and Tables.

Conflicts of Interest

The authors declare that they have no conflicts of interest.

Acknowledgments

The author is grateful to the Chemistry Department at Jouf University Sakaka, KSA, for support and giving the access for analysis.

References

- [1] M. A. El-Khateeb and F. A. El-Gohary, "Combining UASB technology and constructed wetland for domestic wastewater reclamation and reuse," *Water Science and Technology: Water Supply*, vol. 3, no. 4, pp. 201–208, 2003.
- [2] M. A. El-Khateeb, W. M. Emam, and W. A. Mohamed, "Essam Saber, integration of UASB and downflow hanging non-woven fabric (DHNW) reactors for the treatment of sewage water," *Desalination and Water Treatment*, vol. 164, no. 48–55, 2019.
- [3] S. Ahsan, S. Kaneco, K. Ohta, T. Mizuno, and K. Kani, "Use of some natural and waste materials for waste water treatment," *Water Research*, vol. 35, no. 15, pp. 3738–3742, 2001.
- [4] W. Y. Shi, H. B. Shao, H. Li, M. A. Shao, and S. Du, "Progress in the remediation of hazardous heavy metal-polluted soils by natural zeolite," *Journal of Hazardous Materials*, vol. 170, no. 1, pp. 1–6, 2009.
- [5] A. E. A. Nayl, R. A. Elkhatab, T. El Malah et al., "Adsorption studies on the removal of COD and BOD from treated sewage using activated carbon prepared from date palm waste," *Environmental Science and Pollution Research*, vol. 24, no. 28, pp. 22284–22293, 2017.
- [6] S. Lin and R. S. Juang, "Heavy metal removal from water by sorption using surfactant-modified montmorillonite," *Journal of Hazardous Materials*, vol. 92, no. 3, pp. 315–326, 2002.
- [7] K. Swayampakula, V. M. Boddu, S. K. Nadavala, and K. Abburi, "Competitive adsorption of Cu (II), Co (II) and Ni (II) from their binary and tertiary aqueous solutions using chitosan-coated perlite beads as biosorbent," *Journal of Hazardous Materials*, vol. 170, no. 2–3, pp. 680–689, 2009.
- [8] L. Wang, G. Hu, F. Lyu et al., "Application of red mud in wastewater treatment," *Minerals*, vol. 9, no. 5, p. 281, 2019.
- [9] J. Ayala, J. L. Vega, R. Alvarez, and J. Loreda, "Retention of heavy metal ions in bentonites from Grau region (Northern Peru)," *Environmental Geology*, vol. 53, no. 6, pp. 1323–1330, 2008.
- [10] S. S. Prajapati, P. A. Mohamed Najar, and V. M. Tangde, "Removal of phosphate using red mud: an environmentally hazardous waste by-product of alumina industry," *Advances in Physical Chemistry*, vol. 2016, Article ID 9075206, 9 pages, 2016.
- [11] C. O. Ijagbemi, M.-H. Baek, and D.-S. Kim, "Montmorillonite surface properties and sorption characteristics for heavy metal removal from aqueous solutions," *Journal of Hazardous Materials*, vol. 166, no. 1, pp. 538–546, 2009.
- [12] M. Solener, S. Tunali, A. S. Ozcan, A. Ozcan, and T. Gedikbey, "Adsorption characteristics of lead(II) ions onto the clay/poly(methoxyethyl)acrylamide (PMEA) composite from aqueous solutions," *Desalination*, vol. 223, no. 1, pp. 308–322, 2008.
- [13] M. M. Ali and E. E. El-Sayed, "Capability of natural bentonite for removing organic and inorganic pollutants from wastewater," *Journal of Water Research-Photon Foundation*, vol. 138, pp. 361–370, 2017.
- [14] P. B. Cusack, O. Callery, R. Courtney, É. Ujaczki, L. M. T. O'Donoghue, and M. G. Healy, "The use of rapid, small-scale column tests to determine the efficiency of bauxite residue as a low-cost adsorbent in the removal of dissolved reactive phosphorus from agricultural waters," *Journal of Environmental Management*, vol. 241, pp. 273–283, 2019.
- [15] M. M. Ali, E. E. El-Sayed, and M. Z. Kamel, "Removal of hazardous contaminants from wastewater using natural zeolite," *Journal of Water Research-Photon Foundation*, vol. 138, pp. 333–347, 2017.
- [16] A. K. Bhattacharya, S. N. Mandal, and S. K. Das, "Adsorption of Zn(II) from aqueous solution by using different adsorbents," *Chemical Engineering Journal*, vol. 123, no. 1–2, pp. 43–51, 2006.
- [17] N. Ammar, A. Ahmed Fahmy, K. S. H. Youssef, E. M. A. Hamzawy, and M. A. El-Khateeb, "Wollastonite ceramic/CuO nano-composite for cadmium ions removal from waste water," *Egyptian Journal of Chemistry*, vol. 60, no. 5, pp. 817–823, 2017.
- [18] N. M. Khalil, Y. Algamil, and Q. M. Saleem, "Exploitation of petroleum waste sludge with local bauxite raw material for producing high-quality refractory ceramics," *Ceramics International*, vol. 44, no. 15, pp. 18516–18527, 2018.
- [19] American Public Health Association (APHA), *Standard Methods for the Examination of Water and Wastewater*, APHA, Washington, DC, USA, 22nd edition, 2012.
- [20] Metcalf and Eddy, *Wastewater Engineering Treatment, Disposal and Reuse*, McGraw-Hill, New York, NY, USA, 4th edition, 2005.
- [21] B. W. N. Grehs, A. R. Lopes, N. F. F. Moreira et al., "Removal of microorganisms and antibiotic resistance genes from treated urban wastewater: a comparison between aluminium sulphate and tannin coagulants," *Water Research*, vol. 166, p. 115056, 2019.
- [22] G. Zhu, H. Zheng, W. Chen, W. Fan, P. Zhang, and T. Tshukudu, "Preparation of a composite coagulant: polymeric aluminum ferric sulfate (PAFS) for wastewater treatment," *Desalination*, vol. 285, pp. 315e–323e, 2012.
- [23] A. E. Aboubaraka, E. F. Aboelfetoh, and El-Z. M. Ebeid, "Coagulation effectiveness of graphene oxide for the removal of turbidity from raw surface water," *Chemosphere*, vol. 181, pp. 738e–746e, 2017.

Research Article

Ultrasonic-Assisted Synthesis and Characterization of Chitosan-Graft-Substituted Polyanilines: Promise Bio-Based Nanoparticles for Dye Removal and Bacterial Disinfection

Mutairah Shaker Alshammari ¹, Amr A. Essawy ^{1,2}, A. M. El-Nggar,³ and S. M. Sayyah³

¹Chemistry Department, College of Science, Jouf University, P.O. Box 2014, Sakaka, Aljouf, Saudi Arabia

²Chemistry Department, Faculty of Science, Fayoum University, 63514 Faiyum, Egypt

³Polymer Research Laboratory, Chemistry Department, Faculty of Science, Benisuef University, 62514 Benisuef, Egypt

Correspondence should be addressed to Amr A. Essawy; aaessawy@ju.edu.sa

Received 13 November 2019; Accepted 2 January 2020; Published 31 January 2020

Guest Editor: Mohammad Saad Algamdi

Copyright © 2020 Mutairah Shaker Alshammari et al. This is an open access article distributed under the Creative Commons Attribution License, which permits unrestricted use, distribution, and reproduction in any medium, provided the original work is properly cited.

The sonication-mediated oxidative-radical copolymerization using ammonium persulfate in acidic medium provides a new successful avenue to graft Chitosan with three methylaniline derivatives. The synthesized Chitosan-graft-polymethylanilines (CGPMA) were characterized using FTIR, UV-vis diffuse reflectance spectroscopy, XRD, thermogravimetric analysis (TGA), elemental analysis, and transmission electron microscopy (TEM). XRD spectra revealed that CGPMA have a higher crystallinity degree compared to the pristine Chitosan. In addition, a methyl position-dependent crystallinity is noticeable for the grafted copolymers. This could be confirmed from TEM images that reflect structure-affected morphologies of different ordering for the graft spherical nanoparticles. Interestingly, the copolymers prepared under ultrasonic irradiation show a high potency in dye uptake compared to nonsonicated ones. Moreover, an antibacterial preliminary test on the as-prepared materials was accomplished. We have achieved promising results, which encourages us to conduct more studies to process these materials in developing biomedical active composites.

1. Introduction

Recently, conducting polymers have taken a great consideration in the field of scientific research, especially in material science. Among conductive polymers, either polyaniline (PANI) or its derivatives are unique materials in many aspects such as handy preparation, considerable stability, and favored electrochemical features including the magnificent conduction mechanism and their wonderful optical, electrical, and catalytic properties [1]. However, polyaniline has a lack of process ability; this drawback was overcome either by protonation with suitable reactive acids or by preparation of polymer derivatives. The polymer deriving can be achieved through replacing hydrogen atoms either at nitrogen atom or in the aromatic rings of the polymer by active substituents [2]. PANI has promising

applications in many fields, for example, rechargeable batteries, protection of metals against corrosion, gas-separation membranes, and molecular sensors [3, 4]. It is catchy and commercialized owing to its facile preparation, due to electrochemical or chemical processes and inexpensive production in large quantities [5]. It offers great environmental, chemical, and thermal stability [6]. PANI can be converted into protonated or deprotonated form via processing with acids or bases. The emeraldine salt of PANI is an acid doped conducting polymer, and its emeraldine base is an insulator polymer [7]. PANI also shows high antibacterial properties [8, 9].

Chitosan is a naturally occurring, biodegradable, non-toxic, nonallergenic biopolysaccharide derived from chitin, found abundantly in nature [10, 11]. Chitosan exhibits a broad particle use in many fields; it is a friable substance

which has a tendency to absorb some moisture. In addition, it is relatively inexpensive and of high molar mass with interesting physicochemical features [12].

The grafting of Chitosan could be achieved through the introduction of functional derivatives onto Chitosan via covalent bonding [13]. The grafting process on Chitosan is one of the routes to improve its characteristics, for example, enhancing chelation [14] or antibacterial impact [15] or boosting adsorption characteristics [16].

Chitosan and water insoluble Chitosan derivatives have a high adsorption power against toxic, fatty acids and dangerous heavy metal ions like Sn^{2+} and Sn^{4+} of inorganic or organic confinement, Hg^{2+} , Pb^{2+} , U^{6+} , and transition metal ions such as Ni^{2+} , Cu^{2+} , V^{4+} , Cd^{2+} , Cr^{3+} , and Zn^{2+} [17]. Chitosan and its derivatives have unique applications in biological field, such as antibacterial agents.

Recently, nanomaterials, including metallic, inorganic, and polymeric substances with a size of 1–100 nm, have attracted an increasing attention of many scientific interests [18]. Ultrasonication could result in new chemical reactivity within promoted reaction rate and thus reveals a new directory in chemistry, that is, sonochemistry [19]. In particular, sonochemistry that depends on highly intense ultrasound provides mediation to promote chemical reactions. The activation effect refers to the crushing, dispersion, and emulsifying processes that prevent particle aggregation and minimize its size. This enables particle preparation within a better and controlled shape, especially on the solid material, such as polyaniline [20]. In addition, the simplicity and safety of the sonochemical technique positioned it as a powerful tool in the field of green chemistry [21].

Therefore, this work presents a new avenue implying ultrasound mediated oxidative-radical copolymerization to graft the polysaccharide, Chitosan, with three methylaniline derivatives. The optimized grafting copolymerization parameters were studied. Interestingly, the as-prepared grafted copolymers exhibit structure-affected crystallinity, uniformity, and thermal stability. The preliminary test reveals potent adsorptivity to Remazol Red RB 133 (RR), a commonly used water-soluble azo dye. A crucial rule for ultrasonication in improving the grafted copolymer adsorptivity has been indicated by comparing the adsorption capacity of sonicated grafted copolymers with nonsonicated ones. Furthermore, the developed grafted copolymers were investigated for their efficacy in bacterial disinfection. Extensive studies on these applications will be conducted in further work.

2. Experimental

2.1. Materials and Methods. N-Methylaniline (NMA), 2-Methylaniline (2MA), and 3-Methylaniline (3MA) (Sigma Aldrich). Starting with the shrimp shells, Chitosan was extracted according to the methodology described in literature [22, 23] (M. Wt. ~109,000; deacetylation degree >85%). Ammonium persulfate and N-methyl-2-pyrrolidone (Loba Chemie, India) and acetic acid, hydrochloric acid, and acetone were supplied from El-Nasr Chemical Co. (Egypt). The

azo dye, Remazol Red 133 of commercial grade, was used as received.

2.2. Synthesis of CGPMA. Chitosan solution (1.0 g/L) was prepared by adding appropriate Chitosan amount to acetic acid solution (2%) in a flask and stirring for 2 hours at room temperature ($25^\circ\text{C} \pm 2$). A mixture solution of substituted aniline solution (1.0×10^{-2} mol/L) and HCl (0.2 mol/L) was added to the solution of Chitosan at 5°C , under continuous stirring for 20 min. Ammonium persulfate (7.5×10^{-2} mol/L) in HCl (0.2 mol/L) was put drop-wisely to the mixture and the mixture was stirred for 5 hours at 5°C . Over the suite of polymerization, ultrasonic irradiation of the reaction course is employed by using an ultrasonic processor of 120 W and 38 kHz. The final admixture was separated, and the resulting precipitate was leached with deionized water, N-methyl-2-pyrrolidone, and acetone, respectively, to remove possibly present impurities, that is, monomers residue, initiator, and homopolymers chains; then, it was finally dried for 24 hours in a vacuum oven at 50°C .

It is important to mention that the prepared grafted copolymers are insoluble in almost all solvents either on cold or by heating. The grafting percentage was calculated by

$$\text{Grafting (G)\%} = \left(\frac{W - W_o}{W_o} \right) \times 100, \quad (1)$$

where W = the weight of CGPMA and W_o = the weight of original Chitosan.

2.3. Instrumental. FTIR spectra were measured on an IR spectrometer, Shimadzu model Affinity-1S. The diffuse reflectance spectroscopy along the ultraviolet-visible range was recorded on a Shimadzu Japan 3101 p spectrophotometer. X-ray of wavelength (1.54 Å) within a Cu detector in the X-ray diffractometer (D/Max2500VB2+/Pc, Rigaku Company) was employed to conclude the graft crystallinity. For TEM analysis, samples were taken on (JEOL, JEM-2100, Japan). The thermogravimetric analysis of the polymers was conducted using an Netzsch TGA 204 (Germany) in the presence of an N_2 atmosphere from 25°C to 600°C . A CHN Perkin-Elmer analyzer (USA) was used to address the elemental analyses of the developed grafts. A spectrophotometer (Agilent Cary 60) was used to monitor the absorption profile in the UV-vis range.

3. Results and Discussion

3.1. Characterization of the Grafted Chitosan. Representative sonicated CGPMA samples were distinguished by reflectance spectroscopy, FTIR, TEM, XRD, TGA, and elemental analysis.

3.1.1. FTIR Spectra. The IR spectroscopy shows a viable role for confirming the grafting copolymerization between Chitosan and substituted polyanilines.

The IR spectra of Chitosan and CGPMA were depicted in Figure 1. As seen for Chitosan, the overlapping due to NH_2

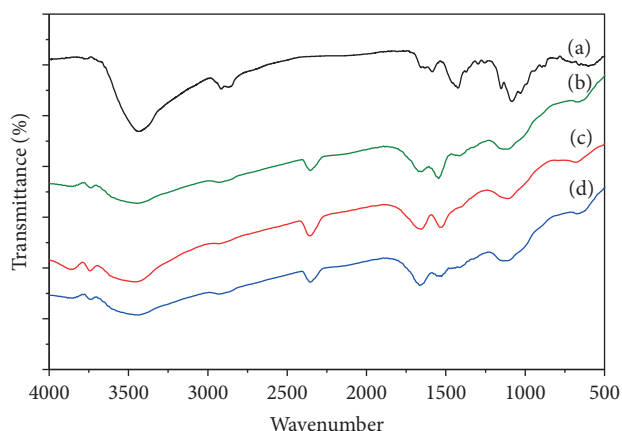


FIGURE 1: FTIR spectra of (a) Chitosan, (b) CGPNMA, (c) CGP2MA, and (d) CGP3MA.

and OH stretching vibrations resulted in the peak assigned at 3438 cm^{-1} , while the peaks found in the range of $2870\text{--}2920\text{ cm}^{-1}$ could be related to the symmetric-CH stretching. Moreover, the peak assigned at 1589 cm^{-1} is rendered to bending of NH_2 [24] and the peak assigned at 1426 cm^{-1} is related to the- CH_2 bending [22]. The revealed peak at 1154 cm^{-1} is due to the C-O-C bridge antisymmetric stretching, while that indicated at 1085 cm^{-1} is assigned to the C-O skeletal stretching vibration that are characteristics of the saccharide structure of Chitosan [25].

The IR spectra of Chitosan-graft-substituted polyanilines confirm the effective grafting of substituted polyanilines on Chitosan by the peaks at 1612 , 1610 , and 1607 cm^{-1} for CGPNMA, CGP2MA, and CGP3MA, respectively, owing to the distinctive peaks of quinonoid nitrogen (Q) and the peaks manifested at 1497 , 1494 , and 1493 cm^{-1} for CGPNMA, CGP2MA, and CGP3MA, respectively, accompanied by the benzenoid ring present in the substituted polyaniline. The peaks found at 1329 , 1328 , and 1326 cm^{-1} for CGPNMA, CGP2MA, and CGP3MA, respectively, are related to the C-N and C=N stretching vibration in substituted polyanilines [26, 27]. Additionally, the peak of N=Q=N bending vibrations of substituted polyaniline was indicated around 1150 cm^{-1} [28, 29]. Further, the shift of these peaks to lower wavenumber 1112 , 1108 , and 1106 cm^{-1} for CGPNMA, CGP2MA, and CGP3MA, respectively, was owing to hydrogen bonding between Chitosan and substituted polyanilines [30].

3.1.2. UV-Vis Diffuse Reflectance Spectra. The UV-vis DRS of the CGPMA are shown in Figure 2. The conductive polymers have some usual transitions in the UV-visible region, such as $\pi\text{-}\pi^*$, polaron- π^* , and π -polaron transitions, respectively. CGPMA (with aniline pattern) are predicted to have three peaks in the range of 320 nm , 400 nm , and $600\text{--}620\text{ nm}$; the first absorption peak comes from $\pi\text{-}\pi^*$ electron transfer in the benzenoid fragments, while the second and third absorption bands are due to the development of conducting polarons (quinoid segments), respectively, which are characteristics of the protonated type of substituted polyaniline [31].

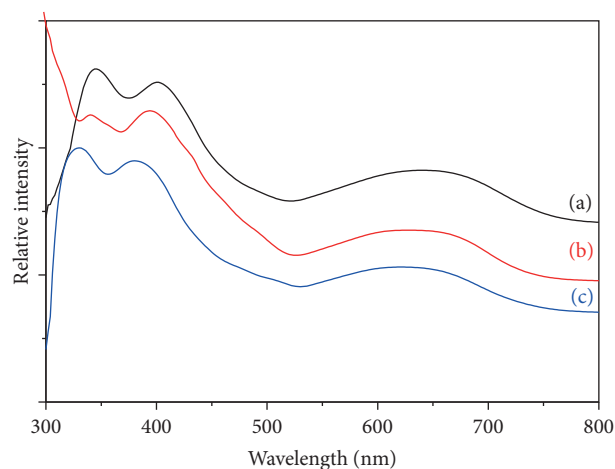


FIGURE 2: UV-vis diffuse reflectance spectra of (a) CGPNMA, (b) CGP2MA, and (c) CGP3MA.

In general, extending the double bond conjugation along the polymeric chain reveals a $\pi\text{-}\pi^*$ energy difference decrease that corresponds to an increase in the wavelength indicating the interaction of Chitosan with substituted polyanilines. The recorded UV-vis spectra of CGPMA show that peaks of $\pi\text{-}\pi^*$ excitation have been transferred from 321 , 346 nm , and 338 nm for CGPNMA, CGP2MA, and CGP3MA, respectively; moreover, the peaks assigned at $\approx 400\text{ nm}$ and $600\text{--}620\text{ nm}$ were transferred to around 406 nm and 650 nm [32, 33]. There are no significant absorption peaks for Chitosan in CGPMA spectrum that is expected at 330 nm which is related to the glucopyranoside structure of Chitosan because of overlapped benzenoid moieties of the grafted substituted polyanilines around 350 nm [34].

3.1.3. XRD Diffraction Patterns. Figure 3 displayed the XRD of chitosan and CGPMA. For the grafted Chitosan, the XRD spectra showed crystallinity from $20^\circ\text{--}32^\circ$ due to the grafting of substituted polyanilines onto the Chitosan backbone, whereas X-ray diffractogram of Chitosan showed amorphous pattern [30]. The crystallinity was noticeably amended due to hydrogen bonding interactions of inter- and intramolecular nature [35]. The XRD patterns b and especially c, d in Figure 3 show sharp and well defined peaks, which indicate the crystalline nature of CGPMA. Furthermore, the degree of crystallinity of CGP3MA and CGP2MA is noticeably higher than that of CGPNMA. This order of crystallinity of three different grafted copolymers can be explained according to the correlation between crystallinity and thermal stability shown in TGA results, similar to trends reported in literatures [36, 37]. This is due to a considerable localization of the electrons over the polymeric chain that leads to a decrease in the crystallinity [38–40]. The increasing localization depending on the methyl group position on the aniline monomer in the order: N-position, ortho-position, and meta-position leads thereby to the resulting order of crystallinity [39].

3.1.4. Transmission Electron Microscopy (TEM). In the present study, TEM images show the morphological features

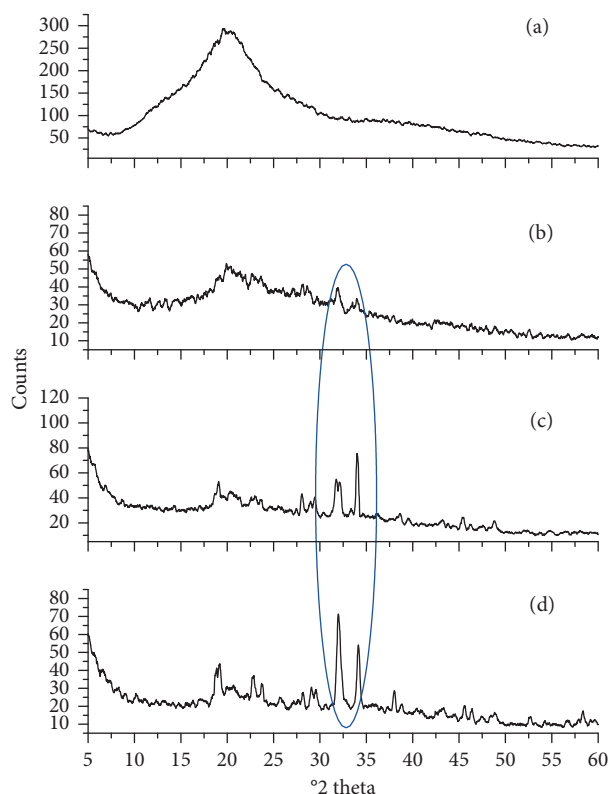


FIGURE 3: XRD spectra of (a) Chitosan, (b) CGPNMA, (c) CGP2MA, and (d) CGP3MA.

and surface appearance of Chitosan and CGPMA. Chitosan is shown in a network shape but CGPMA are shown as spherically shaped, smooth-surface nanoparticles of size range 2.8–16 nm as depicted in Figure 4. These features could be attributed to the added value of the applied ultrasonication along with the grafting process. The ultrasonication exerts immense shocking of ultrasonic waves, resulting in functionalities of dispersion, pulverization, and emulsification, revealing smaller particles within steady matrix [18].

3.1.5. Thermogravimetric Analysis (TGA). The thermal resistance of CGPMA was investigated taking the thermogravimetric behavior of Chitosan as a reference. TGA curves of Chitosan and CGPMA samples are displayed in Figure 5. First weight losses of all the samples (6–9%) observed between 30 and 100°C could be due to the loss of water content. Chitosan offers a distinct weight loss at 270–320°C, assigned to the decomposition of Chitosan chains. The residue for Chitosan at 600°C was 39%. The weight loss of CGPMA in the range of 100–240°C is corresponding to dopant molecules removal from the grafted copolymer structure. In the subsequent stage, the weight loss appeared between 220 and 390°C of CGPMA owing to the degradation of the CGPMA chain. About 8–14% of loosed weight within temperature gradient (400–600°C) was estimated for grafted copolymer due to the loosing of Chitosan side chain. At the end of the experiment at 600°C, nearly 56, 52 and 49% of CGP3MA, CGP2MA, and CGPNMA, respectively, remained as residue

while, for Chitosan, 39% remained as a residue showing the greater thermal stability of CGPMA over Chitosan owing to the introduction of substituted polyanilines into Chitosan. Comparing the thermal stability of samples, Chitosan shows the highest foremost decomposition temperature (270–320°C), while CGPMA possess a higher residual amount and decompose at a relatively higher temperature (600°C) than Chitosan. This indicates that CGPMA have a relatively higher thermal stability than pure Chitosan perhaps due to an improvement in the intramolecular and intermolecular H-bonds in the structural skeleton of the copolymer [26, 41]. These findings are greatly compatible with results concluded from XRD and TEM analyses.

3.1.6. Elemental Analysis. Table 1 shows Chitosan elementary analysis, CGPMA, and the corresponding estimates of grafting percent (G%). Comparing elemental analysis of Chitosan with those of CGPMA indicated a noticeable increase in carbon and nitrogen contents as the monomer weight fraction was increased. These findings are consistent with G%.

3.2. Preliminary Study of Adsorption Process. We conducted a preliminary study to investigate the adsorption effect of Ch-g-PNMeANI as an example of Ch-g-MPANI copolymers. In a batch of experiments, fixed adsorbent amounts were added to 75 mL of RR solution (60 mg/L) in Erlenmeyer flask of 100 mL, which was then concussed using a horizontal shaker at $25 \pm 2^\circ\text{C}$. The uptake of Remazol Red dye

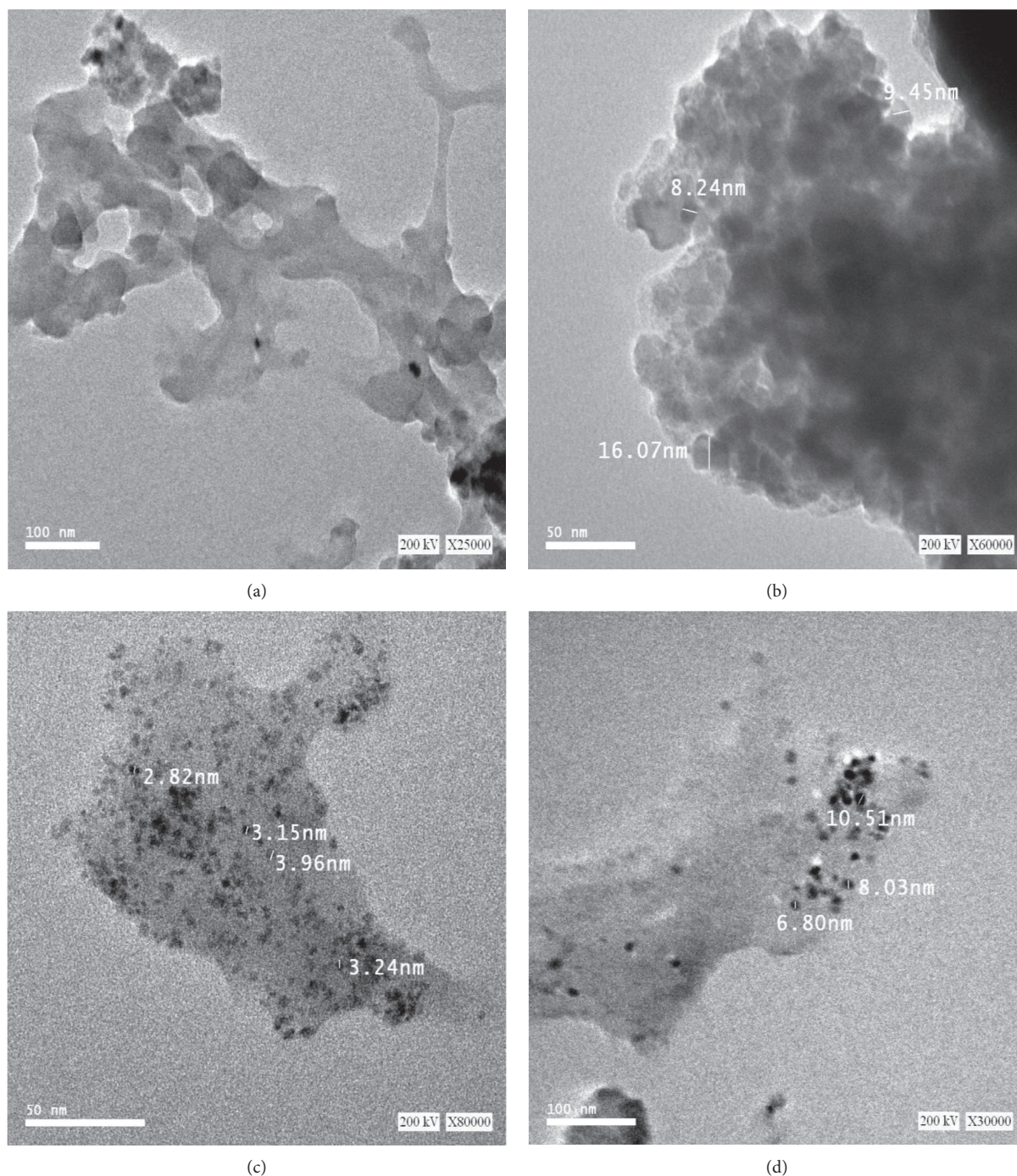


FIGURE 4: TEM images of (a) Chitosan, (b) CGPNMA, (c) CGP2MA, and (d) CGP3MA.

from aqueous solution in the adsorption process is shown in Figure 6(a). The adsorbent was isolated and the residual dye was analyzed via ultraviolet-visible absorption spectrophotometry at $\lambda_{\max} = 520 \text{ nm}$ at different contact times, as shown in Figure 6(b). According to the calibration plot, the amount of dye sequestration by the adsorbents was estimated from (2):

$$q = \frac{[(C_o - C_f) \times V]}{m}, \quad (2)$$

where q is the sequestered amount of dye due to adsorbents (mg/g), C_o is the concentration of RR initially allowed to be contacting to the adsorbent (mg/L), C_f is the [dye] (mg/L) after the removal operation, V is the volume of dye solution (L) allowed to be contacting to the adsorbent, and m is the adsorbent mass (g). It can be seen that the characteristic absorption band of RR around 520 nm decreased rapidly with increasing the adsorption time and finally nearly disappeared in about 50 min. It is important to point out that the Ch-g-PNMeANI prepared using the developed synthetic

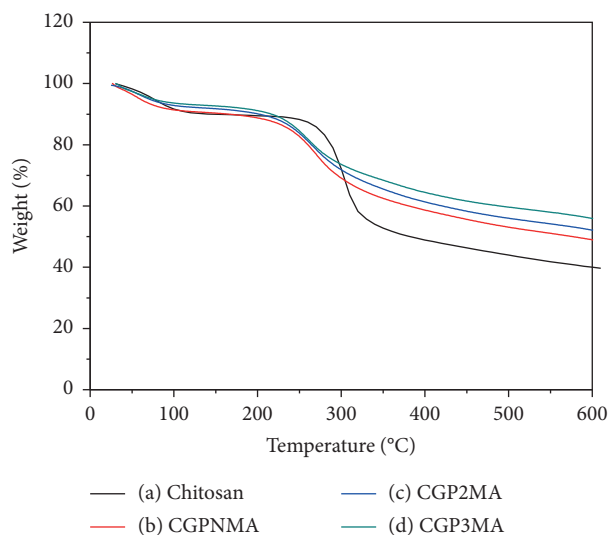
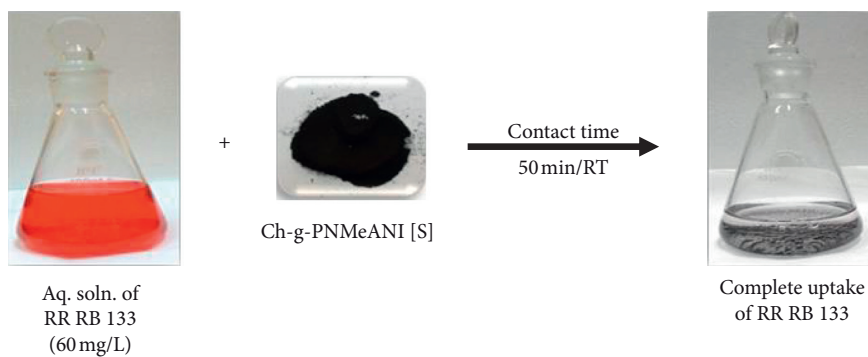


FIGURE 5: TGA of (a) Chitosan, (b) CGPNMA, (c) CGP2MA, and (d) CGP3MA.

TABLE 1: The elemental analysis of Chitosan and CGPMA and the calculated grafting percent.

Material	Grafting (%)	C (%)	H (%)	N (%)
Chitosan	—	39.88	4.63	6.30
CGPNMA	196	53.98	5.90	10.60
CGP2MA	187	43.42	6.37	8.60
CGP3MA	179	40.81	5.97	7.36



(a)

FIGURE 6: Continued.

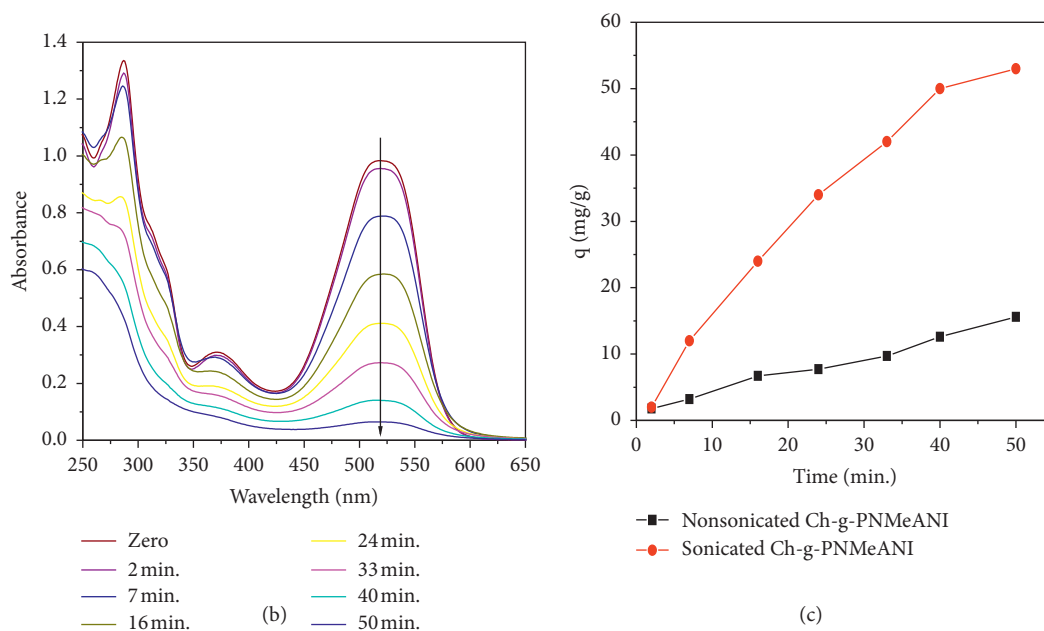


FIGURE 6: (a) Image shows the complete uptake of RR by Ch-g-PNMeANI adsorbent. (b) Adsorption-induced changes of the absorption spectrum of RR after different contact times with Ch-g-PNMeANI. (c) The variation of adsorption capacity with adsorption time for aqueous solution of RR dye onto nonsonicated (black line) and sonicated (red line) Ch-g-PNMeANI.

route is highly adsorptive and practically adsorbs all RR (60 mg/L), referring to a promising nanoparticle for water detoxification. On the other hand, the same weight from the nonsonicated Ch-g-PNMeANI has much lower adsorption capacity compared to the sonicated one, although all experimental conditions were the same, as shown in Figure 6(c). This interestingly highlights the crucial rule of ultrasonication in developing materials of highly desirable properties that maximize the environmental impact of the presented copolymers. More in-depth studies on this application will be under focus of further work.

3.3. Preliminary Study of Antibacterial Activity. A preliminary investigation was carried out to evaluate the antibacterial effect of CGPNMA as an example of CGPMA copolymers versus *Escherichia coli* (Gram-negative) in addition to *Staphylococcus aureus* (Gram-positive) that are provided from reference collection by determining the growth inhibitory effect of CGPNMA in broth bacterial suspension (10^8 CFU/mL) as a reference to quantify the initial colony that is employed in the plate counting method to be determined. The spectrophotometric analysis was conducted to quantify the CFU via the comparison of absorption optical density of standard CFU with unknown CFU at wavelength 625 nm. In a typical procedure, within an absorption range of optical density (0.08–0.13) due to McFarland standard 0.5 ($1-2 \times 10^8$ CFU/mL), the absorbance will be adapted by appropriate addition of sterilized distilled water. Then, the bacterial suspension (10^8 CFU/mL) was directly enrolled in the antibacterial tests for CGPNMA. In a sterilized Erlenmeyer flask, CGPNMA (0.1 g) was added to 10 mL of the bacterial suspension. Next, the flask was shaken

for 2 hours at 250 rpm, and then 1.0 mL of this mixture was used to determine the change in the absorption optical density [42, 43]. The growth inhibitory % was counted as follows:

$$\text{Inhibition \%} = \frac{(\text{Control conc.} - \text{Test conc.})}{\text{Control conc.}} \times 100. \quad (3)$$

The CGPNMA composite NPs were tested for antibacterial activity by addressing the inhibition % of bacterial growth where estimates of 87% and 92% are recorded for *S. aureus* and *E. coli*, respectively. Such promising antibacterial potentiality could be attributed to the synergism within the conductive polymeric poly N-methylaniline grafted onto the Chitosan skeleton [41]. More in-depth studies on this application will be under focus of further work.

4. Conclusions

CGPMA were prepared via the sonication-mediated chemical oxidation. FTIR ascertained Chitosan grafting by substituted polyanilines. Compared to the pristine amorphous Chitosan, the degree of crystallinity for both CGP3MA and CGP2MA is higher than CGPNMA that is attributed to the inter- and intramolecular hydrogen bonding. TEM analysis of CGPMA confirmed the presence of nanoparticles that have a nearly spherical shape and smooth surface. These features could result from the added value of ultrasonication along with the grafting process. Moreover, all grafted copolymers reveal a higher final degradation temperature than Chitosan. Furthermore, the provided new sonication-mediated synthetic route of the grafted copolymers results in high potency for dye uptake compared to the nonsonicated ones. Moreover, the

developed polymeric composites show promising antibacterial properties for both Gram-negative and Gram-positive bacteria. Thus, the developed sonicated-assisted synthetic route maximizes the environmental impact of the presented copolymers in either detoxification or disinfection of dye/bacterial enriched wastewaters.

Data Availability

The original data of this manuscript will be available upon request from the corresponding author.

Conflicts of Interest

The authors declare that they have no conflicts of interest.

References

- [1] A. A. M. Farag, A. Ashery, and M. A. Shenashen, "Optical absorption and spectrophotometric studies on the optical constants and dielectric of poly (o-toluidine) (POT) films grown by spin coating deposition," *Physica B: Condensed Matter*, vol. 407, no. 13, pp. 2404–2411, 2012.
- [2] Z. H. Wang, A. Ray, A. G. MacDiarmid, and A. J. Epstein, "Electron localization and charge transport in poly(o-toluidine): a model polyaniline derivative," *Physical Review B*, vol. 43, no. 5, pp. 4373–4384, 1991.
- [3] H. Karami, M. F. Mousavi, and M. Shamsipur, "A new design for dry polyaniline rechargeable batteries," *Journal of Power Sources*, vol. 117, no. 1-2, pp. 255–259, 2003.
- [4] P. P. Sengupta, S. Barik, and B. Adhikari, "Polyaniline as a gas-sensor material," *Materials and Manufacturing Processes*, vol. 21, no. 3, pp. 263–270, 2006.
- [5] S. M. Sayyah, A. A. Aboud, A. B. Khaliel, and S. M. Mohamed, "Oxidative chemical polymerization of ortho-toluidine in acid medium using $K_2Cr_2O_7$ as oxidizing agent and characterization of the obtained polymer," *International Journal of Advanced Research*, vol. 2, no. 6, pp. 586–607, 2014.
- [6] J. Prokeš and J. Stejskal, "Polyaniline prepared in the presence of various acids: 2. Thermal stability of conductivity," *Polymer Degradation and Stability*, vol. 86, pp. 187–195, 2004.
- [7] P. K. Kahol, K. K. Sathesh Kumar, S. Geetha, and D. C. Trivedi, "Effect of dopants on electron localization length in polyaniline," *Synthetic Metals*, vol. 139, no. 2, pp. 191–200, 2003.
- [8] M. R. Gizdavic-Nikolaidis, J. R. Bennett, S. Swift, A. J. Easteal, and M. Ambrose, "Broad spectrum antimicrobial activity of functionalized polyanilines," *Acta Biomaterialia*, vol. 7, no. 12, pp. 4204–4209, 2011.
- [9] S. H. I. Nanlin, X. Guo, H. Jing, J. Gong, C. Sun, and K. Yang, "Antibacterial effect of the conducting polyaniline," *Journal of Materials Science and Technology*, vol. 22, pp. 289–290, 2009.
- [10] K. Aoi, A. Takasu, and M. Okada, "New chitin-based polymer hybrids. 2. Improved miscibility of chitin derivatives having monodisperse poly(2-methyl-2-oxazoline) side chains with poly(vinyl chloride) and poly(vinyl alcohol)1," *Macromolecules*, vol. 30, no. 20, pp. 6134–6138, 1997.
- [11] T. A. Khan, K. K. Peh, and H. S. Ch'ng, "Mechanical, bio-adhesive strength and biological evaluations of chitosan films for wound dressing," *Journal of Pharmacy and Pharmaceutical Sciences*, vol. 3, pp. 303–311, 2000.
- [12] V. Singh, D. N. Tripathi, A. Tiwari, and R. Sanghi, "Microwave promoted synthesis of chitosan-graft-poly(acrylonitrile)," *Journal of Applied Polymer Science*, vol. 95, no. 4, pp. 820–825, 2005.
- [13] M. Ignatova, N. Manolova, and I. Rashkov, "Novel antibacterial fibers of quaternized chitosan and poly(vinyl pyrrolidone) prepared by electrospinning," *European Polymer Journal*, vol. 43, no. 4, pp. 1112–1122, 2007.
- [14] H. Wang, W. Li, Y. Lu, and Z. Wang, "Studies on chitosan and poly(acrylic acid) interpolymer complex. I. Preparation, structure, pH-sensitivity, and salt sensitivity of complex-forming poly(acrylic acid): chitosan semi-interpenetrating polymer network," *Journal of Applied Polymer Science*, vol. 65, no. 8, pp. 1445–1450, 1997.
- [15] S.-G. Hu, C.-H. Jou, and M.-C. Yang, "Surface grafting of polyester fiber with chitosan and the antibacterial activity of pathogenic bacteria," *Journal of Applied Polymer Science*, vol. 86, no. 12, pp. 2977–2983, 2002.
- [16] D. Mahanta, U. Manna, G. Madras, and S. Patil, "Multilayer self-assembly of TiO_2 nanoparticles and polyaniline-grafted-chitosan copolymer (CPANI) for photocatalysis," *ACS Applied Materials & Interfaces*, vol. 3, no. 1, pp. 84–92, 2010.
- [17] M.-Y. Lee, K.-J. Hong, T. Kajuchi, and J.-W. Yang, "Synthesis of chitosan-based polymeric surfactants and their adsorption properties for heavy metals and fatty acids," *International Journal of Biological Macromolecules*, vol. 36, no. 3, pp. 152–158, 2005.
- [18] H. Xia and Q. Wang, "Synthesis and characterization of conductive polyaniline nanoparticles through ultrasonic assisted inverse microemulsion polymerization," *Journal of Nanoparticle Research*, vol. 3, pp. 399–409, 2001.
- [19] T. J. Mason and J. P. Lorimer, *Sonochemistry: Theory, Applications and Uses of Ultrasound in Chemistry*, Ellis Horwood, Chichester, UK, 1998.
- [20] K. S. Suslick, T. Hyeon, and M. Fang, "Nanostructured materials generated by high-intensity ultrasound: sonochemical synthesis and catalytic studies," *Chemistry of Materials*, vol. 8, no. 8, pp. 2172–2179, 1996.
- [21] P. Cintas and J.-L. Luche, "Green chemistry," *Green Chemistry*, vol. 1, no. 3, pp. 115–125, 1999.
- [22] M. H. M. Hussein, M. F. El-Hady, W. M. Sayed, and H. Hefni, "Preparation of some chitosan heavy metal complexes and study of its properties," *Polymer Science Series A*, vol. 54, no. 2, pp. 113–124, 2012.
- [23] M. H. Hussein, M. F. El-Hady, H. A. H. Shehata, M. A. Hegazy, and H. Hefni, "Preparation of some eco-friendly corrosion inhibitors having antibacterial activity from sea food waste," *Journal of Surfactants and Detergents*, vol. 16, pp. 233–242, 2013.
- [24] S. Ramanathan, V. Ponnuswamy, B. Gowtham, K. Premnazeer, and S. C. Murugavel, "Effect of ammonium persulfate (aps) concentration on chitosan grafted polyaniline," *Journal of Optoelectronics and Advanced Materials*, vol. 14, pp. 1011–1015, 2012.
- [25] X. H. Xu, G. L. Ren, J. Cheng, Q. Liu, D. G. Li, and Q. Chen, "Self-assembly of polyaniline-grafted chitosan/glucose oxidase nanolayered films for electrochemical biosensor applications," *Journal of Materials Science*, vol. 41, no. 15, pp. 4974–4977, 2006.
- [26] R. Karthik and S. Meenakshi, "Removal of Pb(II) and Cd(II) ions from aqueous solution using polyaniline grafted chitosan," *Chemical Engineering Journal*, vol. 263, pp. 168–177, 2015.
- [27] A. Yağan, N. Ö. Pekmez, and A. Yildiz, "Electropolymerization of poly (N-methylaniline) on mild steel: synthesis, characterization and corrosion protection," *Journal of Electroanalytical Chemistry*, vol. 578, no. 2, pp. 231–238, 2005.

- [28] C.-T. Kuo, S.-Z. Weng, and R.-L. Huang, "Field-effect transistor with polyaniline and poly(2-alkylaniline) thin film as semiconductor," *Synthetic Metals*, vol. 88, no. 2, pp. 101–107, 1997.
- [29] B. Narayanasamy and S. Rajendran, "Electropolymerized bilayer coatings of polyaniline and poly(N-methylaniline) on mild steel and their corrosion protection performance," *Progress in Organic Coatings*, vol. 67, no. 3, pp. 246–254, 2010.
- [30] A. Tiwari and V. Singh, "Synthesis and characterization of electrical conducting chitosan-graft-polyaniline," *Express Polymer Letters*, vol. 1, no. 5, pp. 308–317, 2007.
- [31] J. Wei, Q. Zhang, Y. Liu, R. Xiong, C. Pan, and J. Shi, "Synthesis and photocatalytic activity of polyaniline-TiO₂ composites with bionic nanopapilla structure," *Journal of Nanoparticle Research*, vol. 13, no. 8, pp. 3157–3165, 2011.
- [32] S. Sedaghat, "Synthesis and evaluation of chitosan-polyaniline copolymer in presence of ammonium persulfate as initiator," *Journal of Applied Chemical Research*, vol. 8, pp. 47–54, 2014.
- [33] A. T. Ramaprasad, V. Rao, G. Sanjeev, S. P. Ramanani, and S. Sabharwal, "Grafting of polyaniline onto the radiation crosslinked chitosan," *Synthetic Metals*, vol. 159, no. 19-20, pp. 1983–1990, 2009.
- [34] M. Cabuk, M. Yavuz, and H. I. Unal, "Electrokinetic properties of biodegradable conducting polyaniline-graft-chitosan copolymer in aqueous and non-aqueous media," *Colloids and Surfaces A: Physicochemical and Engineering Aspects*, vol. 460, pp. 494–501, 2014.
- [35] W. Zheng, M. Angelopoulos, A. J. Epstein, and A. G. MacDiarmid, "Experimental evidence for hydrogen bonding in polyaniline: mechanism of aggregate formation and dependency on oxidation state," *Macromolecules*, vol. 30, no. 10, pp. 2953–2955, 1997.
- [36] Y. Shi, F. Chen, J. Yang, and M. Zhong, "Crystallinity and thermal stability of LDH/polypropylene nanocomposites," *Applied Clay Science*, vol. 50, no. 1, pp. 87–91, 2010.
- [37] C.-Y. Hung, C.-C. Wang, and C.-Y. Chen, "Enhanced the thermal stability and crystallinity of polylactic acid (PLA) by incorporated reactive PS-b-PMMA-b-PGMA and PS-b-PGMA block copolymers as chain extenders," *Polymer*, vol. 54, no. 7, pp. 1860–1866, 2013.
- [38] J. Joo, Z. Oblakowski, G. Du et al., "Microwave dielectric response of mesoscopic metallic regions and the intrinsic metallic state of polyaniline," *Physical Review B*, vol. 49, no. 4, pp. 2977–2980, 1994.
- [39] A. G. MacDiarmid, J. M. Weisinger, and A. J. Epstein, "Advanced research workshop on applications intrinsically conducting polymer," *The Bulletin of the American Physical Society*, vol. 38, p. 311, 1993.
- [40] A. G. MacDiarmid and A. J. Epstein, "The concept of secondary doping as applied to polyaniline," *Synthetic Metals*, vol. 65, no. 2-3, pp. 103–116, 1994.
- [41] M. Cabuk, Y. Alan, M. Yavuz, and H. I. Unal, "Synthesis, characterization and antimicrobial activity of biodegradable conducting polypyrrole-graft-chitosan copolymer," *Applied Surface Science*, vol. 318, pp. 168–175, 2014.
- [42] G. Singh, E. M. Joyce, J. Beddow, and T. J. Mason, "Evaluation of antibacterial activity of ZnO nanoparticles coated sonochemically onto textile fabrics," *Journal of Microbiology, Biotechnology and Food Sciences*, vol. 2, p. 106, 2012.
- [43] I. Wiegand, K. Hilpert, and R. E. W. Hancock, "Agar and broth dilution methods to determine the minimal inhibitory concentration (MIC) of antimicrobial substances," *Nature Protocols*, vol. 3, no. 2, pp. 163–175, 2008.

Research Article

Continuous Adsorption Modeling and Fixed Bed Column Studies: Adsorption of Tannery Wastewater Pollutants Using Beach Sand

Ghita El Mouhri ¹, Mohammed Merzouki,² Hajar Belhassan,² Youssef Miyah,³ Halima Amakdouf,² Rabea Elmountassir,¹ and Anissa Lahrichi¹

¹Laboratory of Biochemistry, Faculty of Medicine and Pharmacy, University Sidi Mohammed Ben Abdellah, Fez, Morocco

²Laboratory of Biotechnology, Faculty of Sciences Dhar El Mahraz, P.O. Box 1796, Atlas-Fez, Morocco

³Laboratory of Catalysis, Materials and Environment, School of Technology, University Sidi Mohammed Ben Abdellah, Fez, Morocco

Correspondence should be addressed to Ghita El Mouhri; elm.ghita@gmail.com

Received 17 October 2019; Revised 17 December 2019; Accepted 19 December 2019; Published 24 January 2020

Guest Editor: Mohamed R. Berber

Copyright © 2020 Ghita El mouhri et al. This is an open access article distributed under the Creative Commons Attribution License, which permits unrestricted use, distribution, and reproduction in any medium, provided the original work is properly cited.

This study deals with the removal of residual pollutants from tanning wastewater by continuous adsorption mechanism, using local sand as a low-cost adsorbent. The possibility of pretreating a complex tannery effluent heavily loaded with a natural material such as sand is significant. The characterization of the adsorbent before and after continuous adsorption was performed by X-ray diffraction, Fourier transform infrared spectroscopy, and scanning electron microscopy. Column studies were also carried out to evaluate the performance of the adsorbent and the efficiency of column adsorption. The adsorption kinetic rate seems to be strongly influenced by certain parameters such as the particle size of the material used, the withdrawal rate of the influent and the height of the adsorbent bed, and optimized parameters were found to be 63 μm , 15 $\text{ml}\cdot\text{min}^{-1}$, and 7 cm, respectively, and the color removal has achieved maximum values which vary between 95 and 100%. The results suggest that sand can be used as an economical adsorbent for the removal of color from the wastewater of the tanning industries.

1. Introduction

Industrial tanning is one of the most important sectors in Morocco's economy [1]. Consequently, the consumption of huge quantities of water during all leather processing operations and the discharge of untreated effluents leads to very serious problems, particularly on water quality and human health, and makes it one of the main pollutants that influence the ecological balance negatively [2–5].

Both scientists and health authorities have spent the effort considered in pollution clean-up and prevention [3, 5, 6]. Many types of treatment systems have been considered to eliminate heavy metal contamination in the environment [7–9], including ion exchange, flocculation, coagulation, chemical oxidation, chemical precipitation,

ozonation, membrane filtration, electrochemical filtration, and activated carbon adsorption [10–15]. However, the main limiting factors against the use of these processes are high operational costs, low disposal efficiency, generation of toxic byproducts and sludge, and difficulty of implementation and time [11, 16].

Among the different processes for purifying effluents loaded with heavy metals, adsorption, which involves fixing the pollutant load at the interface through physical or chemical bonds, offers better performance and fewer problems compared with other advanced processes [17, 18]. Adsorption also offers an economical solution by developing sorbents with a much lower cost [18–22].

In this study, the use of continuous adsorption was chosen for the treatment of larger volumes and to remove as

many pollutants as possible from the tannery effluent. Preliminary experimental studies were conducted to understand the general mechanism of adsorption, the different characteristics and limitations in column design. Adsorption was designed in continuous mode by percolating effluents through fixed bed columns with detailed kinetic modeling to evaluate the variation in some operating parameters such as granulometry, adsorbent bed height, and influent withdrawal rate.

2. Materials and Methods

2.1. Materials. The effluent from the tannery's activity was collected from an industrial unit located in the Dokkarat district of Fez and stored at a temperature of 4°C until use. The adsorbent material used is sand from a Moroccan beach, and this adsorbent has undergone several rinses with ultrapure water until the removal of residues and neutralization of the pH. It is then dried in an oven overnight at 80°C for total removal of water, ground, and sieved to obtain a fraction in the range of 63–80 µm in diameter [3, 18, 23]. The physicochemical characteristics of the tannery effluent are shown in Table 1.

2.2. Instrumental Analysis. The granulometric curve of the sand and the simple percentages (%) of each granular fraction were established using a vibrating sieve shaker (RETSCH AS 200) [24], and the crystalline structure of the sand powder was analyzed by X-ray diffractometry (Diffractometer X'Pert PRO); the Fourier transform infrared spectroscopy was carried out to study the particular types of chemical bonds and groups existing in the sample, and morphological analysis of the sand before and after saturation by effluent components was performed by scanning electron microscope, equipped with an X-ray energy dispersion spectrometer (EDX).

2.3. Adsorption Studies in a Continuous System. The treatment of the tannery effluent was carried out with an experimental system made of a glass column, with a dimension of 3 cm in inner diameter and 50 cm in height. The sand bed was packed into the column and wetted with ultrapure water to release the trapped air between the particles. Tannery wastewater was continuously supplied through the column using a peristaltic pump. Every 10 minutes, the treated influent was collected, and the optimal parameters were selected using a spectrophotometer (UV-Visible BioSpec-mini) at a maximum wavelength (λ_{\max}) of 400 nm Figure 1.

2.3.1. Effect of Sand Granulometry. To evaluate the effect of particle size, five sand fractions were varied at different diameters: 63, 125, 200, 315, and 400 µm. These granular fractions were filled into separate columns to form compacted beds with a height of 5 cm. The withdrawal flow rate has been set at 15 ml·min⁻¹.

TABLE 1: Physicochemical characteristics of real tannery wastewater.

Parameter	Values
pH	6,25
Temperature (°C)	25
Electrical conductivity (µs·cm ⁻¹)	10900
COD (mg·L ⁻¹)	11800
BOD5 (mg·L ⁻¹)	1200
Total chromium (mg·L ⁻¹)	32,2
Color	Dark blue

2.3.2. Effect of the Withdrawal Rate. To choose the most appropriate withdrawal rate for the treatment of tannery effluent, we opted for a grain size of 63 µm in diameter, a compacted bed of 3 cm in height, and adjusted the withdrawal rates of the influents to values of 15, 65, 115, and 170 ml·min⁻¹.

2.3.3. Effect of the Adsorbent Bed Height. After the determination of the two parameters: grain size and flow rate, the effect of filter bed height on the rate of discolouration was studied to determine which one provides better continuous adsorption. And, for this, the sand beds were varied according to different masses, namely, 20.2, 36, and 50 g, and the heights of the sand beds were measured at 3, 5, and 7 cm, respectively.

3. Results and Discussion

3.1. Particle Size Curve of Sand. The descriptive percentages of the granulometric analyses are illustrated in Figure 2; the figure shows the allocation of 7 fractions for the granulometric distribution of sand, and the preponderant size which predominates is 200 µm with a percentage of 61.5%. This size is less than 500 µm, which gives it the class of fine sands.

3.2. X-Ray Diffraction. The crystalline composition of the sand particles before and after adsorption is shown in Figure 3. The X-ray diffractograms of the sand before and after adsorption shows almost the same appearance and reveal the existence of several characteristic peaks of quartz and calcite [25, 26]. For unsaturated sand, these two elements have a codominance indicated by the major peaks corresponding to the position 2θ , 27.7° and 29.7°, respectively [27–31]. Whereas for saturated sand, quartz predominates over calcite with the appearance of two unidentified peaks at 2θ , 43.41° and 51.08°, which can be attributed to the effluent components of the tannery.

3.3. Infrared Spectroscopy Analysis. Figure 4 and Table 2 present the main functional groups of the specific elements of natural sand and the possible modifications after the adsorption process. On one hand, the examination of these results show no change in the basic structure of Lowded Sand (LS) particles and this allows us to say that adsorption is done by physical interaction forces [25]. On other hand, the maximum intensities have decreased slightly; this may be related to an energy variation due to the bonds established

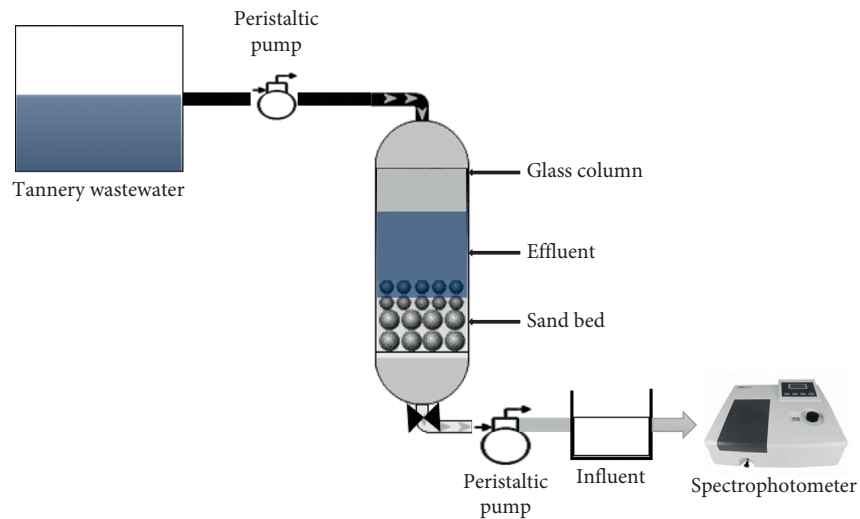


FIGURE 1: Experimental device.

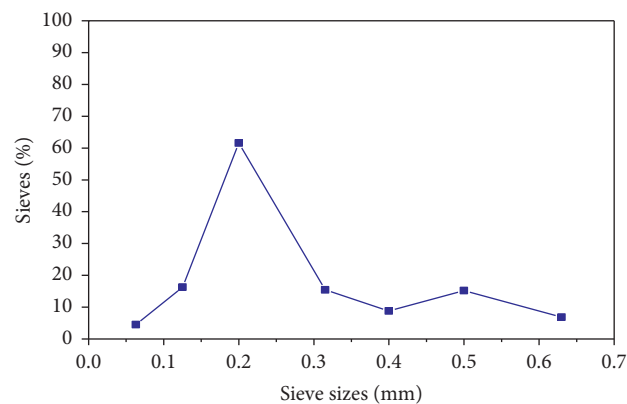


FIGURE 2: Granulometric curve of the sand used.

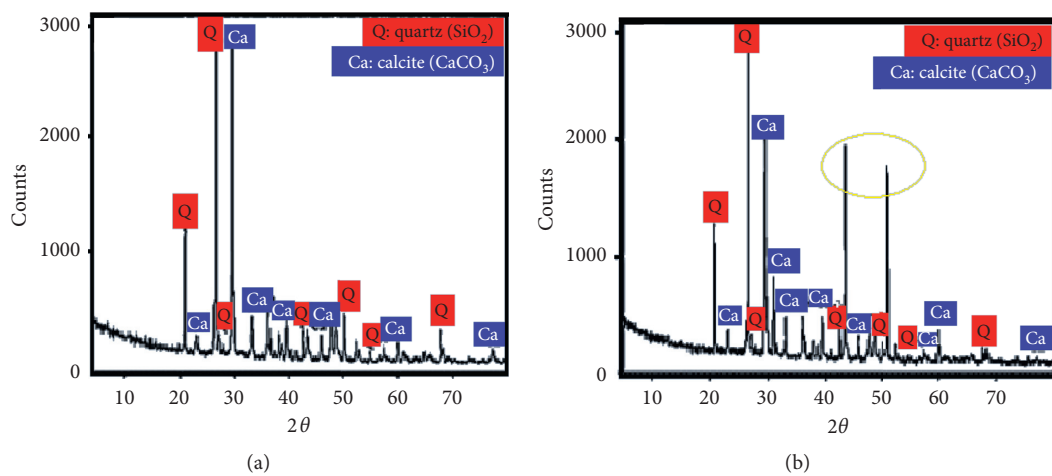


FIGURE 3: Diffractometric analysis of (a) natural sand and (b) loaded sand.

with the pollutants in the effluent, and a small shift has been observed in the position of the adsorption bands, which probably justifies the feasibility of adsorption [18].

These results also confirm the existence of the bonds characterizing calcite and quartz previously revealed by diffractometric analysis.

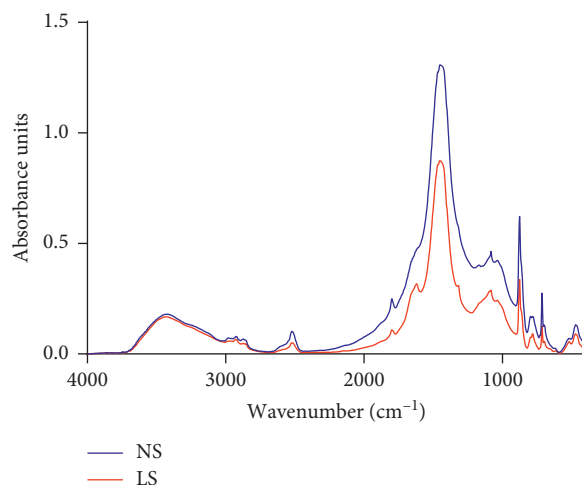


FIGURE 4: Infrared spectrum of natural sand (NS) and loaded sand (LS).

TABLE 2: Sand infrared bands and their assignments.

Natural sand position (cm ⁻¹)	Loaded sand position (cm ⁻¹)	Assignments	Reference
3419.60	3427.62	OH group stretch vibration	[18, 32, 33]
2922.88	2924.36	C-H asymmetrical stretching vibrations	[25, 32, 34]
2519.05	2518.98	C-H asymmetrical stretching vibration	[25]
1797.17	1796.91	Typical vibration of the OH stretching group	[3]
—	1620.91	OH group stretch vibration	[18]
1450.90	1452.76	CO ₃ stretching of calcite	[3, 35]
1082.85	1083.32	Valence vibration of the Si-O-Si bond	[18, 23, 32]
874.56	874.60	CO ₃ stretching of calcite	[35]
779.91	780.64	O-Si-O stretching	[25]
712.48	712.55	O-Si-O stretching	[25]
469.17	469.92	Valence vibration of the Si-O-Si bond	[25]

3.4. Scanning Electron Microscopy Coupled with the EDX.

The SEM results coupled with the EDX of the sand before and after saturation as well as the mass percentages of each element are shown in Figure 5 and Table 3. The internal microstructure of unmodified sands shows a rough, irregular, and proportionally porous and cracked appearance with the presence of some luminous and relatively ordered aggregations, that probably indicate the existence of quartz crystals previously detected by the DRX analysis [18, 36]. This mineralogical composition allows the interchanges of substances with adjacent cells and thus makes the adsorption mechanism possible (Figure 5(a)).

Microstructural analysis reveals significant changes in the surface morphology of the sand after adsorption of the effluent. We notice the formation of a dense and compact matrix with a decrease in the degree of porosity and luminosity, and this can be explained by the adsorption of the molecules contained in the treated solute on the sand cracks and pores (Figure 5(b)) [18].

The chemical analysis by EDX proves the validity of spectral analysis with regard to the chemical composition of the sand used and shows that it consists mainly of C, O, Ca, and Si. The results also indicate the appearance of certain elements involved in the chemical composition of tannery

effluent such as nitrogen, sulfur, chlorine, and chromium. The mass percentage of some elements such as O, Mg, Si, Fe, and Na decreased slightly after adsorption; this leads us to suppose that they were involved in the adsorption process of the effluent components Table 3 and Figure 5.

3.5. Column Experiments

3.5.1. Effect of Sand Grain Size on Effluent Discolouration. Figure 6 shows the tannery effluent discolouration kinetics that have been studied for the different grain sizes of sand powder from 63 μm to 400 μm .

The results show that the highest rate of discolouration is represented by the preponderant size of 63 μm , and discolouration decreases with the increase in the diameter of the sand particles. The graphical presentation also shows that the fading rate is optimal and provides total fading of 100% for the 63 μm grain size, while the fading rate does not exceed 82% for the 400 μm grain size. The discolouration rates for the 125 μm , 200 μm , and 315 μm particle sizes are 97.2%, 94.4%, and 93.61%, respectively. As a conclusion, it can be said that the particle size is an important factor, which affects the adsorption capacity, and the fixation of the organic matter on the surface of the adsorbent material is

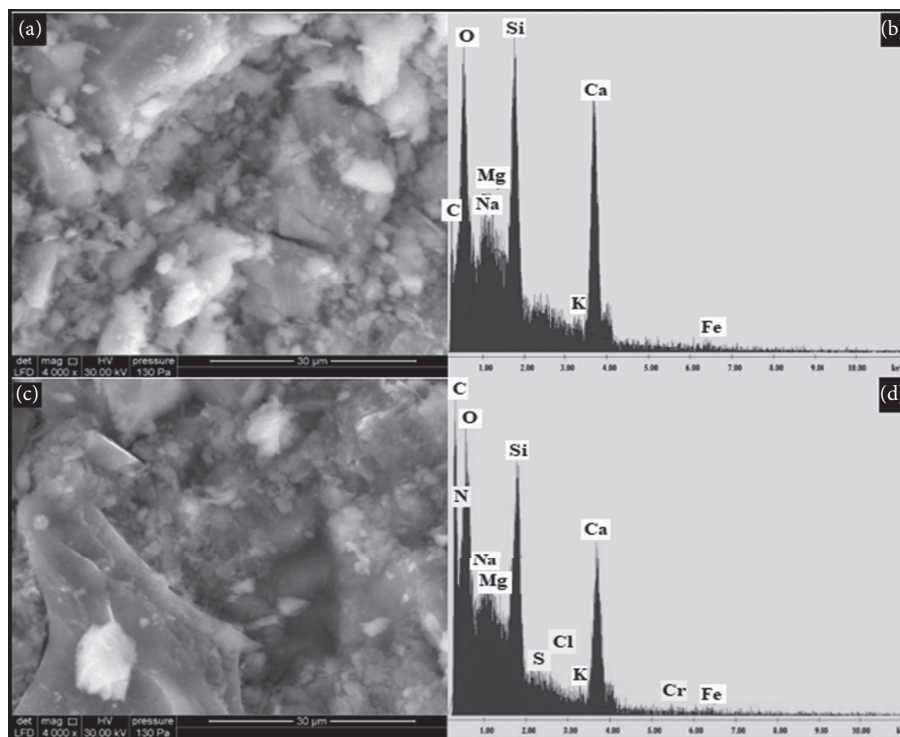


FIGURE 5: Morphological examination of natural sand (a, b) and loaded sand (c, d) by SEM-EDX.

TABLE 3: Percentage of elements found by X-ray energy dispersion EDX in natural and loaded sand.

Elements	Natural sand (NS)	Loaded sand (LS)
C	26.34	32.05
O	46.18	18.12
N	—	34.55
Na	3.42	1.45
Mg	0.94	0.45
Si	8.66	5.36
S	—	0.40
Cl	—	0.43
K	0.54	0.37
Ca	12.63	5.98
Cr	—	0.27
Fe	1.3	0.58
Total	100	100

generally more important when the grain size of the material is small [37].

The studies of Sakr et al. conducted on the adsorption of methylene blue on cactus found similar results to those of our study with regard to the effect of particle size, and the highest percentages of adsorption were obtained using a size of 0.04 mm of cactus [38]. And, according to Guiza and Bagane who have worked with bentonite for the adsorption of Congo Red; an increase in particle diameter leads to a decrease in the transfer rate of the material [39].

3.5.2. Effect of Flow Rate on Effluent Discolouration. The experimental results shown in Figure 7 show that the

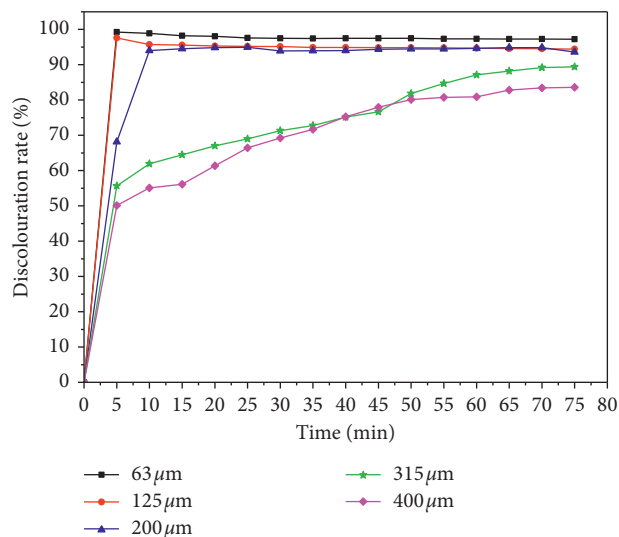


FIGURE 6: Effect of sand grain size on the discolouration rate.

discolouration capacity of the tannery effluent by sand is proportionally inverse to the withdrawal rate.

The rate of discolouration is maximum with a value of 95.6% for low flow which is equal to $15 \text{ ml} \cdot \text{min}^{-1}$ and minimum with a value of 90.4% for flow increased to $170 \text{ ml} \cdot \text{min}^{-1}$. From the results, it can be seen that the increase in the withdrawal rate causes a decrease in the residence time of the effluent molecules in the column. Thus, the exchange speed decreases, resulting in a loss of adsorption efficiency. Experimentally, the increase in flow rate

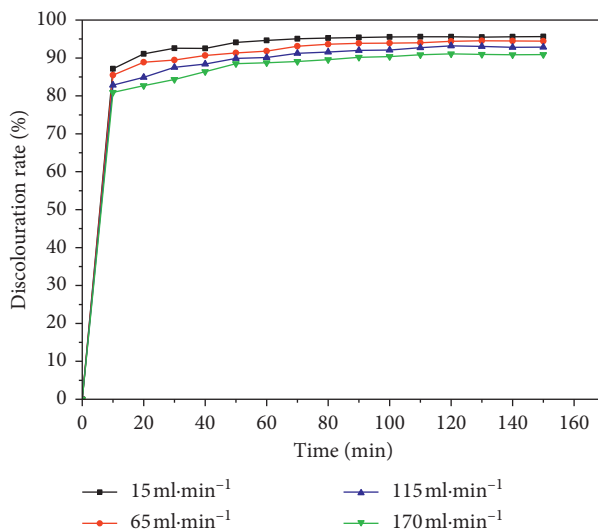


FIGURE 7: Effect of the withdrawal rate on the discoloration rate.

causes a rapid saturation of the filter bed, and this is due to the increase in the exchange speed.

Research carried out by Biswas and Mishra has also found that an increase in the withdrawal rate reduces the adsorbent-adsorbate contact time [40]. And, according to Sathvika et al., low flows increase the adsorption efficiency and increase the contact time between chromium VI solution and the biosorbent used [41].

3.5.3. Effect of Filter Bed Height on Effluent Discolouration.

Figure 8 shows the effect of sand bed height on the rate of effluent discoloration. The results show that the total adsorption capacity increases with increasing bed height. The 3 cm and 5 cm beds have discoloration rates of 95.4% and 97.4%, respectively. The maximum fading rate is given by the 7 cm bed with a percentage that is close to 100%. From these results, it can be deduced that the height of the bed through which the effluent passes is one of the parameters that influence the performance of continuous adsorption and the operation of the column. The amount of adsorbent material used affects significantly the residence time, discoloration rate and volume of the treated effluent. The contact time becomes shorter as the height of the adsorbent bed decreases. This indicates that the bed with the minimum height of 3 cm is saturating faster. Whereas increasing the height of the adsorbent to 7 cm slows down the rate of solute-solid exchange and thus increases the residence time and improves the availability of active adsorption sites, which quantitatively and qualitatively promotes the retention of pollutants present in the tannery effluent [42].

Similar results were found by Lim and Aris who showed that the adsorption of CD(II) and Pb(II) is higher for the longest bed of the dead limestone skeletons and which is 2.20 cm equivalent of 40 g [8]. In another study conducted by (Tsai et al.), the results showed that the increase in the height of the activated carbon bed leads to a decrease in the

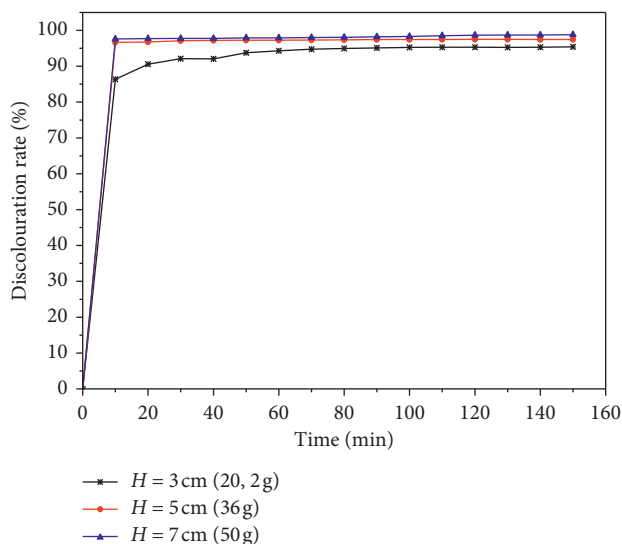


FIGURE 8: Effect of the sand bed height on the discoloration rate.

concentration of Pb (II), Cu (II), and Ni (II) in the influent [43].

3.5.4. Visual Appearance of the Raw Effluent and the Adsorbates.

The visual appearance and reduction of the coloration of the raw effluent from the tannery (A0, B0, and C0) according to the different effects are shown in Figure 9. These results show that the adsorbates (A1, A2, A3, and A4) have a slight coloration compared with the raw effluent A0, and this coloration decreases as the size of the sand grains decreases until an almost colourless influent is obtained (A5) (Figure 9(a)). The visual aspect of the adsorbates obtained at different flow rates (B1, B2, and B3) also show increasing discoloration with the decrease in the withdrawal rate Figure 9(b). For the effect of the height of the adsorbent bed,

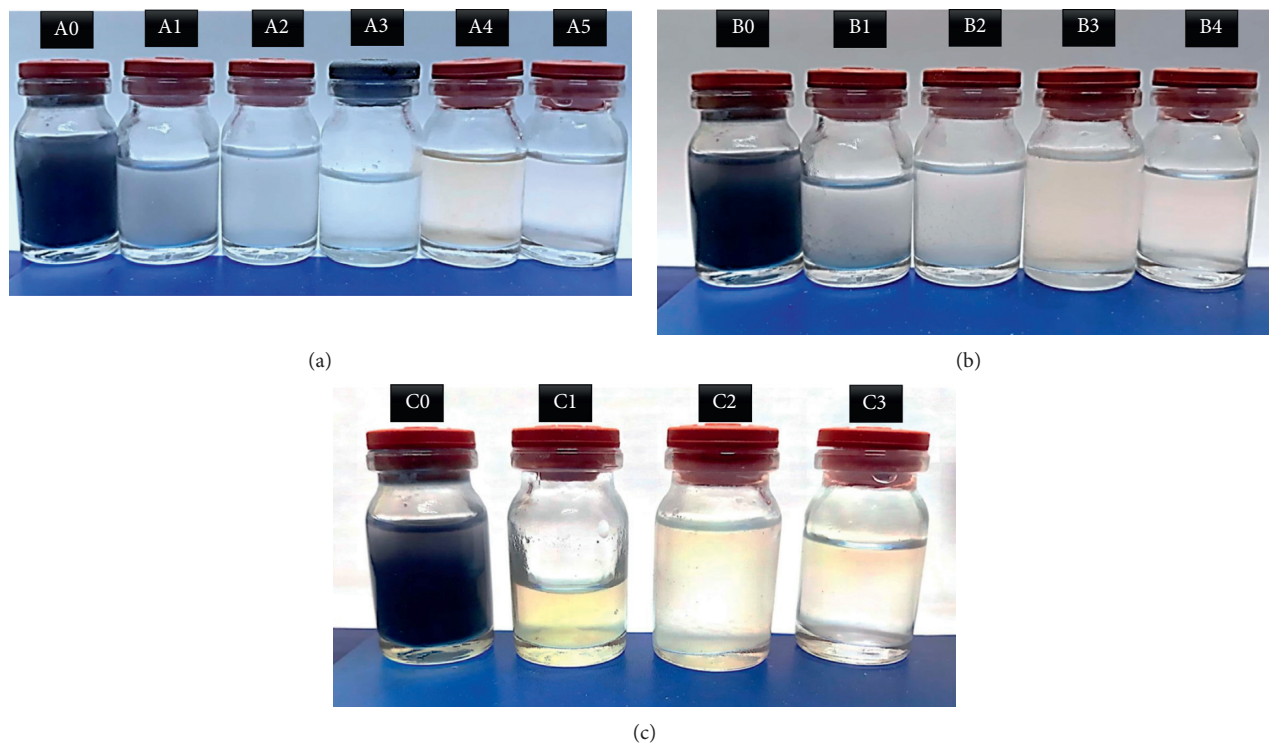


FIGURE 9: Visual appearance of the raw effluent and the adsorbates obtained according to the different effects.

we notice that, from a dark blue effluent C0, we obtain translucent adsorbates with a slightly yellowish coloration for C1, while C3 and C4 have practically the same aspect as indicated by the graphical data (Figure 9(c)).

4. Conclusion

The treatment of effluent from tanning activity by a biological process appears to be difficult, as it is highly loaded with heavy metals and has a toxic environment for microbial biomasses. This study proved the effectiveness of marine sands in cleaning up industrial tanning water and removing micro-pollutants as a pretreatment step. Experimental tests show that the discoloration rate is optimal and close to 100% for the sand grain size of $63\ \mu\text{m}$. The rate of discoloration is maximum with a value of 95.6% for the low flow rate which is equal to $15\ \text{ml}\cdot\text{min}^{-1}$. The maximum fading rate is given by the 7 cm sand bed with a value of 98.7%.

The characterization of the sand by the different FTIR, SEM, and X-RD techniques has revealed modifications in the surface as well as the crystalline and chemical structure of the sand after adsorption which means the retention of effluent pollutants through pores and cracks in marine sand.

Data Availability

The data used to support the findings of this study are available from the corresponding author upon request.

Conflicts of Interest

The authors declare that they have no conflicts of interest.

References

- [1] Y. Metarfi, K. El Rhazi, F. Z. El Madani, A. Omor, and Z. Rais, "Risques professionnels liés à la manipulation du chrome au sein des tanneries modernes de la ville de Fès, Maroc," *Revue d'Épidémiologie et de Santé Publique*, vol. 66, p. S187, 2018.
- [2] S. Elabbas, N. Ouazzani, L. Mandi et al., "Treatment of highly concentrated tannery wastewater using electrocoagulation: influence of the quality of aluminium used for the electrode," *Journal of Hazardous Materials*, vol. 319, pp. 69–77, 2016.
- [3] G. El Mouhri, M. Merzouki, Y. Miyah et al., "Valorization of two biological materials in the treatment of tannery effluents by filtration treatment of tannery effluents by filtration," *Moroccan Journal of Chemistry*, vol. 7, pp. 183–193, 2019.
- [4] S. Ramírez, G. Torrealba, E. Lameda-Cuicas, L. Molina-Quintero, A. I. Stefanakis, and M. C. Pire-Sierra, "Investigation of pilot-scale constructed wetlands treating simulated pre-treated tannery wastewater under tropical climate," *Chemosphere*, vol. 234, pp. 496–504, 2019.
- [5] M. N. Hairuddin, N. M. Mubarak, M. Khalid, E. C. Abdullah, R. Walvekar, and R. R. Karri, "Magnetic palm kernel biochar potential route for phenol removal from wastewater," *Environmental Science and Pollution Research*, vol. 26, no. 34, pp. 35183–35197, 2019.
- [6] J. L. Perrin, N. Raïs, N. Chahinian, P. Moulin, and M. Ijjaali, "Water quality assessment of highly polluted rivers in a semi-arid Mediterranean zone Oued Fez and Sebou River (Morocco)," *Journal of Hydrology*, vol. 510, pp. 26–34, 2014.
- [7] R. R. Karri and J. N. Sahu, "Modeling and optimization by particle swarm embedded neural network for adsorption of zinc (II) by palm kernel shell based activated carbon from aqueous environment," *Journal of Environmental Management*, vol. 206, pp. 178–191, 2018.

- [8] A. P. Lim and A. Z. Aris, "Continuous fixed-bed column study and adsorption modeling: removal of cadmium (II) and lead (II) ions in aqueous solution by dead calcareous skeletons," *Biochemical Engineering Journal*, vol. 87, pp. 50–61, 2014.
- [9] R. R. Karri, J. N. Sahu, and B. C. Meikap, "Improving efficacy of Cr (VI) adsorption process on sustainable adsorbent derived from waste biomass (sugarcane bagasse) with help of ant colony optimization," *Industrial Crops and Products*, vol. 143, Article ID 111927, 2020.
- [10] S. Boumchita, A. Lahrichi, Y. Benjelloun, S. Lairini, V. Nenov, and F. Zerrouq, "Application of peanut shell as a low-cost adsorbent for the removal of anionic dye from aqueous solutions," *Journal of Materials and Environmental Science*, vol. 8, pp. 2353–2364, 2017.
- [11] M. Liu, X. Li, Y. Du, and R. Han, "Adsorption of methyl blue from solution using walnut shell and reuse in a secondary adsorption for Congo red," *Bioresource Technology Reports*, vol. 5, pp. 238–242, 2019.
- [12] H. N. Bhatti, A. Jabeen, M. Iqbal, S. Noreen, and Z. Naseem, "Adsorptive behavior of rice bran-based composites for malachite green dye: isotherm, kinetic and thermodynamic studies," *Journal of Molecular Liquids*, vol. 237, pp. 322–333, 2017.
- [13] M. T. Yagub, T. K. Sen, S. Afroze, and H. M. Ang, "Dye and its removal from aqueous solution by adsorption: a review," *Advances in Colloid and Interface Science*, vol. 209, pp. 172–184, 2014.
- [14] R. R. Karri, J. N. Sahu, and N. S. Jayakumar, "Optimal isotherm parameters for phenol adsorption from aqueous solutions onto coconut shell based activated carbon: error analysis of linear and non-linear methods," *Journal of the Taiwan Institute of Chemical Engineers*, vol. 80, pp. 472–487, 2017.
- [15] R. R. Karri, N. S. Jayakumar, and J. N. Sahu, "Modelling of fluidised-bed reactor by differential evolution optimization for phenol removal using coconut shells based activated carbon," *Journal of Molecular Liquids*, vol. 231, pp. 249–262, 2017.
- [16] Y. Benjelloun, A. Lahrichi, S. Boumchita et al., "Removal of crystal violet by wet oxidation with H_2O_2 over an iron oxide catalyst synthesized from fly ash," *Journal of Materials and Environmental Science*, vol. 8, pp. 2259–2269, 2017.
- [17] A. Fegousse, A. El Gaidoumi, Y. Miyah, R. E. Mountassir, and A. Lahrichi, "Pineapple bark performance in dyes adsorption: optimization by the central composite design," *Journal of Chemistry*, vol. 2019, Article ID 3017163, 11 pages, 2019.
- [18] A. Sharma, Z. Syed, U. Brighu, A. B. Gupta, and C. Ram, "Adsorption of textile wastewater on alkali-activated sand," *Journal of Cleaner Production*, vol. 220, pp. 23–32, 2019.
- [19] M. Mirzaeinejad, Y. Mansoori, and M. Amiri, "Amino functionalized ATRP-prepared polyacrylamide-g-magnetite nanoparticles for the effective removal of Cu(II) ions: kinetics investigations," *Materials Chemistry and Physics*, vol. 205, pp. 195–205, 2018.
- [20] Y. Cui and J. D. Atkinson, "Ultrasonic spray pyrolysis synthesis of nitrogen-doped porous Fe/C composites from glycerol for hexavalent chromium removal," *Materials Chemistry and Physics*, vol. 221, pp. 29–33, 2019.
- [21] M. Ghaedi, S. Hajjati, Z. Mahmudi et al., "Modeling of competitive ultrasonic assisted removal of the dyes—methylene blue and Safranin-O using Fe_3O_4 nanoparticles," *Chemical Engineering Journal*, vol. 268, pp. 28–37, 2015.
- [22] Y. Miyah, A. Lahrichi, M. Idrissi, A. Khalil, and F. Zerrouq, "Adsorption of methylene blue dye from aqueous solutions onto walnut shells powder: equilibrium and kinetic studies," *Surfaces and Interfaces*, vol. 11, pp. 74–81, 2018.
- [23] V. Khatibikamal, A. Torabian, H. Ahmad panahi, and M. Baghdadi, "Stabilizing of poly(amidoamine) dendrimer on the surface of sand for the removal of nonylphenol from water: batch and column studies," *Journal of Hazardous Materials*, vol. 367, pp. 357–364, 2019.
- [24] K. B. Amey, K. Neglo, S. Tamba, A. Kodjo, and C. Johnson, "Caractérisation physique de sables silteux au Togo," *Afrique Science: Revue Internationale des Sciences et Technologie*, vol. 10, pp. 53–69, 2014.
- [25] Z. Yin, Y. Wang, K. Wang, and C. Zhang, "The adsorption behavior of hydroxypropyl guar gum onto quartz sand," *Journal of Molecular Liquids*, vol. 258, pp. 10–17, 2018.
- [26] B. V. Bajoria, D. K. Parbat, and P. B. Nagarnaik, "XRD Analysis of Natural sand, Quarry dust, waste plastic (ldpe) to be used as a fine aggregate in concrete," *Materials Today: Proceedings*, vol. 5, no. 1, pp. 1432–1438, 2018.
- [27] C. Jiang, W. Guo, H. Chen, Y. Zhu, and C. Jin, "Effect of filler type and content on mechanical properties and microstructure of sand concrete made with superfine waste sand," *Construction and Building Materials*, vol. 192, pp. 442–449, 2018.
- [28] A. Zalaghi, F. Lamchouri, H. Toufik, and M. Merzouki, "Valorization of natural porous materials in the treatment of leachate from the landfill uncontrolled city of Taza," *Journal of Materials and Environmental Science*, vol. 5, pp. 1643–1652, 2014.
- [29] M. Benafqir, Z. Anfar, M. Abbaz et al., "Hematite-titaniferous sand as a new low-cost adsorbent for orthophosphates removal: adsorption, mechanism and Process Capability study," *Environmental Technology & Innovation*, vol. 13, pp. 153–165, 2019.
- [30] M. L. Mechri, S. Chihi, N. Mahdadi, and S. Beddiaf, "Study of heat effect on the composition of dunes sand of Ouargla (Algeria) using XRD and FTIR," *Silicon*, vol. 9, no. 6, pp. 933–941, 2017.
- [31] M. L. Mechri, S. Chihi, N. Mahdadi, and S. Beddiaf, "Diagnosis of the heating effect on the electrical resistivity of Ouargla (Algeria) dunes sand using XRD patterns and FTIR spectra," *Journal of African Earth Sciences*, vol. 125, pp. 18–26, 2017.
- [32] J. Liu, X. Zhu, H. Zhang, F. Wu, B. Wei, and Q. Chang, "Superhydrophobic coating on quartz sand filter media for oily wastewater filtration," *Colloids and Surfaces A: Physicochemical and Engineering Aspects*, vol. 553, pp. 509–514, 2018.
- [33] C. Jia, Z. Wang, H. Liu, J. Bai, M. Chi, and Q. Wang, "Pyrolysis behavior of Indonesia oil sand by TG-FTIR and in a fixed bed reactor," *Journal of Analytical and Applied Pyrolysis*, vol. 114, pp. 250–255, 2015.
- [34] M. Tiwari, T. D. Rathod, P. Y. Ajmal, R. C. Bhangare, and S. K. Sahu, "Distribution and characterization of microplastics in beach sand from three different Indian coastal environments," *Marine Pollution Bulletin*, vol. 140, pp. 262–273, 2019.
- [35] P. Yuan, F. Annabi-Bergaya, Q. Tao et al., "A combined study by XRD, FTIR, TG and HRTEM on the structure of delaminated Fe-intercalated/pillared clay," *Journal of Colloid and Interface Science*, vol. 324, no. 1-2, pp. 142–149, 2008.
- [36] N. Kouras, A. Harabi, F. Bouzerara et al., "Macro-porous ceramic supports for membranes prepared from quartz sand and calcite mixtures," *Journal of the European Ceramic Society*, vol. 37, no. 9, pp. 3159–3165, 2017.
- [37] L. P. Lingamdinne, K. R. Vemula, Y.-Y. Chang, J.-K. Yang, R. R. Karri, and J. R. Koduru, "Process optimization and

- modeling of lead removal using iron oxide nanocomposites generated from bio-waste mass,” *Chemosphere*, vol. 243, Article ID 125257, 2020.
- [38] F. Sakr, A. Sennaoui, M. Elouardi, M. Tamimi, and A. Assabbane, “Étude de l’adsorption du Bleu de Méthylène sur un biomatériau à base de Cactus,” *Journal of Materials and Environmental Science*, vol. 6, pp. 397–406, 2015.
- [39] S. Guiza and M. Bagane, “Étude cinétique de l’adsorption du rouge de Congo sur une bentonite,” *Revue des sciences de l’eau*, vol. 26, no. 1, pp. 39–50, 2013.
- [40] S. Biswas and U. Mishra, “Continuous fixed-bed column study and adsorption modeling: removal of lead ion from aqueous solution by charcoal originated from chemical carbonization of rubber wood sawdust,” *Journal of Chemistry*, vol. 2015, Article ID 907379, 9 pages, 2015.
- [41] T. Sathvika, Manasi, V. Rajesh, and N. Rajesh, “Adsorption of chromium supported with various column modelling studies through the synergistic influence of *Aspergillus* and cellulose,” *Journal of Environmental Chemical Engineering*, vol. 4, no. 3, pp. 3193–3204, 2016.
- [42] R. Elmountassir, B. Bennani, Y. Miyah et al., “Microbiological and physicochemical characterization of hospital effluents before and after treatment with two types of sawdust,” *Journal of Chemistry*, vol. 2019, Article ID 3275101, 10 pages, 2019.
- [43] W. C. Tsai, M. D. G. De Luna, H. L. P. Bermillo-Arriegas, C. M. Futralan, J. I. Colades, and M. W. Wan, “Competitive fixed-bed adsorption of Pb(II), Cu(II), and Ni(II) from aqueous solution using chitosan-coated bentonite,” *International Journal of Polymer Science*, vol. 2016, Article ID 1608939, 11 pages, 2016.

Research Article

Synthesis, Characterization, and Evaluation of Evaporated Casting MWCNT/Chitosan Composite Membranes for Water Desalination

Mohammed Alsuhybani,¹ Ahmed Alshahrani ,² and Ahmed S. Haidyrah³

¹National Center for Irradiation Technology, King Abdulaziz City for Science and Technology, Riyadh 11442, Saudi Arabia

²National Center for Radioactive Waste Treatment, King Abdulaziz City for Science and Technology (KACST), P.O. Box 6086, Riyadh 11442, Saudi Arabia

³National Center for Nuclear Technology, King Abdul Aziz City for Science & Technology, Riyadh 11442, Saudi Arabia

Correspondence should be addressed to Ahmed Alshahrani; ashahrni@kacst.edu.sa

Received 6 November 2019; Accepted 30 December 2019; Published 22 January 2020

Guest Editor: Hassan M. A. Hassan

Copyright © 2020 Mohammed Alsuhybani et al. This is an open access article distributed under the Creative Commons Attribution License, which permits unrestricted use, distribution, and reproduction in any medium, provided the original work is properly cited.

Fresh water scarcity and pollution turn out to be a most serious issue throughout the world due to the rapid population growth. The application of nanomaterials (NMs) for the removal of pollutants from water has attracted significant attention. The nanofiltration membrane was fabricated through the evaporative casting (EC) method using multiwalled carbon nanotubes (MWCNT) and chitosan (CHIT) as the surfactant to enable water purification. The developed EC membrane properties were characterized in mechanical, surface charging (zeta potential), surface morphology, and hydrophobicity properties. Results demonstrated that incorporation of MWCNT and the biopolymers (chitosan) resulted in suitable developments in mechanical properties of the membrane. For example, the membrane has shown values for tensile strength (28 ± 1 MPa), elongation ($10.2 \pm 1.2\%$), Young's modulus (1.2 ± 0.1 GPa), and toughness of (1.9 ± 0.2 J/g). When more significant changes were investigated on the surface morphology of the EC membrane, it was observed that the pores on the surface morphology of the EC membrane decreased as the evaporative casting method was used. Moreover, the permeability of the membrane towards water, inorganic salts, and pH effect on salt rejections was studied using the NF/RO system. These established nanocomposite membranes signify the promising candidates for fresh water desalination and elimination of organic impurities.

1. Introduction

The progress in rapid population of growth united with untenable use of water resources and scarcity of water have turn out to be a major significant task in the world. It is vital to improve the capable approaches for water treatment. Efforts have been made over the past few decades to improve water desalination systems for providing fresh water from the saline water using several desalination techniques such as distillation, freezing, electrodialysis, and solar-powered membrane separation [1–5]. While these processes have evolved, there are still some obstacles. For instance, there are key issues for reverse osmosis (RO) membrane fouling and scaling and also other problems where high energy consumption is needed in thermal desalination [6]. Therefore, an effective, energy-efficient alternative to traditional

processes for desalination of seawater must be created. Consequently, nanofiltration (NF) is one of the membrane processes, which is pressure-driven, and have the properties of nanofiltration (NF) such as pore size, water permeability, and salt rejection between reverse osmosis (RO) and ultrafiltration (UF) membranes [7]. NF can be operated using low-pressure, comparing to reverse osmosis (RO), and it has several benefits, which are lower operating pressures, higher fluxes, high rejection of divalent ions, and lower energy consumption [7]. These advantages allow NF membranes to be employed in many applications such as biotechnology, pharmaceutical, and food industry. Moreover, the NF membranes also can be used particularly in desalination and wastewater treatment [7, 8]. Currently, advances in NF membranes were developed for removal of monovalent ions from the surface water, underground water, brackish water,

and seawater [7, 9]. The NF was used as a first stage before the RO process, and this leads to many benefits like higher monovalent ion rejection, accomplished higher RO design flux and recovery in water desalination plants, and increase in membrane lifetime [6]. However, NF membranes still need to discover new materials in order to improve a high selectivity for monovalent ions. In this context, carbon materials, for instance, activated carbons, graphene, and carbon nanotubes (CNTs), have been extensively castoff in water purification approaches [10].

During the last few decades, carbon nanotubes (CNTs) have become increasingly attracted by scientists for a wide range of applications [11–14]. CNTs are mainly useful for making membranes because they possess unique properties such as fast transport rates and small pore openings [15]. However, there are difficulties that limit the usage of carbon nanotubes in larger scale because carbon nanotube fabrication is quit expensive and limited to small-scale production. Another problem related to carbon nanotubes is hydrophobicity that can limit its application in the membranes field [14, 16]. Otherwise, carbon nanotubes can be dispersed in a polymer matrix, which may provide an appealing route for production of mixed matrix membranes with a high mass transport rate. In addition, dispersion in a polymer can also help to reduce the hydrophobicity of CNTs, making it easy to use as membranes.

The sonication method is considered one of the most successful ways of dispersing CNTs through a polymer due to easy filtering of the resulting dispersions in order to produce the membrane, which is also called as “buckypapers” [17]. A number of studies have shown that when ultrasonic energy is used to disperse large amount of CNTs, the resulting products are stabilized by non-covalent interactions with the polymer molecule (surfactant) [18, 19]. For example, both single-walled carbon nanotubes (SWNTs) and multiwalled carbon nanotubes (MWCNTs) were very effectively dispersed to produce membranes using the nonionic surfactant octylphenol ethoxylate (Triton X-100). Resulted dispersions are very stable to the proper membrane due to the aromatic rings of Triton X-100 p-stack onto the external graphene lattice of the CNTs [20, 21]. Another study demonstrated that high power tip sonication was used to fabricate membranes containing different surfactants mixed with multiwalled carbon nanotubes (MWCNTs) and multiwalled carbon nanotubes functionalized with carboxylic acid groups (MWCNT-COOH) or amine groups (MWCNT-NH₂) [22]. In addition, the membrane fabricated using MWCNT and Triton X-100 as the surfactant exhibited more than 80% removal efficiency for 11 out of the 12 trace organic contaminants (TrOCs) [23]. A few studies have used the same method (ultrasonic energy) to disperse CNTs (SWNTs and MWCNTs) for preparing a number of membranes using different surfactants [20, 24].

Moreover, among the various adsorbents like zeolite, organoclays, biochar, metal-organic frameworks, and carbon nanotubes for the exclusion of nitrophenolic compounds from aqueous solutions [25–33], CNTs have been

acknowledged as the productive adsorbents for elimination of them. This CNT application can be associated to electrostatic interactions and high surface areas, and the equilibrium time is shorter compared to the other materials. A number of biopolymers have been examined to disperse CNTs and their ability to prepare membranes [34–37]. Furthermore, the CNT performance as an adsorbent significantly enhanced through the modification with polymer materials like chitosan. Chitosan (CHIT) is an abundant biopolymer which has been extensively castoff in numerous applications such as industrial and biomedical [25, 38], enzyme immobilization [26], and water treatment [27–29], as well as used as transporters for controlled drug delivery [30]. These applications can be associated to the existence of quantities of the reactive amino and hydroxyl groups in the molecular chain of chitosan. Therefore, CNTs/chitosan composites, which are developed by imbedding functional groups of the chitosan to CNTs, have been developed to adsorb the pollutions or toxic metals from the wastewaters [31–33, 39].

Chitosan has the ability to disperse CNTs in an aqueous medium, and it can wrap around CNTs separately based on changes in their diameter [40]. A previous study showed that multiwalled carbon nanotubes and the chitosan composite membrane (MWCNT/CHIT) could be highly effective for removing salts from water [41]. This study used MWCNT/CHIT fabricated by depositing MWCNT mixed with chitosan 0.2% (w/v) onto a paper of polyvinylidene fluoride (PVDF). The result revealed effective removal of four inorganic electrolytes (NaCl, Na₂SO₄, MgSO₄, and MgCl₂) from water by this MWCNT/CHIT membrane.

The aim of this work was to improve the composite NF membrane from CNTs (MWCNT) and chitosan using the evaporative casting method in order to use for desalination process. The morphology, mechanic properties, and hydrophobicity of the composite membrane were characterized. In addition, the water permeability and the rejection performance of the composite membrane to inorganic electrolytes and pH effect of solution were also investigated in this study.

2. Materials and Methods

2.1. Materials. MWCNT was purchased from Hanwha Nanotech Corporation Ltd, Seoul, South Korea. The outer diameter ranges from 3–10 nm. All other materials used in this study were purchased from Sigma-Aldrich (USA) and used without further purification.

2.2. Preparation of Dispersions. The chitosan (CHIT) solution was prepared as mentioned in the previous study [41]. MWCNTs (15 mg) were added to the CHIT solution 0.2% w/v (15 ml) for preparing the dispersant using an ultrasonic processor 750 (750 W, ultrasonic digital probe sonicator with a diameter of 10 mm). The sonication was performed at an amplitude of 30% and pulses of 0.5 s “on” and 0.5 s “off,” with a total “on” time of 30 minutes. Vials containing MWCNTs and the CHIT solution (0.2% w/v) were placed in a water bath to reduce temperature changes from the heat

that was generated from this process. The above method was repeated 10 times to produce homogeneous dispersions (150 ml) containing MWCNTs and CHIT and were then diluted up to 250 ml.

2.3. Preparation of Casting Membrane. The evaporative casting membrane was fabricated using a custom-made unit and rectangular polyvinylidene difluoride (PVDF) membrane. The dispersion solution (MWCNT/CHIT) was deposited on the surface of the PVDF membrane (6.0 cm × 12.0 cm) and then was evaporated by using a vacuum oven, which typically operated at 35°C for 24–48 hours. Once the dispersant had evaporated, the resulting EC membranes were washed with sodium hydroxide (NaOH) followed by Milli-Q water to remove the remaining acetic acid. The EC membranes (Figure 1) were then dried for 24 hours in a controlled temperature at 21°C and removed from the support membranes (PVDF).

2.4. Characterization Techniques. The surface morphology of the EC membrane (Figure 1) was analyzed using field emission scanning electron microscopy (FESEM) (JEOL, Japan). Samples were prepared by putting small pieces of EC membranes on to the SEM's stage using a conductive carbon tape. The small pieces of EC membranes were imaged with gold sputter coating.

The hydrophobicity property was studied by using the contact angle instrument (sessile drop method). Deionized water (2 μl) was dropped on the surface of the membrane and an image was taken. The values of the contact angle were then estimated by constructing triangles on the obtained images.

The mechanical properties of membranes were studied in a controlled temperature at 21°C using a tensile tester. Prior to testing, five sample strips from each EC membrane were examined with a dimension 20 mm by 3 mm with thickness 0.5 measured using a micrometer. The samples were examined using a strain rate of 0.5 mm/min and a gauge length of 10 mm. The tensile strength of each sample was measured as the maximum stress, and Young's modulus was calculated from the slope of the linear part of the stress-strain diagram. Elongation and stress were calculated at the break.

Surface charge of the EC membranes was studied using a SurPASS electrokinetic analyzer. Zeta potential (ZP) was measured using 1 mM KCl of background electrolyte solution, and the pH was adjusted by automatic titration using HCl and KOH solutions.

The permeability towards water of large EC membranes was determined using the cross-flow NF/RO filtration system (CF042 membrane cell), as shown in Figure 2. The experiment was carried out using rectangular pieces (6.0 cm × 12.0 cm) of membranes, which were placed between two halves of the transport cell. A digital flow meter (FlowCal, GJC Instruments Ltd, Cheshire, UK) linked with a PC was used to evaluate the flux flow. Deionized (DI) water was applied to the membrane which was set at a pressure of 22 bar to compact the membranes for nearly 1 h until a

steady baseline flux was achieved. Permeate flux of DI water was estimated at different applied pressures. Resulting data were then used to calculate the water permeability (f) of the EC membrane using the following equation:

$$f = \frac{J}{A \cdot \Delta P} \quad (1)$$

where J is the volume of the permeate flux, A is the effective area of the membrane exposed to water (40 m²), and ΔP is the applied pressure on the membrane (bar).

The measurements of salt rejection were performed using each individual salt solution (NaCl, MgSO₄, MgCl₂, and Na₂SO₄) of 2 g/L separately and a cross-flow of 100 l/h. The temperature of the feed solution was kept at 20 ± 2°C throughout the experiment using a chiller, while the pH and conductivity were measured by using a conductivity meter. The percentage observed rejection ($R\%$) of the salts is determined from the permeate and feed samples using the following equation [41]:

$$R\% = \left(1 - \frac{C_p}{C_f}\right) 100\%, \quad (2)$$

where C_p and C_f are the salt concentrations on the permeate and the feed streams, respectively.

3. Results and Discussion

3.1. Surface Morphology of Membrane. A previous study reported that a sonication time of 20 min was suitable for MWCNT/CHIT (0.2% w/v) dispersions [41]. Accordingly, all dispersions used to prepare membranes in the current study were fabricated using the same sonication time (20 min) in order to simplify the comparison of their physical properties.

Figure 3(a) shows the scanning electron microscopic image (SEM) of the EC membrane with MWCNT/CHIT. In the surface of the EC membrane, it was found that the MWCNT completely covered by CHIT with no pores was observed in the image. In contrast, Figure 3(b) shows a randomly entangled mat/network of MWCNT. The MWCNTs are not well dispersed through the surfactant (chitosan). These images have a number of differences to that of a MWCNT/CHIT reported in previous studies [24, 41]. Sweetman et al. [42] reported that the surface morphology of membranes varied depending on the dispersant and the type of CNT used. In addition to that, SEM provided significant differences between the surface morphology of composite membranes of SWNTs with the same biopolymer dispersants [20]. Moreover, the EC membrane was prepared by the evaporating method. This indicates that the surface morphologies (Figure 3(a)) of the membrane may be affected greatly by using this method. This suggests that there may have been no loss of biopolymer (chitosan) at the surface of the membrane in the case of the evaporating method comparing to other methods such as the vacuum method, which demonstrated a greater range of surface morphologies in SEM studies [21, 24, 41].

Moreover, a cross-section image (Figure 3(b)) reveals that the structure of the EC membrane has many layers of



FIGURE 1: Images of the developed EC membrane.

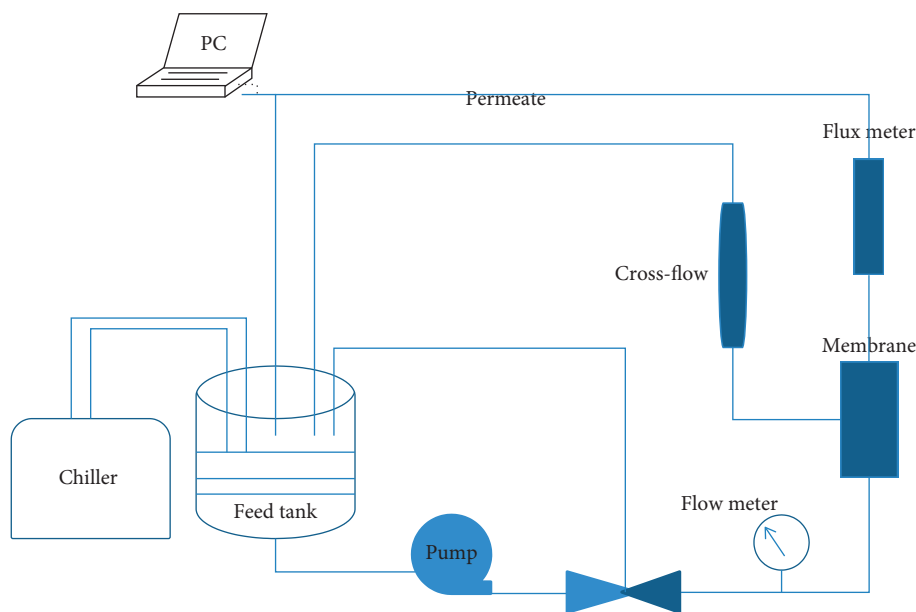


FIGURE 2: Schematic illustration of forward cross-flow filtration system.

MWCNTs, which was aligned with each other with a narrow distance between them. The membrane was found to be similar to those reported recently for other fabricated methods using the same CNT and chitosan ligand dispersant [24, 41].

3.2. Mechanical Properties. Mechanical strength of the membrane is of primary importance in seawater separation mechanisms. The reason beyond that is that the membrane should be able to withstand various pressure loads that were applied and different flow-rates over a long period. Hence, a study of the mechanical features of EC membranes was conducted by employing the tensile testing methodology, and the results obtained are plotted in Figure 4. The plot initially indicates a linear stress vs. strain relationship, which indicates elastic deformation. Still at higher strain levels, little deviations from the linear relationship could be seen, which suggest that the materials have a strong mechanism. The stress vs. strain plot was used to determine mechanical properties such as Young's moduli, toughness, elongation, and tensile strength. Table 1 summarizes the values found for

the EC membrane comparing with other techniques used for the membrane.

In this study, the EC membrane resulting from dispersions in MWCNTs and the surfactant (CHIT 0.2% w/v) showed Young's moduli in the 1.2 ± 0.1 GPa, elongation in the $10.2 \pm 1.2\%$, tensile strength in the 28 ± 1 MPa, and toughness in the 1.9 ± 0.2 J/g. The results observed for the elongation is slightly higher to that previously obtained for MWCNT/CHIT [41]. In addition, the mechanical properties of membranes containing biopolymers were much better among other membranes fabricated using MWCNT and low molecular mass dispersants [23]. The reason for the mechanical characteristics of EC membranes to be greater is due to the high molecular weight of chitosan and the method used for preparing membrane in this study. A recent method (evaporative casting method) indicates that the mechanical properties of the membrane made from MWCNT and CHIT 0.2% w/v were significant increased.

3.3. Contact Angle. Contact angle is one of the important properties for a material that is used as a filtration membrane

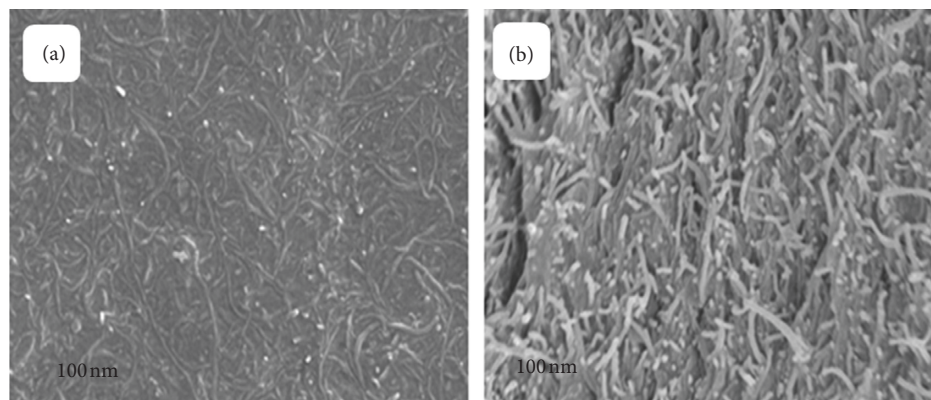


FIGURE 3: SEM of MWCNT/CHIT evaporative cast membrane. (a) Morphology of surface and (b) cross section.

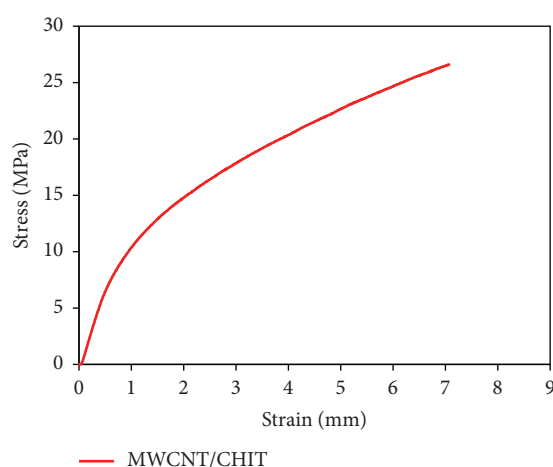


FIGURE 4: The stress vs. strain of MWCNT/CHIT evaporative cast membrane.

TABLE 1: Values found for the EC membrane comparing with other techniques used for the membrane.

Membrane	Tensile strength (MPa)	Elongation (%)	Young's modulus (GPa)	Toughness (J/g)	Contact angle (°)	Permeability (L/m ² ·h·bar)
MWCNT/chitosan*	56 ± 3	5.7 ± 0.	2.9 ± 0.1	2.1 ± 0.3	102 ± 3	0.87 ± 0.03
MWCNT/chitosan-glycerin*	49 ± 4	6.4 ± 2	2.9 ± 0.1	2.2 ± 0.8	80 ± 2	0.61 ± 0.02
MWCNT/chitosan-PEGDE*	59 ± 3	8.1 ± 2	2.7 ± 0.2	2.3 ± 0.2	76 ± 3	0.19 ± 0.01
MWCNT/chitosan	28 ± 1	10.2 ± 1.2	1.2 ± 0.1	1.9 ± 0.2	80 ± 2	0.75 ± 0.1

*Data for MWCNT/chitosan, MWCNT/chitosan-glycerin, and MWCNT/chitosan-PEGDE are taken from reference [41].

for separation of molecules in aqueous solutions. The information about the nature of the membrane surface such as hydrophobicity can be determined by the contact angle [41]. The contact angles values of the EC membranes ($80^\circ \pm 2^\circ$) reported in Table 1 indicate that the membrane is hydrophilic in nature [20, 23]. The contact angle values reported in the current study are lower to those values reported previously for membranes prepared using MWCNT and the same dispersant ($102^\circ \pm 3^\circ$) [41]. This indicates that lower contact angle of these membranes displayed by the method used in the present study provided more amount of dispersants (CHIT 0.2% w/v) at the membrane surface.

3.4. Zeta Potential. Figure 5 shows the membrane-surface charge density of the EC membrane, which is approximately neutral between pH 7 to 8 and it is gradually positive charged below pH 4, while it is negative charged above pH 8. This can be attributed to the deprotonation and protonation of chitosan [41]. This agreed with the behavior observed previously for MWCNT and chitosan as a surfactant, where absorbance was found to be positive charged below pH 4 and significantly negative charged above pH 8 [24, 41]. In addition, the measured membrane-surface charge was lower than to that was analyzed by Zhan et al. [16], due to the functional groups (carboxylic group) present in MWCNT.

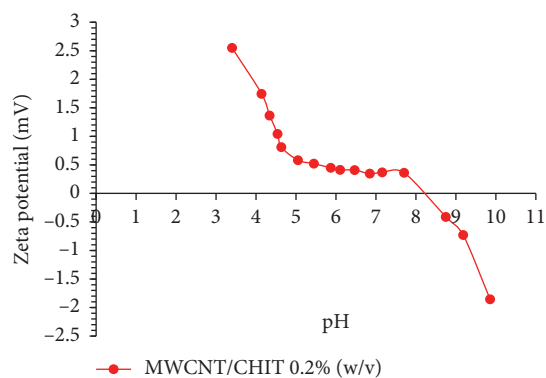


FIGURE 5: Zeta potential of MWCNT/CHIT evaporative cast membrane.

3.5. Permeability Salt Rejection Study of Membrane. The discussion in the previous sections illustrates the possibility of incorporating MWCNT and chitosan in order to develop mechanically strong and hydrophilic membranes. These characteristics are essential for membranes with potential use in nanofiltration and microfiltration processes. The next step in investigating the suitability of the membrane for filtration applications was to test the water permeability of the evaporative cast membrane, using the NF/RO system. Water permeability graph for MWCNT/CHIT is illustrated in Figure 6. Plot of the permeate flux against pressure applied indicates a linear relationship for evaporative cast membrane as illustrated in Figure 6. Equation (1) was used to estimate the membrane flux (f). The water permeability rate of the evaporative cast membrane (MWCNT/chitosan) was approximately $0.75 \pm 0.1 \text{ L}\cdot\text{m}^{-2}\cdot\text{h}^{-1}\cdot\text{bar}$. Resulting value is in good agreement with our previous investigation for the MWCNT/chitosan bucky paper membrane, which was prepared by using the filtration method (our work). In addition, the water permeability of the evaporative cast membrane (MWCNT/Chitosan) was slightly higher than the MWCNT/chitosan-glycerin membrane, while the water permeability of the MWCNT/chitosan-PEGDE membrane was significantly lower than the membrane (MWCNT/chitosan) that was fabricated in this study as shown in Table 1.

Salt rejection of EC membranes was investigated using four inorganic electrolyte solutions (NaCl, Na_2SO_4 , MgSO_4 , and MgCl_2), with a salt concentration of 2 g/l, applied pressure ranging from 3–20 bar, and temperature of $20^\circ\text{C} \pm 2^\circ\text{C}$, using a cross-flow NF/RO system. Figure 7 shows that the rejection of four inorganic electrolyte solutions was found to increase as the applied pressure was increased. The rejection order follows that $R(\text{MgCl}_2) > R(\text{NaCl}) > R(\text{MgSO}_4) > R(\text{Na}_2\text{SO}_4)$. In addition, the rejection of MgCl_2 was demonstrated to be significantly greater than other three inorganic electrolyte solutions (NaCl, MgSO_4 , and Na_2SO_4). The observed behavior of the EC membrane (MWCNT/CHIT) is in good agreement with previous studies, which showed the similar order of rejection as $R(\text{MgCl}_2) > R(\text{NaCl}) > R(\text{MgSO}_4) > R(\text{Na}_2\text{SO}_4)$ [41, 43, 44]. Consequentially, the MWCNT/CHIT membranes demonstrated stronger sorption to Cl^-

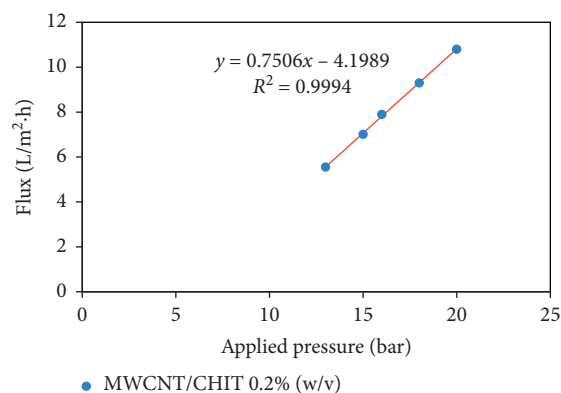


FIGURE 6: Water permeability of the MWCNT/CHIT evaporative cast membrane.

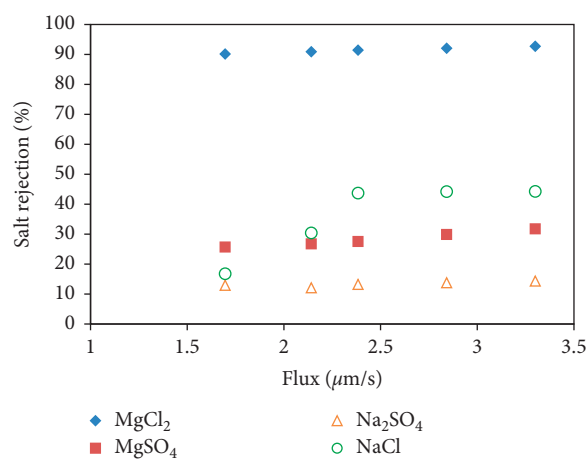


FIGURE 7: Effect of the operating pressure on the rejection performance of the MWCNT/CHIT evaporative cast membrane.

rather than SO_4^{2-} ions. This may be related to stronger interaction among the anions in MgCl_2 and functional groups available on the surface of the EC membrane. In addition, the Mg^{2+} ions can interact with anions on the surface of the membrane leading to decrease in the effective surface charge on the membrane [45]. This in turn makes the ions less absorbable on the surface of the EC membranes. This may be because the cation shield affects the membrane repulsive forces on the anions [46].

3.6. Effect of pH on Salt Rejection. The rejection of NaCl and MgSO_4 was studied on the MWCNT/chitosan EC membrane at $20 \pm 2^\circ\text{C}$ at the pH range from 3 to 10. The pressure was kept at 15 bar to obtain the same permeate flux for studying the effect of pH on the salt rejection as presented in Figure 8. The EC membrane had high salt rejection for both salts when the feed solution became acidic, and NaCl and MgSO_4 were 61 and 27%, respectively. In addition, the salt rejection gradually decreases for both solutions till they reach steady state after pH 9 for NaCl and beyond pH 8 for MgSO_4 . These phenomena show that, it could be attributed to the protonation of free amino groups in chitosan [41]. Based on the previous literature reports which stated

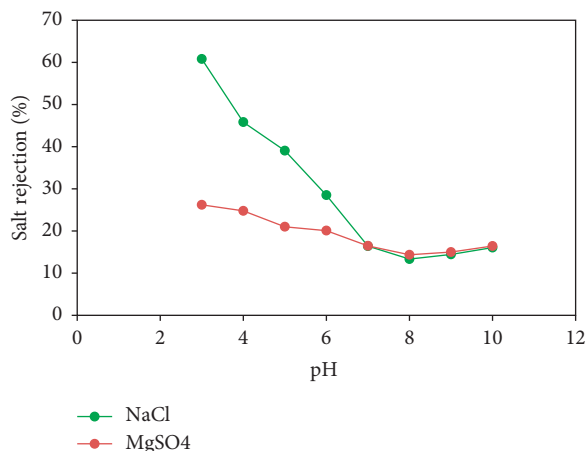


FIGURE 8: Effect of the pH on the rejection performance of the MWCNT/CHIT evaporative cast membrane.

that the amino groups (NH_2) on the chitosan structure can be protonated at low pH, resulting the NH_3^+ groups, which are mainly responsible for significantly increasing the exchange between anions and negatively charged surfaces [47, 48].

4. Conclusion

In the present study, a nanocomposite membrane multi-walled carbon nanotube (MWCNT)/chitosan fabricated by using evaporative casting (EC) method, which effectively elucidates the correlation between permeability and selectivity, was prepared. The simultaneous increase in flux and the high salt rejection ability factor suggested that the amalgamation of MWCNTs could bring about the packing of hydrophilic chains in the matrix, provided that internal nanochannels exist for enriched water permeation through the nanoscale opening of the MWCNTs. The addition of MWCNTs into the chitosan significantly improves crystallinity and tensile strength. A comprehensive study for properties of this membrane was investigated. The EC membrane has high mechanical properties whose tensile strength was 28 ± 1 MPa. In addition, it provided an excellent salt rejection at high acidic media for NaCl than MgSO_4 . Additionally, the incorporation of the MWCNT/chitosan composite also primes to the principally enriched mechanical property of chitosan composite membranes. Also, the composite MWCNT/chitosan may play more significant roles in a wide application, such as separation of biomedical products, wound dressings, and the model for mass transport of the biological membrane.

Data Availability

The data used to support the findings of this study are included within the article.

Conflicts of Interest

The authors declare that they have no conflicts of interest.

Acknowledgments

The authors are grateful to King Abdulaziz City for Science and Technology, Riyadh, Saudi Arabia, for the financial support of this work and the facilities in its labs. In addition, the authors would like to extend their thanks to Mr. Abdulrahman Algiahab for helping with the scanning electron microscope image.

References

- [1] A. D. Khawaji, I. K. Kutubkhanah, and J.-M. Wie, "Advances in seawater desalination technologies," *Desalination*, vol. 221, no. 1–3, pp. 47–69, 2008.
- [2] L. Shen, L. Tian, J. Zuo, X. Zhang, S. Sun, and Y. Wang, "Developing high-performance thin-film composite forward osmosis membranes by various tertiary amine catalysts for desalination," *Advanced Composites and Hybrid Materials*, vol. 2, no. 1, pp. 51–69, 2019.
- [3] T.-D. Lu, B.-Z. Chen, J. Wang et al., "Electrospun nanofiber substrates that enhance polar solvent separation from organic compounds in thin-film composites," *Journal of Materials Chemistry A*, vol. 6, no. 31, pp. 15047–15056, 2018.
- [4] J. Chang, J. Zuo, K.-J. Lu, and T.-S. Chung, "Membrane development and energy analysis of freeze desalination-vacuum membrane distillation hybrid systems powered by LNG regasification and solar energy," *Desalination*, vol. 449, pp. 16–25, 2019.
- [5] A. Kabeel, E. M. El-Said, and S. A. Dafea, "Design considerations and their effects on the operation and maintenance cost in solar-powered desalination plants," *Heat Transfer-Asian Research*, vol. 48, no. 5, pp. 1722–1736, 2019.
- [6] K. Tang, Y.-h. Kim, J. Chang et al., "Seawater desalination by over-potential membrane capacitive deionization: opportunities and hurdles," *Chemical Engineering Journal*, vol. 357, pp. 103–111, 2019.
- [7] Y. Li, E. Wong, Z. Mai, and B. Van der Bruggen, "Fabrication of composite polyamide/Kevlar aramid nanofiber nanofiltration membranes with high permselectivity in water desalination," *Journal of Membrane Science*, vol. 592, Article ID 117396, 2019.
- [8] A. W. Mohammad, Y. H. Teow, W. L. Ang, Y. T. Chung, D. L. Oatley-Radcliffe, and N. Hilal, "Nanofiltration membranes review: recent advances and future prospects," *Desalination*, vol. 356, pp. 226–254, 2015.
- [9] A. Anand, B. Unnikrishnan, J.-Y. Mao, H.-J. Lin, and C.-C. Huang, "Graphene-based nanofiltration membranes for improving salt rejection, water flux and antifouling—a review," *Desalination*, vol. 429, pp. 119–133, 2018.
- [10] M. Sweetman, S. May, N. Mebberson et al., "Activated carbon, carbon nanotubes and graphene: materials and composites for advanced water purification," *Journal of Carbon Research*, vol. 3, no. 4, p. 18, 2017.
- [11] R. H. Baughman, A. A. Zakhidov, and W. A. De Heer, "Carbon nanotubes—the route toward applications," *Science*, vol. 297, no. 5582, pp. 787–792, 2002.
- [12] M. A. L. Machado, L. Valentini, J. Biagiotti, and J. M. Kenny, "Thermal and mechanical properties of single-walled carbon nanotubes-polypropylene composites prepared by melt processing," *Carbon*, vol. 43, no. 7, pp. 1499–1505, 2005.
- [13] G. M. Spinks, V. Mottaghitlab, M. Bahrami-Samani, P. G. Whitten, and G. G. Wallace, "Carbon-nanotube-reinforced polyaniline fibers for high-strength artificial muscles," *Advanced Materials*, vol. 18, no. 5, pp. 637–640, 2006.

- [14] C. Tang, Q. Zhang, K. Wang, Q. Fu, and C. Zhang, "Water transport behavior of chitosan porous membranes containing multi-walled carbon nanotubes (MWNTs)," *Journal of Membrane Science*, vol. 337, no. 1-2, pp. 240-247, 2009.
- [15] S. Kim, J. R. Jinschek, H. Chen, D. S. Sholl, and E. Marand, "Scalable fabrication of carbon nanotube/polymer nanocomposite membranes for high flux gas transport," *Nano Letters*, vol. 7, no. 9, pp. 2806-2811, 2007.
- [16] Y. Zhan, L. Pan, C. Nie, H. Li, and Z. Sun, "Carbon nanotube-chitosan composite electrodes for electrochemical removal of Cu(II) ions," *Journal of Alloys and Compounds*, vol. 509, no. 18, pp. 5667-5671, 2011.
- [17] S. Bandow, A. M. Rao, K. A. Williams, A. Thess, R. E. Smalley, and P. C. Eklund, "Purification of single-wall carbon nanotubes by microfiltration," *The Journal of Physical Chemistry B*, vol. 101, no. 44, pp. 8839-8842, 1997.
- [18] D.-Q. Yang, J.-F. Rochette, and E. Sacher, "Functionalization of multiwalled carbon nanotubes by mild aqueous sonication," *The Journal of Physical Chemistry B*, vol. 109, no. 16, pp. 7788-7794, 2005.
- [19] M. in het Panhuis, A. Maiti, A. B. Dalton et al., "Selective interaction in a polymer-single-wall carbon nanotube composite," *The Journal of Physical Chemistry B*, vol. 107, no. 2, pp. 478-482, 2003.
- [20] J. Boge, L. J. Sweetman, M. in het Panhuis, and S. F. Ralph, "The effect of preparation conditions and biopolymer dispersants on the properties of SWNT buckypapers," *Journal of Materials Chemistry*, vol. 19, no. 48, pp. 9131-9140, 2009.
- [21] M. Rashid, *Synthesis, characterisation and water purification properties of carbon nanotube membranes (buckypapers)*, Ph.D. thesis, University of Wollongong, Wollongong, Australia, 2016.
- [22] Z. Zhao, Z. Yang, Y. Hu, J. Li, and X. Fan, "Multiple functionalization of multi-walled carbon nanotubes with carboxyl and amino groups," *Applied Surface Science*, vol. 276, pp. 476-481, 2013.
- [23] M. H.-O. Rashid, S. Q. T. Pham, L. J. Sweetman et al., "Synthesis, properties, water and solute permeability of MWNT buckypapers," *Journal of Membrane Science*, vol. 456, pp. 175-184, 2014.
- [24] M. H.-O. Rashid, G. Triani, N. Scales, M. in het Panhuis, L. D. Nghiem, and S. F. Ralph, "Nanofiltration applications of tough MWNT buckypaper membranes containing biopolymers," *Journal of Membrane Science*, vol. 529, pp. 23-34, 2017.
- [25] S. Dimassi, N. Tabary, F. Chai, N. Blanchemain, and B. Martel, "Sulfonated and sulfated chitosan derivatives for biomedical applications: a review," *Carbohydrate Polymers*, vol. 202, pp. 382-396, 2018.
- [26] Y. Liu, H. Lu, W. Zhong et al., "Multilayer-assembled microchip for enzyme immobilization as reactor toward low-level protein identification," *Analytical Chemistry*, vol. 78, no. 3, pp. 801-808, 2006.
- [27] M. Kamal, E. M. Abdelrazek, N. M. Sellow, and A. M. Abdelghany, "Synthesis and optimization of novel chitosan/cellulose acetate natural polymer membrane for water treatment," *Journal of Advances in Physics*, vol. 14, no. 1, pp. 5303-5311, 2018.
- [28] R. Brion-Roby, J. Gagnon, J.-S. Deschênes, and B. Chabot, "Development and treatment procedure of arsenic-contaminated water using a new and green chitosan sorbent: kinetic, isotherm, thermodynamic and dynamic studies," *Pure and Applied Chemistry*, vol. 90, no. 1, pp. 63-77, 2018.
- [29] K. Z. Elwakeel, "Environmental application of chitosan resins for the treatment of water and wastewater: a review," *Journal of Dispersion Science and Technology*, vol. 31, no. 3, pp. 273-288, 2010.
- [30] H. Du, M. Liu, X. Yang, and G. Zhai, "The design of pH-sensitive chitosan-based formulations for gastrointestinal delivery," *Drug Discovery Today*, vol. 20, no. 8, pp. 1004-1011, 2015.
- [31] C.-Y. Ma, S.-C. Huang, P.-H. Chou, W. Den, and C.-H. Hou, "Application of a multiwalled carbon nanotube-chitosan composite as an electrode in the electrosorption process for water purification," *Chemosphere*, vol. 146, pp. 113-120, 2016.
- [32] M. Abbasi and M. M. Habibi, "Optimization and characterization of direct blue 71 removal using nanocomposite of chitosan-MWCNTs: central composite design modeling," *Journal of the Taiwan Institute of Chemical Engineers*, vol. 62, pp. 112-121, 2016.
- [33] L. Yanyan, T. A. Kurniawan, A. B. Albadarin, and G. Walker, "Enhanced removal of acetaminophen from synthetic wastewater using multi-walled carbon nanotubes (MWCNTs) chemically modified with NaOH, HNO₃/H₂SO₄, ozone, and/or chitosan," *Journal of Molecular Liquids*, vol. 251, pp. 369-377, 2018.
- [34] H. Warren, R. D. Gately, H. N. Moffat, and M. in het Panhuis, "Conducting carbon nanofibre networks: dispersion optimisation, evaporative casting and direct writing," *RSC Advances*, vol. 3, no. 44, pp. 21936-21942, 2013.
- [35] J. Tkac, J. W. Whittaker, and T. Ruzgas, "The use of single walled carbon nanotubes dispersed in a chitosan matrix for preparation of a galactose biosensor," *Biosensors and Bioelectronics*, vol. 22, no. 8, pp. 1820-1824, 2007.
- [36] M. in het Panhuis, A. Heurtematte, W. R. Small, and V. N. Paunov, "Inkjet printed water sensitive transparent films from natural gum-carbon nanotube composites," *Soft Matter*, vol. 3, no. 7, pp. 840-843, 2007.
- [37] R. Bandyopadhyaya, E. Nativ-Roth, O. Regev, and R. Yerushalmi-Rozen, "Stabilization of individual carbon nanotubes in aqueous solutions," *Nano Letters*, vol. 2, no. 1, pp. 25-28, 2002.
- [38] M. G. Pellá, M. K. Lima-Tenório, E. T. Tenório-Neto, M. R. Guilherme, E. C. Muniz, and A. F. Rubira, "Chitosan-based hydrogels: from preparation to biomedical applications," *Carbohydrate Polymers*, vol. 196, pp. 233-245, 2018.
- [39] F. Hashemzadeh, A. Hassani, H. A. Panahi, and S. Borghei, "Evaluation of the removal of heavy metals (cadmium lead, and zinc) from aqueous solutions using multi-walled carbon nanotubes modified with chitosan," *Journal of Water and Wastewater*, vol. 29, no. 3, pp. 31-41, 2018.
- [40] H. Yang, S. C. Wang, P. Mercier, and D. L. Akins, "Diameter-selective dispersion of single-walled carbon nanotubes using a water-soluble, biocompatible polymer," *Chemical Communications*, no. 13, p. 1425, 2006.
- [41] A. A. Alshahrani, H. Al-Zoubi, L. D. Nghiem, and M. in het Panhuis, "Synthesis and characterisation of MWNT/chitosan and MWNT/chitosan-crosslinked buckypaper membranes for desalination," *Desalination*, vol. 418, pp. 60-70, 2017.
- [42] L. J. Sweetman, L. J. Alcock, J. D. McArthur et al., "Bacterial filtration using carbon nanotube/antibiotic buckypaper membranes," *Journal of Nanomaterials*, vol. 2013, Article ID 781212, 11 pages, 2013.
- [43] X. Tongwen and Y. Weihua, "A novel positively charged composite membranes for nanofiltration prepared from poly (2,6-dimethyl-1,4-phenylene oxide) by in situ amines cross-linking," *Journal of Membrane Science*, vol. 215, no. 1-2, pp. 25-32, 2003.

- [44] J. Berger, M. Reist, J. M. Mayer, O. Felt, and R. Gurny, "Structure and interactions in chitosan hydrogels formed by complexation or aggregation for biomedical applications," *European Journal of Pharmaceutics and Biopharmaceutics*, vol. 57, no. 1, pp. 35–52, 2004.
- [45] J. Miao, G.-h. Chen, and C.-j. Gao, "A novel kind of amphoteric composite nanofiltration membrane prepared from sulfated chitosan (SCS)," *Desalination*, vol. 181, no. 1–3, pp. 173–183, 2005.
- [46] M. D. Afonso and M. N. de Pinho, "Transport of MgSO_4 , MgCl_2 , and Na_2SO_4 across an amphoteric nanofiltration membrane," *Journal of Membrane Science*, vol. 179, no. 1–2, pp. 137–154, 2000.
- [47] O. S. Amuda, A. A. Giwa, and I. A. Bello, "Removal of heavy metal from industrial wastewater using modified activated coconut shell carbon," *Biochemical Engineering Journal*, vol. 36, no. 2, pp. 174–181, 2007.
- [48] S. M. Nomanbhay and K. Palanisamy, "Removal of heavy metal from industrial wastewater using chitosan coated oil palm shell charcoal," *Electronic Journal of Biotechnology*, vol. 8, no. 1, pp. 43–53, 2005.

Research Article

Environmentally Friendly and Recyclable Natural-Mediator-Modified Magnetic Nanoparticles for Laccase-Catalyzed Decolorization

Kun Zhang,¹ Yeying Wu,² Juan Huang^{1,3} ,³ and Youxun Liu¹ 

¹School of Basic Medical Sciences, Xinxiang Medical University, Jinsui Avenue 601, Xinxiang, Henan 453003, China

²School of Life Science, Wuchang University of Technology, Jiangxia Avenue 16, Wuhan, Hubei 430223, China

³School of Life Sciences and Technology, Xinxiang Medical University, Jinsui Avenue 601, Xinxiang, Henan 453003, China

Correspondence should be addressed to Juan Huang; huangjuan@xxmu.edu.cn and Youxun Liu; liuyouxun@xxmu.edu.cn

Received 30 September 2019; Revised 17 November 2019; Accepted 25 November 2019; Published 11 December 2019

Guest Editor: Ibrahim H. Alsohaimi

Copyright © 2019 Kun Zhang et al. This is an open access article distributed under the Creative Commons Attribution License, which permits unrestricted use, distribution, and reproduction in any medium, provided the original work is properly cited.

The high cost, potential toxicity, and possible enzyme inhibition ability of artificial mediators have limited the large-scale application of laccase (Lac)/mediator systems. Here, sinapic acid (SA), a natural mediator, was covalently attached to amino-functionalized magnetic nanoparticles (MNPs) via amide bond formation. The as-prepared SA@MNPs were characterized by Fourier-transform infrared spectroscopy, scanning electron microscopy, cyclic voltammetry, and thermogravimetric analysis. The SA@MNPs were then applied to evaluate the activity of the immobilized mediator for Lac-catalyzed dye decolorization using indigo carmine (IC) as a model dye. When SA and SA@MNPs were used as Lac mediators, IC decolorization yields of ~93% and 96%, respectively, were obtained after 60 min. Moreover, SA@MNPs exhibited an IC decolorization yield of ~90% after being reused for 8 cycles. The Lac/SA@MNP system was shown to degrade IC by breaking down the chromophoric group. The easy recyclability, good reusability, nontoxicity, and relatively low cost of SA@MNPs make this immobilized natural mediator a promising tool for dye treatment.

1. Introduction

Laccases (Lacs; *p*-diphenol:oxygen oxidoreductase EC 1.10.3.2) are multicopper oxidases that can use molecular oxygen to oxidize a great variety of aromatic substrates, typically phenolic compounds [1]. However, the direct oxidation of nonphenolic compounds by Lacs is limited because the redox potentials of these enzymes (typically 0.5–0.8 V) are lower than those of such substances [2]. However, Lacs are able to oxidize nonphenolic substrates with the help of redox mediators, which are small molecules that facilitate electron transfer between enzymes and substrates [3]. Because Lacs exhibit substrate universality and produce water as the sole reaction byproduct, they are considered green biocatalysts. Thus, there has been increasing interest in the application of Lacs in various fields

such as wood pulping, electrochemical analysis, organic synthesis, and, especially, detoxification of recalcitrant environmental pollutants or decolorization of synthetic dyes [4].

Lac mediators are divided into two types: artificial and natural. Artificial mediators are synthetic small molecules such as 2,2-azino-bis-(3-ethylbenzothiazoline)-6-sulfonic acid (ABTS), 1-hydroxybenzotriazole (HBT), and 2,2,6,6-tetramethylpiperidine 1-oxyl (TEMPO). Such mediators have been applied in Lac-mediator-based catalytic reactions, and the oxidation mechanisms have been elucidated [3, 5–7]. However, the large-scale application of artificial mediators has been limited by their high cost, potential toxicity and possible enzyme inhibition activity. Therefore, great efforts have been made to find alternative mediators of natural origin. In the past decade, many natural mediators, typically

lignin-related phenols including sinapic acid (SA), syringaldehyde, ferulic acid, acetosyringone, vanillin, and acetovanillone, have been investigated [8, 9]. Some natural mediators have been found to be as efficient as artificial mediators [10]. In particular, dimethoxyphenol compounds show even higher efficiencies than artificial mediators for the oxidation of recalcitrant pollutants by Lac [11]. Furthermore, compared with artificial mediators, natural mediators are environmentally friendly, relatively inexpensive, and nontoxic.

Typically, mediators are dissolved in solution during use, which makes recovery from the reaction medium and reuse difficult, leading to a significant cost increase for large-scale industrial applications [3, 12, 13]. Thus, a few researchers have made great efforts towards recovering and reusing mediators by immobilizing them on support materials. For instance, ABTS immobilized on silica nanoparticles or encapsulated in a metal-organic framework (MIL-100(Fe)) has been successfully applied as a mediator for Lac-catalyzed decolorization [14, 15]. However, to the best of our knowledge, there has been little research on the immobilization of natural Lac mediators.

SA, a precursor of lignin, has been confirmed to act as a highly efficient mediator for Lac oxidation of various recalcitrant compounds, including industrial dyes [11]. The oxidation mechanism of the Lac/SA system has been elucidated and is similar to a hydrogen atom transfer oxidation mechanism. SA, a substituted phenol, is a good Lac substrate because its electrochemical potential is well matched to that of Lac. Oxidation of SA by Lac results in the fast production of highly reactive phenoxyl radicals (PhO), which play a similar role to nitroxyl radicals ($>N-O\cdot$) generated by the oxidation of an artificial mediator (HBT) through a hydrogen atom transfer oxidation mechanism. Subsequently, these phenoxyl radicals can oxidize target substrates. It has been confirmed that fast oxidation of SA by Lac provides a stable, high concentration of phenoxyl radicals that efficiently promote the Lac-catalyzed decolorization of various dyes [4, 11, 16]. For practical applications of the Lac/SA system to dye decolorization, the immobilization of SA would improve the reusability of the mediator, thus reducing the running cost. The molecular structure of SA consists of a phenol moiety and a carboxyl moiety (Figure 1(a)). As the phenol group of SA is responsible for the mediator activity of this compound, the carboxyl group could potentially be exploited to attach SA to an immobilization matrix such as magnetic nanoparticles (MNPs). However, it is necessary to determine whether the mediator activity of SA is maintained following immobilization.

In the present work, our main aim was to immobilize a natural mediator, SA, on MNPs to facilitate its recovery and reuse. First, SA was covalently attached to amino-modified MNPs via amide bond formation. Second, the feasibility of using SA-modified MNPs (SA@MNPs) as a Lac mediator was evaluated for the Lac-catalyzed decolorization of the dye indigo carmine (IC). Finally, it was confirmed that the SA@MNPs could be easily recovered by magnetic separation and effectively reused as a Lac mediator.

2. Materials and Methods

2.1. Materials. Lac (EC 1.10.3.2, enzyme activity ≥ 0.6 U/mg) was provided by Sunson Industry Group (Beijing, China). ABTS was supplied by Sigma-Aldrich (St. Louis, MO, USA). SA and 3-aminopropyltriethoxysilane (APTES) were purchased from Energy Chemical (Shanghai, China). All other chemicals and reagents were of analytical grade.

2.2. Preparation of SA-Immobilized MNPs. Amino-modified Fe_3O_4 nanoparticles were synthesized according to the method described by Mohapatra et al. [17] with slight modifications. Briefly, 0.324 g of $FeCl_3$ and 0.278 g of $FeSO_4 \cdot 7H_2O$ were added to 40 mL of deoxygenated water in a 100 mL three-necked flask. The mixture was stirred vigorously at room temperature for 20 min under nitrogen protection. Then, 3 mmol of APTES was added to the stirred reaction mixture over a period of 10 min. Subsequently, 3 mL 25% NH_3 solution was quickly added to the flask. After 30 min of vigorous stirring, the black precipitate was separated and washed ten times with deionized water via magnetic decantation. The resulting nanoparticles were dried at $60^\circ C$ under vacuum for 8 h. The obtained material is referred to as APTES@MNPs. The control MNPs were prepared without using APTES.

The MNPs coated with APTES can provide active amino groups for amide bond formation with SA. Thus, the SA-modified MNPs were fabricated as follows. First, 0.25 g of SA was dissolved in 10 mL of *N,N*-dimethylformamide in a 50 mL three-necked flask at $0^\circ C$. After 10 min, 0.28 g of *N*-ethyl-*N'*-(3-dimethylaminopropyl)carbodiimide hydrochloride was added, and the reaction mixture was stirred for another 10 min at $0^\circ C$. Subsequently, 0.4 g of APTES@MNPs, 0.2 g of 4-dimethylaminopyridine, and 0.3 mL of triethylamine were added, and the reaction mixture was stirred for 24 h under nitrogen protection at room temperature. The black precipitate was recovered and then washed five times with *N,N*-dimethylformamide and five times with deionized water, respectively. The resulting nanoparticles were dried at $60^\circ C$ under vacuum for 12 h. The obtained material is referred to as SA@MNPs.

2.3. Dye Decolorization and Measurement Activity of Lac. IC (Figure 1(b)) was used as the model pollutant for enzymatic decolorization. As IC is not a phenolic substrate, Lac needs the help of a mediator to decolorize IC completely. To determine the optimal conditions for SA oxidation by Lac, three buffers at pH 4.5 were used: 0.2 M sodium acetate buffer, 0.2 M citrate buffer, and 0.2 M sodium citrate buffer. The effects of pH on Lac-catalyzed decolorization using both SA@MNPs and SA were examined between pH 3.0 and 7.0 in 0.2 M sodium acetate buffer. The optimum pH was used for further experiments. The decolorization conditions were as follows: 20 mg/L dye, 3000 U/L Lac, and either the immobilized mediator (0.02 g/L SA@MNPs) or the free mediator (15.4 μM SA) at pH 5.0. Unless otherwise specified, the decolorization experiments were carried out in 5 mL centrifuge tubes and the mixtures were shaken at 150 rpm at

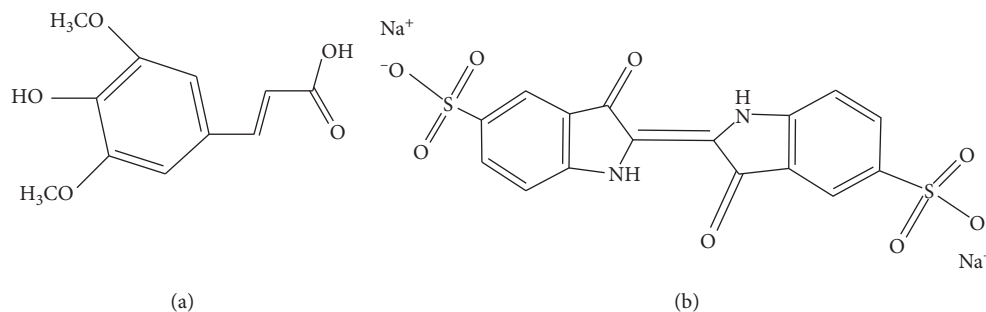


FIGURE 1: Molecular structures of (a) SA and (b) IC.

room temperature. Control reactions were also performed to study the decolorization efficiency using Lac or SA@MNPs alone. Dye degradation was monitored using UV-Vis spectroscopy by recording the absorbance spectrum of the dye between 250 and 800 nm. The extent of IC decolorization was determined based on the decrease in absorbance at $\lambda_{\max} = 615$ nm using the following formula: decolorization (%) = $(A_0 - A_t)/A_0$, where A_0 is the initial absorbance of the dye at $\lambda_{\max} = 615$ nm and A_t is the absorbance after the specified reaction time. In addition, the band at 515 nm was used as a characteristic absorption peak to monitor SA oxidation in solution. All experiments were performed at least in triplicate. The data presented herein correspond to mean values with standard errors.

Assays of Lac activities were conducted spectrophotometrically using ABTS as a substrate [13]. The reaction was initiated by adding 0.1 mL of the Lac solution into 2.7 mL of sodium acetate buffer solution (50 mM, pH 4.0) and 0.2 mL of ABTS (4 mmol/L), and then the mixtures are incubated at 25°C for 3 min. The increase in absorbance of the solution was recorded at the wavelength of 420 nm.

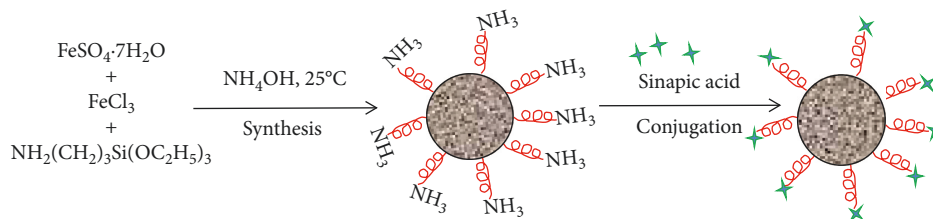
2.4. Reusability and Stability of SA@MNPs. The reusability of the SA@MNPs was assessed over 8 decolorization cycles. At the end of each cycle, the SA@MNPs was recovered with a magnet, washed three times with distilled water, and then used for a new cycle. The data presented herein are average values of triplicate measurements. The storage stability of the SA@MNPs was evaluated by storing the SA@MNPs at room temperature in water and in pH 5.0 and 9.0 disodium hydrogen phosphate-citric acid buffers. The amount of SA in the supernatant was determined periodically over 10 days by monitoring changes in the UV-Vis absorbance spectrum. In addition, the characteristic Fourier-transform infrared (FT-IR) vibration bands of the as-prepared SA@MNPs were compared with those of the SA@MNPs after 8 catalytic cycles. The statistical significance of differences was compared and analyzed using Student's *t* tests or one-way analysis of variance by GraphPad Prism7 Software. Differences with *p* values of less than 0.05 were considered statistically significant.

2.5. Characterization Methods. Transmission electron microscopy (TEM) was carried out using a model 9000

transmission electron microscope (Hitachi, Japan). Field-emission scanning electron microscopy (SEM) and energy-dispersive X-ray spectroscopy (EDS) were performed with a JSM 6700F scanning electron microscope (JEOL, Japan). FT-IR spectra were recorded with a Tensor 27 spectrometer (Bruker, Germany) using the KBr pellet technique. Cyclic voltammetry (CV) measurements were performed with a CHI600E electrochemical workstation (CH Instruments, USA). Thermogravimetric analysis (TGA) of the as-synthesized MNPs was carried out using a LENSES STAPT-1000 calorimeter (Germany) by scanning up to 700°C at a heating rate of 10°C/min. UV-Vis spectroscopy was performed with a CARY 50 spectrophotometer (Varian, USA).

3. Results and Discussion

3.1. Synthesis and Characterization of SA-Immobilized MNPs. Owing to their attractive features, such as easy surface modification, convenient separation, and nontoxicity [18–20], Fe_3O_4 MNPs were selected as a support material for the immobilization of SA. The preparation of SA@MNPs is illustrated in Scheme 1. The FT-IR spectra of MNPs, SA, APTES@MNPs, and SA@MNPs are given in Figure 2. Compared with the FT-IR spectrum of the MNPs, the FT-IR spectrum of APTES@MNPs exhibited new peaks at 1052 cm^{-1} , corresponding to the Si–O–Si stretching vibration, $\sim 1125\text{ cm}^{-1}$, corresponding to the C–N stretching vibration, and ~ 3420 and $\sim 1620\text{ cm}^{-1}$, corresponding to the $-\text{NH}_2$ groups of the APTES [21]. In addition, a strong peak was observed at $\sim 575\text{ cm}^{-1}$ corresponding to the Fe–O–Fe vibration. These results indicated that the MNPs were successfully coated with APTES to give amino-functionalized MNPs. In the FT-IR spectrum of SA@MNPs, peaks were observed at ~ 3352 and 1680 cm^{-1} corresponding to the $-\text{NH}$ stretching vibration and C=O stretching vibration, respectively, of an amide bond [21]. Amide bond formation occurred via the reaction between the carboxyl group of SA and an amino group on the APTES@MNPs. Furthermore, a comparison of the FT-IR spectra of SA, APTES@MNPs, and SA@MNPs shows that the characteristic bands of both of SA and APTES@MNPs are clearly observable in the FT-IR spectrum of SA@MNPs, indicating that the amino-functionalized MNPs were successfully modified with SA. Owing to magnetic dipole interactions, both MNPs and APTES@MNPs tended to agglomerate, resulting in clusters, as shown



SCHEME 1: Schematic illustration of the preparation strategy for SA@MNPs.

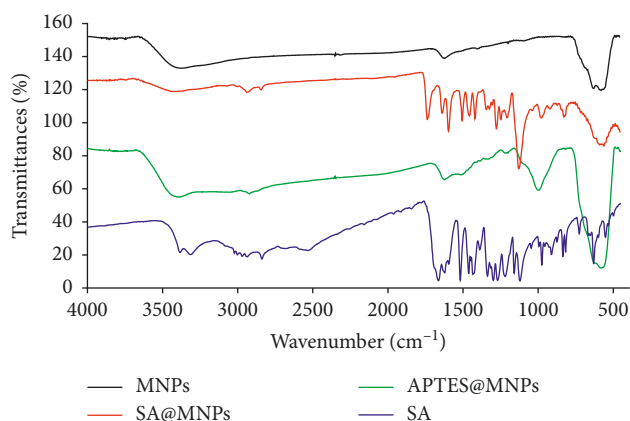


FIGURE 2: FT-IR spectra of MNPs, SA, APTES@MNPs, and SA@MNPs.

in the TEM images (Figures 3(a) and 3(b)). As observed in the TEM images, the mean size of the APTES@MNPs was slightly larger than that of the MNPs, and this difference was attributed to the APTES coating.

TGA showed that MNPs, APTES@MNPs, and SA@MNPs had different decomposition temperatures (Figure 4). The total weight loss observed for the MNPs was $\sim 4\%$, whereas that for the APTES@MNPs was $\sim 10\%$. Unlike the MNPs, the APTES@MNPs showed a two-step decomposition process. The first weight loss ($115\text{--}200^\circ\text{C}$) corresponded to the loss of water from the sample. The second significant weight loss of $\sim 6\%$ ($250\text{--}420^\circ\text{C}$) corresponded to the thermal degradation of APTES. Notably, the total weight loss of SA@MNPs was much greater ($\sim 28\%$) and a three-step decomposition process was observed. The first two weight loss steps were similar to those of the APTES@MNPs, whereas the third weight loss step of approximately 15% was assigned to the thermal decomposition of SA. These results indicated that the MNPs were coated with APTES and that SA was covalently attached to the APTES@MNPs.

As shown in Figure 5(a), the SEM-mapping images confirm the presence of C, Si, and Fe in the SA@MNPs. In addition, the dispersion of Si and C on the surfaces of the SA@MNPs suggests that the MNPs were homogeneously coated with APTES and SA. Moreover, the EDS spectrum (Figure 5(b)) further confirmed that C, O, N, Si, and Fe were present in the SA@MNPs, providing clear evidence for the formation of SA@MNP nanocomposites. The amount of amino groups on the surface of MNPs was determined using a spectrophotometric assay according to the method described by Mohapatra et al. [17]. The change in the amount

of amino groups before and after SA grafting indicated that the concentration of SA on the surface of MNPs was $\sim 770 \mu\text{mol/g}$.

The electrochemical behavior was examined by CV using glassy carbon electrode (GCEs) coated with films of the as-synthesized MNPs at pH 5.0 in sodium acetate buffer (Figure 6). Although the electrochemical behavior of APTES@MNPs/GCE and SA@MNPs/GCE was similar, different behavior was observed in the presence of Lac. Lac/APTES@MNPs/GCE exhibited no obvious redox peaks at applied potentials between 0 and $+1.0 \text{ V}$, whereas Lac/SA@MNPs/GCE showed a well-defined reversible signal at 0.4 V , which was ascribed to the reversible oxidation of immobilized SA by Lac. This result indicated that SA immobilized on MNPs plays a role in electron transfer between the electrode and Lac and can still act as a Lac mediator, similar to free SA.

3.2. Effects of pH on Dye Decolorization. To explore the ability of SA to act as a Lac mediator, the effects of the buffer type and pH on SA oxidation by Lac were evaluated. To monitor SA oxidation, the absorbance spectra of the SA were recorded between 200 and 750 nm before and after Lac oxidation. As shown in Figure 7(a), SA in solution showed two characteristic absorption bands at 232 and 300 nm . Upon incubation of SA with Lac at pH 5 in sodium acetate buffer for approximately 30 min, an intense brown-red color appeared. Simultaneously, the band at 300 nm nearly disappeared and a new band appeared at 515 nm suggesting the formation of the new product resulting from SA oxidation by Lac. Therefore, the band at 515 nm was used as a characteristic absorption peak to monitor SA oxidation in solution. The catalytic activity of Lac for SA oxidation was compared in various buffers. As shown in Figure 7(b), the oxidation rate in sodium acetate buffer was highest in three kinds of buffer ($F(2, 6) = 64.24$, $p < 0.05$). Thus, sodium acetate buffer was used for further experiments. In addition, the optimum pH for maximizing SA oxidation by Lac was found to be 5.0, as shown in Figure 7(c).

The effects of pH on dye decolorization by Lac, Lac with the free mediator (SA), and Lac with the immobilized mediator (SA@MNPs) were then evaluated in sodium acetate buffer between pH 3.0 and 7.0. Figure 7(d) shows that the maximum decolorization by Lac was achieved at pH 4.5, likely because the catalytic activity Lac for decolorization of IC was maximized at this pH value [14]. However, both the Lac/SA system and the Lac/SA@MNP system exhibited maximum decolorization at pH 5.0. This slight shift in the

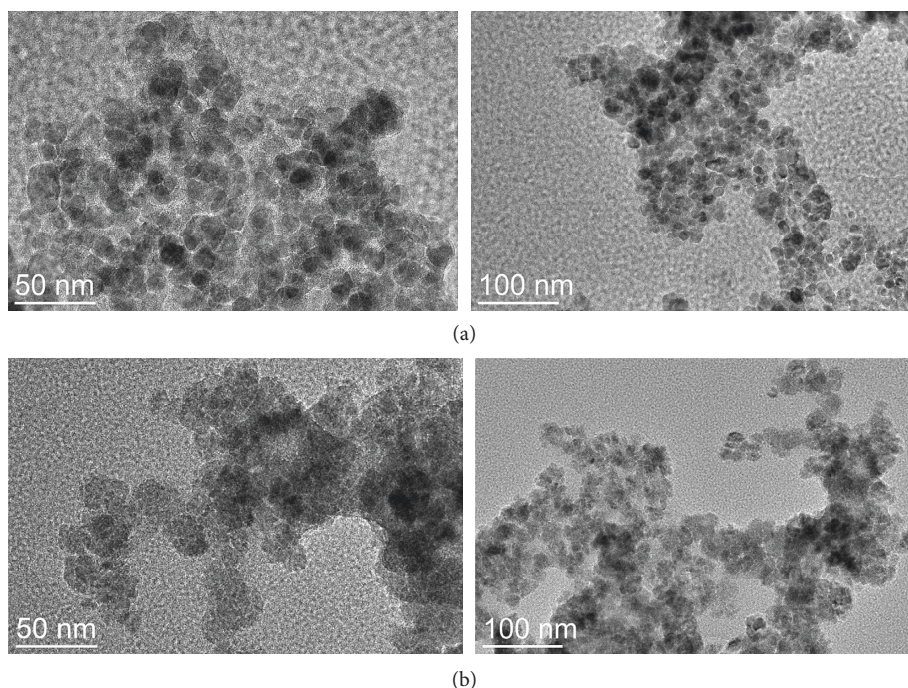


FIGURE 3: TEM images of (a) MNPs and (b) APTES@MNPs.

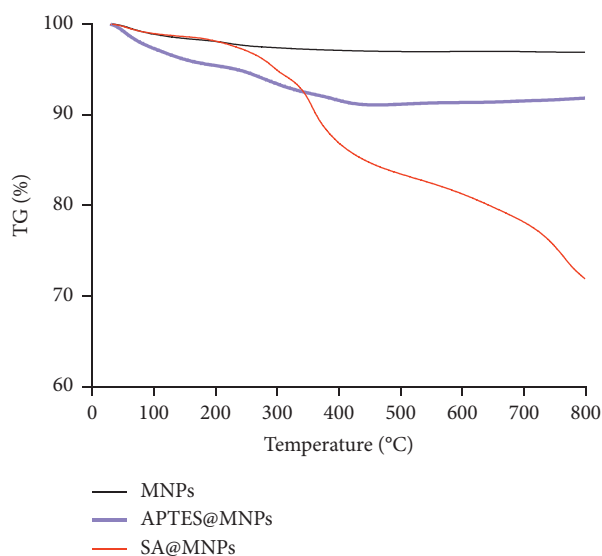


FIGURE 4: TGA thermograms of MNPs, APTES@MNPs, and SA@MNPs.

optimum pH relative to that for Lac alone may be attributable to the fact that the optimum pH for oxidation of SA by Lac was 5.0, as shown in Figure 7(c). It is also possible that electron transfer between the dye molecules, the SA mediator, the MNPs, and Lac is more favorable at pH 5.0. Many studies have found that acidic pH values enhance the activities of most Lacs [22–24]. Increasing the pH further resulted in an evident decrease in the decolorization activities of both the Lac/SA and Lac/SA@MNP systems. However, the latter displayed higher decolorization activities

than the former at pH values above 5.0, suggesting that the environmental pH value had little influence on the activity of SA as mediator following immobilization.

3.3. Dye Decolorization Efficiencies. To evaluate the effect of the SA@MNPs on Lac-catalyzed decolorization, the decolorization efficiency of the Lac/SA@MNP system was compared with those of the Lac/SA system, SA@MNPs, and Lac alone (Figure 8). For Lac alone, only ~10% dye decolorization was obtained within 30 min. Previous reports have shown that Lac is not able to degrade IC completely without a mediator because IC is a nonphenolic compound, which is not a typical substrate for Lac [14]. In the case of SA@MNPs, negligible decolorization (~6%) was obtained after 30 min, and this value remained almost constant throughout the reaction time. Thus, the observed decolorization is mainly due to the adsorption of the dye molecules on the SA@MNPs. These results implied that Lac degradation alone and nanoparticle adsorption have negligible effects on the decolorization of IC. In comparison, Lac with the free mediator (Lac/SA) achieved almost complete decolorization of IC (~93%) within 60 min, and Lac with the immobilized mediator (SA@MNPs) realized a similar decolorization efficiency (~96%) within 60 min. These results indicated that SA immobilized on the MNPs maintained the same activity as free SA for mediating Lac-catalyzed dye decolorization. Notably, these high decolorization efficiencies were due to the effect of the mediator instead of Lac alone or the MNPs. In comparison, our previous reports have shown that ABTS, an artificial mediator, immobilized on silica nanoparticles or encapsulated in a metal-organic framework exhibited a higher

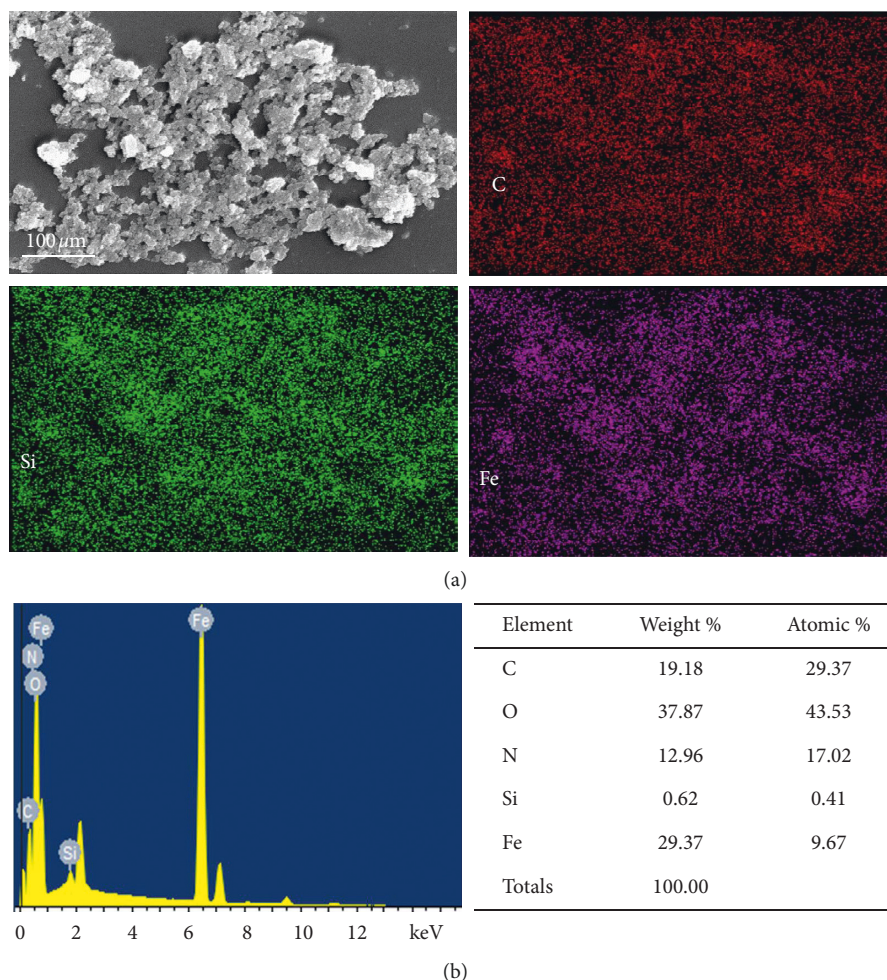


FIGURE 5: (a) SEM-mapping images of the distribution of various elements on the surfaces of SA@MNPs. (b) EDS spectrum and corresponding relative elemental contents.

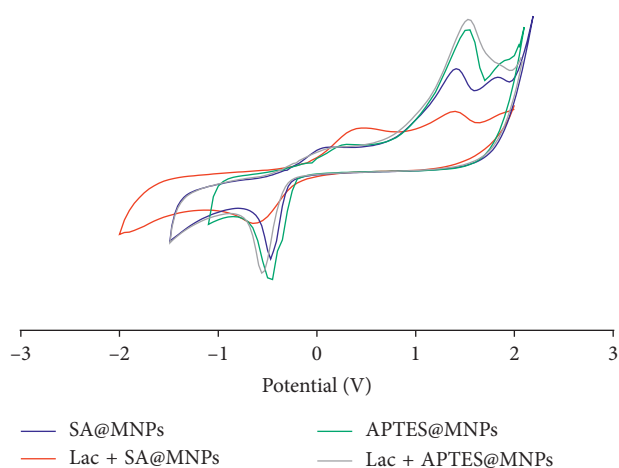


FIGURE 6: Cyclic voltammograms of APTES@MNPs and SA@MNPs coated on GCEs at a sweep rate of 20 mV/s in 0.05 M sodium acetate buffer at pH 5.0 in the absence and presence of Lac.

decolorization efficiency than SA@MNPs, which may attribute to the oxidation mechanism of SA and ABTS as mediators in the Lac-catalyzed reaction [14, 15]. It had been

reported that ABTS-mediated oxidations belong to an electron transfer mechanism, and SA-mediated oxidations are a hydrogen atom transfer mechanism [11].

3.4. Reusability of SA@MNPs. To evaluate the reusability of the immobilized mediator, the SA@MNPs were recovered and reused for dye decolorization for up to 8 cycles, as shown in Figure 9(a). Using a reaction time of 60 min, very high decolorization rates were obtained by employing the same SA@MNPs over 8 runs. However, the decolorization efficiency decreased significantly ($F(7, 16) = 2.786$, $p < 0.05$) after 8 cycles, and approximately 90% decolorization was achieved. On the one hand, this decrease may be due to partial destruction of the SA@MNPs during the reaction and/or the loss of some SA@MNPs during magnetic recovery. Similar observations have been reported previously for immobilized-mediator-catalyzed dye decolorization reactions [15, 25, 26]. On the other hand, the accumulation of dye degradation products on the surface of the SA@MNPs may depress the activity of the enzyme, resulting in a reduction in the decolorization efficiency during the subsequent cycle [27].

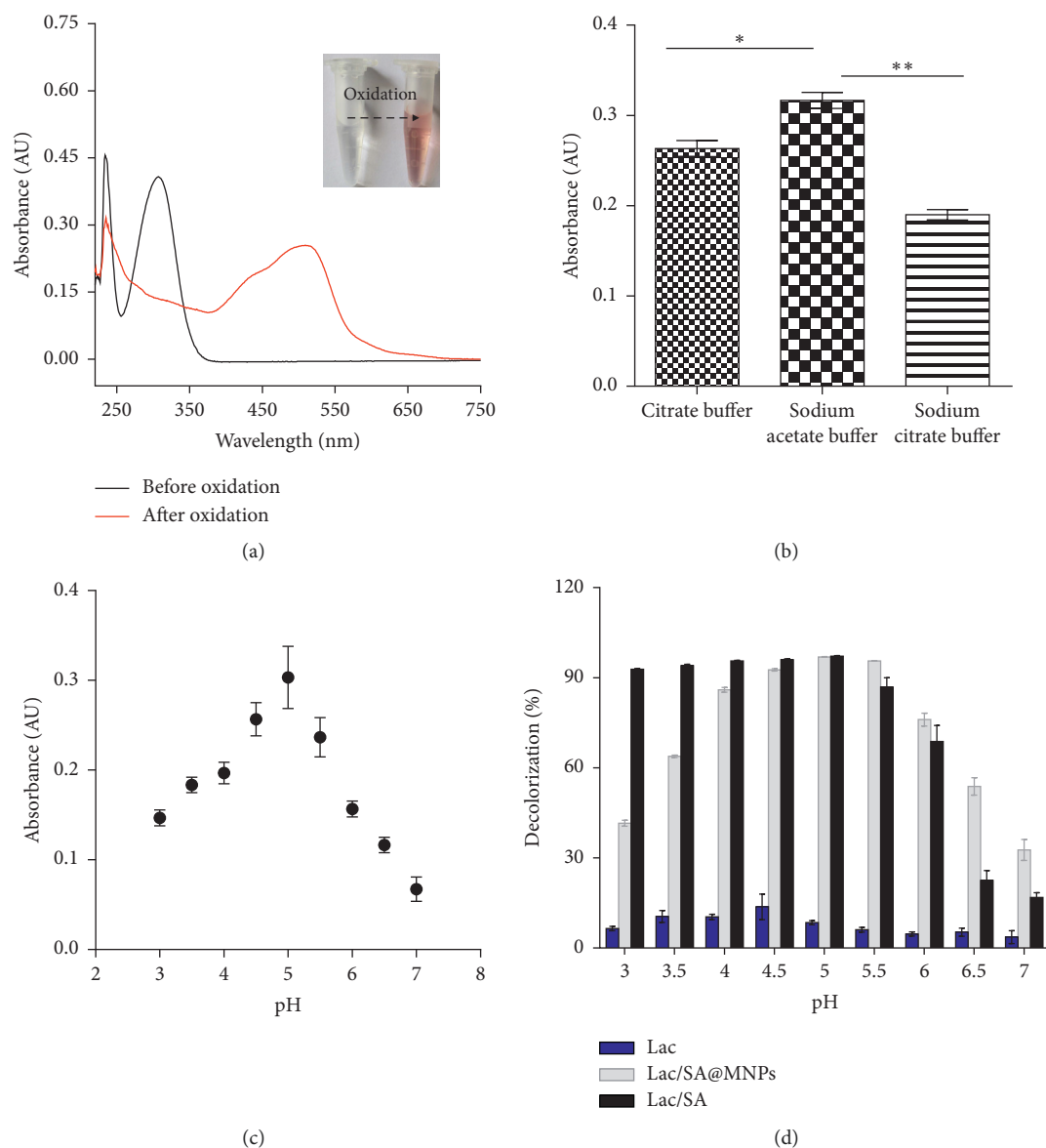


FIGURE 7: (a) UV-Vis spectra of SA before and after oxidation by Lac. (b) Effects of buffer type on SA oxidation by Lac. (c) Effects of pH on SA oxidation by Lac. (d) Effects of pH on dye decolorization by Lac, Lac/SA@MNPs, and Lac/SA.

As shown in Figure 9(b), the UV-Vis absorption spectrum of IC exhibits two characteristic absorption bands at 288 and 615 nm. The blue color of the solution decreased in intensity following treatment with the Lac/SA@MNP system, with the reaction mixture turning pale yellow after complete decolorization. Simultaneously, the absorbance peaks at 288 and 615 nm disappeared. These results indicated that destruction of the molecular structure of the dye was catalyzed by Lac in the presence of the SA@MNPs, resulting in complete decolorization of IC. According to the previous reports, the decomposition of chromophores and benzene rings removes the toxicity of dyes by preventing the formation of aromatic amines [28].

Although Lac mediators have been used in various applications, their high cost, especially for artificial mediators, has limited large-scale applications [29]. Moreover,

most mediators used in various applications are dissolved in the reaction medium. Thus, after use and abandonment, the potential toxicity of the mediators can cause environmental problems [30]. Considering the potential economic and environmental benefits, it is very important to recover and reuse mediators for large-scale applications of Lac/mediator systems in various fields [8, 10, 30, 31]. It has been reported that mediator immobilization is an effective way to achieve this goal, and the successful immobilization of several artificial on various materials has been reported. For example, a Lac redox mediator (ABTS) was immobilized on a macroporous cryogel by electron irradiation to assist the Lac-catalyzed degradation of bisphenol A [32]. In addition, ABTS had been successfully attached to silica nanoparticles and a mesoporous metal-organic framework, and the immobilized ABTS played a similar role to free ABTS in

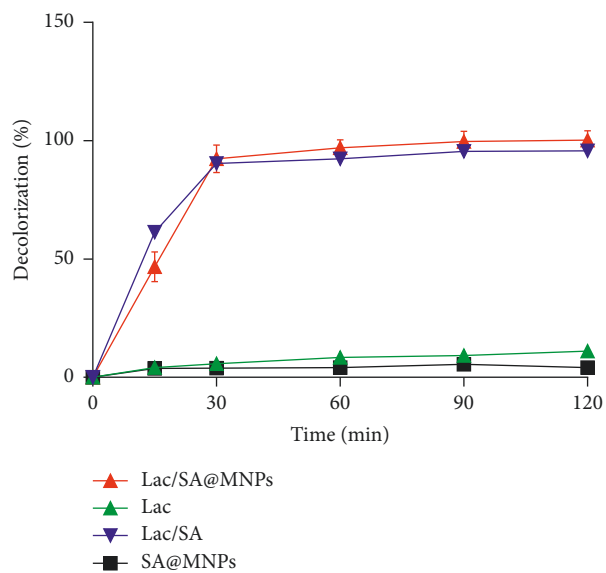
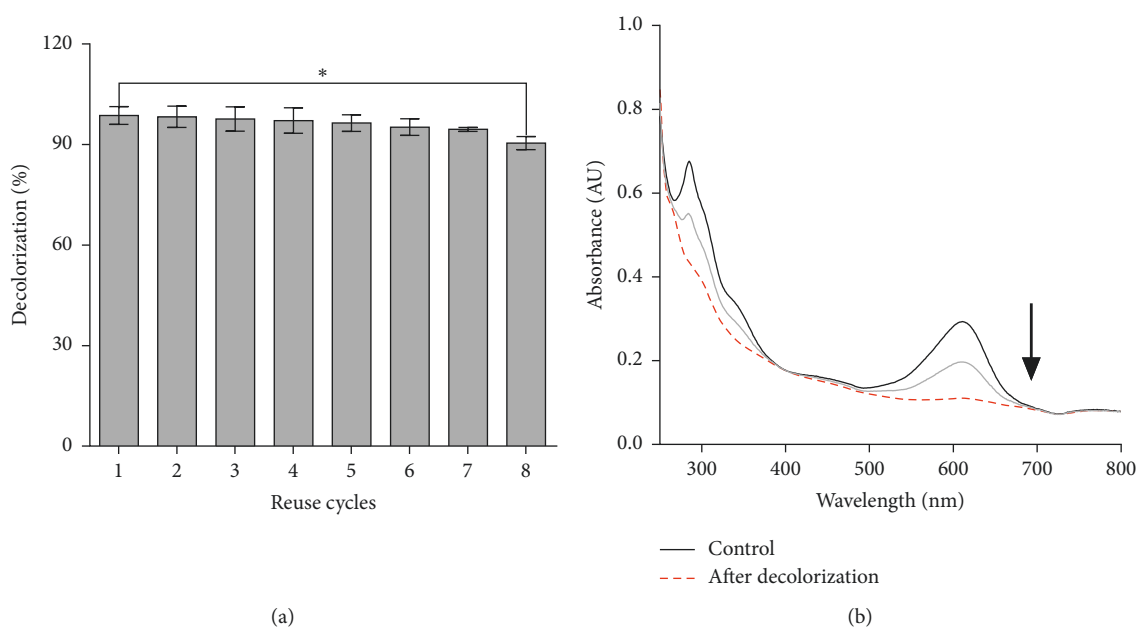
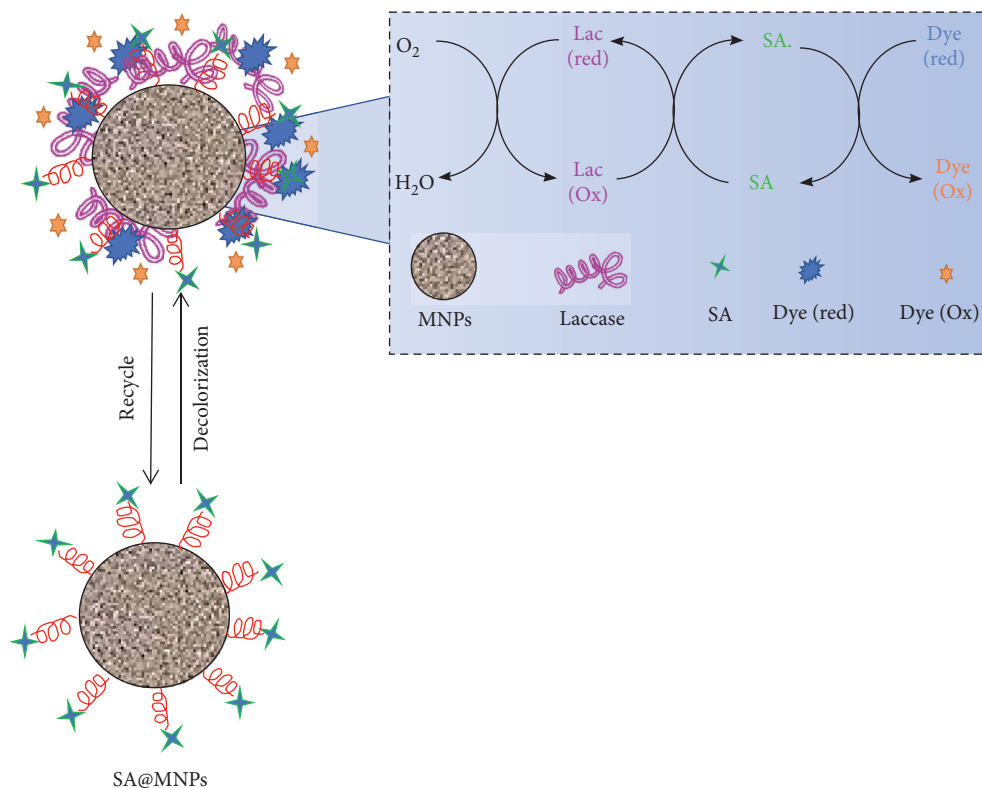


FIGURE 8: Dye decolorization by Lac/SA@MNPs, Lac/SA, SA@MNPs, and Lac alone as a function of time.



(c)

FIGURE 9: (a) Reusability of SA@MNPs over 8 successive cycles. (b) UV-Vis spectra of IC at various times during the enzymatic degradation process. (c) Photograph of the dye solutions before and after decolorization and the magnetic recovery of SA@MNPs.



SCHEME 2: Schematic illustration of the catalytic cycle of SA@MNPs.

mediating Lac-catalyzed dye decolorization [14, 15]. Moreover, polyethylene glycol was modified with TEMPO, and the resulting immobilized redox mediator exhibited reusability for Lac-catalyzed dye decolorization [26]. Furthermore, efficient catalytic performance and easy recoverability were achieved by co-immobilization of Lac and a mediator in the same matrix [33, 34]. In this work, the natural mediator SA was immobilized on magnetically separable MNPs to facilitate its recovery and reuse. As shown in Figure 9(c), the SA@MNPs could be efficiently separated from the reaction solution using a magnet after being applied as a decolorization mediator. This strategy provides two advantages. First, the easy recoverability of the SA@MNPs contributes to this system having lower running costs than systems with nonmagnetic immobilization matrices. Second, and more importantly, as SA is a natural compound that is environmentally friendly and nontoxic, this system avoids the environmental problems that may be associated with the use of artificial mediators.

However, there is an important limitation that should also be pointed out. In fact, a powdered form of SA@MNPs is too small to leak out easily from wastewater treatment systems. One solution to the problem is to entrap SA@MNPs and laccase together into polysaccharides like chitosan, pectin, and alginate, to form beads. Another solution to the problem is to co-immobilize SA@MNPs and laccase onto the membrane to form enzymatic membrane bioreactor. It has been reported that the degradation of phenolic and non-phenolic trace organic contaminants was significantly enhanced in enzymatic membrane bioreactor fabricated by

laccase and redox-mediator [35]. Thus, these methods will further contribute to the reusability of SA@MNPs. In addition, as a new system, there are some problems remain unresolved, one of which is the environmental safety of the usage of the nanoparticles.

3.5. Catalytic Cycle of SA@MNPs. Several authors have described the role of mediators in Lac/mediator catalytic systems [35, 36]. Previous reports have suggested that a hydrogen atom transfer oxidation mechanism can be used to understand the role of SA as a mediator in the Lac-catalyzed reaction [11]. The catalytic cycle of the SA@MNPs in Lac-catalyzed dye decolorization is shown in Scheme 2. First, SA covalently attached to the MNPs is oxidized by Lac to form highly reactive phenoxyl radicals (SA·). Subsequently, the phenoxyl radicals participate in nonenzymatic oxidation reactions with dye molecules cannot be efficiently oxidized by Lac alone. The phenoxyl radicals can be reduced to their original form by dye molecules, resulting in the simultaneous oxidation of the dye molecules to their intermediates, thus completing one catalytic cycle. After the dye is completely decolorized by Lac/SA@MNPs-catalyzed oxidation, the SA@MNPs are recovered and recycled. The redox mediators act as electron shuttles and provide an indirect oxidation step. The oxidized radical form of the SA is able to oxidize a wide range of substrates, including compounds with a high redox and/or nonphenolic compound. Previous research has reported that phenolic compounds related to lignin have shown their capability and efficiency to act as

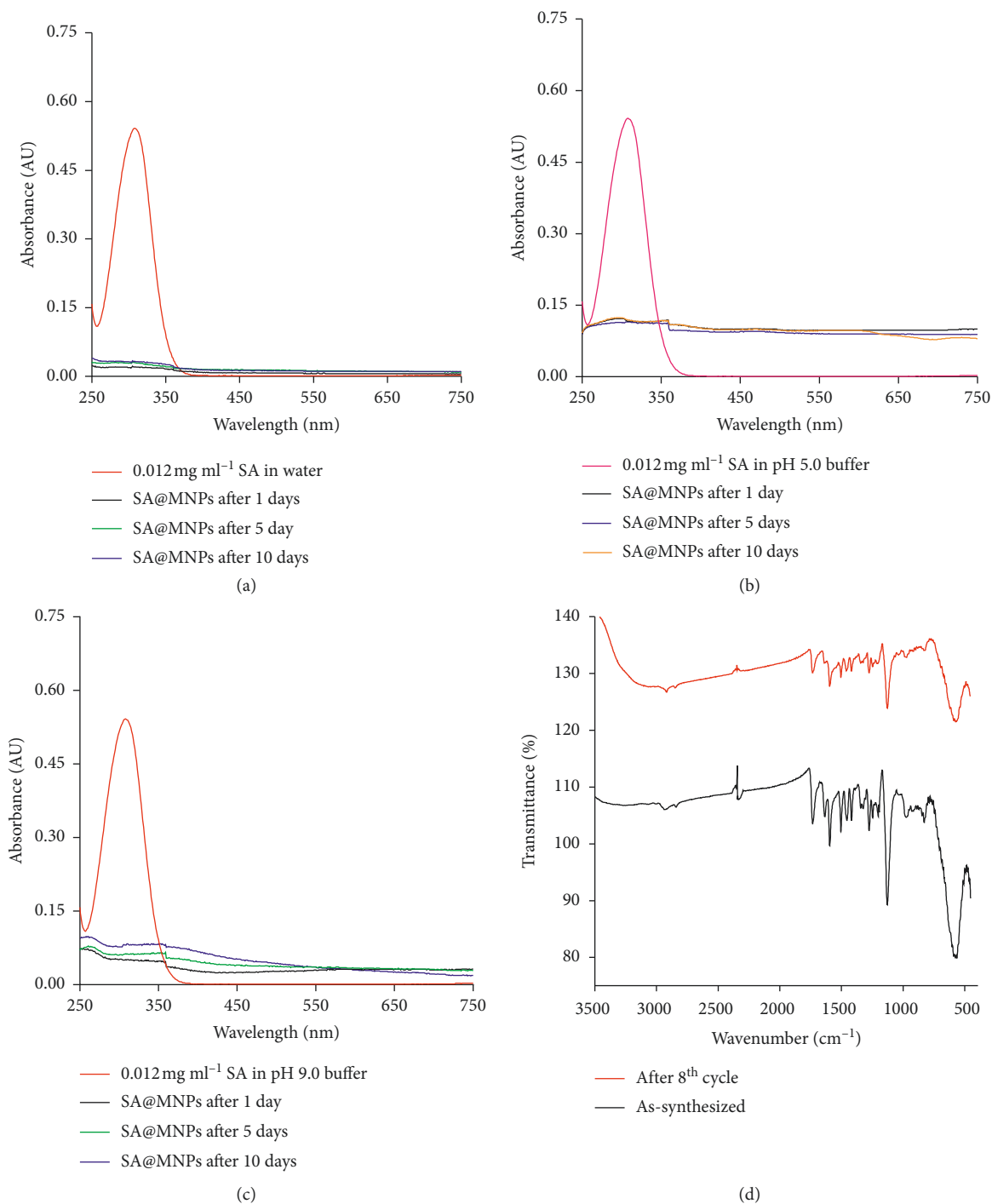


FIGURE 10: UV-Vis spectra of SA@MNPs dispersed in (a) water, (b) pH 5.0 buffer, and (c) pH 9.0 buffer for 1, 10, and 5 d (d) FT-IR spectra of the as-synthesized and recycled SA@MNPs samples.

natural Lac mediators [37]. Although ABTS and HBT are well-known artificial redox mediators for Lac, these mediators are not economically feasible. Furthermore, Lac stability and activity was decreased when incubated with artificial these redox mediators in the long run. Thus, natural mediators have been used due to their environmental friendliness, low-cost, and good biocompatibility to laccase [38].

3.6. Stability Analysis. Recovery and recycling of the mediator will only be efficient if the SA@MNPs are stable in various solutions. Thus, the storage stability of the SA@MNPs and the potential detachment of SA from the SA@MNPs should be assessed. The characteristic absorption band of unoxidized SA at 300 nm (Figure 7(a)) was used to estimate the concentration of SA in solution. As shown in Figures 10(a)–10(c), following the dispersion of the SA@

MNPs in water, pH 5.0 buffer, and pH 9.0 buffer, respectively, little SA was observed in the supernatant solution after 1, 5, and 10 d, implying that SA was not detached from the SA@MNPs via hydrolysis of the amide bond. These results confirmed that the SA@MNPs exhibited good stability in solution under different pH conditions. In addition, the characteristic FT-IR bands of the SA@MNPs after 8 catalytic cycles were compared with those of the as-prepared SA@MNPs, as shown in Figure 10(d). There were no obvious changes in the characteristic bands, which further confirmed that the structure of the SA@MNPs was maintained with negligible loss of SA. This stability may be attributed to the fact that SA was covalently attached to the MNPs rather than adsorbed on the surface.

4. Conclusion

In view of the high costs of synthetic mediators and their potential toxicities, the practical application of Lac/mediator systems on a large scale is severely limited. In this work, a natural mediator (SA) was covalently attached to amino-modified MNPs via amide bond formation. Similar to free SA, SA immobilized on the MNPs was shown to be an efficient mediator for Lac-catalyzed dye decolorization. Moreover, the structure of the SA@MNPs was maintained over 8 cycles and essentially no SA was released into the supernatant after storage in solution for 10 days, thus confirming the stability of the SA@MNPs. Furthermore, the SA@MNPs were magnetically separable, facilitating easy recovery and recycling. These results confirmed that SA@MNPs can improve the efficiency of mediator utilization and reduce both the costs and the secondary pollution associated with the use of synthetic mediators. Thus, this immobilized natural mediator shows potential for practical application in the treatment of dye wastewater.

Data Availability

The data used to support the findings of this study are available from the corresponding author upon request.

Conflicts of Interest

The authors declare that they have no competing financial interest.

Acknowledgments

This work was generously supported by the Youth Backbone Teacher Training Program (no. 2016GGJS-104) and by the Key Project of Science and Technology of the Henan Province (No. 192102310235).

References

- [1] P. Baldrian, "Fungal laccases— occurrence and properties," *Fems Microbiology Reviews*, vol. 30, no. 2, pp. 215–242, 2006.
- [2] A. Leonowicz, N. Cho, J. Luterek et al., "Fungal laccase: properties and activity on lignin," *Journal of Basic Microbiology*, vol. 41, no. 3–4, pp. 185–227, 2001.
- [3] O. V. Morozova, G. P. Shumakovich, S. V. Shleev, and Y. I. Yaropolov, "Laccase-mediator systems and their applications: a review," *Applied Biochemistry and Microbiology*, vol. 43, no. 5, pp. 523–535, 2007.
- [4] R. Bourbonnais and M. G. Paice, "Oxidation of non-phenolic substrates," *FEBS Letters*, vol. 267, no. 1, pp. 99–102, 1990.
- [5] M. Fabbrini, C. Galli, and P. Gentili, "Comparing the catalytic efficiency of some mediators of laccase," *Journal of Molecular Catalysis B: Enzymatic*, vol. 16, no. 5–6, pp. 231–240, 2002.
- [6] G. Cantarella, C. Galli, and P. Gentili, "Free radical versus electron-transfer routes of oxidation of hydrocarbons by laccase/mediator systems: catalytic or stoichiometric procedures," *Journal of Molecular Catalysis B: Enzymatic*, vol. 22, no. 3–4, pp. 135–144, 2003.
- [7] R. Hilgers, J.-P. Vincken, H. Gruppen, and M. A. Kabel, "Laccase/mediator systems: their reactivity toward phenolic lignin structures," *ACS Sustainable Chemistry & Engineering*, vol. 6, no. 2, pp. 2037–2046, 2018.
- [8] A. I. Cañas and S. Camarero, "Laccases and their natural mediators: biotechnological tools for sustainable eco-friendly processes," *Biotechnology Advances*, vol. 28, no. 6, pp. 694–705, 2010.
- [9] S. Riva, "Laccases: blue enzymes for green chemistry," *Trends in Biotechnology*, vol. 24, no. 5, pp. 219–226, 2006.
- [10] K. Murugesan, I.-H. Yang, Y.-M. Kim, J.-R. Jeon, and Y.-S. Chang, "Enhanced transformation of malachite green by laccase of *Ganoderma lucidum* in the presence of natural phenolic compounds," *Applied Microbiology and Biotechnology*, vol. 82, no. 2, pp. 341–350, 2009.
- [11] S. Camarero, A. I. Cañas, P. Nousiainen et al., "p-Hydroxycinnamic acids as natural mediators for laccase oxidation of recalcitrant compounds," *Environmental Science & Technology*, vol. 42, no. 17, pp. 6703–6709, 2008.
- [12] D. E. Dodor, M. Miyittah, and B. D. K. Ahiabor, "Immobilized laccase mediator-catalyzed oxidation of aqueous mixtures of polycyclic aromatic hydrocarbons," *Polycyclic Aromatic Compounds*, pp. 1–11, 2018.
- [13] T. Kenzom, P. Srivastava, and S. Mishra, "Structural insights into 2,2'-azino-bis(3-ethylbenzothiazoline-6-sulfonic acid) (ABTS)-Mediated degradation of reactive blue 21 by engineered *Cyathus bulleri* laccase and characterization of degradation products," *Applied and Environmental Microbiology*, vol. 80, no. 24, pp. 7484–7495, 2014.
- [14] Y. Liu, M. Yan, Y. Geng, and J. Huang, "ABTS-modified silica nanoparticles as laccase mediators for decolorization of indigo carmine dye," *Journal of Chemistry*, vol. 2015, Article ID 670194, 7 pages, 2015.
- [15] Y. Liu, Y. Geng, M. Yan, and J. Huang, "Stable ABTS immobilized in the MIL-100(Fe) metal-organic framework as an efficient mediator for laccase-catalyzed decolorization," *Molecules*, vol. 22, no. 6, p. 920, 2017.
- [16] S. Camarero, D. Ibarra, M. J. Martínez, and A. T. Martínez, "Lignin-derived compounds as efficient laccase mediators for decolorization of different types of recalcitrant dyes," *Applied and Environmental Microbiology*, vol. 71, no. 4, pp. 1775–1784, 2005.
- [17] S. Mohapatra, N. Pramanik, S. Mukherjee, S. K. Ghosh, and P. Pramanik, "A simple synthesis of amine-derivatised superparamagnetic iron oxide nanoparticles for bioapplications," *Journal of Materials Science*, vol. 42, pp. 7566–7574, 2007.
- [18] R. A. Frimpong and J. Z. Hilt, "Magnetic nanoparticles in biomedicine: synthesis, functionalization and applications," *Nanomedicine*, vol. 5, no. 9, pp. 1401–1414, 2010.

- [19] A.-H. Lu, E. L. Salabas, and F. Schüth, "Magnetic nanoparticles: synthesis, protection, functionalization, and application," *Angewandte Chemie International Edition*, vol. 46, no. 8, pp. 1222–1244, 2007.
- [20] M. Zhang, D. Cheng, X. He, L. Chen, and Y. Zhang, "Magnetic silica-coated sub-microspheres with immobilized metal ions for the selective removal of bovine hemoglobin from bovine blood," *Chemistry-An Asian Journal*, vol. 5, pp. 1332–1340, 2010.
- [21] J. Wang, S. Zheng, Y. Shao, J. Liu, Z. Xu, and D. Zhu, "Amino-functionalized $\text{Fe}_3\text{O}_4/\text{SiO}_2$ core-shell magnetic nanomaterial as a novel adsorbent for aqueous heavy metals removal," *Journal of Colloid and Interface Science*, vol. 349, no. 1, pp. 293–299, 2010.
- [22] M. B. Asif, F. I. Hai, B. R. Dhar et al., "Impact of simultaneous retention of micropollutants and laccase on micropollutant degradation in enzymatic membrane bioreactor," *Bioresource Technology*, vol. 267, pp. 473–480, 2018.
- [23] J. M. Bollag, K. L. Shuttleworth, and D. H. Anderson, "Laccase-mediated detoxification of phenolic compounds," *Applied and Environmental Microbiology*, vol. 54, no. 12, pp. 3086–3091, 1988.
- [24] A. I. Yaropolov, O. V. Skorobogat'ko, S. S. Vartanov, and S. D. Varfolomeyev, "Laccase," *Applied Biochemistry and Biotechnology*, vol. 49, no. 3, pp. 257–280, 1994.
- [25] A. Rekuć, J. Bryjak, K. Szymańska, and A. B. Jarzebski, "Very stable silica-gel-bound laccase biocatalysts for the selective oxidation in continuous systems," *Bioresource Technology*, vol. 101, no. 7, pp. 2076–2083, 2010.
- [26] L. Mendoza, M. Jonstrup, R. Hatti-Kaul, and B. Mattiasson, "Azo dye decolorization by a laccase/mediator system in a membrane reactor: enzyme and mediator reusability," *Enzyme and Microbial Technology*, vol. 49, no. 5, pp. 478–484, 2011.
- [27] Y. Liu, M. Yan, Y. Geng, and J. Huang, "Laccase immobilization on Poly(p-Phenylenediamine)/ Fe_3O_4 nanocomposite for reactive blue 19 dye removal," *Applied Sciences*, vol. 6, no. 8, pp. 232–239, 2016.
- [28] S. Akhtar, A. Khan, and Q. Husain, "Partially purified bitter gourd () peroxidase catalyzed decolorization of textile and other industrially important dyes," *Bioresource Technology*, vol. 96, no. 16, pp. 1804–1811, 2005.
- [29] R. Khlifi, L. Belbahri, and S. Woodward, "Decolourization and detoxification of textile industry wastewater by the laccase-mediator system," *Journal of Hazardous Materials*, vol. 175, no. 1–3, pp. 802–808, 2009.
- [30] M. Chhabra, S. Mishra, and T. R. Sreekrishnan, "Laccase/mediator assisted degradation of triarylmethane dyes in a continuous membrane reactor," *Journal of Biotechnology*, vol. 143, no. 1, pp. 69–78, 2009.
- [31] K. Vijayaraghavan, S. W. Won, and Y.-S. Yun, "Treatment of complex Remazol dye effluent using sawdust- and coal-based activated carbons," *Journal of Hazardous Materials*, vol. 167, no. 1–3, pp. 790–796, 2009.
- [32] E. Jahangiri, S. Reichelt, I. Thomas, K. Hausmann, D. Schlosser, and A. Schulze, "Electron beam-induced immobilization of laccase on porous supports for waste water treatment applications," *Molecules*, vol. 19, no. 8, pp. 11860–11882, 2014.
- [33] G. Yaohua, X. Ping, J. Feng, and S. Keren, "Co-immobilization of laccase and ABTS onto novel dual-functionalized cellulose beads for highly improved biodegradation of indole," *Journal of Hazardous Materials*, vol. 365, pp. 118–124, 2019.
- [34] J. Huang, Y. Yang, Y. Wang, M. Zhang, and Y. Liu, "Immobilization of a laccase/2,2'-azino-bis-(3-ethylbenzothiazoline)-6-sulfonic acid system to layered double hydroxide/alginate biohybrid beads for biodegradation of malachite green dye," *BioMed Research International*, vol. 2018, pp. 1–15, 2018.
- [35] A. Wells, M. Teria, and T. Eve, "Green oxidations with laccase-mediator systems," *Biochemical Society Transactions*, vol. 34, no. 2, pp. 304–308, 2006.
- [36] M. Asif, F. Hai, J. Kang et al., "Degradation of trace organic contaminants by a membrane distillation-enzymatic bioreactor," *Applied Sciences*, vol. 7, no. 9, p. 879, 2017.
- [37] A. Blázquez, J. Rodríguez, V. Brissos et al., "Decolorization and detoxification of textile dyes using a versatile, streptomycetes, laccase-natural mediator system," *Saudi Journal of Biological Sciences*, vol. 26, no. 5, pp. 913–920, 2018.
- [38] P. Mani, V. T. F. Kumar, T. Keshavarz, T. S. Chandra, and G. Kyazze, "The role of natural laccase redox mediators in simultaneous dye decolorization and power production in microbial fuel cells," *Energies*, vol. 11, p. 345, 2018.

Research Article

Adsorption of COD in Coking Wastewater on Nitric Acid-Modified Blue Coke Activated Carbon

Xu Jiang ^{1,2}, Xinzhe Lan,¹ Yonghui Song,¹ and Xiangdong Xing ¹

¹School of Metallurgical Engineering, Shaanxi Province Metallurgical Engineering and Technology Research Centre, Xi'an University of Architecture and Technology, Xi'an 710055, China

²Research Institute of Energy and Chemical Industry, Xianyang Vocational Technical College, Xianyang 712000, China

Correspondence should be addressed to Xiangdong Xing; xaxingxiangdong@163.com

Received 25 September 2019; Accepted 18 November 2019; Published 6 December 2019

Guest Editor: Hassan M. A. Hassan

Copyright © 2019 Xu Jiang et al. This is an open access article distributed under the Creative Commons Attribution License, which permits unrestricted use, distribution, and reproduction in any medium, provided the original work is properly cited.

The blue coke activated carbon (BAC) modified by nitric acid at different concentrations was used as an adsorbent to remove COD from coking wastewater. Characterization of BAC was performed using N₂ adsorption/desorption techniques, scanning electron microscope (SEM), Fourier transform infrared spectroscopy (FTIR), and Boehm titration. The results showed the Brunner–Emmet–Teller (BET) specific surface area and iodine value of BAC became higher after modification, and the adsorption capacity of BAC for coking wastewater was effectively improved with nitric acid modification. The optimal nitric acid concentration for modification was 3 mol/L (BAC-N3), which had more acid functional group contents than unmodified. The chemical oxygen demand (COD) removal rate was to reach 77.05% when 4 g BAC-N3 was added into 50 mL coking wastewater in 120 min with a shaking speed of 100 rpm at 25°C. Langmuir model could better describe equilibrium adsorption data by BAC-N3, and the kinetic study showed that the adsorption process was best fitted by the pseudo-second-order kinetic model.

1. Introduction

Blue coke consists of solid carbon materials and is prepared by medium- and low-temperature dry distillation with Jurassic nonstick coal and slightly caked coal as raw materials, which are widespread in the Shaan-Gan-Ning-Meng-Jin Region of northwestern China [1]. In these areas, blue coke plays an important role in the coal chemical industry because of its high fixed carbon content, specific resistance, chemical activity, and low ash content, sulfur content, phosphorus content, and volatility [2].

Nowadays, carbon solid wastes are used as raw materials for the preparation of activated carbon (AC) in addition to traditional wood, fruit shell, and coal [3–5]. Blue coke powder, a by-product of blue coke production, transportation, and storage, has a grain size of less than 6 mm and has been associated with environmental challenges [6]. However, blue coke powder offers potential as a high-quality and cheap raw material for AC production because of its previously mentioned characteristics. A type of BAC was

prepared from blue coke powder using KOH activation by Song et al. [2], yielding a product with a 733.48 mg/g iodine adsorption value at 800°C. BAC with a BET specific surface area of 738.75 m²/g was prepared by steam activation at 900°C [6]. Mesoporous BAC, with a BET specific surface area reaching 513.62 m²/g, was prepared by Tian et al. through KOH activation within microwave [7]. However, the above BAC suffers from drawbacks of pore structure irregularity, low surface area, disordered pore size distribution, and limited surface chemical properties. For obtaining quality AC according to different purposes, physical and chemical modifications were employed to adjust the pore structure and improved the surface chemical properties of AC, which have important significance for the development of AC industry.

Acid oxidation modification is one of the common methods that can dredge the AC-blocked pores, improve pore structure, and increase the number of oxygen-containing functional groups on the surface and enhance their hydrophilicity. Many scholars have studied AC modification

by using nitric acid, which is a commonly used modifier [8]. Soltani et al. [9] modified cigarette filter AC by using nitric acid under different concentrations and contact time, and the AC had more mesopores and had a 57.8% increase in the surface acidity compared to the nonmodified AC. Tong et al. [10] found that modification by nitric acid can increase the number of oxygen-containing functional groups and nitrogen-containing functional groups in the AC surface and improve the adsorption effect on mercury. Zhang et al. [11] studied the adsorption of benzothiophene in simulated gasoline by nitric acid-modified AC and found a 33.7% increase in absorption capacity after modification. Babel et al. [12] investigated the HNO₃- and H₂SO₄-modified AC's ability to remove Cr(VI) from synthetic wastewater, and they found that the HNO₃-modified AC exhibits an improved adsorption effect because the number of oxygen-containing functional groups was increased by the modification, which caused electrostatic attraction, hydrophobic interaction, and chemical bonding.

Coking wastewater, which is produced from coking, gas purification, and chemical product recovery, is a highly concentrated, highly polluting, and highly toxic industrial organic wastewater. Coking wastewater is harm to the environment due to its high concentration of NH₄⁺-N, phenols, poison, and its difficult degradation by using organisms [13]. Moreover, AC is widely used to treat coking wastewater because of its simple operation, strong adsorption, good stability, and convenient regeneration. Many scholars have done a lot of research studies on physical structure and chemical property improvements of AC and enhancement of adsorption effect, and these studies have been made a lot of achievements. To date, however, few studies have directly addressed modification of BAC which was prepared by blue coke powder.

Although nitric acid is one of the most common AC modifiers, few studies have focused on the BAC which was prepared by disused blue coke powder. In this paper, BAC was modified using nitric acid at different concentrations. We analyzed the effect of the modification on pore structure and surface chemical properties. Then, the optimal technological process and adsorption thermodynamics and kinetics of COD from coking wastewater onto BAC were studied for the modified AC technology and reasonable discharge of coking wastewater.

2. Materials and Methods

2.1. Materials. The blue coke powder was provided by a blue coke enterprise in Shaanxi Province, China. The industrial and elemental analyses of which are shown in Table 1. As shown in Table 1, the blue coke powder has more ash content, which is significantly higher than other raw materials of AC.

The experimental coking wastewater was obtained from a coal chemical enterprise in Shaanxi Province, and the main index of which is presented in Table 2.

The reagents used in the experiment were as follows: HNO₃, AgSO₄, Na₂S₂O₃, K₂Cr₂O₇, HCl, H₂SO₄, (NH₄)₂Fe(SO₄)₂·6H₂O, I₂, KI, starch indicator, and ferrous metal indicator, all of which were analytically pure.

TABLE 1: Proximate and elemental analyses of blue coke powder.

Blue coke powder	Proximate analysis				Elemental analysis				
	M_t	A_{ad}	V_{ad}	FC_{ad}	C_{ad}	O_{ad}	H_{ad}	N_{ad}	$S_{t,ad}$
	2.15	16.77	12.07	69.01	72.88	0.3	1.06	0.88	0.6

Note: M_t is the total moisture content, A_{ad} is the ash content as air dry basis, V_{ad} is the volatile content as air dry basis, FC_{ad} is the fixed carbon content as air dry basis, C_{ad} is the carbon element content as air dry basis, O_{ad} is the oxygen element content as air dry basis, H_{ad} is the hydrogen element content as air dry basis, N_{ad} is the nitrogen element content as air dry basis, and $S_{t,ad}$ is the sulphur element content as air dry basis.

TABLE 2: Main index of coking wastewater.

	COD (mg/L)	NH ₄ ⁺ -N (mg/g)	Phenol (mg/g)	pH
Coking wastewater	3 604	303.15	911.26	8.74

2.2. Methods

2.2.1. Preparation of BAC. BAC was produced via steam activation at 900°C, which is based on a preliminary study [7], and yielded a product termed BAC-0.

2.2.2. Modification of BAC. BAC was modified by nitric acid as follows: under the room temperature, 10 g of BAC-0 was impregnated with 50 mL of HNO₃ (the concentrations were 1 mol/L, 2 mol/L, 3 mol/L, and 4 mol/L, respectively) in a joined conical bottle that was placed in a rotating water bath oscillator (HY-8) for 4 h at a shaking speed of 100 rpm. Afterward, the mixture was filtered and the solid was washed with sufficient distilled water until the pH of the solution closed to neutral. The resulting materials were termed as BAC-N1, BAC-N2, BAC-N3, and BAC-N4, respectively.

2.2.3. Adsorption of Coking Wastewater

Effect of Modification Conditions. 5 g of BACs was dispersed in a conical bottle containing 50 mL of coking wastewater, respectively. The mixture was then agitated at 25°C in a rotating water bath oscillator at 100 rpm for 4 h for equilibrium. The COD removal rate could be calculated using the following equation:

$$\text{COD removal rate} = \frac{c_o - c_e}{c_o} \times 100\%, \quad (1)$$

$$q_e = \frac{(c_o - c_e)V}{m}, \quad (2)$$

where q_e is the equilibrium adsorption capacity (mg/g), c_o is the COD of the raw coking wastewater (mg/L), c_e is the COD of coking wastewater after adsorption equilibrium (mg/L), m is the addition amount of adsorbent (g), and V is the volume of coking wastewater (L).

Effect of Addition Amount and Isothermal Adsorption Experiment. A predetermined amount of adsorbent was

dispersed in a conical bottle containing 50 mL of coking wastewater. The mixture was agitated at 25°C in a rotating water bath oscillator at 100 rpm for 4 h. The COD removal rate and equilibrium adsorption capacity were calculated using equations (1) and (2), respectively. The Langmuir and Freundlich equations were used to fit the isothermal adsorption process.

Influence of Shaking Speed and Adsorption Kinetics Experiment. The optimum addition amount of optimal adsorbents was dispersed in a conical bottle containing 50 mL of coking wastewater. The mixture was agitated in a rotating water bath oscillator at 25°C. The shaking speed was set at 0 rpm, 100 rpm, and 200 rpm, and sampling was performed at 10 min, 30 min, 60 min, 90 min, 120 min, 150 min, and 180 min. The q_t and COD removal rate were calculated using equations (3) and (1), respectively:

$$q_t = \frac{(c_0 - c_t)V}{m}, \quad (3)$$

where q_t is the adsorption capacity of time t (mg/g) and c_t is the COD of coking wastewater at time t (mg/L).

2.3. Characterization of Prepared BAC and Coking Wastewater. The COD was determined by GB 11914-1989 (China). Iodine number was determined by GB/T 7702.7-2008 (China). The yield (Y) was estimated from the mass ratio of modified BAC to unmodified BAC. The BET specific surface area and pore structure of the BAC were obtained using a fully automatic physical adsorption apparatus (ASAP2420) by a nitrogen adsorption/desorption isotherm that was determined at 77.35 K. The morphology of the BACs was examined by scanning electron microscopy (JSM-6700F). The functional groups on the surface of the BAC were identified by Fourier transform infrared spectroscopy.

In general, although the kind and relative content of surface functional group of BAC can be analysed by FTIR, the actual content cannot be obtained. Well, the Boehm titration can solve this problem perfectly. According to the definition of the Boehm titration, the alkaline solutions with different basicity can only react with different acidity functional group on the surface of BAC. For example, NaHCO_3 only reacts with carboxyl group, Na_2CO_3 can react with carboxyl and lactone groups, and NaOH can react with carboxyl group, lactone group, and phenolic hydroxyl group. Similarly, HCl can neutralize the basic functional group on the surface of BAC.

The determination method is as follows: 1.00 g of BAC was impregnated with in four 100 mL conical bottles, respectively, which impregnated in 50 mL of HCl , NaOH , Na_2CO_3 , and NaHCO_3 solution, respectively (the concentration is 0.05 mol/L). These were placed in a rotating water bath oscillator for 48 h at 25°C with a shaking speed of 100 rpm. Afterward, the solution was filtered and stored in sealed condition. 10 mL of HCl filtrate was added into a conical bottle which was titrated with 0.05 mol/L NaOH solution. 10 mL of NaOH , Na_2CO_3 , and NaHCO_3 filtrate was added into the conical bottle, respectively, which were

titrated with 0.05 mol/L HCl solution. The consumption of HCl and NaOH solution can be calculated.

The specific calculation method of functional groups content is as follows:

- (i) The content of basic functional group (n_{basicity})

The HCl neutralized the basic functional group on the surface of BAC, and the consumption of HCl ($n_{\text{HCl,consume}}$) can be calculated by NaOH titration, which equals the content of basic functional group:

$$n_{\text{basicity}} = n_{\text{HCl,consume}} \quad (4)$$

- (ii) The content of carboxyl group (n_{ROOH})

The NaHCO_3 neutralized the carboxyl group on the surface of BAC, and the consumption of NaHCO_3 ($n_{\text{NaHCO}_3,consume}$) can be calculated by HCl titration, which equals the content of carboxyl group:

$$n_{\text{ROOH}} = n_{\text{NaHCO}_3,consume} \quad (5)$$

- (iii) The content of lactone group ($n_{\text{RCOOCOR'}}$)

The Na_2CO_3 neutralized with carboxyl and lactone groups on the surface of BAC, the consumption of Na_2CO_3 ($n_{\text{Na}_2\text{CO}_3,consume}$) can be calculated by HCl titration, and the content of lactone group is calculated as follows:

$$n_{\text{RCOOCOR'}} = n_{\text{Na}_2\text{CO}_3,consume} - n_{\text{NaHCO}_3,consume} \quad (6)$$

- (iv) The content of phenolic hydroxyl group (n_{AROH})

The NaOH neutralized with carboxyl group, lactone group, and phenolic hydroxyl group on the surface of BAC, the consumption of NaOH ($n_{\text{NaOH,consume}}$) can be calculated by HCl titration, and the content of phenolic hydroxyl group is calculated as follows:

$$n_{\text{AROH}} = n_{\text{NaOH,consume}} - n_{\text{Na}_2\text{CO}_3,consume} \quad (7)$$

- (v) The content of acidity functional group (n_{acidity})

The content of acidity functional group equals the consumption of NaOH solution ($n_{\text{NaOH,consume}}$), and it is also equal to the sum of n_{acidity} , n_{AROH} , $n_{\text{RCOOCOR'}}$, and n_{ROOH} .

$$n_{\text{Acidity}} = n_{\text{NaOH,consume}} = n_{\text{AROH}} + n_{\text{RCOOCOR'}} + n_{\text{ROOH}} \quad (8)$$

3. Results and Discussion

3.1. Adsorbent Characterization

3.1.1. Effect of Pore Structure. The pore structure parameters, iodine value yield, and ash content of BACs are shown in Table 3. The iodine value and BET specific surface area of BAC after modification were higher than those of unmodified, and the value increased with concentration rising from 1 mol/L to 3 mol/L. This finding was partly because the blue coke powder, which was the raw material of BAC,

TABLE 3: Pore structure parameters, iodine value yield, and ash content of BACs.

Sample	S_{BET} ($\text{m}^2 \cdot \text{g}^{-1}$)	S_{micro} ($\text{m}^2 \cdot \text{g}^{-1}$)	V_{total} ($\text{cm}^3 \cdot \text{g}^{-1}$)	V_{micro} ($\text{cm}^3 \cdot \text{g}^{-1}$)	$V_{\text{micro}}/V_{\text{total}}$ (%)	d_{ave} (nm)	Iodine value ($\text{mg} \cdot \text{g}^{-1}$)	Y (%)	A_{ad}
BAC-0	641.84	469.17	0.3720	0.2011	54.06	2.318	738.75	–	16.64
BAC-N1	693.59	435.14	0.3427	0.2020	58.94	2.008	776.14	87.23	2.16
BAC-N2	739.14	483.69	0.3744	0.2209	59.00	2.026	789.99	85.36	1.93
BAC-N3	801.51	519.38	0.3977	0.2374	59.69	1.985	828.17	82.41	1.61
BAC-N4	689.13	448.47	0.3460	0.2077	60.03	1.976	751.70	78.19	1.57

Note: S_{BET} is the BET specific surface area, S_{micro} is the microporous specific surface area, V_{total} is the total pore volume, V_{micro} is the microporous pore volume, $V_{\text{micro}}/V_{\text{total}}$ is the micropore ratio, and d_{ave} is the average pore size.

exhibited significantly more ashes than other raw materials of AC. Thus, a large number of ashes remained on the BAC will block the pores, nitric acid can dissolve them. This function is called hole-throughing. This process was further aggravated with the increase in concentration. As seen from Table 3, the ash content of BACs after nitric acid modification reduces obviously. Meanwhile, the carbon activity sites in the surface of BAC exhibited high affinity, and these activity sites reacted with nitric acid molecules, which is a strong oxidizer. Thus, a small amount of carbon on the surface has been dissolved and the pore surface was etched, more micropore structures were formed, and this process is called hole-making function. The higher the nitric acid concentration, the more the microporosity, and the microporous specific surface area and microporous pore volume of BAC were then increased. This finding indicated that the yield of BAC decreases slightly with the increase in concentration, which proved that as nitric acid reacts with BAC, the pore structure was improved.

However, the BET specific surface area was reduced from $801.51 \text{ m}^2 \cdot \text{g}^{-1}$ to $689.13 \text{ m}^2 \cdot \text{g}^{-1}$ and the total pore volume was reduced from $0.3977 \text{ cm}^3 \cdot \text{g}^{-1}$ to $0.3460 \text{ cm}^3 \cdot \text{g}^{-1}$, when the concentration reached 4 mol/L , and the microporous specific surface area, microporous pore volume, and iodine value decreased as well. This is probably because nitric acid oxidation enhanced at this time, the BAC corrosion was serious, and the skeleton of some micropores was damaged, which resulted in significant pore wall thinning, and the additional mesopores and macropores were formed from the collapse of micropores, and the hole-enlargement function took place and became dominant. Furthermore, the collapsed carbon in the BAC and the oxygen-containing functional groups produced by nitric acid oxidation would plug the pores [14], and these were caused by the decline of the pore structure parameters and the iodine adsorption value also. Similar conclusions were obtained by Gil [15], who exhibited a significantly increasing trend in the porosity and the BET specific surface area after acid oxidation.

3.1.2. Surface Morphology of BACs. SEM was used to observe the surface physical morphology of the BACs. The SEM images of the BAC that was modified at different concentrations are shown in Figure 1.

As shown in Figure 1(a), there are many circular pores with different apertures in the material surface, which were formed into a honeycomb cavernous structure [16]. Figure 1 also shows that the BAC modified by nitric acid has more honeycomb-like shape and rough surface than unmodified, and the pore of BAC is nearly ellipse. The surface morphology of the material was different with varied nitric acid concentration. The etching of nitric acid mainly develops from the surface to the interior, and the higher the nitric acid concentration is, the more the activity effect occurs on material etching. Thus, the pore quantity of BAC increased, and the layered structure and honeycomb pore on the local area of the material surface became evident as the concentration increased. When the nitric acid concentration increased to 4 mol/L , the nitric acid oxidation was intense and the etching actions aggravated. Figure 1(e) illustrates that the number of micropores in BAC-N4 is markedly reduced, large pores rose, and the pore structure on the surface of BAC is irregular after modification. However, the overmodification led to a large number of pores of big- and medium-size collapse inside the BAC-N4 while some pores were blocked, reducing the BET specific surface area of BAC-N4. This result was consistent with that presented in Table 3.

3.1.3. Effect of Surface Chemical Properties. In general, besides the pore structure, the surface chemical properties of BAC will be changed after nitric acid modification. The FTIR spectra of BAC-0 and BAC-N3 are shown in Figure 2.

Figure 2 illustrates that BAC-0 and BAC-N3 have similar changes in the FTIR spectra. The absorption bands at $3250\text{--}3650 \text{ cm}^{-1}$ were due to the O–H stretching vibration of hydroxyl and carboxyl groups or due to the adsorbed water molecules during BAC steam activation preparation. The peak strength of BAC-N3 was larger than that of BAC-0, showing that the BAC-N3 exhibited additional oxygen-containing groups, such as hydroxyl and carboxyl. Correlated bands were centered at $1570\text{--}1700 \text{ cm}^{-1}$, which could be attributed to the stretching of C=O and/or C=C on carboxyl, lipophilic, and unsaturated hydrocarbons in the BAC surface. The peak strength increased after modification, proving that additional carboxyl groups and their derivatized groups were present in the inner part and surface of the BAC-N3. The bands at $1000\text{--}1250 \text{ cm}^{-1}$ were attributed to

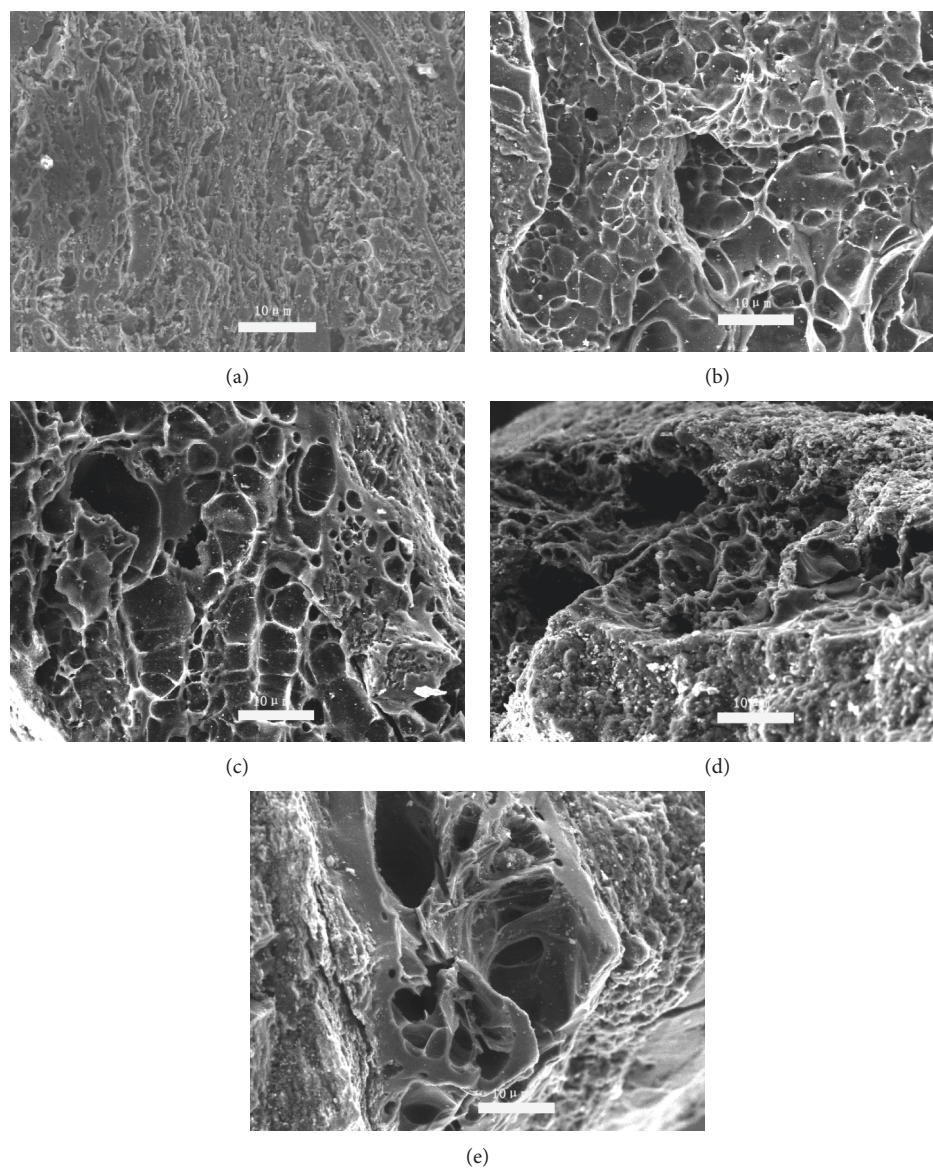


FIGURE 1: SEM photographs of BACs: (a) BAC-0, (b) BAC-N1, (c) BAC-N2, (d) BAC-N3, and (e) BAC-N4.

C–O stretching vibrations, which resulted from ether linkage. However, the peak strength decreased after modification, possibly because ether linkage oxidation was continuous during nitric acid oxygenation [17]. In conclusion, the content of oxygen-containing groups evidently increased after modification.

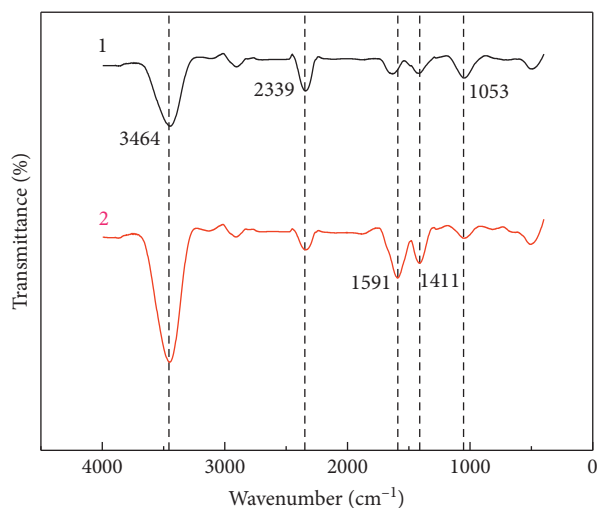
The content of carboxyl, phenolic hydroxyl, total acid, and total basic groups on the surface of BACs can be analysed by the Boehm titration, and the results of the titration experiment are listed in Table 4. As seen from Table 4, with the increase of nitric acid concentration, the acid functional group content in the surface of BAC increased markedly, but the basicity dropped, which is consistent with the FTIR results. The carbon atom on the verge of BAC exhibited increased activity and combined with additional oxygen atoms via nitric acid oxidation, allowing additional oxygen functional group to form [18]. El-Hendawy et al. [19] found that HNO_3 treatment gave rise to a greater increase in

carboxylic acid, lactone, carbonyl, ethers, phenols, and hydroxyl groups in corncob-based activated carbon, which had the increase of surface acidity. The adsorption capacity of Pb^{2+} from aqueous solution was more than 3 times higher than unmodified.

3.2. Effect of Modification Treatments on Adsorption

3.2.1. *Effect of Modification Conditions.* The effect of modification conditions on the COD removal rate is shown in Figure 3.

Figure 3 shows that nitric acid-modified BAC exhibits better adsorption performance than unmodified. As nitric acid concentration increased, the COD removal rate initially increased and then decreased. BAC-N3 exhibited the best adsorption efficiency, and the COD removal rate was 78.70%, which was higher than the unmodified BAC by



1 BAC-0
2 BAC-N3

FIGURE 2: FTIR of BAC-0 (1) and BAC-N3 (2).

TABLE 4: Content of oxygen functional groups on the surface of BACs.

Sample	Carboxyl (mmol·g ⁻¹)	Phenolic hydroxyl (mmol·g ⁻¹)	Acidity (mmol·g ⁻¹)	Basicity (mmol·g ⁻¹)
BAC-0	0.1052	0.0585	0.1784	0.5875
BAC-N1	0.6095	0.0676	0.6917	0.2001
BAC-N2	0.6945	0.0607	0.7571	0.1792
BAC-N3	0.7032	0.0540	0.8589	0.1413
BAC-N4	0.7243	0.0674	0.8842	0.0986

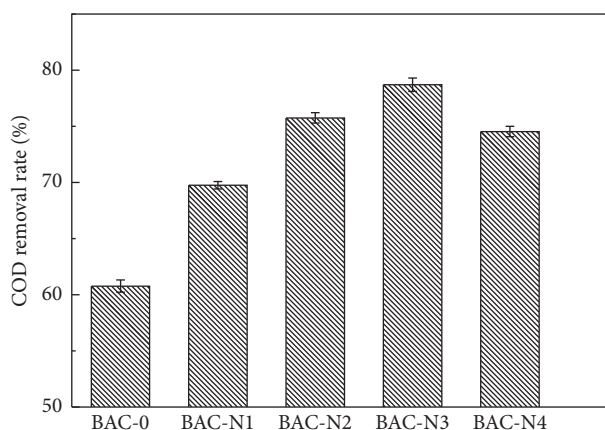


FIGURE 3: Effects of modification condition of BAC on the COD removal rate (the error bars indicate standard deviation of the mean of three sets of data).

22.78%. This is because the modified BAC exhibited higher specific surface area and pore volume. The highest value of COD obtained in BAC-N3 indicates the best adsorption effect. Moreover, increase in the content of oxygen-containing groups enhanced the affinity on polar organic compounds, which positively affected adsorption [20]. Fan et al. [21] showed that the AC significantly affects the adsorption of organic pollutants not only because of the increased contents of carboxyl, phenol hydroxyl, and lactone

groups on the AC surface but also the improvement in the surface hydrophobicity and the reduced zero point charge in the surface of AC. Tong et al. [10] suggested that oxygen-containing functional groups on the surface of AC are probably active adsorption sites. The increase in oxygen-containing functional groups may indicate the increase in active adsorption sites, which contributes to the enhancement of adsorption effect. In summary, the effect of nitric acid oxidation on the pore structure and surface chemical properties of the BAC improved the treatment efficiency of coking wastewater. Based on the experimental results, the selected nitric acid concentration was 3 mol/L.

3.2.2. Effect of Addition Amount and Adsorption Isotherm.

The effect of the BAC-N3 addition amount on the COD removal rate is shown in Figure 4. As seen in Figure 4, the COD removal rate increased firstly and then became stable with the increasing amount of BAC-N3, and the process underwent the following three stages. When the addition of BAC-N3 increased from 0.5 g to 2 g per 50 mL of wastewater, the COD removal rate increased from 29.58% to 65.76%, which is the rapid increase stage. This is because the adsorption of COD mainly depends on the number of unoccupied adsorption sites on the surface of adsorbent; the greater the amount of BAC-N3 added, the more the unoccupied adsorption sites were present. In this stage, the pollutants easily adsorbed in coking wastewater were

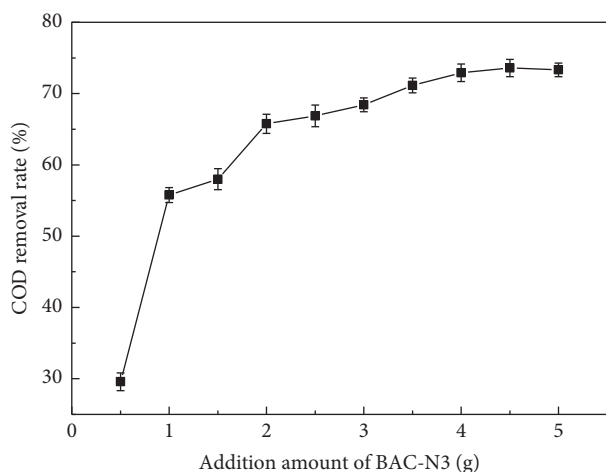


FIGURE 4: Effects of addition amount on the COD removal rate (the error bars indicate standard deviation of the mean of three sets of data).

rapidly attached to the surface of BAC-N3. When BAC-N3 has been increased to 4 g, the increasing speed of the COD removal rate slowed down, which is the increasing slowed down stage. When adsorbent continues to rise, the COD removal rate almost does not increase, which is the adsorption stabilization stage. Although the active sites further increased with the addition of BAC-N3, the concentration of organic matter between adsorbents and adsorbate closes to accordant, which caused the decreased concentration gradient and diffuse motivation [22], and the growth in COD removal rate slowed down or remained stable. After comprehensive analysis of adsorption effect and cost factor, it can be concluded that the optimal amount of BAC-N3 is 4 g in 50 mL of coking wastewater.

Two models of Langmuir and Freundlich equations were used to fit the isothermal adsorption process of BAC-N3 on coking wastewater at 298 K. The Langmuir equation is based on the adsorption model of a monomolecular layer. According to the mode, the surface of adsorbents is uniform, which allows no competition and indiscrimination in all of the adsorption sites and exhibits the same chemical properties [23]. Freundlich equation assumes that the structure in the surface of adsorbents is nonhomogeneous and that many interactions exist between adsorbents and adsorbate or among adsorbates. The results of the fitting are shown in Figure 5 and Table 5:

$$\text{Langmuir equation: } \frac{1}{q_e} = \frac{1}{q_m} + \frac{1}{q_m a c_e}, \quad (9)$$

$$\text{Freundlich equation: } \lg q_e = \frac{1}{n} \lg c_e + \lg K_F,$$

where q_m is the maximum adsorption capacity (mg/g), a is the Langmuir constant ($\text{L}\cdot\text{mg}^{-1}$), and K_F and n are the adsorption constants.

The linear regression constant (R^2) of Langmuir equations is higher than that of Freundlich equations, as illustrated in Figure 5; this shows that the adsorption equilibrium data were fitted with the Langmuir equation well, and the

adsorption involved monolayer adsorption [24, 25]. The maximum adsorption capacity at 298 K, as calculated by the Langmuir model, was $115.69 \text{ mg}\cdot\text{g}^{-1}$, which is coincided with the experimental data ($106.6 \text{ mg}\cdot\text{g}^{-1}$). The constant n^{-1} in the Freundlich equation is the constant which could characterize the affinity between the adsorbent and the adsorbate in the system; furthermore, this constant could also affect the extent of the difficulty in the adsorption process [26], and adsorption was easily performed when $0.1 < n^{-1} < 5$; however, adsorption forces weakened and pollutants became extremely difficult to expunge when $n^{-1} > 2$ [24, 27]. As calculated by the Freundlich equation, $n^{-1} = 0.428$, proving that the pollutants were easily anchored to the BAC-N3.

3.2.3. Effect of Shaking Speed. The effect of the shaking speed on the COD removal rate at 25°C is shown in Figure 6. It can be seen that the adsorption effect improves as shock speed increases from 0 rpm to 100 rpm or 200 rpm.

In static conditions, adsorption equilibrium at 90 min was reached, but the COD removal rate was only 43.07%. When the shaking speed was increased to 100 rpm, the equilibrium adsorption rate was 75.62% at 120 min, which was increased by 34.91% relative to that at 0 rpm. However, the COD removal rate decreased as the adsorption time increased. Adsorption equilibrium was reached after 150 min of shaking at a shaking speed of 200 rpm. During this time, the COD removal rate was 72.34%, which increased by 2.4% relative to that obtained at 100 rpm. This is because the interaction between BAC-N3 and wastewater was improved via rapid shaking, allowing sufficient contact sites between the adsorption sites and the pollutant. However, when the number of adsorption sites stopped increasing, the adsorption effect became less obvious as the shaking speed continuously increased. Moreover, adsorbent collides with each other more violently with the shaking speed gone up, which was easy to break up the BAC into small particles or powder, and the adsorption effectiveness would be affected. Considering adsorption effect and energy consumption, the ideal shaking speed was 100 rpm, and the BAC-N3 adsorption to COD reached equilibrium after 120 min.

3.2.4. Adsorption Kinetics. Kinetics studies were performed using four ordinary models such as pseudo-second-order model, Bangham model, Elovich model, and intraparticle diffusion model at different shaking speeds. The fitting results are shown in Tables 6 and 7 and Figure 7.

$$\text{Pseudo-second-order kinetic: } \frac{t}{q_t} = \frac{1}{K_2 q_e^2} + \frac{t}{q_e}, \quad (10)$$

where K_2 is the adsorption rate constant of the pseudo-second-order kinetic model ($\text{g}/(\text{mg}\cdot\text{h})$).

$$\text{Elovich model: } q_t = A + K_e \ln t, \quad (11)$$

where K_e is the adsorption rate constant of the Elovich model ($\text{g}/(\text{mg}\cdot\text{h})$) and A is a constant.

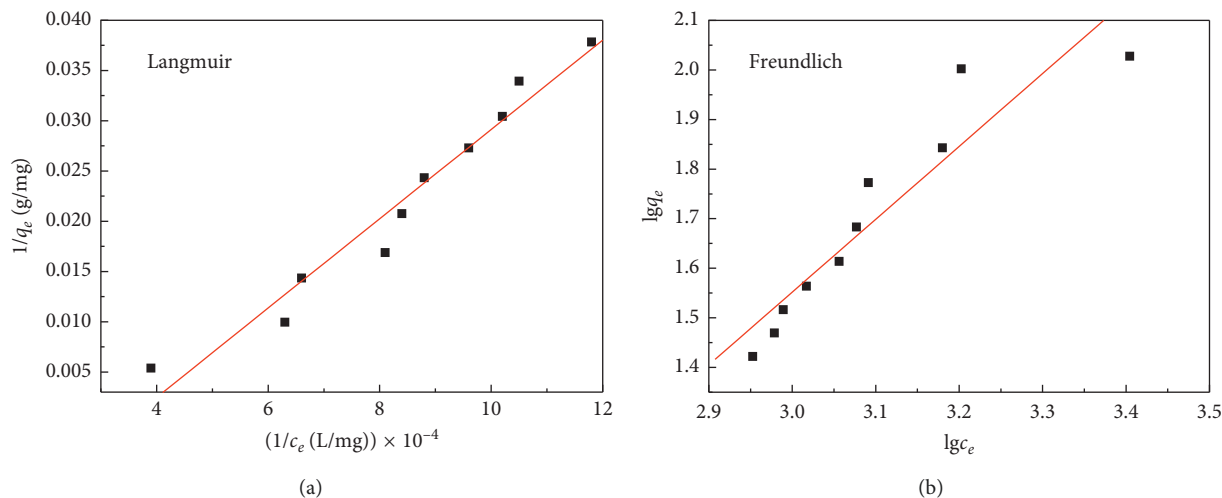


FIGURE 5: Adsorption isotherm: (a) Langmuir equation; (b) Freundlich equation.

TABLE 5: Adsorption isotherm parameter.

Langmuir equation		Freundlich equation			
q_m ($\text{mg}\cdot\text{g}^{-1}$)	a ($\text{L}\cdot\text{mg}^{-1}$)	R^2	K_F	n^{-1}	R^2
115.69	2.06×10^{-3}	0.9786	126.18	0.428	0.9337

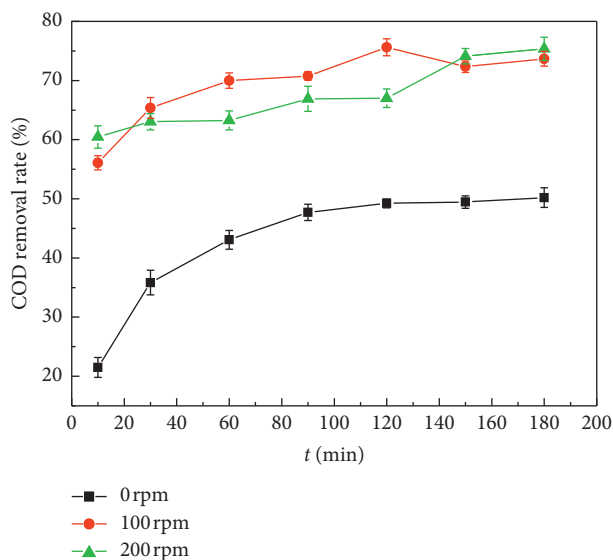


FIGURE 6: Effects of shaking speed on the COD removal rate (the error bars indicate standard deviation of the mean of three sets of data).

$$\text{Bangham model: } \lg q_t = \lg k + \frac{1}{m} \lg t, \quad (12)$$

where m^{-1} is the adsorption rate constant of the Bangham model ($\text{g}/(\text{mg}\cdot\text{h})$) and k is a constant.

$$\text{Intraparticle diffusion model: } q_t = K_p t^{1/2} + C, \quad (13)$$

where K_p is the adsorption rate constant of the intraparticle diffusion model ($\text{mg}/(\text{g}\cdot\text{h}^{0.5})$) and C is a constant.

The results of the kinetic studies showed that the adsorption process of coking wastewater by BAC-N3 followed the pseudo-second-order kinetic model. Some corresponding dynamic parameters were obtained, and the linear regression constant R^2 was $>99\%$. The equilibrium adsorption capacity fitting by using the model was consistent with the experimental values (0 rpm: 22.18 mg/g, 100 rpm: 34.07 mg/g, and 200 rpm: 33.39 mg/g). The pseudo-second-order model could comprehensively affect all adsorption processes, such as liquid film diffusion, particle diffusion, and surface adsorption. Moreover, this model is applicable for the reaction of existing saturation adsorption sites, and the adsorption rate is decided by the square of adsorptive vacancy not occupied in the surface of adsorbents [28]. Tofighy et al. [29] found that the motive force of the pseudo-second-order model is the actions of ionic bonds and covalent bonds between adsorbate and adsorbent, which can conclude the main motive force of BAC adsorption for the removal of COD in coking wastewater is chemisorption processes.

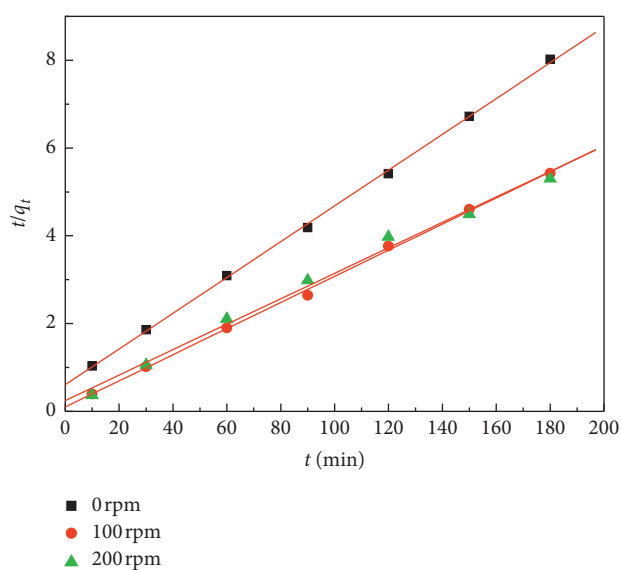
The adsorption mechanism and rate-controlling step can be analysed by the intraparticle diffusion model. As shown in Table 7 and Figure 7, there is a dual linear relation in the adsorption process. The pollutants exist in coking wastewater spread to the adsorbent surface in the first stage, and the second stage indicated that the pollutants were absorbed gradually in adsorbents. Intraparticle diffusion plays a leading role in this stage. Moreover, the slope of the first stage (k_{p1}) is larger than that of the second stage (k_{p2}), which shows that the adsorption rate in the first stage is higher. This is possibly because of a large number of unoccupied active sites in adsorbents at the beginning of adsorption. When adsorption of the pollutant on BAC-N3 surface reached saturation, intraparticle diffusion occurred. In this time, the

TABLE 6: Kinetic parameters of adsorption using pseudo-second-order model, Elovich kinetic model, and Bangham kinetic model.

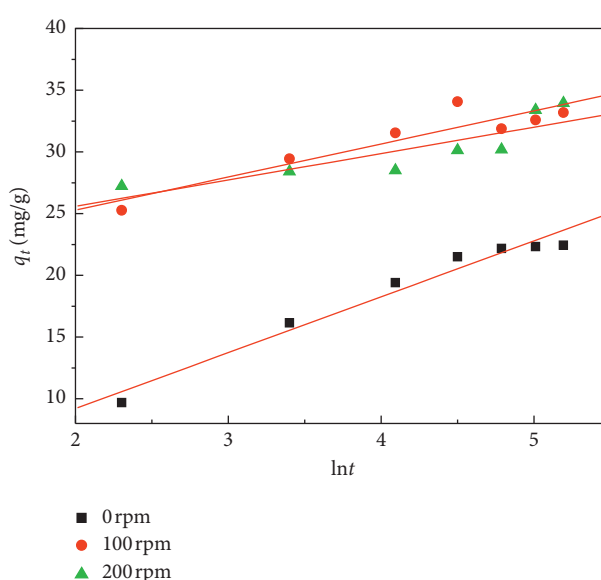
Shaking speed (rpm)	Pseudo-second-order model			Elovich kinetic model			Bangham kinetic model		
	q_e (mg·g ⁻¹)	K_2 (g/(mg·h))	R^2	k_e (g/(mg·h))	A	R^2	k (g/(mg·h))	m	R^2
0	24.528	0.0028	0.9994	4.5270	0.1538	0.9831	5.5101	3.4642	0.9641
100	33.602	0.0089	0.9993	2.6838	19.909	0.9279	21.125	10.903	0.9298
200	34.483	0.0034	0.9959	2.1392	21.308	0.8602	22.434	14.126	0.8733

TABLE 7: Kinetic parameters of adsorption using the intraparticle diffusion model.

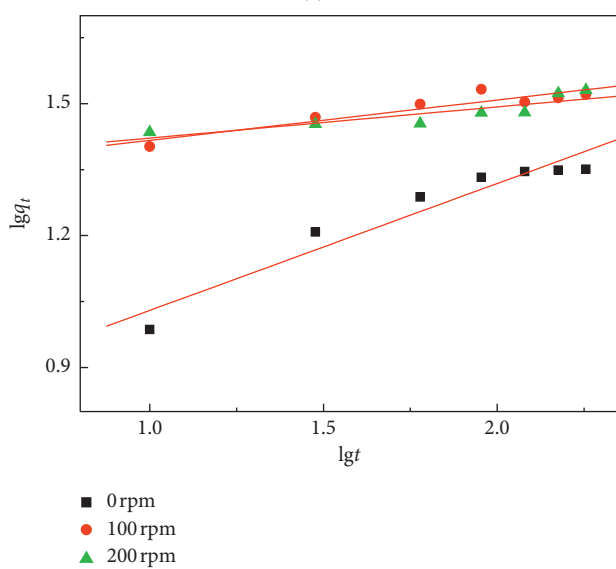
Shaking speed (rpm)	Intraparticle diffusion model					
	k_{p1}	C_1	R^2	k_{p2}	C_2	R^2
0	1.8389	4.7896	0.9799	0.1074	20.9996	0.9983
100	1.3427	21.3931	0.9916	0.5324	26.0552	0.9998
200	1.5439	25.9375	0.9372	0.4070	13.6655	0.9373



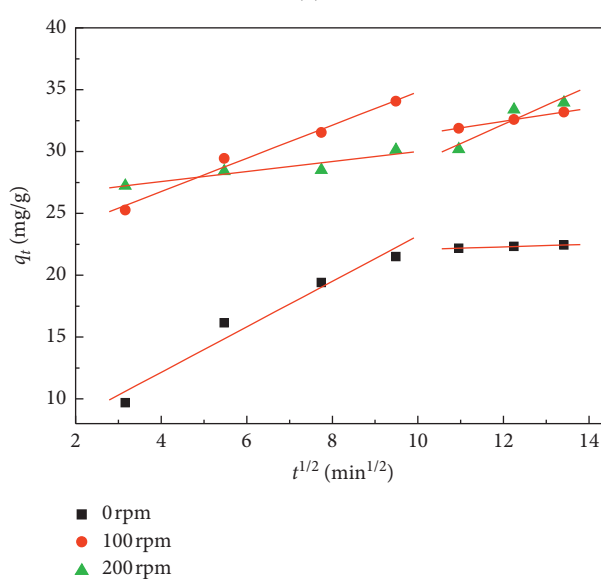
(a)



(b)



(c)



(d)

FIGURE 7: Fitting curves of adsorption kinetic equations: (a) pseudo-second-order kinetic model; (b) Elovich model; (c) Bangham model; (d) intraparticle diffusion model.

adsorption resistance increased, which causes adsorption rate to decline.

4. Conclusions

In this work, BAC was developed by nitric acid modification at different concentrations for coking wastewater treatment. The BACs' pore structure, surface chemical properties, and their ability to remove COD from coking wastewater were investigated. The effects of nitric acid concentration, addition amount, shaking speed, and adsorption time were studied. And the adsorption isotherm and thermodynamics of the adsorption process were studied. The conclusions are as follows:

- (1) After modification by nitric acid, the BET specific surface area, iodine adsorption value, and the oxygen-containing functional groups of BAC increase, and the adsorption effect of COD from coking wastewater was also better. The best modification effect was obtained under the 3 mol/L. At this time, the COD removal rate was improved by 22.78% relative to that of unmodified BAC.
- (2) The optimized conditions for the adsorption of coking wastewater were as follows: 4 g of additional BAC-N3 per 50 mL of coking wastewater, 100 rpm shaking speed, and 120 min adsorption time; the COD removal rate is 77.05%, and the adsorption effect was better than that of chitosan flocculent [30], coke powder [31], and some coal-based adsorbent [32].
- (3) The adsorption process was fitted by the pseudo-second-order kinetic model, and the Langmuir equation could better describe equilibrium adsorption data compared with the Freundlich equation.

Data Availability

The data used to support the findings of this study are available from the corresponding author upon request.

Conflicts of Interest

The authors declare that they have no conflicts of interest regarding the publication of this article.

Acknowledgments

The authors wish to thank the Science and Technology Projects of Xianyang (2018k02-19) for their financial support of this work.

References

- [1] X. Jiang, X. Z. Lan, X. P. Jing, Y. H. Song, and X. D. Xing, "Research on experiment of blue coke-based activated carbon by physical activation in different medium," *Coal Conversion*, vol. 42, no. 2, pp. 65–71, 2019.
- [2] Y. H. Song, Q. N. Ma, X. Li, J. Zhou, and Y. H. Tian, "The Influence of activation temperature on structure and properties of semi-coke-based activated carbon," *Materials Review*, vol. 30, no. 1, pp. 34–37, 2016.
- [3] S. R. Sivakkumar and A. G. Pandolfo, "Evaluation of lithium-ion capacitors assembled with pre-lithiated graphite anode and activated carbon cathode," *Electrochimica Acta*, vol. 65, no. 30, pp. 280–287, 2012.
- [4] Y. N. Ye, L. J. Chen, L. Q. Liu et al., "Effect of preparation procedure of coal-based activated carbons on iodine adsorption," *Materials Review*, vol. 29, no. s1, p. 327, 2015.
- [5] M.-X. Wang, C.-Y. Wang, M.-M. Chen et al., "Preparation of high-performance activated carbons for electric double layer capacitors by KOH activation of mesophase pitches," *New Carbon Materials*, vol. 25, no. 4, pp. 285–290, 2010.
- [6] Y. H. Song, L. Zhang, X. Jiang, and Y. H. Tian, "Effect of reaction temperature on activated carbon by steam activation from blue-coke powder," *Coal Conversion*, vol. 40, no. 5, pp. 56–62, 2017.
- [7] Y. H. Tian, X. Z. Lan, J. Zhou, X. Y. Chen, and J. Zhou, "Reparation of activated carbon from blue coke powder by microwave radiation and KOH activation," *Chemical Engineering*, vol. 38, no. 10, pp. 225–228, 2010.
- [8] N. Wibowo, L. Setyadhi, D. Wibowo, J. Setiawan, S. Ismadji et al., "Adsorption of benzene and toluene from aqueous solutions onto activated carbon and its acid and heat treated forms: influence of surface chemistry on adsorption," *Journal of Hazardous Materials*, vol. 146, no. 1-2, pp. 237–242, 2007.
- [9] S. M. Soltani, S. K. Yazdi, S. Hosseini, and M. K. Gargari, "Effect of nitric acid modification on porous characteristics of mesoporous char synthesized from the pyrolysis of used cigarette filters," *Journal of Environmental Chemical Engineering*, vol. 2, no. 3, pp. 1301–1308, 2014.
- [10] L. Tong, W. Q. Xu, H. Qi et al., "Enhanced effect of O/N groups on the Hg removal efficiency over the HNO₃-modified activated carbon," *Acta Physico-Chimica Sinica*, vol. 31, no. 3, pp. 512–518, 2015.
- [11] Z. G. Zhang, Y. Y. Ma, J. G. Fan, X. L. Sun, and W. X. Li, "Adsorption of benzothiophene in simulated gasoline on nitric acid modified activated carbon," *Acta Petrolei Sinica (Petroleum Processing Section)*, vol. 30, no. 1, pp. 47–52, 2014.
- [12] S. Babel and T. A. Kurniawan, "Cr(VI) removal from synthetic wastewater using coconut shell charcoal and commercial activated carbon modified with oxidizing agents and/or chitosan," *Chemosphere*, vol. 54, no. 7, pp. 951–967, 2004.
- [13] C. H. Wei, M. H. He, Y. Ren, B. G. Li, and J. G. Chen, "Pollution characteristics of coking wastewater and control strategies: biological treatment process and technology," *Acta Scientiae Circumstantiae*, vol. 27, no. 7, pp. 1083–1093, 2007.
- [14] M. Seredych and T. J. Bandosz, "Adsorption of dibenzothiophenes on nanoporous carbons: identification of specific adsorption sites governing capacity and selectivity," *Energy & Fuels*, vol. 24, no. 6, pp. 3352–3360, 2010.
- [15] A. Gil, G. De La Puente, and P. Grange, "Evidence of textural modifications of an activated carbon on liquid phase oxidation treatments," *Microporous Materials*, vol. 12, no. 1–3, pp. 51–61, 1997.
- [16] X. Lan, X. Jiang, Y. Song, X. Jing, and X. Xing, "The effect of activation temperature on structure and properties of blue coke-based activated carbon by CO₂ activation," *Green Processing and Synthesis*, vol. 8, no. 1, pp. 837–845, 2019.
- [17] L. A. Laura and D. H. Fairbrother, "Effect of wet chemical treatments on the distribution of surface oxides on carbonaceous materials," *Carbon*, vol. 45, no. 1, pp. 47–54, 2007.
- [18] V. L. Snoeyink and W. J. Weber, "The surface chemistry of active carbon; a discussion of structure and surface functional

- groups," *Environmental Science & Technology*, vol. 1, no. 3, pp. 228–234, 1967.
- [19] A.-N. A. EL-Hendawy, "Influence of HNO₃ oxidation on the structure and adsorptive properties of corncob-based activated carbon," *Carbon*, vol. 41, no. 4, pp. 713–722, 2003.
- [20] M. Seredych, J. Lison, U. Jans, and T. J. Bandoz, "Textural and chemical factors affecting adsorption capacity of activated carbon in highly efficient desulfurization of diesel fuel," *Carbon*, vol. 47, no. 10, pp. 2491–2500, 2009.
- [21] Y. Z. Fan, B. Z. Wang, L. Wang, and M. Yu, "Adsorption of organic micropollutants on modified activated carbons," *Environmental Chemistry*, vol. 20, no. 5, pp. 444–448, 2001.
- [22] W. W. Gao, Y. Gong, Y. N. Gao, B. Chen, and X. Jiang, "Adsorption of semi-coking wastewater on activated carbon loaded cerium and manganese," *Bulletin of the Chinese Ceramic Society*, vol. 36, no. 1, pp. 197–204, 2017.
- [23] J. Liu, Y. Feng, X. W. Tan, Y. Yan, and H. P. Zhang, "Adsorption of EDTA wastewater by acid modified activated carbon," *Materials Review*, vol. 29, no. 10, pp. 81–86, 2015.
- [24] X. Liang, L. Q. Li, Z. Liu et al., "Effect of microwave and alkaline solution modification activated carbons on adsorption properties of acetone," *Journal of Central South University (Science and Technology)*, vol. 46, no. 2, pp. 743–750, 2015.
- [25] V. Vimonses, S. Lei, B. Jin, C. W. K. Chow, and C. Saint, "Kinetic study and equilibrium isotherm analysis of Congo Red adsorption by clay materials," *Chemical Engineering Journal*, vol. 148, no. 2-3, pp. 354–364, 2009.
- [26] J. Liu, Q. X. Zhu, X. W. Tan, Y. Yan, and H. P. Zhang, "Adsorption of methyl orange on modified activated carbon," *The Chinese Journal of Process Engineering*, vol. 16, no. 2, pp. 222–227, 2016.
- [27] M. Sarkar and P. Majumdar, "Application of response surface methodology for optimization of heavy metal biosorption using surfactant modified chitosan bead," *Chemical Engineering Journal*, vol. 175, no. 15, pp. 376–387, 2011.
- [28] W. W. Gao, T. Su, Y. Gong et al., "Study of adsorption property of coking wastewater on activated carbon loaded copper," *Non-Metallic Mines*, vol. 39, no. 1, pp. 40–43, 2016.
- [29] M. A. Tofiqy and T. Mohammadi, "Adsorption of divalent heavy metal ions from water using carbon nanotube sheets," *Journal of Hazardous Materials*, vol. 185, no. 1, pp. 140–147, 2011.
- [30] W. B. Ou, F. Zhu, P. Wang, and C. M. Shi, "Study of chitosan flocculant to the COD removal of coking wastewater effluent," *Science Technology and Engineering*, vol. 14, no. 21, pp. 167–172, 2014.
- [31] B. H. Yan, X. L. Li, Q. Jiang, L. Xu, and X. X. Ma, "Study on advanced treatment of coking wastewater by coke powder adsorption," *Clean Coal Technology*, vol. 25, no. 1, pp. 160–167, 2019.
- [32] Z. P. Li, Q. Y. Gao, D. Chen et al., "Experimental study on treatment of coking wastewater by coal-based adsorbent," *Applied Chemical Industry*, vol. 48, no. 10, pp. 2403–2406, 2019.

Research Article

Synthesis of a Superhydrophobic Polyvinyl Alcohol Sponge Using Water as the Only Solvent for Continuous Oil-Water Separation

Junyong Chen, Junhui Xiang , Xian Yue, Huaxin Li, and Xianbo Yu

Center of Materials Science and Optoelectronic Engineering, College of Materials Science and Optoelectronic Technology, University of the Chinese Academy of Sciences, Beijing 100048, China

Correspondence should be addressed to Junhui Xiang; xiangjh@ucas.edu.cn

Received 15 July 2019; Revised 5 September 2019; Accepted 10 September 2019; Published 20 October 2019

Guest Editor: Mohamed R. Berber

Copyright © 2019 Junyong Chen et al. This is an open access article distributed under the Creative Commons Attribution License, which permits unrestricted use, distribution, and reproduction in any medium, provided the original work is properly cited.

Few cases of hydrophobic materials synthesized in water have been reported. In this work, water, as the only solvent, is used to prepare a superhydrophobic sponge via a facile and environment-friendly route. The as-prepared sponge, namely silylated polyvinyl alcohol (PVA) sponge, exhibits superhydrophobic and superoleophilic characters. It has the static water contact angle (WCA) of 152 ± 1 and the static oil contact angle (OCA) of 0° , which can lead to excellent selectivity for oil-water separation. Besides, the methyltriethoxysilane (MTES) can form a stable mixed structure with the PVA skeleton, resulting in the rare shedding of polymethylsiloxane nanoparticles and the long-term stability for oil-water separation. Furthermore, the silylated sponge shows a high separation efficiency ($>99.6\%$), removing oil up to 6200~14000 times of its own mass. The findings demonstrated that the silylated superhydrophobic sponge can be a promising candidate in water treatment application.

1. Introduction

Along with increasing offshore oil extraction and transportation, oil contamination problems are becoming serious, posing a threat to the living environment and human health [1, 2]. Therefore, cleaning oil from water is an urgent and challenging task [3]. A wide variety of strategies [4] have been developed to eliminate oil pollution, such as burning [5], mechanical extraction [6], coagulation [7], and absorption [8]. Among these technologies, the application of absorbents is considered to be the most attractive for oil removal because of the high efficiency and ease of operation [9]. Till date, a variety of absorbing materials, including commercial resins [10], fibers [11], and mineral products [12], have been developed and widely applied in oil-water separation field. However, these traditional absorbents exhibit poor selectivity, low absorptivity, or difficulty in scale-up. Moreover, many of them are undesirable due to the poor abilities in regeneration and recycling. Recently, a large variety of novel, efficient absorbents are becoming a hotspot in oil-water separation, such as carbon nanotubes (CNTs) [12–14], graphene-based materials [15–17], nanocellulose

[18], polyurethane (PU) [19–21], and PVA-based absorbents [22].

Among them, commercial PU and PVA sponges are viewed as the most potential materials in oil-water separation, because of their low cost, high porosity, and high absorption ability, as well as their easy mass production. At present, the PU- and PVA-based materials with surface hydrophobicity modification have made remarkable achievements in oil-water separation. For example, Pan et al. [23] reported a magnetic polymer-based graphene foam with high oil wettability for oil-water separation; nevertheless, the complicated synthesis route limited its application. Pan et al. [23] and coworkers prepared hydrophobic polyvinyl formaldehyde sponges by one-step surface modification, but massive pyridine, a strong virose organic reagent, is involved as the solvent. Yuan [24] and coworkers designed a hollow $\text{SiO}_2@ \text{MnO}_2$ modified PU foam for high-efficiency oil-water separation; however, MnO_2 may introduce heavy metals (Mn^{4+}) and lead to secondary pollution. Given limits of the cases discussed above, we raised a facile and green one-pot synthesis of silylated PVA sponge for oil-water separation, possessing advantages (e.g., high porosity, stable structure,

and low cost). The raw materials, i.e., PVA and MTES, are biocompatible and environment-friendly. The solvent, other than commonly used organic solvent, is only deionized water. The as-made modified PVA sponge exhibited superhydrophobic and superoleophilic properties [25]. Furthermore, the modified PVA sponge could remove oil from water under the pressure of a pump, featuring in high separation capacity, excellent efficiency, and reusability. To sum up, this work provides a facile and green one-pot strategy to prepare modified PVA sponge, which can be applied for practical oil spill treatment and environment protection.

2. Materials and Methods

2.1. Materials. The reagents, including methyltriethoxysilane (MTES, $\geq 98\%$), hydrochloric acid (HCl, AR), and ammonia (NH_4OH , $\geq 28\%$), were bought from Sinopharm Chemical Reagent Co., Ltd (Shanghai, China). Sudan III and Methyl blue were purchased from Sigma chemistry Co. Ltd (Shanghai, China). Organic solvents, including dichloromethane (AR), chloroform (AR), *n*-hexane (AR), toluene (AR), and chlorobenzene (AR), were obtained from Beijing Chemical Reagents Co. (Beijing, China). Gasoline was purchased from Sinopec Corp. Commercial PVA sponge was supplied by Alibaba Enterprise. The deionized water was used to make up all mixed solutions and throughout the experiments.

2.2. Preparation of Silylated PVA Sponge. A facile and green technological approach was carried out to produce the silylated PVA sponge. Firstly, methyltriethoxysilane (3 ml), with a certain amount of deionized water, was added into a beaker successively, and 0.2 ml of hydrochloric acid catalyst (w/w 1% HCl) was added into the flask in a moment, and then stirred for 0.5 h. Observing a uniformly continuous phase of the mixture, a certain amount of dilute ammonia (0.5 mol/L) was added rapidly and was then kept stirring for a minute at room temperature. Secondly, soak the pre-prepared dried PVA sponge in the mixture for one minute, and then ageing was done at 50°C for 3 hours. Subsequently, the wet sponge was washed with deionized water for several times. Finally, the wet sponge was freeze-dried for 24 h at room temperature to get the silylated PVA sponge. The preparation process and mechanism of the silylated sponge were shown schematically in Figure 1.

2.3. Characterization. The morphologies of the pure and silylated PVA sponge were obtained by a scanning electron microscope (SEM S-4800 HITACHI). The Fourier transform infrared (FTIR) spectra of the two samples were observed by a VERTEX 70 FTIR spectrometer (Bruker, Germany). All spectra were recorded between 4000 and 500 cm^{-1} with a 4 cm^{-1} and 16 scans per sample. The crystal structures of them were measured by MSAL-XD2 X-ray diffractometer in the range of 5 – 40° (2θ). Static contact angle measurements of the two samples were performed by the contact angle measuring system (JC2000C1, POWEREACH).

2.4. Oil-Water Separation Experiments. First of all, a silylated PVA sponge was prepared with the size of $3 \times 3 \times 3\text{ cm}^3$. After that, a simple vacuum suction device is established, as shown in Figure 2. The silylated PVA sponge is connected to a pipe and the other hand of the pipe is connected to a micropump. The silylated PVA sponge is placed at oil-water interface, for the purpose of continuous oil removal from water. When the micropump works, the oil will be pumped to the pipe through the sponge and then collected into an oil collector. At the same time, water will be blocked by the hydrophobic sponge and remain. All the separation tests were operated at room temperature. Through continuous oil-removal tests, we can obtain the separation efficiency (R). R was calculated according to the following equation:

$$R\% = \left(\frac{M}{M_0} \right) \times 100\%, \quad (1)$$

where M_0 is the weight of the original oil mass in the mixture liquid and M is the weight of the collected oil after separation.

3. Results and Discussion

3.1. Characterization

3.1.1. SEM. The surface morphologies of the pure and silylated PVA sponge were observed by the scanning electron microscopy at different magnifications (Figure 3). SEM images of Figures 3(a) and 3(b) reveal that pure PVA sponge exhibits porous three-dimensional interconnected network structure and smooth surface morphology. After MTES coating on the PVA skeleton surface, the PVA skeleton surface exhibits a relatively rough texture. Meanwhile, the high-magnification SEM image indicates that lots of polymethylsiloxane nanoparticles are successfully modified to the PVA skeleton surface. Nevertheless, there are not any large bulks and deep grooves on the surface, as depicted in Figures 3(c) and 3(d). As a result, nanoscaled polymethylsiloxane nanoparticles were uniformly deposited on the PVA skeleton surface. It can be seen from the SEM photographs that a layer of nanostructured particles is attached to the surface of the three-dimensional microporous skeletons of PVA sponge. This typical micronanostructure is the key to superhydrophobic of the hybrids [26, 27].

3.1.2. XRD. In addition, Figure 4 shows the XRD diffraction patterns of PVA sponge and the silylated PVA sponge. As shown in Figure 4(a), the XRD patterns of the PVA sponge demonstrate a typical diffraction peak of PVA at $2\theta = 19.5^\circ$ [28]. As displayed in Figure 4(b), a broad peak appeared at 10° of the silylated PVA sponge, which corresponded to the amorphous peak of SiO_2 , which also indicates the existence of the polymethylsiloxane nanoparticles coatings on the PVA skeleton surface.

3.1.3. FTIR. The surface chemistry of pure PVA sponge and the silylated PVA sponge can be confirmed from the FTIR spectra, as shown in Figure 5. Firstly, Figure 5(a) reveals the

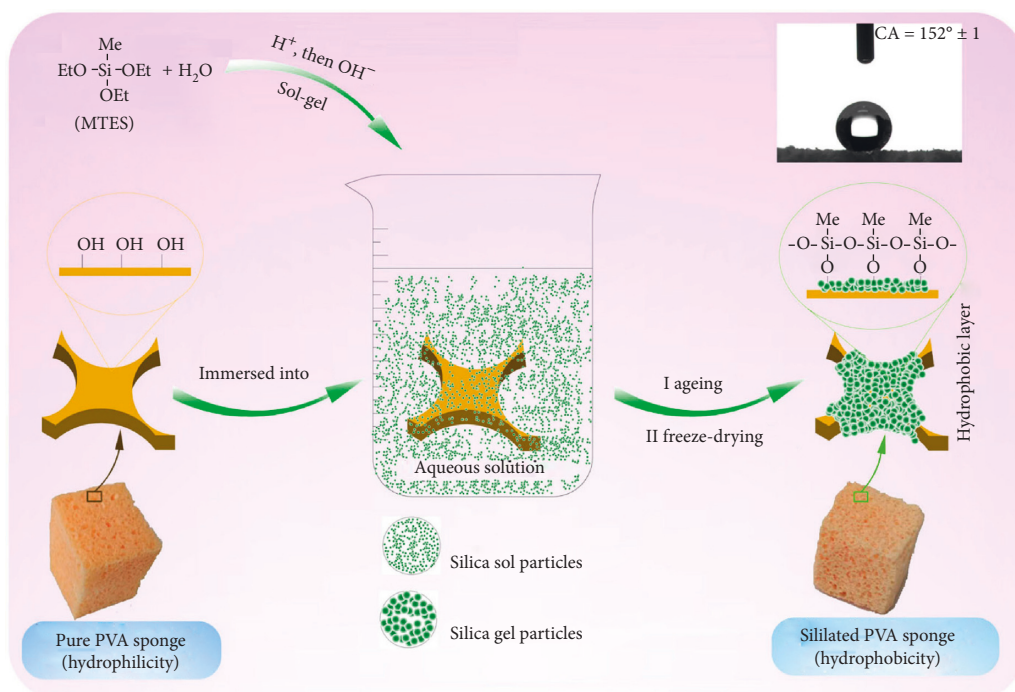


FIGURE 1: Schematic illustration of preparing the silylated PVA sponge by one-pot method.

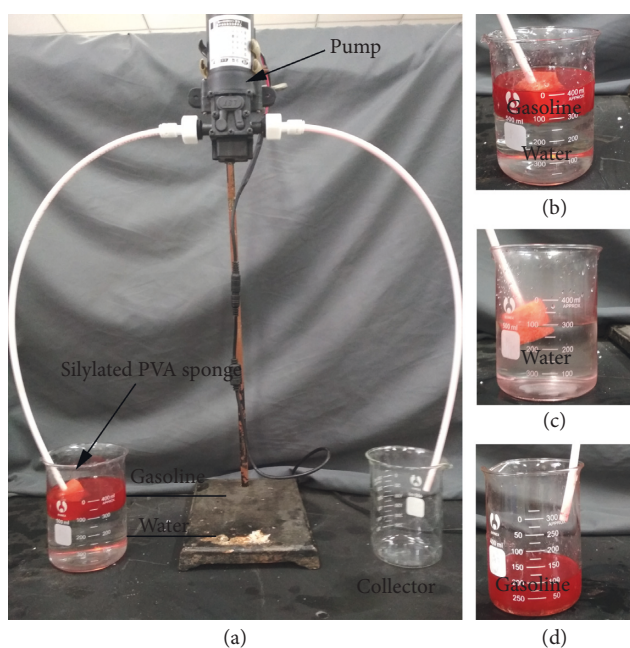


FIGURE 2: Photographs of (a) the continuous oil-water separation device, (b) oil-water mixture image, (c) water left in the beaker after continuous adsorption, and (d) oil collected during continuous adsorption.

FTIR figure of pure PVA sponge. As expected, the FTIR spectrum of PVA shows a broad and strong band at among 3550~3200 cm⁻¹, which corresponded to O-H stretching vibration. Furthermore, the stretching vibration absorption peaks of C-H appear at between 2980 and 2950 cm⁻¹. Comparing the FTIR spectrum of the silylated PVA sponge (Figure 5(b)) [29, 30], besides the typical peaks of PVA sponge, the peak at 1080 cm⁻¹ is attributed to the asymmetric

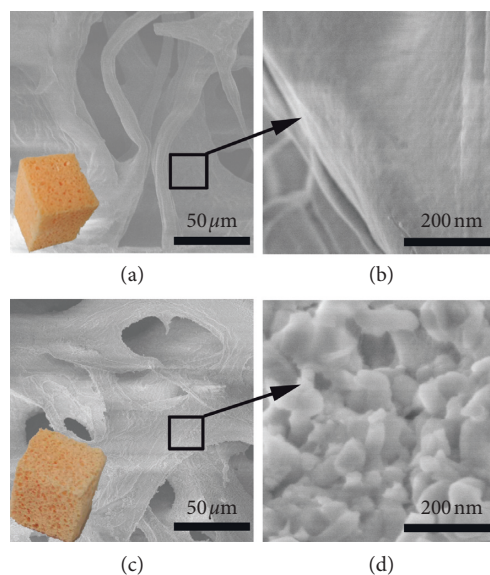


FIGURE 3: SEM images with different magnifications for pure PVA sponge (a, b) and the silylated PVA sponge (c, d). Insets are their corresponding digital photographs.

stretching vibration of Si-O-Si, and the characteristic peak at 800 cm⁻¹ corresponds to the Si-O-Si symmetric stretching vibration [31–33]. Moreover, due to the successful modification of MTES on the surface of PVA sponge, the O-H stretching vibration of PVA is significantly weakened. This series of data indicate that the MTES has successfully connected onto the surface of the porous PVA sponge.

3.1.4. Wettability. The wetting property of the pure and silylated PVA sponge was studied by contact angle

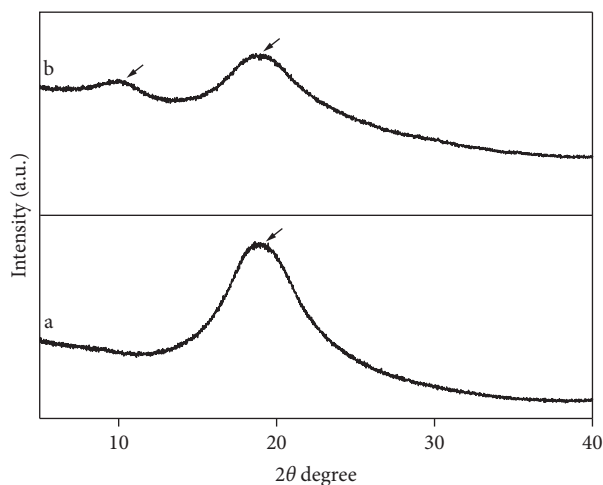


FIGURE 4: XRD spectra of pure PVA sponge (a) and the silylated PVA sponge (b).

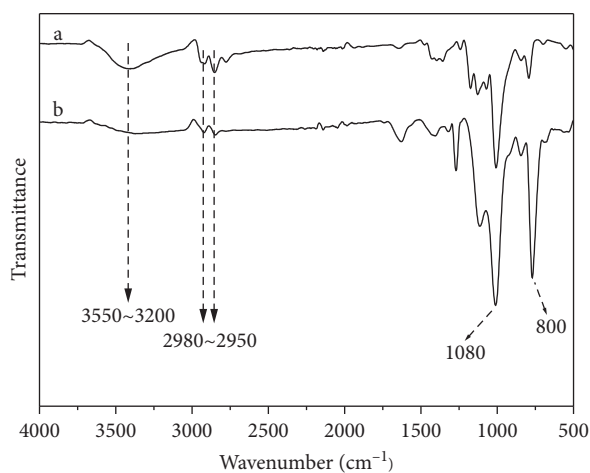


FIGURE 5: FTIR spectra of pure PVA sponge (a) and the silylated PVA sponge (b).

measurement, and the static WCAs were measured at room temperature. As shown in Figure 6, droplets of water and gasoline were deposited onto the pure and silylated PVA skeleton surface. Obviously, the pure PVA sponge showed a strong lyophilic property, as both water and gasoline droplets were absorbed instantaneously (Figure 6(a)). In Figure 6(b), the gasoline immediately penetrated into the silylated PVA sponge, while water remained at the surface, demonstrating that the silylated sponge has combined hydrophobic and oleophilic properties. Figure 6(c) indicated that the static contact angle of the pure PVA sponge is 0° . On the contrary, the silylated PVA sponge displayed a high contact angle, up to $152^\circ \pm 1$, as shown in Figure 6(d). The wettability of material depends on both chemical composition and geometrical microstructure of the solid interface, on the basis of Wenzel's theory [34–36]. According to thermodynamic equilibrium, the apparent contact angle and the roughness factor have the following relationship:

$$\cos \theta^w = r \cos \theta, \quad (2)$$

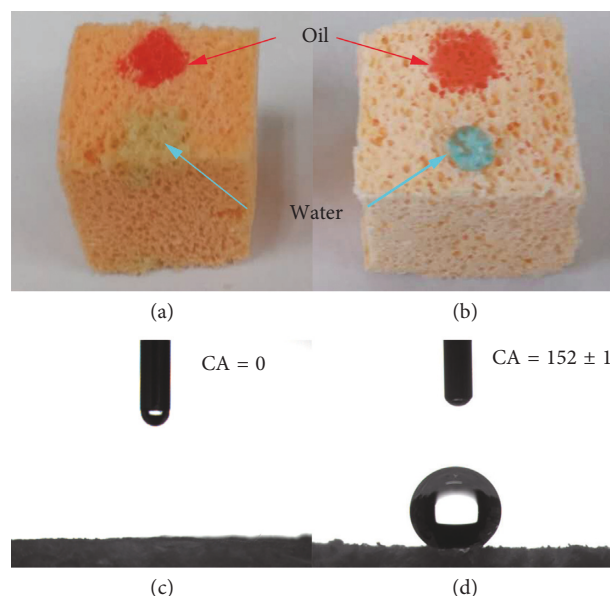


FIGURE 6: Water (colored blue) and oil (colored red) dropped onto the surface of pure PVA sponge (a) and the silylated PVA sponge (b). WCAs of pure PVA sponge (c) and the silylated PVA sponge (d). Plant oil is colored red with Sudan III and water is colored blue with Methyl blue in advance, respectively.

where θ^w refers to the apparent contact angle, r corresponds to the roughness factor of the given interface, and θ represents Young's angle. Herein, the surface energy of the sponge was effectively decreased by the polymethylsiloxane groups. Besides, the PVA sponge coated with polymethylsiloxane nanoparticles exhibits superhigh surface roughness. Hence, the composites displayed excellent hydrophobicity with a surprisingly high contact angle ($152^\circ \pm 1$). In this study, the surface of silylated PVA sponge consists of disorder and dispersive nanometer-sized polymethylsiloxane particles; therefore, it owns high roughness and exhibits superhydrophobic property.

3.2. Absorption Selectivity. In our case, in order to verify the super oil-removal ability, oil-water separation experiments were implemented with two different densities of oil (Figure 7). Gasoline and chloroform were dropped onto the surface and bottom of aqueous phase, respectively. The silylated PVA sponge can easily remove the gasoline and chloroform from water. The result shows that the silylated PVA sponge has excellent absorption selectivity, whether used on the surface or bottom of the water. In addition, we investigated the selectivity of separation of hydrophobic solvents (various types of oil). However, it showed no selectivity toward the mixture of various hydrophobic solvents. As shown in Figure S2, the static contact angle of the prepared material was zero for all kinds of hydrophobic solvents and there was no difference in the contact angle among different kinds of hydrophobic solvents. Therefore, except for water drops, other different kinds of oil can be well absorbed by the prepared material quickly. This is the reason why reported materials can remove various types of oil pollution from water quickly and efficiently.

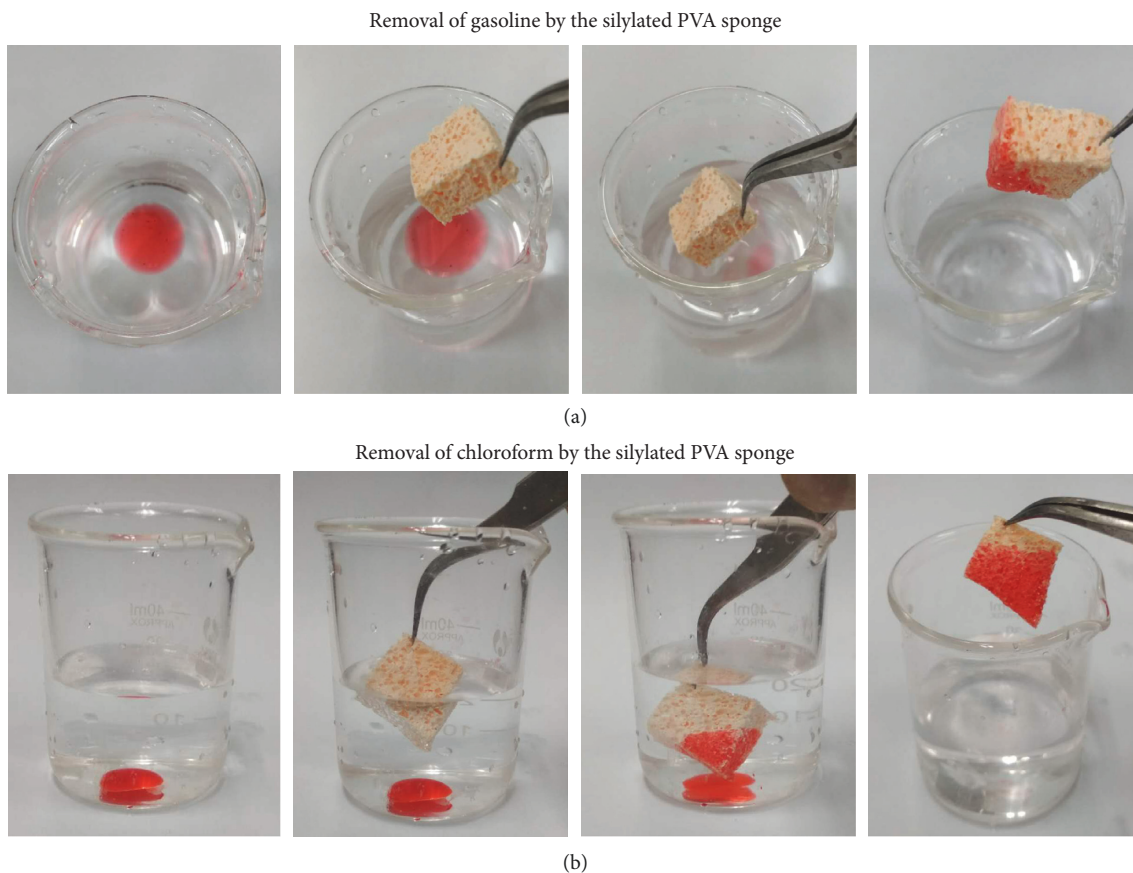


FIGURE 7: Selected removal of gasoline (a) and chloroform (b) from water with the silylated PVA sponge. Gasoline and chloroform are colored red with Sudan III in advance.

3.3. Continuous Oil Removal and Absorption Capability.

Because of the superhydrophobic properties, the silylated PVA sponge may become a potential oil-water separation material. In this study, a continuous oil-water separation device was established to evaluate the absorption capacity of the synthetic absorbent. In the experiment, a functionalized PVA sponge (specification: $3 \times 3 \times 3 \text{ cm}^3$, 2.21 g) was placed in a container with oil-water mixture (300 ml water and 100 ml oil). The functionalized PVA sponge was connected to the micropump through a pipe (Figure 2). With the aid of the negative pressure generated by the micropump, oil easily passed through the silylated PVA sponge, while water was blocked to achieve selective separation. The whole experiment was completed within 1 minute, leaving clean water in the container.

In order to examine the oil-removal capacity of the silylated PVA sponge, various types of oil and organic solvents are selected to implement continuous separation experiments for two hours. Then, the oil mass flux and separation efficiency are listed in Figure 8. Oil and organic solvents used in this study included dichloromethane, chloroform, *n*-hexane, toluene, chlorobenzene, and gasoline. As shown in Figure 8(a), the silylated PVA sponge exhibits oil mass fluxes ranging from 353 to $480 \text{ L}\cdot\text{m}^{-2}\cdot\text{min}^{-1}$. Moreover, the separation efficiency of the absorbent still reaches up to 99.6% during an hour separation. Such high mass fluxes meant the silylated PVA sponge could remove

oil from the water up to 6200~14000 times of its own mass, which is significantly higher than all the materials mentioned in Table 1. As a comparison, the unmodified PVA sponge was used for separating oil from water. As shown in Figure S3, the unmodified PVA sponge is placed at the oil-water interface. Under the pressure of the pump, water is absorbed together with gasoline; so, the unmodified PVA sponge shows no effect on oil-water separation. This is because the PVA sponge exhibits amphiphilic property before hydrophobic modification, which is also confirmed by Figure 6(a). Therefore, the PVA sponge before modification has no selectivity for oil-water separation.

Moreover, we investigated the durability and repeatability of the silylated PVA sponge. As shown in Figure S1, the silylated PVA sponge did not suffer from obviously damage and any loss in separation capacity even after 10 cycles. This is because that MTES could form a stable mixed structure with the PVA skeleton in synthesis, resulting in the rare shedding of polymethylsiloxane nanoparticles and the long-term stability for oil-water separation. The results demonstrated the as-made sponge presented excellent separation capacity and reusability.

3.4. Comparison of Various Absorbents. Saturated absorption capacity depends mainly on the parameters such as the

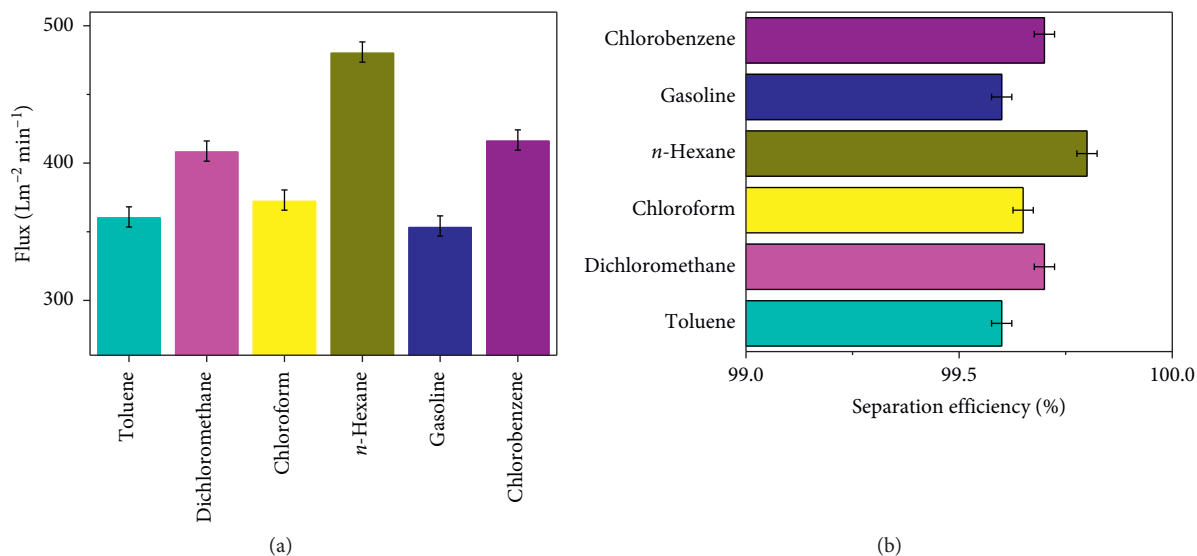


FIGURE 8: (a) The absorption flux and (b) the separation efficiency of the silylated PVA sponge for oil and organic solvents during 1-hour separation.

TABLE 1: Comparison of the absorption capability of various absorbents.

Absorbent	Cost	Oil	Sorption capacity, g/g		Oil recovery method	Ref.
			Once	Total		
Silane-modified nanocellulose	+	Toluene	~170	1020	Distillation	[37]
Functional bacterial cellulose	++	Diesel	120	1200	Squeezing	[19]
Grapheme sponge	++	Dodecane	~20	200	Burning	[38]
CNTs hybrids	++	Chloroform	~95	570	Acetone extraction	[39]
Attapulgite coated PU sponge	—	Kerosene	—	3200	Continuous separation	[40]
Silylated PVA sponge	—	Toluene	—	7600	Continuous separation	Present work

Note: "once" means saturated absorption capacity; "total" is calculated through saturated absorption capacity multiplied by the number of cycles, or mass flux multiplied by the running time.

absorbent's own density and the type of absorbed oil. It is inevitably biased to evaluate the capability of absorbents only according to their saturated absorption capacity. Because the service life of absorbent (cycle number or accumulated use time) is also an important factor used for evaluation of the capacity of absorbent. The separation efficiency of adsorbent often decreases after repeated recycling, which may be due to the loss of functional groups and the decrease of material roughness. Hence, in this work, the total absorption capacity will be calculated according to the number of cycles and the saturated absorption capacity of a part of absorbents reported in recent years. The capability of absorbents was evaluated with comparison of the total absorption capacity. A variety of absorbents and their performances are listed in Table 1. Carbonized materials and absorbents, such as graphene or carbon nanotubes, can be used as the representatives of novel absorbents, revealing excellent absorption performance. Thus, the complexity of the preparation process and high cost limit their practical application. Nanocellulose fiber-based absorbents exhibited excellent absorption capacity for oil and organic solvents, because of its low density. Besides, functionalized 3D PU-based absorbents have become a kind of hot material

pursued by scientists, due to its low cost and compressibility. In the present work, the silylated PVA sponge could be used to separate oil up to 6200~14000 times of its own mass, which is significantly higher than all the absorbents mentioned above. This means that it is an excellent superabsorbent for oil removal and collection. The raw materials of the silylated PVA sponge are really cheap and can be produced on a large scale. Moreover, MTES and PVA are classified as environmentally friendly materials. Besides, the preparation of the silylated PVA sponge is carried out in an aqueous solution, and the process is nonpolluting. These results are encouraging and suggest that the silylated PVA sponge has great potential in practical application.

4. Conclusions

In summary, a facile and environment-friendly synthetic route has been proposed to successfully prepare the silylated PVA sponge with superhydrophobicity and superoleophilicity, without using any organic solvent and multistep reaction. SEM photographs revealed that the surface of interconnected pores in the original PVA skeleton was coated with polymethylsiloxane nanoparticles through an

environment-friendly synthesis method, forming a firm substructure. But, at the same time, the silylated PVA sponge retained original PVA structural integrity. Owing to the silylation of the skeleton surface and such characteristic nanomicro substructures, the silylated PVA sponge possessed superhydrophobicity and superoleophilicity, with the static WCAs running up to $152^\circ \pm 1$. This functionalized sponge could be used as a selective filter to realize continuous and effective oil-water separation with the help of a micropump. The absorbent was chemically robust, and the oil-absorption flux reached ranged from 353 to 480 L·m⁻²·min⁻¹ with excellent separation efficiency (>99.6%). Hence, the silylated PVA sponge, as a promising superabsorbent, may become one of the most potential candidates in water treatment applications.

Data Availability

The data used to support the findings of this study are available from the corresponding author (Junhui Xiang; xiangjh@ucas.edu.cn) upon request.

Conflicts of Interest

The authors declare that they have no conflicts of interest.

Acknowledgments

This work was financially supported by the National Nature Science Foundation of China (No. 50872149).

Supplementary Materials

Figure S1: (a) separation cycles of oil-water mixture; (b) SEM image of the silylated PVA sponge before toluene-water separation; (c) SEM image of the silylated PVA sponge after 10 separation cycles of toluene-water. Figure S2: photograph of water (colored blue) and kinds of hydrophobic solvents (colored red) dropped onto the surface of the silylated PVA sponge. Hydrophobic solvents are colored red with Sudan III and water is colored blue with methyl blue in advance, respectively. Figure S3: photographs of (a) the continuous oil-water separation device and (b) oil-water mixture image after continuous adsorption. Gasoline is colored red with Sudan III in advance. (*Supplementary Materials*)

References

- [1] T. Dalton and D. Jin, "Extent and frequency of vessel oil spills in US marine protected areas," *Marine Pollution Bulletin*, vol. 60, no. 11, pp. 1939–1945, 2010.
- [2] M. Santander, R. T. Rodrigues, and J. Rubio, "Modified jet flotation in oil (petroleum) emulsion/water separations," *Colloids and Surfaces A: Physicochemical and Engineering Aspects*, vol. 375, no. 1–3, pp. 237–244, 2011.
- [3] E. B. Barbier, D. Moreno-Mateos, A. D. Rogers et al., "Ecology: protect the deep sea," *Nature*, vol. 505, no. 7484, pp. 475–477, 2014.
- [4] Z. Xue, Y. Cao, N. Liu, L. Feng, and L. Jiang, "Special wettable materials for oil/water separation," *Journal of Materials Chemistry A*, vol. 2, no. 8, pp. 2445–2460, 2014.
- [5] J. V. Mullin and M. A. Champ, "Introduction/overview to *in situ* burning of oil spills," *Spill Science & Technology Bulletin*, vol. 8, no. 4, pp. 323–330, 2003.
- [6] S. A. Shedid, J. H. Abou-Kassem, and A. Y. Zekri, "Mechanical cleaning of oil spills in seawater using circular conduits," *Energy Sources*, vol. 27, no. 13, pp. 1257–1268, 2005.
- [7] F. Zhang, W. B. Zhang, Z. Shi, D. Wang, J. Jin, and L. Jiang, "Nanowire-haired inorganic membranes with superhydrophilicity and underwater ultralow adhesive superoleophobicity for high-efficiency oil/water separation," *Advanced Materials*, vol. 25, no. 30, pp. 4192–4198, 2013.
- [8] X. Yue, T. Zhang, D. Yang et al., "The synthesis of hierarchical porous Al₂O₃/acrylic resin composites as durable, efficient and recyclable absorbents for oil/water separation," *Chemical Engineering Journal*, vol. 309, pp. 522–531, 2017.
- [9] K. Li, X. Zeng, H. Li, and X. Lai, "Facile fabrication of a robust superhydrophobic/superoleophilic sponge for selective oil absorption from oily water," *RSC Advances*, vol. 4, no. 45, pp. 23861–23868, 2014.
- [10] S. Maiti, I. M. Mishra, S. D. Bhattacharya, and J. K. Joshi, "Removal of oil from oil-in-water emulsion using a packed bed of commercial resin," *Colloids and Surfaces A: Physicochemical and Engineering Aspects*, vol. 389, no. 1–3, pp. 291–298, 2011.
- [11] D. Li, F. Z. Zhu, J. Y. Li, P. Na, and N. Wang, "Preparation and characterization of cellulose fibers from corn straw as natural oil sorbents," *Industrial & Engineering Chemistry Research*, vol. 52, no. 1, pp. 516–524, 2013.
- [12] R. Wahi, L. A. Chuah, T. S. Y. Choong, Z. Ngaini, and M. M. Nourouzi, "Oil removal from aqueous state by natural fibrous sorbent: an overview," *Separation and Purification Technology*, vol. 113, pp. 51–63, 2013.
- [13] H. Wang, E. Wang, Z. Liu et al., "A novel carbon nanotubes reinforced superhydrophobic and superoleophilic polyurethane sponge for selective oil-water separation through a chemical fabrication," *Journal of Materials Chemistry A*, vol. 3, no. 1, pp. 266–273, 2015.
- [14] X. Su, H. Li, X. Lai, Z. Chen, and X. Zeng, "3D porous superhydrophobic CNT/EVA composites for recoverable shape reconfiguration and underwater vibration detection," *Advanced Functional Materials*, vol. 29, no. 24, pp. 1900554–1900564, 2019.
- [15] Z. Li, J. Chen, and Y. Ge, "Removal of lead ion and oil droplet from aqueous solution by lignin-grafted carbon nanotubes," *Chemical Engineering Journal*, vol. 308, pp. 809–817, 2017.
- [16] D. Chakravarty, C. S. Tiwary, L. D. Machado et al., "Zirconia-nanoparticle-reinforced morphology-engineered graphene-based foams," *Advanced Materials*, vol. 27, no. 31, pp. 4534–4543, 2015.
- [17] L. Zhang, H. Li, X. Lai, X. Su, T. Liang, and X. Zeng, "Thiolated graphene-based superhydrophobic sponges for oil-water separation," *Chemical Engineering Journal*, vol. 316, pp. 736–743, 2017.
- [18] P. Saha and L. Dashairya, "Reduced graphene oxide modified melamine formaldehyde (rGO@MF) superhydrophobic sponge for efficient oil-water separation," *Journal of Porous Materials*, vol. 25, no. 5, pp. 1475–1488, 2018.
- [19] H. Sai, R. Fu, L. Xing et al., "Surface modification of bacterial cellulose aerogels' web-like skeleton for oil/water separation," *ACS Applied Materials & Interfaces*, vol. 7, no. 13, pp. 7373–7381, 2015.
- [20] S. Zhou, G. Hao, X. Zhou et al., "One-pot synthesis of robust superhydrophobic, functionalized graphene/polyurethane sponge for effective continuous oil-water separation," *Chemical Engineering Journal*, vol. 302, pp. 155–162, 2016.

- [21] N. Cao, B. Yang, A. Barras, S. Szunerits, and R. Boukherroub, "Polyurethane sponge functionalized with superhydrophobic nanodiamond particles for efficient oil/water separation," *Chemical Engineering Journal*, vol. 307, pp. 319–325, 2017.
- [22] Y. Hu, Y. Zhu, H. Wang et al., "Facile preparation of superhydrophobic metal foam for durable and high efficient continuous oil-water separation," *Chemical Engineering Journal*, vol. 322, pp. 157–166, 2017.
- [23] Y. Pan, K. Shi, C. Peng, W. Wang, Z. Liu, and X. Ji, "Evaluation of hydrophobic polyvinyl-alcohol formaldehyde sponges as absorbents for oil spill," *ACS Applied Materials & Interfaces*, vol. 6, no. 11, pp. 8651–8659, 2014.
- [24] D. Yuan, T. Zhang, Q. Guo, F. Qiu, D. Yang, and Z. Ou, "A novel hierarchical hollow $\text{SiO}_2/\text{MnO}_2$ cubes reinforced elastic polyurethane foam for the highly efficient removal of oil from water," *Chemical Engineering Journal*, vol. 327, pp. 539–547, 2017.
- [25] C. Liu, J. Yang, Y. Tang, L. Yin, H. Tang, and C. Li, "Versatile fabrication of the magnetic polymer-based graphene foam and applications for oil-water separation," *Colloids and Surfaces A: Physicochemical and Engineering Aspects*, vol. 468, pp. 10–16, 2015.
- [26] S. Wang and L. Jiang, "Definition of superhydrophobic states," *Advanced Materials*, vol. 19, no. 21, pp. 3423–3424, 2007.
- [27] S. Wang, L. Feng, and L. Jiang, "One-step solution-immersion process for the fabrication of stable bionic superhydrophobic surfaces," *Advanced Materials*, vol. 18, no. 6, pp. 767–770, 2006.
- [28] H. Sai, L. Xing, J. Xiang et al., "Flexible aerogels with interpenetrating network structure of bacterial cellulose-silica composite from sodium silicate precursor via freeze drying process," *RSC Advances*, vol. 4, no. 57, pp. 30453–30461, 2014.
- [29] D. Ghanbari, M. Salavati-Niasari, and M. Ghasemi-Kooch, "A sonochemical method for synthesis of Fe_3O_4 nanoparticles and thermal stable PVA-based magnetic nanocomposite," *Journal of Industrial and Engineering Chemistry*, vol. 20, no. 6, pp. 3970–3974, 2014.
- [30] T. Pirzada, S. A. Arvidson, C. D. Saquing, S. S. Shah, and S. A. Khan, "Hybrid silica-PVA nanofibers via sol-gel electrospinning," *Langmuir*, vol. 28, no. 13, pp. 5834–5844, 2012.
- [31] S. Kim, A. Cho, S. Kim et al., "Multi-purpose overcoating layers based on PVA/silane hybrid composites for highly transparent, flexible, and durable AgNW/PEDOT: PSS films," *RSC Advances*, vol. 6, no. 23, pp. 19280–19287, 2016.
- [32] L.-Y. Yu, Z.-L. Xu, H.-M. Shen, and H. Yang, "Preparation and characterization of PVDF- SiO_2 composite hollow fiber UF membrane by sol-gel method," *Journal of Membrane Science*, vol. 337, no. 1-2, pp. 257–265, 2009.
- [33] X. Su, H. Li, X. Lai et al., "Vapor-liquid sol-gel approach to fabricating highly durable and robust superhydrophobic polydimethylsiloxane@silica surface on polyester textile for oil-water separation," *ACS Applied Materials & Interfaces*, vol. 9, no. 33, pp. 28089–28099, 2017.
- [34] Y. Wang, X. Su, P. Ding, S. Lu, and H. Yu, "Shape-controlled synthesis of hollow silica colloids," *Langmuir*, vol. 29, no. 37, pp. 11575–11581, 2013.
- [35] R. J. Good, "A thermodynamic derivation of wenzel's modification of young's equation for contact angles-together with a theory of hysteresis," *Journal of the American Chemical Society*, vol. 74, no. 20, pp. 5041–5042, 1952.
- [36] K. L. Johnson, K. Kendall, and A. D. Roberts, "Surface energy and the contact of elastic solids," *Proceedings of the Royal Society A: Mathematical, Physical and Engineering Sciences*, vol. 324, no. 1558, pp. 301–313, 1971.
- [37] F. Jiang and Y.-L. Hsieh, "Amphiphilic superabsorbent cellulose nanofibril aerogels," *Journal of Materials Chemistry A*, vol. 2, no. 18, pp. 6337–6342, 2014.
- [38] R. Wu, B. Yu, X. Liu et al., "One-pot hydrothermal preparation of graphene sponge for the removal of oil and organic solvents," *Applied Surface Science*, vol. 362, pp. 56–62, 2016.
- [39] X. Dong, J. Chen, Y. Ma et al., "Superhydrophobic and superoleophilic hybrid foam of graphene and carbon nanotube for selective removal of oil or organic solvents from the surface of water," *Chemical Communications*, vol. 48, no. 86, pp. 10660–10662, 2012.
- [40] J. Li, C. Xu, Y. Zhang, R. Wang, F. Zha, and H. She, "Robust superhydrophobic attapulgite coated polyurethane sponge for efficient immiscible oil/water mixture and emulsion separation," *Journal of Materials Chemistry A*, vol. 4, no. 40, pp. 15546–15553, 2016.